SUPPORTED VANADIUM OXIDE CATALYSTS IN OXIDATION AND OXIDATIVE DEHYDROGENATION REACTIONS: STRUCTURE AND CATALYTIC PROPERTIES

A thesis submitted to the

UNIVERSITY OF PUNE

for the degree of

DOCTOR OF PHILOSOPHY

(in Chemistry)

BY

SHIJU. N. R.

CATALYSIS DIVISION

NATIONAL CHEMICAL LABORATORY

PUNE- 411008

INDIA

APRIL 2004

Dedicated to My Family

CERTIFICATE

Certified that the work incorporated in the thesis, **"Supported Vanadium Oxide Catalysts in Oxidation and Oxidative Dehydrogenation Reactions: Structure and Catalytic Properties"** submitted by **Mr. N. R. Shiju,** for the Degree of **Doctor of Philosophy**, was carried out by the candidate under my supervision in the Catalysis Division, National Chemical Laboratory, Pune - 411008, India. Materials obtained from other sources have been duly acknowledged in the thesis.

Dr. B. S. Rao

(Research Supervisor)

ACKNOWLEDGEMENTS…

It is my great pleasure to express my heartfelt gratitude to my research supervisor, Dr. B. S. Rao, for his unending support and invaluable guidance throughout the period of this investigation. I sincerely thank him for the care and affection that I received from him in the entire period.

I take this opportunity to express my deepest sense of gratitude towards Dr. C. V. V. Satyanarayana for his timely help, constant support and valuable guidance. I have to acknowledge that, because of him, I didn't feel the absence of Dr. B. S. Rao from NCL. I sincerely thank him.

I am very much grateful to Dr. S. Sivasanker, Head, Catalysis and Inorganic Chemistry Division, NCL, who is very kind and generous towards me and the help I received from him is gratefully acknowledged.

I am also grateful to Dr. A. V. Ramaswamy, former Head of the Division for his support and help during the period of my research work.

I also thank Dr. S. P. Mirajkar for his cooperation and valuable support during the entire period. I have to acknowledge the friendly and cooperative attitude of all scientific staff of our Division. I would like to thank Dr. C. S. Gopinath, Dr. A. P. Singh, Dr. S. B. Halligudi, Dr. S. G. Hegde, Dr. S. Umbarkar, Dr. D. Srinivas, Ms. Violet Samuel, Ms. Agashe, Mrs. Nalini Jacob, Dr. Belhekar, Dr. Awate, Mr. S. C. Jha for their valuable help and cooperation given to me in completing my research work successfully. I am also grateful to Dr. S. P. Gokhale (CMC, NCL) and Prof. M. S. Hegde (IISc, Bangalore) for their generous help in carrying out my research studies.

I also thank Dr. R. Vetrivel, Dr. C. Gopinathan, Dr. Sarada Gopinathan, Mr. V. V. Bokade, Dr. Rajiv Kumar, Dr. P. A. Joy, Dr. Vijayamohanan, Dr. Rajamohanan, Dr. Veda Ramaswamy, Dr. H. S. Soni, Dr. Budhkar, Dr. T. Raja, Dr. Selvaraj, Dr. Manikandan, Dr. A. J. Chandwadkar, Dr. Dongare, Dr. R. A. Shaikh, Mr. C. V. Kavedia, Mr. K. Ramakrishnan for their help on various occasions. I would like to acknowledge the help recieved from Mr. Karunakaran, Mr. Madhu, Mr. Milind and Mr. Katti.

I would like to thank Kalachechi and family, Tresa and family, Mr. Purushothaman and family, Suresh uncle and family for their love and help extended to me throughout my stay in NCL.

I sincerely thank my labmates for their friendly help and kind cooperation during the period of my work. I also thank all my friends in the division and in NCL for their help and support in one way or other, which made my work much easier. I specially thank all my mallu friends, many of them are abroad now, for their love, support and help. They made my life in NCL much better.

I would like to thank all my teachers in various classes for the love and encouragement that I received from them. I have to acknowledge especially my teachers in B.Sc. class who really nourished my interest in Chemistry. I take this occasion to thank all my classmates till M.Tech course whose cooperative attitude helped me very much. Also I thank all well-wishers and friends whose names are not mentioned here.

I would like to thank Dr. S. Sivaram, Director, NCL and Dr. P. Ratnasamy (former Director, NCL) for allowing me to carryout the research work at NCL and CSIR, New Delhi, India, for the financial support in the form of junior and senior research fellowships.

Words are not enough to express my love and gratitude to my family members. It is their love, blessings and prayers that helped me throughout my life. I am very much indebted to them.

Above all, I thank God for his blessings, for forgiving my mistakes, for leading me in the right path and for being there whenever I needed.

Shiju.

CONTENTS

ABBREVIATIONS

BE	**Binding energy**
DRS	**Diffuse reflectance spectroscopy**
DTA	**Differential thermal analysis**
DTG	**Differential thermogravimetry**
EB	**Ethylbenzene**
EPR	**Electron Paramagnetic Resonance**
FTIR	**Fourier Transform Infrared**
FWHM	**Full width at half maximum**
GC-IR	**Gas chromatograph-Infrared spectrometer**
GC-MS	**Gas chromatograph-Mass spectrometer**
GHSV	**Gas hourly space velocity**
ICP-AES	**Inductively coupled plasma atomic emission spectroscopy**
I.D.	**Internal diameter**
LCT	**Lower energy charge transfer**
LRS	**Laser Raman spectroscopy**
MAS	**Magic angle spinning**
MFC	**Mass flow controller**
NMR	**Nuclear Magnetic Resonance**
ODH	**Oxidative dehydrogenation**
PROX	**Preferential oxidation**
SEM	**Scanning electron microscopy**
ST	**Styrene**
TCD	**Thermal conductivity detector**
TG	**Thermogravimetry**
TOS	**Time on stream**
TPR	**Temperature programmed reduction**
WHSV	**Weight hourly space velocity**
XPS	**X-ray photoelectron spectroscopy**
XRD	**X-ray diffraction**

CHAPTER 1
Introduction

1.1. SUPPORTED VANADIUM OXIDE CATALYSTS IN HETEROGENEOUS CATALYSIS

1.1.1. Introduction

Vanadium was first discovered in a Mexican lead ore by the Spanish mineralogist Andrés Manuel del Rio in 1801, who named the new element erythronium [1-4] even before Dalton's atomic theory (1803-1808). However, in 1805, the French chemist H.V. Collet-Descotils erroneously concluded that this new element was only impure chromium and brown ore was a basic lead chromate. Later on, in 1830, the Swedish chemist Nils Gabriel Sefström rediscovered the element from samples of iron smelted from a mine in Sweden and named it vanadium after Vanadis, the old Norse name for the Scandinavian goddess Freyja—the goddess of beauty—because of the richness and variety of colors of its compounds. In 1831, Sefström, J. J. Berzelius and Friedrich Wöhler established unambiguously the chemical uniqueness of vanadium and its identity with del Rio's erythronium [5]. The lead mineral is now known as vanadinite, $Pb_5(VO_4)_3Cl$. Vanadium was isolated in nearly pure form by Roscoe, in 1867, who reduced the chloride with hydrogen.

Vanadium is found in about 152 different minerals among which the important ones are carnotite, roscoelite, vanadinite, and patronite. It is one of the most abundant and widely distributed metals in the earth's crust. It is also found in phosphate rock, certain iron ores and also present in some crude oils in the form of organic complexes, e.g. V–porphyrin complexes [6,7]. The major sources of vanadium are titaniferrous magnetite ores from mines in Australia, China, Russia and South Africa. Much of the vanadium metal being produced is now made by calcium reduction of vanadium pentoxide in a pressure vessel, an adaption of a process developed by McKechnie and Seybair. The annual world production of vanadium is about 38,000 tonnes and almost 80% of this is used as ferrovanadium or as a steel additive, as it makes steel shock- and vibration-resistant. Vanadium alloys are used in aerospace industry also, e.g. titanium–aluminum–vanadium alloys for aero-engine gas turbines and undercarriages of planes. Vanadium is also used in ceramics, electronics, dyes for textiles and leather [1].

1.1.2. Atomic and physical properties of vanadium

The atomic number and atomic weight of vanadium are 23 and 50.9415 respectively. The electron configuration is [Ar] $3d^3$ $4s^2$ and the main oxidation states are +2, +3, +4 and +5. V^{5+} (d^0) can be present in tetrahedral (VO_4), pentahedral (VO_5) and octahedral (VO_6) coordination environment and tends to form polyoxoanions [1]. V^{4+} (d^1) is also stable and is mostly present in square pyramidal or pseudo-octahedral coordination as an isolated cation. Other oxidation states such as V^{3+} (d^2) and V^{2+} (d^3) are less stable and only present under reducing conditions. The melting point of vanadium is 1915^0C and boiling point is 3350^0C [5].

1.1.3. The importance of vanadium in heterogeneous catalysis

Vanadium is the most important metal used in metal oxide catalysis [1, 8-14]. About 5% of the annual production of vanadium is used in catalysis, which is its most dominant non-metallurgical use. The catalysts containing vanadia, whether pure or mixed with other oxides have been used in many industrial processes, which yield valuable products. Some of the industrial catalytic processes based on vanadium oxides are shown in Table 1.1. In fact all the heterogeneous oxide catalysts used on industrial scale for production of organic anhydrides and acids contain vanadium as a main component of the active phase [15]. These industrial processes include synthesis of maleic anhydride, originally from benzene (V-Mo-O catalysts) and recently from n-butane (V-P-O system), phthalic anhydride from o-xylene (V_2O_5/TiO_2 catalysts) and acrylic acid from acrolein (V-Mo-O system). Vanadia catalysts also appear promising for the oxidation of toluene to benzaldehyde, methanol to formaldehyde and to methyl formate (V-Ti-O catalysts), oxidation of polycyclic aromatic hydrocarbons such as naphthalene, anthracene, phenanthrene and fluorene to dicarboxylic acids and quinones (V-Fe-O system). Vanadium containing systems are used not only for the manufacture of important chemicals but also for the reduction of environmental pollution (e.g. removal of nitrogen oxides from flue gas of power plants by selective reduction with NH_3).

Table 1.1: Industrial catalytic processes using vanadium oxides [1,8-14]

Industrial process	Catalyst material
Oxidation of SO_2 to SO_3 in the production of sulfuric acid	V_2O_5
Oxidation of benzene to maleic anhydride	V_2O_5
Oxidation of naphthalene to phthalic anhydride	V, Mo oxides
Oxidation of butene to phthalic anhydride	V, P oxides
Oxidation of o-xylene to phthalic anhydride	V, Ti oxides
Selective reduction of NO_x with NH_3	$V_2O_5/WO_3/TiO_2$

Apart from the industrial perspective, the systems containing vanadia are also a rich source of fundamental problems closely related to the theory of catalysis on oxides [8]. Some essential concepts in this domain, like the mechanism of heterogeneous oxidation, were formulated based on vanadia systems. Mars and Van Krevelen proposed this mechanism based on the studies on the oxidation of SO_2 and of naphthalene, both using vanadia catalysts.

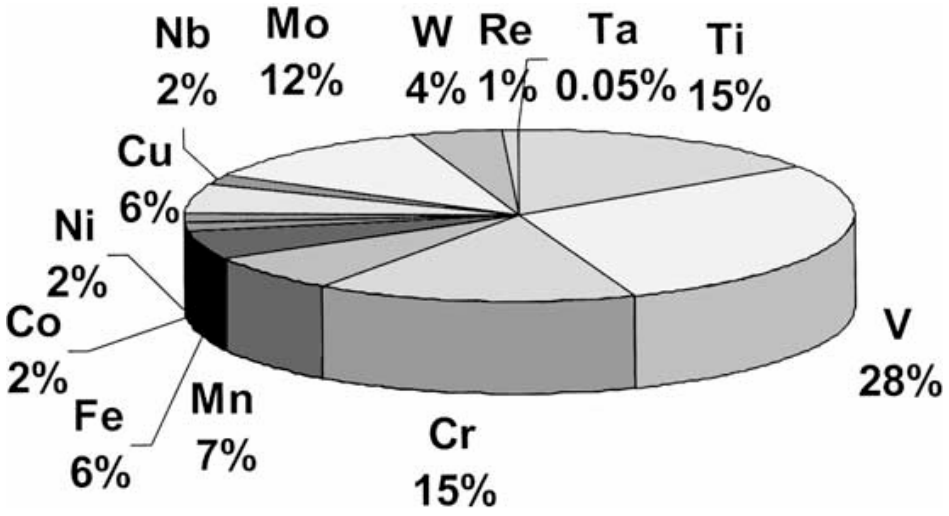

Fig. 1.1: *Overview of the importance of vanadium in supported metal oxide catalysis. The numbers are based on open literature search in the period 1967–2000 [1].*

Figure 1.1 summarizes the number of papers (expressed as a percentage of the total number of papers) of several transition metals in the field of metal oxide catalysis, which can be found in the open literature [1]. The fact that the highest number of papers is published on the vanadium based catalysts underlines the importance of vanadium in supported metal oxide catalysis.

1.1.4. Vanadium pentoxide (Unsupported vanadia)

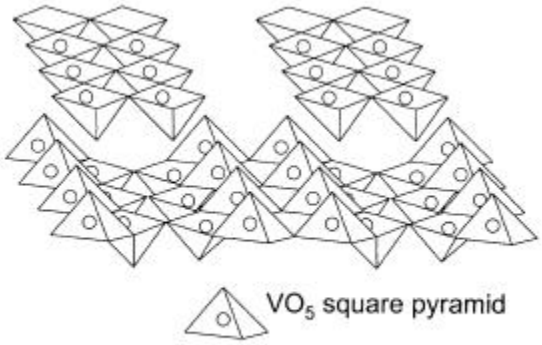

Fig. 1.2: *Schematic representation of structure of V_2O_5 [1], which can be approximated by zigzag ribbons of square pyramids of VO_5.*

At normal temperature and pressure, vanadium pentoxide (V_2O_5) is thermodynamically most stable among the oxides of vanadium [16]. V_2O_5 is an orange-red and acidic oxide. The stereochemistry of vanadium ions in V_2O_5 may be considered to be either distorted trigonal bipyramid (five V-O bond lengths of 1.58-2.02 Å), distorted tetragonal pyramid or a distorted octahedron (the sixth V-O bond length of 2.79 Å) [16]. The structure of V_2O_5 is often approximated by zigzag ribbons of square pyramids of VO_5 (Fig. 1.2) [1]. Each vanadium atom and its five nearest oxygen neighbors create VO_5 pyramids, which share their corners, building double chains along the *b*-direction. These chains are connected by their edges and the resulting layers are stacked along the *c*-direction. As a result, a vanadium oxide unit consists of an octahedrally coordinated VO_6, with three distinct vanadium-oxygen bond distances [1]. The vanadium ion is slightly displaced from the basal plane towards the apex of the pyramid, which creates a strong and

short $V{=}O_{(1)}$ bond of 1.58 Å. The $V\text{-}O_{(3)}$ distance in opposite direction is much longer (2.79 Å). The four $V\text{-}O_{(2)}$ bonds to the oxygen in the basal plane have a length of 1.83 Å. Three types of oxygen atoms are present in the lattice: vanadyl oxygen atoms O(1) coordinated only to one vanadium atom, and bridging oxygen atoms O(2) and O(3) coordinated to two and three vanadium atoms [16]. Equilibration of gas phase oxygen with vanadium oxides results in the formation of the intrinsic defect structure of V_2O_5 consisting of oxygen vacancies. Vanadium (V) oxide is a well-established catalyst for the partial oxidation of hydrocarbons to oxygenated products [17].

1.1.5. Molecular structures of vanadium oxides in aqueous media

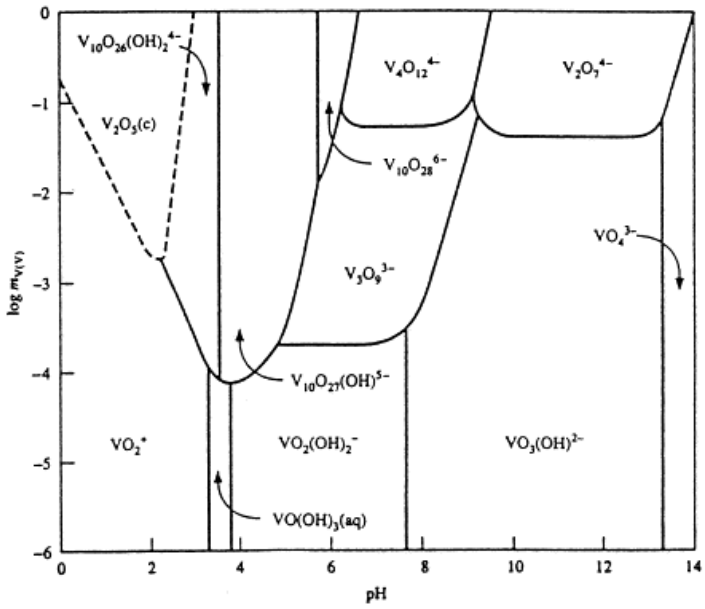

Fig. 1.3: *The Pourbaix diagram of vanadium, expressing the vanadium speciation as a function of pH and potential at 25 °C and an ionic strength of 1 M [1].*

V^{5+} and V^{4+} are the most important oxidation states in aqueous solution [1]. The nature of vanadium oxide species present in solution depends on the pH and the vanadium oxide concentration of that solution. This is illustrated in the Pourbaix diagram for V^{5+} (Fig. 1.3), which shows the change in structure of vanadium oxide species with change in

pH and concentration [1,18]. The hydrolysis of V^{5+} may lead to any of 12 different species-monomer as well as polymeric species-in aqueous solutions. V^{4+} is particularly stable as the vanadyl ion (VO^{2+}), which is one of the most stable oxy-metal ions. In water it appears in the form of a tetragonal bipyramidal coordination ($VO(H_2O)_5^{2+}$). Other V^{4+} species hydrolyze to give dimeric species, even in dilute solutions (10^{-3} M). V^{2+} as well as V^{3+} are unstable and are oxidized by water and air, respectively.

1.1.6. Molecular structures of vanadium oxides in the solid state

The most important oxides of vanadium are V_2O_5, VO_2, V_2O_3 and VO [1] in which, the formal oxidation state of vanadium decreases from +5 to +2. Vanadium oxide also form mixed valence compounds, such as V_3O_5, V_4O_7 and V_7O_{13}, and have the general formula V_nO_{2n-1}.

As mentioned earlier, the structure of V_2O_5 is often approximated by zigzag ribbons of square pyramids of VO_5. V_2O_5 is only slightly soluble in water, resulting in a pale yellow solution with some colloidal character. It also dissolves in NaOH to give colorless solutions containing the vanadate ion, VO_4^{3-}. On acidification, a complicated series of reactions occur involving the formation of hydroxyanions and polyanions (e.g. decavanadate), as shown in Fig. 1.3. In very strong acid solutions, the dioxovanadium or pervanadyl ion (VO_2^{+}) is formed.

The mild reduction of V_2O_5 leads to VO_2 oxide, which is dark blue in color and has a distorted rutile-like structure [1]. It is an amphoteric oxide, dissolving in non-oxidizing acids to give the blue VO^{2+}, which appears in water in the form of a tetragonal bipyramid of the form $VO(H_2O)_5^{2+}$. In alkali media, it will transform to the yellow to brown $V_4O_9^{2-}$ or at high pH to VO_4^{4-}. The black V_2O_3 has a corundum structure and is basic. It is obtained by reduction of V_2O_5 with hydrogen or carbon monoxide. It dissolves in aqueous acids to give blue or green V^{3+} solutions, which are strongly reducing. The grey-colored VO or V_2O_2 has somewhat metallic behavior and possess a defect rock-salt structure. It is prone to non-stoichiometry and can dissolve in mineral acids to give violet air-sensitive V^{2+} solutions. The oxidation of V^{2+} by air is complicated and appears to proceed in part by direct oxidation to VO^{2+} and in part by way of an intermediate species of type VOV^{4+}.

1.1.7. Supported vanadium oxide catalysts

Generally, bulk V_2O_5 exhibits poor thermal stability and mechanical strength. The catalytic properties of vanadia can be improved by depositing on an appropriate support, such as alumina, silica, titania, zirconia. The activity and selectivity of supported metal oxide catalysts are significantly affected by the properties of the support oxide material, which is generally known as the metal oxide-support effect [1,15,17]. Supported vanadium oxides show chemical and electronic properties, which are entirely different from those found for unsupported vanadium pentoxide (V_2O_5), in aqueous media and in the solid state [1-4]. The fundamental basis for the catalytic performances of supported vanadium oxides lies in the variability in geometric and electronic structure of surface vanadium oxides and the current knowledge about the chemistry of supported vanadium oxides are discussed in the following sections.

1.1.8. Molecular structures of vanadium oxides in the supported state

The common feature of all the vanadia-based catalysts is the presence of the V-O_x groups. Vanadium ions in these units can be present in tetrahedral, octahedral and square pyramid environment. Surface vanadium oxide phases are formed when vanadium oxide is deposited on an oxide support. The supported vanadium oxide phase, like other supported metal oxide phases, can simultaneously exist in several different structural states (bulk crystallites, mixed phases with the support like ZrV_2O_7, or two-dimensional overlayers).

The surface structures and oxidation states of the surface vanadia species are dynamic and are strongly dependent on the environment (coverage, oxidizing and reducing gases, moisture and temperature). The structure of the monolayer species and coverage with them even for the same support is not completely solved and depends on the preparation method, presence of impurities in the support, its morphology etc [15]. The structure and properties of the dispersed species are influenced also by the type of the support: the basic and amphoteric oxides favor the bidimensional dispersion (in some cases with the formation of surface vanadium compounds e.g. the vanadates), whereas the acidic ones, e.g. SiO_2, the formation of tridimensional micro units of V_2O_5. The detailed structure of the dispersed species and the coverage with them are still matters of debate [19,20].

However, the existence of the V-O-support or more precisely V-O-Me^{n+} bond (where Me^{n+} is a cation) in some fraction of the dispersed species is generally agreed [15]. The degree of ionicity of the V-O bond i.e. nucleophilicity of oxygen and electrophilicity of vanadium ions in V-O-Me^{n+} bonds can be related to the acido-basic properties and reducibility of the system. The higher electro negativity of Me^{n+} element (e.g. P) as compared with that of V ions would render the oxygen atom in the V-O-Me^{n+} unit less nucleophilic (less basic) and vanadium atom more electrophilic (acidic) than in V-O-V bonds. When Me^{n+} is an ion of lower electro negativity than that of V (e.g. Mg^{2+} or K^{+}) oxygen atoms in the V-O--Me^{n+} units become more nucleophilic and vanadium less electrophilic. The experimental data shows that the V-P-O catalysts exhibiting high acidity and low basicity, whereas the inverse is true for the V-Mg-O system.

The formal valence state of vanadium in different vanadia-based systems varies between V^{5+} (V_2O_5, $VOPO_4$, magnesium vanadates, VO_4 tetrahedra and VO_6 octahedra on MgO, hydrotalcite, sepiolite and Al_2O_3) to V^{4+} (vanadyl pyro-phosphate, solid solutions of MoO_3 in V_2O_5) and the mixture of V^{3+} and V^{4+} in vanadium antimonite [15]. In most cases, however, the presence of both V^{5+} and the reduced vanadium ions, irrespective of the formal valence state of a V-compound has been observed even in the fresh catalysts. In the stationary state of the oxidation reactions all catalysts contain both oxidized and reduced vanadium cations, the ratio of them depending on the reaction conditions and the nature of the hydrocarbon which is oxidized.

1.1.9. Evolution of vanadium oxide molecular structures during catalyst synthesis and calcination

Deo and Wachs [21] have shown that the surface vanadium oxide molecular structures on amorphous support oxides depend on the isoelectric point (IEP) of a specific support. The lower the IEP of the amorphous oxide, the higher the H^{+} concentration near the surface, which lead to the formation of more polymerized vanadium oxide species. When the vanadium oxide loading increases, two effects come into play: (1) the pH near the surface is lowered due to the presence of acidic vanadium oxides, and decreases with increasing vanadium oxide loading; and (2) the dispersion depends on the available surface

area as well as the availability of surface hydroxyl groups. Both factors influence the chemistry of vanadium in the same direction, i.e. toward the formation of surface polyvanadates. The evolution of structure of vanadium species with increasing vanadium oxide loading can be written as: orthovanadate (VO_4) ⟶ pyrovanadate (V_2O_7) ⟶ metavanadate $(VO_3)_n$ ⟶ decavanadate ($V_{10}O_{28}$) ⟶ vanadium pentoxide (V_2O_5) [23].

During heating in air (calcination), the water molecules adsorbed on the support and around the supported vanadium oxides are removed and the supported vanadium oxides are oxidized mainly to the +5 oxidation state [1]. The formed dehydrated vanadium oxides directly anchor onto the surface via an esterification reaction with the hydroxyl groups of the amorphous oxide, resulting in the formation of surface vanadium oxides [19,23,24].

1.1.10. Preparation methods of supported vanadium oxide catalysts

Different methods have been used for the preparation of supported vanadium oxide catalysts [1]. These techniques involve two stages: the first stage is dispersion, which is achieved by impregnation, grafting, co-precipitation, or dispersion, while the second stage is calcination. The most important preparation techniques along with their advantages and disadvantages will be discussed briefly in this section.

1.1.10.1. Impregnation

Impregnation is the most simple and widely used preparation technique for making supported vanadium oxide catalysts. Both wet impregnation and incipient wetness impregnation techniques are usually used for the preparation of vanadia catalysts. In incipient wetness impregnation, more precise control over the vanadium oxide loading can be achieved but the maximum loading obtainable in a single impregnation is limited by the solubility of the reagent and multiple impregnation steps are needed for higher loadings. Since V_2O_5 has a low solubility in aqueous and non-aqueous solutions, supported vanadium oxide catalysts are usually prepared by impregnating the support with either an aqueous solution of, e.g. NH_4VO_3 [25-32] or NH_4VO_3 dissolved in aqueous oxalic acid [33-36]. The aqueous impregnation with vanadium oxalate is usually employed for the

commercial preparations because of its high solubility in water and the absence of undesirable volatile organic solvents [19]. The deep blue solution resulting from the dissolution of NH_4VO_3 in aqueous oxalic acid contains the compound $(NH_4)_2[VO(C_2O_4)_2]$. Due to the reducing nature of oxalic acid, vanadium is in +4 oxidation state in this compound [37]. Since NH_4VO_3 is poorly soluble in water, oxalic acid route is the preferred one for the deposition of vanadium oxide and any desired loading of V_2O_5 can be produced by this method. The ionic oxalate complex interacts with the support (denoted as S) via an ion exchange reaction [38]:

$$2S\text{---}OH + (NH_4^+)_2[VO(C_2O_4)_2]^{2-} \longrightarrow (S\text{---}cation^+)_2[VO(C_2O_4)_2]^{2-} + 2NH_4OH \qquad (1.1)$$

Since the impregnating solution is acidic (pH<2), the support surface acquires positive charge by the protonation of surface hydroxyl groups:

$$S\text{---}OH + H^+ \longrightarrow (S\text{---}OH_2)^+ \qquad (1.2)$$

This protonated surface hydroxyl groups can interact with the complex by a ligand substitution reaction also. In this route, functional groups of the support oxide are exchanged by ligands of the metal complex:

$$(S\text{---}OH_2)^+ + [VO(C_2O_4)_2]^{2-} \longrightarrow (S\text{---}O)_{2-x}[VO(C_2O_4)^{2-x}] + x\ H_2C_2O_4 \qquad (1.3)$$

Non-aqueous impregnation methods use, e.g. vanadyl acetylacetonate $(VO(acac)_2)$ as vanadium compound or $VO(OC_2H_5)_3$ or $VO(OC_3H_7)_3$ in methanol or another organic solvent [39-43]. The impregnation process is followed by drying and then calcination in air at high temperatures during which the vanadium oxide compound is chemically anchored onto the support oxide surface as shown in Fig. 1.4.

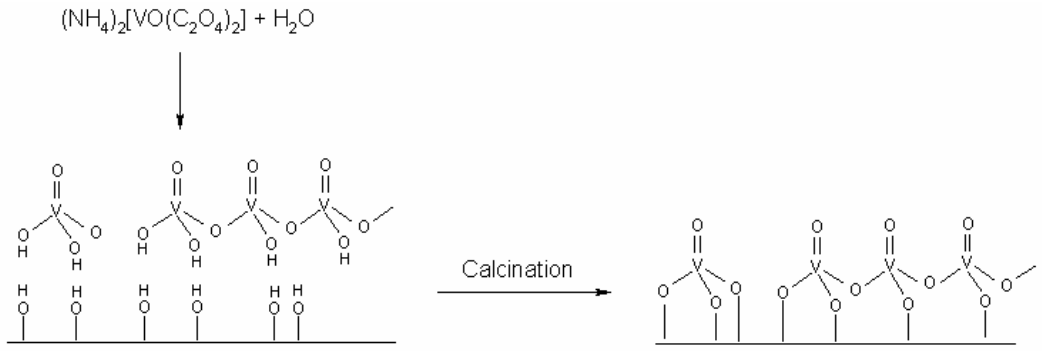

Fig. 1.4: *Schematic representation of impregnation of a support with an aqueous solution of NH_4VO_3 and oxalic acid, followed by calcination in air (based on [1]).*

1.1.10.2. Adsorption from solution (Grafting)

The term grafting is used to describe the removal from solution of a species containing the active element through interaction with the hydroxyl groups on the surface of an inorganic support. For supported vanadia catalysts, a solution of $VOCl_3$ in CCl_4 or in benzene is generally used to obtain a dispersed VO_x phase on various inorganic oxides [44]. Non-aqueous solutions of VO $(O^iBu)_3$, VO $(acac)_2$ dissolved in toluene or ethanol have also been used for the dispersion of VO_x species on various supports [45-48]. A monolayer of vanadium oxide on the support surface can be achieved by multiple grafting followed by calcination.

1.1.10.3. Chemical vapor deposition

In chemical vapor deposition (CVD), the active component is deposited on the surface of the support by reaction of a volatile inorganic or organo-metallic compound with the support hydroxyl groups. The vanadium precursor compounds generally used for this preparation method are gaseous VCl_4 and $VOCl_3$. Their interaction with SiO_2, TiO_2 and Al_2O_3 has been studied in detail [49-52]. A similar synthesis method is atomic layer deposition (ALD) and series of V/SiO_2 and V/Al_2O_3 catalysts were prepared according to this gas phase preparation technique [53].

1.1.10.4. Co-precipitation

Supported vanadium oxide catalysts can be prepared by co-precipitation from a solution containing compounds of each element [1]. In this method, an intimate mixing of the catalytic active phase and the support can be achieved, but the active component is dispersed through the bulk as well as being on the surface [9]. An example of such procedure is the preparation of V/TiO_2 catalysts by adding NH_4OH to a mixed V^{4+} and Ti^{4+} solution [54]. Well-dispersed mixed VO_x-SiO_2 and VO_x-TiO_2 gels have been prepared by hydrolysis of $VO(O^iBu)_3$-$Si(OC_2H_5)_4$ and VO^{2+}-$TiCl_4$ solutions respectively.

1.1.10.5. Thermal spreading

In this preparation technique [55,56], a physical mixture of V_2O_5 and support oxide is heated together which will lead to the spreading of vanadium oxide over the support. This technique makes use of the high mobility of V_2O_5 with a Tamman temperature of 370 °C and has been used for depositing V_2O_5 on a number of oxides. The driving force for this spreading phenomenon is the lowering of the surface free energy by forming a monolayer of surface vanadium oxide species on the high surface free energy oxide support.

All supported vanadium oxide catalysts were found to contain essentially the same vanadium oxide configurations after prolonged calcination treatments irrespective of the synthesis methods used in preparing supported vanadium oxide catalysts [57]. Hence the preparation method does not influence the local coordination environment of supported vanadium oxides but influences the amount of supported vanadium oxides, which can be deposited on a particular support oxide without the formation of crystalline V_2O_5. Thus, the preparation method may affect the vanadium oxide dispersion.

1.1.11. Characterization methods of supported vanadium oxide catalysts

The characterization of the molecular structures of supported vanadium oxides is rather involved, since deposition of this metal oxide on an inorganic oxide can result in diverse vanadia species as discussed previously. No characterization technique

independently will be capable of providing all the information needed for a complete characterization; a multi-technique approach is needed for this purpose [58-62]. A brief overview of characterization techniques is given in next chapter.

1.2. DEHYDROGENATION OF ETHYLBENZENE TO STYRENE

1.2.1. Importance of the reaction

Ethylbenzene is used almost exclusively for the manufacture of styrene (63). Styrene (ST) is an important monomer for the manufacture of polystyrene, ABA resin and synthetic rubber. More than 65% of the styrene produced is converted to polystyrene. About 13% is copolymerized with butadiene in the fabrication of rubber elastomers or different latexes. The production of styrene-acrylonitrile copolymers consumes about 9% and 7% is combined with unsaturated polyester resins [64]. The current annual styrene production is approximately 23×10^6 tonnes per year [65]. USA, Western Europe and Japan are the main producers of styrene and Dow Chemical is the largest single producer [63].

1.2.2. Current industrial processes for styrene production

Currently, there are two main processes for the manufacture of styrene [63,66]. In the first one, which is a modification of the Halcon process, styrene is obtained as a by-product in the epoxidation of propene with ethylbenzene hydroperoxide and Mo complex-based catalysts. This process is commercialized by ARCO Chemical (formerly Oxirane) and by Shell. About 2.5 kg styrene is obtained per kilogram propylene oxide. Approximately 1.2×10^6 t/year are currently produced with this technology [66].

The second one and also the most important manufacturing route to styrene is the direct catalytic dehydrogenation of ethylbenzene (Scheme 1.1) and this process accounts for more than 90% of the worldwide capacity [66]. Infact, the production of styrene monomer from ethylbenzene (EB) is one of the ten largest production processes in the chemical industry.

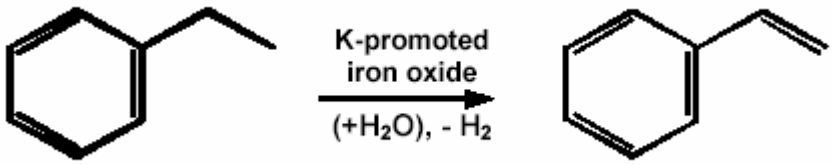

Scheme 1.1: *Direct dehydrogenation of ethylbenzene to styrene as performed in industry.*

1.2.3. Direct dehydrogenation of ethylbenzene

1.2.3.1. The chemistry of the reaction

The following reactions are involved in the dehydrogenation of ethylbenzene; some of these reactions are thermodynamically favored at low temperature, while others are at higher temperatures [66].

Direct reactions:

ethylbenzene $\rightarrow$ styrene + H_2	(dehydrogenation)	(1.4)
ethylbenzene $\rightarrow$ benzene + C_2H_4	(cracking)	(1.5)
ethylbenzene + $H_2 \rightarrow$ toluene + CH_4	(hydrogenolysis)	(1.6)
ethylbenzene + $H_2O \rightarrow$ CO + H_2	(steam reforming)	(1.7)

Consecutive reactions

CO + $H_2O \rightarrow CO_2 + H_2$	(water-gas shift)	(1.8)
styrene $\rightarrow$ precursors of coke	(oligomerization)	(1.9)
precursors of coke + $H_2O \rightarrow CO_2 + H_2$	(water-gas shift)	(1.10)
precursors of coke $\rightarrow$ coke	(dehydrogenation)	(1.11)

Figure 1.5 shows the values of the standard free energy of reaction (referred to one mole of reactant) for the various reactions as a function of temperature [66].

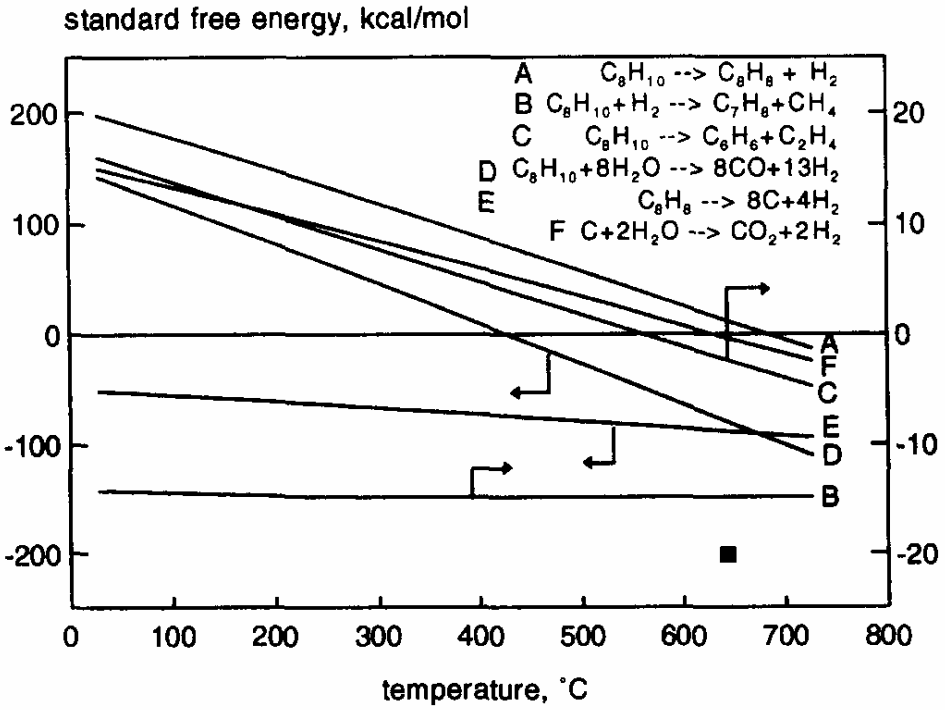

Fig. 1.5: *Standard free energy, referred to as one mole of reactant, for the reactions involved in the ethylbenzene dehydrogenation [66].*

A reaction network, which includes all the main products, is shown in Scheme 1.2 [66].

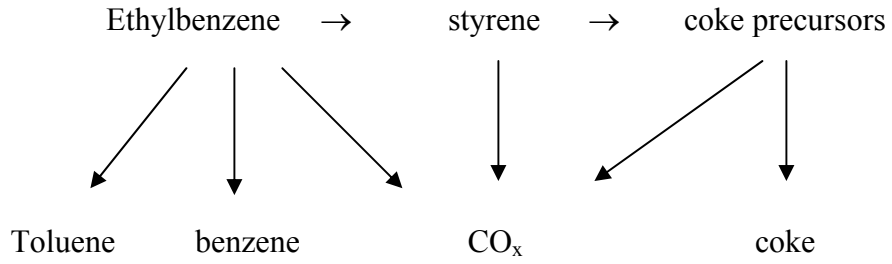

Scheme 1.2: *Reaction network in the dehydrogenation of ethylbenzene [66].*

Approaching equilibrium, the selectivity to styrene decreases due to the inhibition of formation of styrene and the rate of formation of the by-products via parallel routes becomes more relevant. At low conversion, the selectivity to styrene approaches 100% with many different catalyst compositions [66].

1.2.3.2. The thermodynamics of reaction

The reversible conversion of EB to styrene and hydrogen (eq. 1.13) is highly endothermic, ΔH (873 K) being 124.9 kJ mol^{-1} [64,67]. The dependence of the equilibrium constant K on temperature [67] is given by

$$\ln K = -15350 / T + 16.12 \quad (1.12)$$

$$C_6H_5CH_2CH_3 \Leftrightarrow C_6H_5CH{=}CH_2 + H_2 \quad (1.13)$$

Since two moles of products (styrene and H_2) are formed from one mole of EB, a reduced pressure favors the EB conversion.

1.2.3.3. Commercial operating conditions

The commercial process is operated at high temperatures between 600 and 700^0C mainly at atmospheric pressure with an excess of superheated (~700^0C) steam, *i.e.* the steam to EB ratio is 10:1. Industrially, three different types of processes are operated in the gas-phase using fixed bed catalysts and steam as diluting agent [64,67]. It can be run either adiabatically or isothermally over a fixed bed reactor, in which the reactants are passed over the catalyst bed employing radial or axial flow.

The adiabatic process using multiple reactors is used in more than 70% of styrene plants. The heat required for the endothermic dehydrogenation is provided by the injection of superheated steam. The inlet temperature of the feed is about 910 K and the steam:EB molar ratio is about 11-13. EB conversion in the first reactor is about 35 mol% to give a total of 65 mol%. This process is licensed by Badger, ARCO and Shell etc.

In isothermal EBDH process, the reactor is built like a multitube heat exchanger, heated indirectly by the hot flue gas. Vaporized ethylbenzene is mixed with steam (steam:EB molar ratio 3-6) and passed into the tubular reactor (600^0C) filled with suitable catalyst.

In SMART EBDH process, based on UOP technology, H_2 formed by EBDH is oxidized over noble metal catalyst installed between single Fe-catalyst beds. The H_2 oxidation is covering partly the heat balance. The removal of H_2 favors EBDH conversion, which reaches more than 80 mol%, still maintaining a good selectivity.

The catalyst system generally preferred today in most of the industrial processes is based on iron oxide, which was introduced in 1957 [63]. The catalysts usually contain K and Cr oxides and in addition, one or more promoters. The choice and amount of promoters determine patterns of activity/selectivity, range of optimal temperature of operation and of steam-to-hydrocarbon ratio [66]. A typical range of composition for the main elements and for promoters is the following: Fe_2O_3 45-77 wt%, K_2O 10-27%, Cr_2O_3 0-3%, Ce_2O_3 0-5%, MoO_3 0-3%, MgO 0-10%, Al_2O_3 0-0.1%, V_2O_5 0-2.5%, CaO 0-2.5%. The main promoter, potassium, increases the activity of Fe_2O_3 by more than one order of magnitude and also slightly increases the selectivity to styrene and the stability of the catalyst [68]. The promoting ability of potassium is due to the formation of a surface ternary compound, $KFeO_2$, which constitutes the active phase [66,69-72].

The commercial processes use excess of steam with respect to ethylbenzene. The overall effect of the increase of the steam-to-hydrocarbon ratio is to increase the activity, the selectivity at the same level of conversion (or the conversion at the same value of selectivity), the lifetime and stability of the catalyst. The application of steam is proposed to (i) shift the equilibrium towards higher conversions of ethylbenzene by decreasing the partial pressures of ethylbenzene and of hydrogen, (ii) supply the heat of reaction, (iii) limit the build up of coke or of coke precursors on catalyst surface by steam-reforming reactions, (iv) keep the iron oxide in an appropriate oxidation state [73] and (v) increase of the rate of formation of the active phase, $KFeO_2$, and minimization of the deactivation rate under reaction conditions [74,75].

However, the use of steam causes some serious limitations also, namely, (i) consumption of ethylbenzene and of styrene by steam-reforming, (ii) high energy consumption because of the excess amount of steam used and (iii) interaction of steam with K_2CO_3 forming free KOH.

1.2.4. The limitations of current industrial processes

The problems encountered in the current ethylbenzene dehydrogenation process are described below:

1. The dehydrogenation of EB to styrene is equilibrium limited and highly endothermic ($\Delta H°_{298}$ = 28.1 kcal/mol).
2. The industrial process is highly energy consuming because of the excess steam used and the high endothermicity of the reaction.
3. The reversibility of the dehydrogenation process thermodynamically hinders maximum yields of styrene. The technical EB conversion is limited below 60%, to keep an acceptable high selectivity to styrene. The limited styrene yields and the low EB conversions achieved per pass through the reactor lead to the necessity of a reactant recycle.

For styrene polymerization applications, styrene has to be purified to more than 99.8%. The separation of un-reacted EB and co-products from styrene is costly due to the close boiling points, especially for EB and styrene, with 136 and 145 ^{0}C, respectively.
4. The K-Fe catalyst slowly deactivates with operation and typically needs to be replaced every 1-2 year. In view of the scale of the reactors used, this is an expensive operation.

The number of problems that are encountered in the current commercial process for styrene production is the driving force to develop alternative technologies.

1.2.5. Alternative processes for the production styrene

To overcome the above-mentioned drawbacks of dehydrogenation of ethylbenzene in the presence of steam, several alternative processes have been proposed [66]:
1. Dehydrogenation, followed by oxidation of the hydrogen, in order to furnish the heat of reaction from inside and in some cases shift the reaction equilibrium.
2. Membrane catalysis, in order to shift the equilibrium and to carry out the reaction at lower temperature.
3. Oxidative dehydrogenation (ODH), in order to realize an exothermic reaction and shift completely the equilibrium towards the product formation and to carry out the reaction at lower temperature.

The first one**,** dehydrogenation followed by oxidation, is characterized by the injection of a gas containing oxygen either in the effluent or in the feed of a dehydrogenation reactor, in order to catalytically oxidize, either in part or totally, the co-produced or co-fed hydrogen [66]. This type of process is also referred to as 'steam oxidation dehydrogenation'. This technology is applied in the dehydrogenation of ethylbenzene using iron oxide-based catalysts in the presence of steam and in the dehydrogenation of paraffins only with either spinel-type supports or supports based on alumina doped with rare earth, which are particularly stable in the presence of steam.

This method allows one to reach an EB conversion of approximately 80%, by removing the H_2 from the reaction. But it is necessary in this process to mechanically separate the hot aromatics from the oxygen to avoid explosion [76].

The membrane technology has been proposed to modify dehydrogenation and oxidative dehydrogenation processes by removing H_2 *in situ* and to enhance styrene yield [77]. In these ceramic membrane reactors, hydrogen is separated from the product stream of dehydrogenation reaction occurring on one side of the membrane and removed from the other side of the membrane as pure hydrogen or makes it react with an oxygen-containing gas. Another method is to let oxygen diffuse selectively through a membrane in order to make it oxidize either the hydrogen formed or directly the hydrocarbon, on the other side of the membrane [66]. Nevertheless, the realization of an industrial membrane process is complicate and requires certain developments not achieved so far [78].

Among the alternatives proposed, the oxidative dehydrogenation (ODH) of EB to styrene is one of the most elegant and promising reactions and will be discussed in detail in the next section.

1.2.6. Oxidative dehydrogenation of ethylbenzene

The ODH of EB to styrene allows one to realize an exothermic reaction due to water formation as the secondary product. The thermodynamic equilibrium proposes EB conversions as high as 90% at much lower temperatures than in the dehydrogenation reaction. The reaction can be carried out using different oxidizing agents as described below.

1.2.6.1. Oxidative dehydrogenation in presence of O_2

The ODH of ethylbenzene with O_2 can be represented as [66]:

$$C_6H_5\text{-}C_2H_5 + 0.5\ O_2 \rightarrow C_6H_5\text{-}C_2H_3 + H_2O \quad \Delta H^0_{298} = -29.7 \text{ kcal/mol} \qquad (1.14)$$

The reaction with O_2 is highly exothermic so that it can be performed at lower temperatures. It is claimed that almost complete conversion can be obtained which will decrease the separation costs. The use of superheated steam can be eliminated or reduced to minimal levels and higher selectivity (90% in dehydrogenation) can be reached. This minimizes the waste of ethylbenzene, simplifies the removal of the heat of reaction and avoids total consumption of oxygen. The transformation of one mole of ethylbenzene to styrene requires 0.5 O_2 while the combustion to CO_2 requires 13 O_2.

The disadvantage of the ODH with O_2 is that side reactions occur by cracking and by oxygen insertion on ethylbenzene and on styrene [79]. Also, in an industrial operation, problems like mixture flammability and run-away may arise in the presence of molecular oxygen.

The catalysts used for oxidation can be broadly classified into oxides possessing medium strength acidity and with nil or limited redox properties [80] and oxides with redox properties [81,82].

1.2.6.2. Catalytic oxidation with acid oxides

In general, mixed oxide-based catalysts were studied for this reaction. These oxides are active in the temperature range 450 to 600°C and operate with a ratio O_2/EB 0.8-2, a concentration of EB in the range 8-15% and a contact time in the range 0.2-4 $g_{cat}/(g_{EB}$ h) [66]. The carbon molecular sieves and metal phosphates are reported to be good catalysts [83,84]. It is suggested that the active catalyst in ethylbenzene oxidative dehydrogenation is the 'active coke', which forms in the first hours of reaction and reaches a stationary amount on the surface of the oxides [80,85]. Therefore, the investigated oxides are 'carriers of the active component'. The differences in catalytic activity of different classes of metal oxides and phosphates are low since the real catalyst is 'active coke' formed on the oxides and not the oxide itself. This is also the reason for the higher yield in styrene obtained at much lower temperature with molecular sieve carbon. The activity is observed at higher

temperatures with metal oxide carriers since higher temperatures are most likely necessary to form and to maintain a certain stationary amount of 'active coke'.

In the case of 'oxides as carriers' usually conversions not higher than 70% have been reported [66]. This limitation on conversion is essentially due to the fact that the conversion of oxygen reaches 100%. In fact, the oxygen-to-styrene ratio reported in most publications and patents is not higher than 1, with a preferred concentration of ethylbenzene of 10%. The choice of this composition, the best for achieving a good selectivity, requires a costly dilution of air with nitrogen or steam and also causes oxygen starvation at high conversion. However, it is the preferred composition for safe operation, which is outside the flammability region. The strong adsorption of styrene on the oxide carriers also negatively influences the rate of transformation of ethylbenzene and cause non-complete conversion. In order to increase the conversion to values, which are economically competitive with dehydrogenation, an oxide carrier presenting higher selectivity must be developed.

1.2.6.3. Catalytic oxidation with redox oxides

Oxidation of ethylbenzene to styrene has been achieved with redox-type catalysts, which are based on MgO/V_2O_5 and using two different reactor configurations namely catalytic oxidation with air in the presence of steam [79,86] and oxidation of ethylbenzene with oxygen from the catalyst and reoxidation of the reduced catalyst with air [81].

Catalytic oxidation

The performances obtained with redox catalysts are very similar to those obtained with acid oxides. The only difference is that higher amount of steam is needed when redox oxides are used, to suppress bulk combustion. According to some reports [79,86] the active sites for the selective oxydehydrogenation are surface clusters of V^{5+} and V^{4+} in octahedral coordination with MgO/V_2O_5 catalyst. Hanuza *et al* [86] suggested that the sites which abstract hydrogen from ethylbenzene are surface V^{5+}=O bonds, while V^{4+} species dissociate molecular oxygen.

Non-catalytic oxidation

In non-catalytic oxidation [66,81], mixed oxides with composition ranging from 40 to 60 wt% MgO, from 20 to 40 wt% SiO_2 and from 10 to 30 wt% V_2O_5 are used as stoichiometric oxidants of ethylbenzene. The preferred composition is 50 wt% MgO, 30 wt% SiO_2 and 20 wt% V_2O_5. The preferred preparation is spray-drying of a MgO-SiO_2 suspension followed by impregnation of ammonium metavanadate, preferably with a further amount of silica and calcination at temperatures between 500 and 800 °C. In pulse reactor tests, an ethylbenzene conversion of 98.1% and styrene selectivity of 92% were obtained at 505 °C. Tests in fluidized-bed reactor, at a WHSV of 3.4 h^{-1} and at the temperature of 500 °C, gave ethylbenzene conversion of 63% and selectivity of 83.8%. These results, achieved at comparable contact time, are lower than those obtained with acid oxides as carriers.

It should be mentioned that all these methods are at a research level only and the dehydrogenation is the only process widely used at a commercial level [66]. The SMART technology is commercially available, but it has found not much industrial application till now. The oxidative dehydrogenation gives better performances in terms of conversion and selectivity than the industrial dehydrogenation process. The best performance in terms of conversion/selectivity is claimed with the non-catalytic oxidation on redox oxides, where 92% of selectivity was obtained at 98% conversion. However, for these two alternative technologies the lifetime of catalysts has not yet been evaluated and therefore pilot plant studies have to be carried out in order to obtain information about the change of catalytic performance with time-on-stream and about the productivity. It is also necessary to gain a more quantitative knowledge of all the by-products. In fact, even if present in traces, the nature and amount of by-products can determine the final success of these new technologies.

Since the strong reactivity of oxygen causes burning of considerable amounts of ethylbenzene to CO_x, milder oxidizing agents like CO_2 and SO_2 were proposed as alternate to oxygen for ODH reaction [87].

1.2.6.4. Oxidative dehydrogenation in presence of SO_2

The ODH of alkanes and alkenes with SO_2 was investigated in detail by Adams *et al* [88] and they found that much higher yields of dialkenes are obtained from the alkenes than for the corresponding oxidation with oxygen. The overall reaction for the dehydrogenation of ethylbenzene to styrene with SO_2 can be written as

$$3\ C_6H_5C_2H_5 + SO_2 \rightarrow 3\ C_6H_5C_2H_3 + H_2S + 2H_2O \qquad (1.15)$$

Adams *et al* [89] reported high selectivity (~90%) at high EB conversions (90%) at operating pressures from atmospheric to about 6 atm. However, the catalyst gradually gets coked and deactivated. Moreover, the formation of toxic and corrosive by-products like CS_2, COS and benzothiophene during the process prevents the use of SO_2 at an industrial scale.

1.2.6.5. Oxidative dehydrogenation in presence of CO_2

CO_2 is also proposed as an alternative oxidizing agent [90-95]. The dehydrogenation using CO_2 can be represented as

$$C_6H_5CH_2CH_3 + CO_2 \rightarrow C_6H_5CH{=}CH_2 + CO + H_2O \qquad (1.16)$$

ODH by CO_2 shifts the equilibrium to lower temperatures. The realization of such a process leads to a decrease of the amount of energy required and to an increase of the styrene yield. However, this method has the disadvantage that CO_2 blocks the active centers of the catalyst, which leads to quick catalyst deactivation [96,97].

1.2.7. Nitrous oxide as an oxidizing agent

N_2O is a by-product in industrial plants from the production of adipic and nitric acid and from the combustion of fossil fuels and biomass. It is also formed from land cultivation, the regeneration of coked fluid cracking catalysts and the non-selective catalytic reduction of NO_x with ammonia [98]. These sources of N_2O emission cause its concentration to increase in the atmosphere at a rate of about 0.3% per year. The concentration has now reached about 310 ppb [99]. Though the concentration seems to be low, nitrous oxide is strongly involved in the atmospheric greenhouse effect because each

molecule of N_2O present in the atmosphere is characterized by an average lifetime of about 150 years and a net greenhouse effect of about 300 times greater than that of CO_2 [100].

The emission of N_2O can be reduced by catalytic decomposition into nitrogen and oxygen or by utilizing it as a mild oxidizing agent in selective oxidation (or dehydrogenation) of hydrocarbons. Thus N_2O was used for the direct hydroxylation of benzene to phenol and for the selective oxidation of other aromatic compounds like alkyl-, chloro-, and fluorobenzenes to corresponding phenols and diphenols [101]. N_2O was also used for the partial oxidation of ethane to ethylene and acetaldehyde [102,103].

Though nitrous oxide is a potential alternate mild oxidizing agent, the reports on its use for ODH process have been very scarce in the literature. Lopez Nieto *et al* [104] used N_2O for the oxidative dehydrogenation of n-butane and found that selectivity to olefins was higher with N_2O as oxidant than with molecular oxygen. N_2O is also utilized for the oxidative dehydrogenation of propane with enhanced selectivity towards propene for the same degree of propane conversion compared to O_2 [105].

Recently Kustrowski *et al* studied the coupling of N_2O decomposition with ethylbenzene dehydrogenation and obtained promising results with respect to the EB and N_2O conversion [87]. Though nitrous oxide is found to be an effective oxidizing agent in these reports, the number of studies is limited and the application of N_2O as a potential alternate mild oxidizing agent for oxidation processes is not yet explored significantly.

1.3. PREFERENTIAL OXIDATION OF CARBON MONOXIDE IN PRESENCE OF EXCESS OF HYDROGEN

1.3.1. Introduction

Selective oxidation of CO in excess hydrogen (also preferential oxidation, PROX) has attracted renewed interest over the last years due to its use in low-temperature proton exchange membrane fuel cell (PEMFC) technology [106]. As a pollution-free and high efficiency energy conversion device, fuel cells are considered to be one of the most attractive energy conversion technologies of the future, especially for powering transportation vehicles [107,108]. In order to avoid problems associated with hydrogen

distribution and storage, particularly in vehicle applications, H_2 can be produced on-board by autothermal reforming of hydrocarbon fuels, preferably renewable ones, such as methanol. The production of hydrogen actually occurs in three processes: (a) hydrogen is produced by *autothermal reforming* of a hydrocarbon (fuel + O_2 + $H_2O \leftrightarrow CO_x + H_2$), where without water it is *partial oxidation* and without oxygen it is *steam reforming*; (b) the water–gas shift reaction ($CO + H_2O \leftrightarrow CO_2 + H_2$) eliminates most of the CO, producing more hydrogen; and (c) any remaining CO is reduced to parts-per-million levels by preferential oxidation (PROX) [109]. The PROX reaction is the selective catalytic oxidation of CO in the H_2-rich reformates using O_2. The gas at the outlet of a reformer and two-stage water gas shift (WGS) reactor typically contains 45–75 vol.% H_2, 15–25 vol.% CO_2, a few vol.% H_2O, traces of unconverted fuel and 0.5–2 vol.% CO, which is set by the thermodynamic equilibrium of the water–gas shift reaction. The CO thus produced is a catalyst poison for the fuel cell Pt gas diffusion anode, which is sensitive to even low levels (ppm) of CO. Hence it is essential to lower the concentration of CO in the reformer gas below 100 ppm, a concentration tolerable by modern Pt alloy electro catalysts. In order to achieve this low CO concentration, the PROX reactor is placed between the shift reactor and the fuel cell anode. As with many catalytic processes, the challenges here are activity and selectivity. The conversion of CO has to be very high in order to achieve a concentration level of less than 100 ppm. In order to keep the overall energy conversion process as efficient as possible, the CO oxidation must be highly selective. At the same time, the reformate is mostly hydrogen and its oxidation to water obviously reduces the amount of hydrogen needed to operate the fuel cell and decreases the overall energy conversion efficiency [106]. From a process point of view (reformer → two-stage WGS reactor → PROX → fuel cell) there are two temperature levels which are particularly convenient for a PROX reactor: either the PEMFC operating temperature (80–100 ^{0}C) or the temperature of the methanol reformer unit (250–300 ^{0}C) [106,110,111]. Since the PROX unit is placed between the low-temperature shift reactor and the PEFC, it should operate between these temperatures. PROX system operation at low temperature (room temperature) is also very important for start-up in transportation application fuel cells.

Therefore, the PROX system must operate over a wide temperature range to be practical [109,112].

1.3.2. Thermodynamics

Taking into account the composition of the gas mixture at the outlet of the low temperature water gas-shift reactor, one can conclude that there are quite a number of thermodynamically allowed reactions. Even when the gas feed into PROX reactor does not contain CO_2 and H_2O, one has to consider the following set of thermodynamic equilibria [106]:

$$CO + 1/2\ O_2 \Leftrightarrow CO_2 \quad (1.17)$$

$$H_2 + 1/2\ O_2 \Leftrightarrow H_2O \quad (1.18)$$

$$CO + H_2O \Leftrightarrow CO_2 + H_2 \quad (1.19)$$

$$2CO \Leftrightarrow C + CO_2 \quad (1.20)$$

$$CO + 3H_2 \Leftrightarrow CH_4 + H_2O \quad (1.21)$$

$$CO_2 + 4H_2 \Leftrightarrow CH_4 + 2H_2O \quad (1.22)$$

Reaction (1.20) is completely unwanted, because it reduces the activity of a catalyst by coking. Reactions (1.18), (1.21) and (1.22) are also unwanted, because they reduce the selectivity of a catalyst. Consequently, a catalyst with a good selectivity will promote reaction (1.17) or (1.19) at the expense of reactions (1.18), (1.21) and (1.22). Thermodynamic equilibrium constant of the water gas-shift reaction (WGSR) (1.19) is at least 25 orders of magnitude lower than the thermodynamic equilibrium constants of CO and H_2 oxidation reactions at low temperatures (up to about 150 ^{0}C) [106]. It was experimentally observed that the WGSR does not proceed to an appreciable extent over the Cu–Ce(La)O_x [113] and CuO/Al_2O_3–CeO_x [114] catalysts at temperatures below 150 ^{0}C and at high GHSV (> 80,000 h^{-1}). The results from a study over the $Cu_{0.1}Ce_{0.9}O_{2-y}$ nanostructured catalysts also indicate that no reverse WGS reaction is observed at temperatures below 155 ^{0}C [106]. Both methanation reactions (1.21) and (1.22) have extremely low values of the thermodynamic equilibrium constant (on the order of 10−20*)* at temperatures below 150 ^{0}C. The formation of carbon, reaction (1.20) (Boudouard

equilibrium), is favored at low temperatures, but again the thermodynamic equilibrium constant is at least 20 orders of magnitude lower than the thermodynamic equilibrium constants of the CO and H_2 oxidation reactions up to about 150 ^{0}C. From the thermodynamic point of view, there are no restrictions for the oxidation of CO to proceed with 100% selectivity in excess of H_2 if both oxidation reactions proceed near equilibrium.

1.3.3. The need for development of new catalysts

The current PROX reactor catalysts are prepared from costly alumina-supported Pt, Pd, Ru and Rh, which operate at temperatures of 150–200 ^{0}C and significantly lose selectivity at those temperatures [106]. The other crucial requirement for the PROX reactor is a high oxidation rate of CO. The reaction rate over 3 wt.% Au finely dispersed on α-Fe_2O_3 at 30 ^{0}C and $P_{CO} = P_{O2} = 1$ kPa, where the selectivity is 100% and CO conversion is over 90%, is reported to be 5.1×10^{-6} mol/g_{cat} s. However, when the temperature is raised to the PEMFC working temperature, the selectivity drops to only 40%. The reaction rate over 0.5 wt.% Pt finely dispersed on γ -Al_2O_3 at 200 ^{0}C and at the same partial pressures of CO and O_2, where the maximum selectivity is around 40% and CO conversion 100%, is reported to be 5.2×10^{-6} mol/g_{cat} s [106,110,111]. A two-stage CO selective oxidation reactor for PEMFC automotive applications based on a wash-coat Pt and Ru/Al_2O_3 catalyst and on a compact fin heat exchanger design has a volume of 1 L in order to lower the initial CO concentration in the reformer fuel of 0.5% down to less than 20 ppm at 160 ^{0}C and a gas hourly space velocity (GHSV) of 19,000 h^{-1}, i.e., at fuel flow rate equivalent to a PEMFC electrical power output of 5 kW_{el} [115].

The requirements for an effective PROX catalyst can be summarized as: (i) high activity for CO oxidation (ii) higher ease of CO oxidation than H_2 (iii) ability to function at temperatures similar to that of PEM fuel cells (iv) the resistance towards deactivation by CO_2 and water present in the feed. The current noble metal-based catalysts can almost totally convert CO in the presence of oxygen. However, considerable amount of hydrogen is also consumed simultaneously. This fact, together with their higher cost, requires the development of alternate catalysts.

1.4. SCOPE OF THE THESIS

This thesis describes the preparation, characterization and catalytic activity studies of alumina and magnesia supported vanadia (VO_x/Al_2O_3 and V-Mg-O) catalysts. One of the objectives of the work described in this thesis is to explore the possibility of an alternate process for the ODH of EB using N_2O as an oxidizing agent. Since the current processes are equilibrium-limited and energy intensive, a process which can be operated at lower temperatures with comparable or higher conversion and selectivity to that of conventional commercial process can save a huge amount of energy, considering the fact that the current annual styrene production is approximately 23×10^6 tonnes. We have used supported vanadia systems as the catalysts for this reaction since previous studies have demonstrated that supported vanadia systems exhibit high activity and selectivity for alkane oxydehydrogenation. We have selected nitrous oxide as the oxidant since it is a mild oxidizing agent and additionally the gas, which causes global warming, is effectively utilized in this reaction. Another aim of the thesis is to study preferential oxidation of CO in presence of excess of hydrogen, which is an important reaction to avoid CO poisoning of Pt anode in fuel cells. The thesis also intend to investigate the relationship between molecular structure of the above mentioned supported vanadia catalysts and their activity.

The thesis has been divided into six chapters.

Chapter 1 gives a general introduction about supported vanadia catalysts and their use in oxidation reactions. The chapter presents an introduction about the dehydrogenation reaction of ethylbenzene for the production of styrene, an important monomer. This chapter also contains a brief introduction about preferential oxidation of CO in presence of H_2 and CO_2.

Chapter 2 describes the preparation and characterization of VO_x/Al_2O_3 catalysts with different vanadia loadings. The characterization studies of these materials were carried out by XRD, Surface area (by N_2 sorption), SEM, TG-DTA, IR, Laser Raman, ^{51}V NMR, EPR and TPR. For each technique, theory and experimental procedure have been described briefly.

Chapter 3 is divided into three sections. Section A presents the catalytic activity data of oxidative dehydrogenation (ODH) of ethylbenzene using nitrous oxide over

VO_x/Al_2O_3 catalysts in vapor phase down flow reactor. The effect of different parameters like vanadia loading, reaction temperature, space velocity, N_2O flow rate on the reaction rate and selectivity are investigated. The results are compared with those obtained when the reaction is performed in nitrogen atmosphere.

Section B describes the characterization results of catalysts after dehydrogenation reaction in N_2O and N_2 atmosphere. This section also presents the discussion on the relation between catalytic activity and the local structure of vanadia species on alumina surface. The reasons for the enhancement in activity in N_2O atmosphere compared to that in N_2 atmosphere are also discussed. Section C contains the results and discussion of preferential oxidation reaction of CO in presence of excess hydrogen over VO_x/Al_2O_3 catalysts.

Chapter 4 describes the preparation and characterization of V-Mg-O catalysts. The calcined samples were characterized by XRD, surface area (by N_2 sorption), SEM, TG-DTA, IR, Laser Raman, EPR, ^{51}V NMR and TPR. It was found that the nature of vanadium species differs depending on the vanadia loading. At low loadings, vanadia exist as isolated V^{5+} species while magnesium orthovanadate was the predominant phase at high loadings.

Chapter 5 is divided into two sections. Section A presents the catalytic activity data of oxidative dehydrogenation (ODH) of ethylbenzene using nitrous oxide over V-Mg-O catalysts in vapor-phase down flow reactor. The effect of vanadium loading, reaction temperature, space velocity, N_2O flow rate on reaction rate and selectivity are investigated. The results are compared with those obtained when the reaction is performed in nitrogen atmosphere.

Section B describes the characterization results of catalysts after dehydrogenation reaction in N_2O and N_2 atmosphere. It also presents the discussion on the relation between catalytic activity and the local structure of vanadium species on magnesia surface. The reasons for the enhancement in activity in N_2O atmosphere compared to that in N_2 atmosphere are also discussed.

Chapter 6 summarizes the conclusions reached in this thesis and gives suggestions for further research.

1.5. REFERENCES

[1] B. M. Weckhuysen, D. E. Keller, Catal. Today, 78 (2003) 25.

[2] R. J. H. Clark, The chemistry of titanium and vanadium, Elsevier, Amsterdam, 1968.

[3] F. A. Cotton, G. Wilkinson, Advanced Inorganic Chemistry, A Comprehensive Text, 4th ed., Wiley, New York, 1980.

[4] N. N. Greenwood, A. Earnshaw, Chemistry of the Elements, Pergamon Press, Oxford, 1984.

[5] N.N. Greenwood, Catal. Today, 78 (2003) 5.

[6] J. S. Magee, M. M. Mitchel, Stud. Surf. Sci. Catal., 76 (1993) 105.

[7] R. G. Burns, in: A. Putris, R. C. Liebermann (Eds.), Mineralogical Applications of Crystal Field Theory, 2nd ed., Cambridge University Press, Cambridge, 1993.

[8] B. Grzybowska-Świerkosz, Trifirò, Appl. Catal. A Gen., 157 (1997) 1.

[9] G. C. Bond, S. F. Tahir, Appl. Catal., 71 (1991) 1.

[10] G. Deo, I. E. Wachs, J. Haber, Crit. Rev. Surf. Chem. 4 (1994) 141.

[11] G. Ertl, H. Knozinger, J. Weitkamp (Eds.), Handbook of Heterogeneous Catalysis, Wiley–VCH, Weinheim, 1997.

[12] J. M. Thomas, W. J. Thomas, Principles and Practice of Heterogeneous Catalysis, VCH, Weinheim, 1997.

[13] J. Hagen, Industrial Catalysis, A Practical Approach, Wiley–VCH, Weinheim, 1999.

[14] H. F. Rase, Handbook of Commercial Catalysts, CRC Press, New York, 2000.

[15] B. Grzybowska-Świerkosz, Appl. Catal. A., 157 (1997) 409.

[16] J. Haber, M. Witko, R. Tokarz, Appl. Catal. A., 157 (1997) 3.

[17] E. A. Mamedov, V. Cortés Corberan, Appl. Catal. A., 127 (1995) 1.

[18] D.L. Kepert, The Early Transition Elements, Academic Press, London, 1972.

[19] I. E. Wachs, B. M. Weckhuysen, Appl. Catal. A., 157 (1997) 67.

[20] G. C. Bond, Appl. Catal. A., 157 (1997) 91.

[21] G. Deo, I. E. Wachs. J. Phys. Chem. 95 (1991) 5889.

[22] G. Deo, I. E. Wachs. J. Catal. 146 (1994) 335.

[23] B. M. Weckhuysen, I. E. Wachs, in: Handbook of Surfaces and Interfaces of Materials, H. S. Nalwa (Ed.), Vol. 1, p. 613, Academic Press, San Diego, 2001.

[24] B. M. Weckhuysen, J. M. Jehng, I. E. Wachs, J. Phys. Chem. B, 104 (2000) 7382.

[25] B. G. Silbernagel, J. Catal., 56 (1979) 315.

[26] R. K. Sharma, K. N. Rai, R. D. Srivastiva, J. Catal. 106 (1987) 471.

[27] T. Tanaka, M. Ooe, T. Funabaki, S. Yoshida, J. Chem. Soc., Faraday Trans. I, 84 (1988) 3547.

[28] G. Busca, F. Cavani, F. Trifiro, J. Catal., 106 (1987) 471.

[29] B. Jonson, B. Rebenstorf, R. Larsson, S. L. T. Andersson, J. Chem. Soc., Faraday Trans., 84 (1988) 3547.

[30] J. Zhu, S.L.T. Andersson, J. Chem. Soc., Faraday Trans., 85 (1989) 3629.

[31] J. Zhu, B. Rebenstorf, S. L. T. Andersson, J. Chem. Soc., Faraday Trans., 85 (1989) 3645.

[32] N. D. Spencer, C. J. Pereira, J. Catal., 116 (1989) 399.

[33] M. Nakamura, K. Kawai, Y. Fujiwara, J. Catal., 34 (1974) 345.

[34] Y. Murakami, M. Niwa, T. Hattori, S. I. Osawa, I. Igushi, H. Ando, J. Catal., 49 (1977) 83.

[35] D. C. Agarwal, P. C. Nigam, R.D. Srivastava. J. Catal., 55 (1978) 1.

[36] K. Mori, A. Miyamato, Y. Murakami, J. Catal., 95 (1985) 482.

[37] V. I. E. Bruyère, L. A. G. Rodenas, P. J. Morando, M. A. Blesa, J. Chem. Soc., Dalton Trans., 24 (2001) 3593.

[38] O. V. Klimov, M. A. Fedotov, A. N. Startsev., J. Catal., 139 (1993) 142.

[39] M. Baltes, P. Van Der Voort, O. Collart, E.F. Vansant, J. Porous Mater., 5 (1998) 357.

[40] M. Baltes, O. Collart, P. Van Der Voort, E.F. Vansant, Langmuir 15 (1999) 5841.

[41] P. Van Der Voort, M. Baltes and E. F. Vansant, Catal. Today, 68 (2001) 121.

[42] P. Van Der Voort, M. G. White, E. F. Vansant. Langmuir, 14 (1998) 106.

[43] P. Van Der Voort, K. Possemiers, E. F. Vansant, J. Chem. Soc., Faraday Trans., 92 (1996) 843.

[44] A. Wokaun, M. Schraml-Marth, A. Baiker, J. Catal., 116 (1989) 595.

[45] M. D. Amiridis, I. E. Wachs, G. Deo, J. M. Jehng, D. S. Kim, J. Catal., 161 (1996) 247.

[46] P. M. Michalakos, K. Birkeland, H. H. Kung. J. Catal., 158 (1996) 349.

[47] M. A. Vuurman, D. J. Stufkens, A. Oskam, G. Deo, I. E. Wachs, J. Chem. Soc., Faraday Trans. I 92 (1996) 3259.

[48] J. M. Jehng, G. Deo, B. M. Weckhuysen, I. E. Wachs, J. Mol. Catal. A: Chem. 110 (1996) 41.

[49] V. I. Marshneva, E. M. Slavisnkaya, O. V. Kalinkina, G. V. Odegova, E. M. Moroz, G.V. Lavrova, A.N. Salanov, J. Catal., 155 (1995) 171.

[50] K. Inumaru, T. Okuhara, M. Misono, J. Phys. Chem. 95 (1991) 4826.

[51] K. Inumaru, M. Misono, T. Okuhara, Appl. Catal. A: Gen. 149 (1997) 133.

[52] G. Centi, D. Pinelli, F. Trifiro, D. Ghoussoub, M. Guelton, L. Gengembre, J. Catal. 130 (1991) 238.

[53] J. Keranen, A. Auroux, S. Ek, L. Niinisto, Appl. Catal. A: Gen., 228 (2002) 213.

[54] F. Cavani, G. Centi, E. Foresti, F. Trifiro, J. Chem. Soc. Faraday Trans. 1 (1987) 83.

[55] G. Centi, E. Giamello, D. Pijnelli, F. Trifiro, J. Catal. 130 (1991) 220.

[56] D. A. Bulushev, L. Kiwi-Minsker, A. Renken. Catal. Today 57 (2000) 231.

[57] T. Machej, J. Haber, A. M. Turek, I. E. Wachs, Appl. Catal., 70 (1991) 115.

[58] B. M. Weckhuysen, Chem. Commun. 2 (2002) 97.

[59] W. N. Delgass, G. L. Haller, R. Kellerman, J. H. Lunsford, Spectroscopy in Heterogeneous Catalysis, Academic Press, New York, 1979.

[60] I. E. Wachs (Ed.), Characterization of Catalytic Materials, Butterworths–Heineman, New York, 1992.

[61] J. H. Niemantsverdriet, Spectroscopy in Catalysis, An Introduction, VCH, Weinheim, 1993.

[62] F. Dalannay (Ed.), Characterization of Heterogeneous Catalysts, Dekker, New York, 1984.

[63] K. Weissermel, H.-J. Arpe, Industrial organic chemistry, VCH, Weinheim, 1997.

[64] D. H. James, W. M. Castor, Ullmann's Encycl. Ind. Chem. 5th ed., Vol. 25 (1994) p. 329

[65] NOVA Chemical Corporation Supplemental Financial and Product Information (2000) 10.

[66] F. Cavani, F. Trifiro, Appl. Catal. A, 133 (1995) 219.

[67] K. Kochloefl, 'Dehydrogenation of ethylbenzene' in: Handbook of heterogeneous catalysis, G. Ertl, H. Knozinger, J. Weitkamp (Eds), Vol. 5, p.2151, Wiley-VCH, Weinheim (1997).

[68] K. K. Kearby in Catalysis, P. Emmett (Ed.), Rheinhold, New York, Vol. III (1955) 469.

[69] D. E. Stobbe, F. R. van Buren, A. J. van Dillen, J. W. Geus, J. Catal., 135 (1992) 533.

[70] M. Muhler, J. Schiitze, M. Wesemann, T. Rayment, T. Dent, R. Schlögl, G. Ertl, J. Catal., 126 (1990) 339.

[71] T. Hirano, Appl. Catal., 26 (1986) 81.

[72] T. Hirano, Appl. Catal., 28 (1986) 119.

[73] L. Holmlid, P.G. Menon, Appl. Catal. A: General, 212, 1 (2001) 247.

[74] E. H. Lee, Catal. Rev. 8 (1973) 285.

[75] T. Hirano, Appl. Catal., 26 (1986) 65.

[76] Romatier J., Bentham M., Foley T., Valentine J.A. Proc. Dewitt Petrochem. Rev., Houston, Texas, 1992, p. K1.

[77] F. Tiscareno-Lechuga, C. G. Hill, Jr. M. A. Anderson, Appl. Catal. A, 96 (1993) 33.

[78] J. C. S. Wu, P. K. T. Liu, Ind. Eng. Chem. Res., 31 (1992) 322.

[79] I. P. Belomestnykh, E. A. Skrigan, N. N. Rozhdestvenskaya, G. V. Isaguliants, Stud. Surf. Sci. Catal., 72 (1992) 453.

[80] G. E. Vrieland, P. G. Menon, Appl. Catal., 77 (1991) 1.

[81] L. F. L. Delorme, F. Martins Mendes Cerejo, J. F. Grootjans, Eur. 403 462 (1990).

[82] J. N. Michaels, C. G. Vayenas, J. Catal., 85 (1984) 477.

[83] G. C. Grunewald, R. S. Drago, J. Mol. Catal., 58 (1990) 227.

[84] G. E. Vrieland, J. Catal., 111 (1988) 1.

[85] T. G. Alkhazov, A. E. Lisovskii, M. G. Safarov, A. M. Dadasheva, Kinet. Catal., 13 (1972) 509.

[86] J. Hanuza, B. Jezowska-Trzebiatowska, W. Oganowski, J. Mol. Catal., 29 (1985) 109.

[87] P. Kustrowski, M. Zbroja, R. Dziembaj, H. Papp, Catal. Lett., 80 (2002) 1.

[88] C. R. Adams, J. Catal. 11 (1968) 96.

[89] C. R. Adams, T. J. Jennings, J. Catal. 17 (1970) 157.

[90] M. Sugino, H. Shimada, T. Turuda, H. Miura, N. Ikenaga, T. Suzuki, Appl. Catal. A, 121 (1995) 125.

[91] T. Badstube, H. Papp, P. Kustrowski, Dziembaj, Catal. Lett., 55 (1998) 169.

[92] Y. Sakurai, T. Suzaki, K. Nakagawa, N. Ikenaga, H. Aota and T. Suzuki, J. Catal., 209 (2002) 16.

[93] Y. Sakurai, T. Suzaki, N. Ikenaga, T. Suzuki, Appl. Catal. A., 192 (2000) 281.

[94] N. Ikenaga, T. Tsuruda, K. Senma, T. Yamaguchi, Y. Sakurai, T. Suzuki, Ind. Eng. Chem. Res., 39 (2000) 1228.

[95] S. E. Park, J.-S. Chang, V. P. Vislovskiy, M. S. Park, K. Y. Lee, J. S. Yoo, 6th international conference on carbon dioxide utilization, Breckenridge, CO, USA, 2001, Preprinted Abstracts, p. 60.

[96] R. Dziembaj, P. Kustrowski, T. Badstube, H. Papp, Top. Catal., 11/12 (2000) 317.

[97] Mimura, N., Takahara I., Saito M., Hattori T., Ohkuma K, Ando M., Catal. Today, 45 (1998) 61.

[98] F. Kapteijn, J. Rodriguez-Mirasol, J. A. Moulijn, Appl. Catal. B., 9 (1996) 25.

[99] M. A. Wojtowicz, J. R. Pels, J. A. Moulijn, Fuel Proc. Technol., 34 (1993) 1.

[100] S. Kannan, Appl. Clay Sci., 13 (1998) 347.

[101] L. M. Kustov, A. L. Tarasov, V. I. Bogdan, A. A. Tyrlov, J. W. Fulmer, Catal. Today, 61 (2000) 123.

[102] L. Mendelovici and J. H. Lunsford, J. Catal., 94 (1985) 37

[103] A. Erdohelyi, F. Solymosi, J. Catal. 129 (1991) 497

[104] J. M. Lopez Nieto, A. Dejoz, M. I. Vazquez, W. O'Leary, J. Cunningham, Catal.

Today, 40 (1998) 215.

[105] E. V. Kondratenko, M. Baerns, Appl. Catal. A, 222 (2001) 133

[106] G. Sedmak, S. Hočevar, J. Levec, J. Catal. 213 (2003) 135.

[107] C. Özdemir, A. N. Akın, R. Yıldırım, Appl. Catal. A: General 258 (2004) 145.

[108] T. R. Ralph, G. A. Hards, Chem. Ind. 9 (1998) 337.

[109] I. H. Son, M. Shamsuzzoha, A. M. Lane, J. Catal. 210 (2002) 460.

[110] M. J. Kahlich, H. A. Gasteiger, R. J. Behm, J. Catal., 182 (1999) 430.

[111] G. Avgouropoulos, Ch. Ioannides Papadopoulou, J. Batista, S. Hočevar, H. K. Matralis, Catal. Today, 75 (2002) 157.

[112] C. E. Thomas, B. D. James, F. D. Lomax, I. F. Kuhn, Int. J. Hydrogen Energy 25 (2000) 551.

[113] Y. Li, Q. Fu, M. Flytzani-Stephanopoulos, Appl. Catal. B Env., 27 (2000) 179.

[114] K. Sekizawa, S. Yano, K. Eguchi, H. Arai, Appl. Catal. A Gen. 169 (1998) 291.

[115] C. D. Dudfield, R. Chen, P. L. Adcock, J. Power Sources 85 (2000) 237.

CHAPTER 2

Preparation And Characterization Of VO_x/Al_2O_3 Catalysts

2.1. INTRODUCTION

The successful industrial heterogeneous catalysts should possess high catalytic activity for the desired reaction, high selectivity for the desired product and acceptable commercial life. The characterization of catalytic materials is a very important step in the process of catalyst development, which gives insight into the relation between physical and chemical properties of the catalyst and its activity. If the structure and composition of the catalyst can be correlated with its activity and selectivity, the working of the catalyst can be understood.

In this work, the catalysts were prepared by wet-impregnation method and characterized by various physico-chemical methods such as X-ray diffractometry, ICP-AES, infrared spectroscopy, surface area measurements, SEM, TG-DTA, TPR, XPS, EPR, NMR etc.

The theory and experimental procedure of various characterization techniques used for the present study are briefly described in the following section. Wherever possible, the current knowledge about the application of characterization techniques for catalysts containing vanadium is also briefly discussed.

2.2. PREPARATION OF VO_x/Al_2O_3 CATALYSTS

The usual wet impregnation method is used for the preparation of VO_x/Al_2O_3 catalysts. The catalysts were prepared by impregnating γ-Al_2O_3 (Alpha products, UK) with NH_4VO_3 (s. d. fine-chem. ltd., AR grade) dissolved in an aqueous solution of oxalic acid (s. d. fine-chem. ltd., LR grade) in 1:2 weight ratio at a pH of ~ 1.9. After impregnation, the samples were dried in air at 383 K for 12 h and calcined in air at 823 K for 4 h.

The vanadium content was determined by ICP-AES. The different samples are designated in the text as nVO_x/Al_2O_3 where n is an integer corresponding to the loading of vanadia on γ-Al_2O_3 as V_2O_5.

2.3. PHYSICOCHEMICAL CHARACTERIZATION-THEORY AND EXPERIMENTAL PROCEDURE

2.3.1. X-Ray diffraction

XRD is used to identify bulk phases, if desired under *in situ* conditions and is also used to monitor the kinetics of bulk transformations and to estimate particle sizes. In catalyst characterization, diffraction patterns are mainly used to identify the crystallographic phases that are present in the catalyst [1]. The XRD method involves the interaction between the incident monochromatized X-rays (like Cu Kα or Mo Kα source) with the atoms of a periodic lattice. X-rays scattered by atoms in an ordered lattice interfere constructively in directions given by Bragg's law:

$$n\lambda = 2\,d\sin\theta;\ n = 1, 2, 3,\ldots. \qquad (2.1)$$

where λ is the wavelength of the X-rays, d is the distance between two lattice planes, θ is the angle between the incoming X-rays and the normal to the reflecting lattice plane and n is the integer called order of the reflection.

Bragg peaks are measured by observing the intensity of the scattered radiation as a function of scattering angle 2θ. The angles of maximum intensity enable one to calculate the spacings between the lattice planes and allow furthermore for phase identification. The width of diffraction peaks carries information on the dimensions of the reflecting planes. Diffraction lines from the perfect crystals are very narrow. For crystals with size below 100 nm, line broadening occurs due to incomplete destructive interference in scattering directions where the X-rays are out of phase. The width of the diffraction lines can be used to estimate the crystal size by the relation, Debye-Scherrer formula [2],

$$\langle L\rangle = k\lambda/\beta\cos\theta \qquad (2.2)$$

where $\langle L\rangle$, λ, β and θ are the volume averaged particle diameter, X-ray wavelength, full width at half maximum (FWHM), diffraction angle respectively and k is a constant, often taken as 1.

One important limitation of XRD is that this technique requires samples, which possess sufficient long-range order. Amorphous phases and small particles give either broad and weak diffraction lines or no diffraction at all which makes them virtually invisible for XRD.

Powder X-ray diffraction (XRD) patterns of all catalysts reported in this thesis were obtained on a Rigaku Geigerflex diffractometer with a monochromatic Cu Kα radiation (λ= 0.15406 nm, 30 kV, 15 mA) with Ni-filter. Samples were scanned within the 2θ range of $10\text{-}85^0$ with a step size of 0.02.

2.3.2. Infrared Spectroscopy

Infrared spectroscopy (IR) can be considered as the first and the most important of the modern spectroscopic techniques that has found general acceptance in catalysis. The technique is used to identify phases that are present in the catalyst or its precursor stages, the adsorbed species, adsorption sites and the way in which the adsorbed species are chemisorbed on the surface of the catalyst. The first studies in the mid infrared region in catalysis were done in the pioneering work of Eischens and Pliskin, as described in their review of 1958 [3].

Infrared spectroscopy is the most common form of vibrational spectroscopy and it depends on the excitation of vibrations in molecules or in solid lattices by the absorption of photons, which occurs if a dipole moment changes during the vibration. The intensity of the infrared band is proportional to the change in dipole moment. A variety of IR techniques have been used to get information on the surface chemistry of different solids. With respect to the characterization of metal oxide catalysts two techniques largely predominate, namely, the transmission/absorption and the diffuse reflection techniques. In the first case, the sample consists typically of 10-100 mg of catalyst, pressed into a self-supporting disc of approximately 1 cm^2 and a few tenths of a millimeter thickness. In diffuse reflectance mode (DRIFT), samples can be measured by simply depositing on a sample holder, avoiding the tedious preparation of wafers. This technique is especially useful for strongly scattering or absorbing samples.

The infrared absorption spectrum is described by Kubelka Munk function [4,5]:

$$F(R_\infty) = K/S = (1-R_\infty)^2/2R_\infty \qquad (2.3)$$

where K is the absorption coefficient, which is a function of the frequency ν, S is the scattering coefficient and R_∞ is the reflectivity of a sample of infinite thickness, measured as a function of ν.

Regarding supported vanadium oxide catalysts, the infrared spectroscopy technique can provide information on the molecular structure, although the investigation of the surface vanadium oxide vibrations is often complicated due to the overlapping infrared bands of the support oxide [6-14]. IR can also probe the interaction of vanadium oxide with the surface hydroxyl groups of the oxide support since hydroxyl groups give rise to intense infrared absorption bands. The technique is also frequently used to study the interaction of the catalyst material with reactant molecules during adsorption or surface studies. Examples are the oxidation reactions of methanol and toluene.

The Fourier transform-infrared spectra of the catalysts reported here were recorded on Shimadzu 8300 FT-IR spectrometer at ambient conditions. The spectra were recorded using thin self-supporting discs made by pressing the mixture of catalyst sample and KBr.

2.3.3. Laser Raman Spectroscopy (LRS)

Raman spectroscopy is based on the inelastic scattering of photons, which loose energy by exciting vibrations in the sample. A vibration is Raman active if it changes the polarizability of the molecule. Raman and infrared spectroscopies complement each other, in particular for highly symmetrical molecules.

Raman spectroscopy can widely be used for investigations of oxides, supported and bulk metals, supported oxides and at the water-solid interface and has found steadily increasing application for the characterization of supported transition metal oxide catalysts since the early work of Villa *et al* [15] in 1974. LRS is particularly powerful for investigations of the structure of supported oxide catalysts. All characteristic vibrational features of oxides of the transition metals like Mo, W, Cr, V and Re fall into the frequency range below 1100 cm^{-1}. These oxides have high Raman scattering cross-sections because of their relatively high covalent bond character. The usual support materials (particularly alumina and silica) have very low Raman scattering cross-sections and only show weak absorption bands in the 700–1100 cm^{-1} region. Hence LRS has the advantage that the normal modes of the minority components, namely the transition metal oxides dispersed on the supports, can most frequently be detected by LRS with relative ease in the frequency

region from 50 to 100 cm^{-1}. It should be also mentioned that titania and zirconia oxides possess strong Raman absorption bands in the region below 700 cm^{-1}.

The Raman spectroscopy technique can discriminate between different vanadium oxide coordination environments and bond lengths [16-26]. As mentioned previously, vanadium–oxygen vibrations are present below 1100 cm^{-1} in which range, silica and alumina supports show any or only very weak Raman bands. Interaction of the vanadium oxides with the support hydroxyls cannot be easily studied with RS since the hydroxyl groups of the support oxides are weak Raman scatterers. Only for titania and silica, sometimes weak hydroxyl groups can be observed. Various studies have demonstrated that the simultaneous use of reference vanadium oxide compounds and the correlation between Raman frequency and bond length makes RS very well suited to study the molecular structures of supported vanadium oxides. The surface vanadium oxide structure has been studied during the adsorption and oxidation of methanol and methane, and during the selective catalytic reduction of nitrogen oxides.

There are some major problems that may be encountered in LRS like the heating effects of the laser beam, low sensitivity of the technique and background fluorescence.

Laser Raman spectra reported in this thesis were obtained at room temperature using a Spex 1403 spectrometer. The samples were pressed into 9 mm diameter by 1 mm thick wafers and heated at 473 K in air for 2 h and cooled to room temperature before recording the spectra. The 514.5 nm line of an argon ion laser (Spectra Physics 165) was used for excitation. The laser power at the sample was approximately 40 mW. The scattered light was collected in the backscattering geometry and detected with a thermoelectrically cooled photomultiplier (RCA, type C31034).

2.3.4. Diffuse reflectance UV-visible spectroscopy

Diffuse reflectance spectroscopy (DRS) is a spectroscopic technique based on the reflection of light in the ultraviolet (UV), visible (VIS) and near-infrared (NIR) region by a powdered sample. In a DRS spectrum, the ratio of the light scattered from an “infinitely thick” closely packed catalyst layer and the scattered light from an infinitely thick layer of an ideal non-absorbing (white) reference sample is measured as a function of the

wavelength λ. The scattered radiation, emanating from the sample, is collected in an integration sphere and detected. The most popular continuum theory describing diffuse reflectance effect is Schuster-Kubelka-Munk (SKM) theory. If the sample is infinitely thick, the diffuse reflection of the sample (R_∞) is related to an apparent absorption (K) and apparent scattering coefficient (S) by the SKM equation [27,28]:

$$F(R_\infty) = (1-R_\infty)^2 / 2R_\infty = K/S \qquad (2.4)$$

At low concentrations of supported transition metal ions (TMI), this equation is a good representation of the absorbing spectrum and allows a quantitative determination of the TMI.

$$F(R_\infty) = (1-R_\infty)^2 / 2R_\infty = K/S = \alpha C_{TMI} / S = k\, C_{TMI} \qquad (2.5)$$

When at a given wavelength λ, S is constant, the above equation gives a linear relation between $F(R_\infty)$ and the TMI concentration, $C_{TMI.}$ The coefficients α and k are proportionality constants.

DRS is a particularly suitable technique for studying the speciation of supported TMIs because it measures both their d-d transitions and charge transfer bands. The obtained information is directly chemical since the outer shell electrons are probed. The DRS technique can be used under *in situ* conditions. DRS technique can be applied at different levels of sophistication, from merely detecting the presence of a certain oxidation state of a supported TMI up to a detailed distribution of different oxidation states and coordination environments under catalytic conditions. If the spectra are complex, encompassing several broad and overlapping bands, chemometrical techniques need to be employed for correct spectral analysis.

In the case of supported vanadium oxides, the diffuse reflectance spectroscopy (DRS) technique in the UV-Vis-NIR region can provide insight on the different oxidation states and coordination geometries [29-33]. The DRS technique probes the charge transfer transitions as well as the d–d transitions of vanadium ions at the catalyst surface. The technique is quantitative at least for low vanadium oxide loadings and can be used under *in situ* conditions. The disadvantage is that the DRS signals are usually broad and overlap with each other, leading to a biased spectral analysis. In addition, the origin of the specific

electronic transition is sometimes difficult to isolate due to its dependence on the local coordination environment, the polymerization degree and the specific oxidation state.

Diffuse reflectance UV-visible spectra of the present samples were recorded using a Shimadzu UV-2550 spectrophotometer. The reflectance spectra were converted into the Kubelka-Munk function, F(R) that is proportional to the absorption coefficient for low values of F(R). The spectra were measured in the range of 200-800 nm in air at room temperature.

2.3.5. Surface area determination by BET method

The most common method of measuring surface area of catalytic materials is that based on the theory developed by Brunauer, Emmett and Teller in 1938 considering the multilayer adsorption. The isotherm points are transformed with the linear version of BET equation [2]:

$$p/V(p_0-p) = 1/cV_m + [(c-1)/cV_m]\ (p/p_0) \qquad (2.6)$$

where p is adsorption equilibrium pressure, p_0 is saturation vapor pressure of the adsorbate at the experimental temperature, V is volume of gas adsorbed at pressure p, V_m is volume of adsorbate required for monolayer coverage and c, a constant that is related to the heat of adsorption and liquefaction. A linear relationship between $p/V(p_o/p)$ and p/p_o is required to obtain the quantity of nitrogen adsorbed. This linear portion of the curve is restricted to a limited portion of the isotherm, generally between 0.05-0.30. The monolayer volume, Vm is given by 1/(S+I), where S is the slope and is equal to $(c-1)/cV_m$ and I is the intercept and is equal to $1/cV_m$. The surface area of the catalyst (S_{BET}) is related to V_m, by the equation,

$$S_{BET} = (V_m/22414)\ N_a\ \sigma \qquad (2.7)$$

where N_a is Avogadro number and σ is mean cross sectional area covered by one adsorbate molecule. The σ value generally accepted for N_2 is 0.162 nm^2.

The BET surface area, S_{BET}, of the catalysts was measured by nitrogen adsorption-desorption method at 77 K using NOVA 1200 surface area analyzer (Quantachrome). The catalyst samples were evacuated at 573 K for 3 h till the residual pressure was 2×10^{-3} Torr before nitrogen sorption. The isotherms were analyzed in a conventional manner in the region of the relative pressure, p/p_0 = 0.05 to 0.3.

2.3.6. Scanning electron microscopy (SEM)

Scanning electron microscopy is a rather straightforward technique to study overall topography [36]. SEM scans over a sample surface with a probe of electrons (5-50 kV) and detects the yield of either secondary or back-scattered electrons as a function of the position of the primary beam. Parts of the surface facing the detector appear brighter than parts of the surface with their surface normal pointing away from the detector. Magnification of 20-50,000 is possible with a resolution of about 5 nm. Crystallite shape, size and size distributions are easily obtained for particles larger than 5 nm. The size and morphology of the catalysts of the present study were examined using a JEOL JSM-840A scanning electron microscope.

2.3.7. Thermal analysis (TG, DTG and DTA)

Thermo analytical techniques involve the measurements of the response of the solid under study (energy or mass released or consumed) as a function of temperature (or time) dynamically by application of a linear temperature program. Thermogravimetry is a technique measuring the variation in mass of a sample when it undergoes temperature scanning in a controlled atmosphere. This variation in mass can be either a loss of mass (vapor emission) or a gain of mass (gas fixation). Differential thermal analysis is a technique measuring the difference in temperature between a sample and a reference (a thermally inert material) as a function of the time or the temperature, when they undergo temperature scanning in a controlled atmosphere. The DTA method enables any transformation to be detected for all the categories of materials, providing information on exothermic and endothermic reactions taking place in the sample, which include phase transitions, dehydration, decomposition, redox, or solid-state reactions. In catalysis, these techniques are used to study the genesis of catalytic materials via solid-state reactions.

In the present work, thermogravimetry and differential thermal analysis measurements of the as synthesised samples were performed with a Mettler Toledo TA-1 apparatus equipped with a control and data acquisiton system developed by the Anatech Bv. The analyses were carried out in air (80 ml min^{-1}) at a heating rate of 10 K min^{-1} using about 10 mg samples in an alumina pan. The reference material was α-alumina powder.

2.3.8. Temperature programmed techniques: TPR

Temperature programmed reaction methods typically involve monitoring surface or (bulk) processes between the solid catalyst and its gaseous environment via continuous analysis of the gas phase composition as the temperature is raised linearly in time. Instrumentation for temperature-programmed investigations consists of a reactor, charged with catalyst, in a furnace that can be temperature programmed and a thermal conductivity detector to measure the concerned active gas of the gas mixture before and after reaction. All these techniques are applicable to real catalysts and single crystals. Interpretation on a qualitative basis is rather straightforward, however quantitative analysis is more complicated.

Temperature programmed reduction (TPR) determines the number of reducible species present in the catalyst and reveals the temperature at which the reduction occurs. An important aspect of TPR analyses is that the sample need not have any special characteristics other than containing reducible metals.

In a TPR experiment, the catalyst material is placed in a fixed-bed reactor in a flow of a reducing gas mixture (typically, argon or nitrogen containing a few volume percent of hydrogen) and subjected to a linear temperature ramp. The consumption of hydrogen by adsorption/reaction is continuously measured by monitoring the change in composition of the gas mixture after passing through the reactor. The degree of reduction can be calculated from the amount of hydrogen consumed.

The temperature programmed reduction experiments were carried out with a Micromeritics Autochem 2910 catalyst characterization system, equipped with a TCD detector. Fresh, dried samples were pretreated by passing high purity (99.9%) argon (20 ml/min) at 773 K for 3 h. After cooling to ambient temperature, argon atmosphere is replaced by 5% H_2/Ar mixture. The catalyst samples were heated in this atmosphere to 1273 K at a heating rate of 5 K/min. The flow rate of H_2/Ar mixture was kept at 40 ml/min throughout the experiment. The water produced during the reduction was condensed in a cold trap immersed in a slurry of isopropanol and liquid nitrogen. The amount of catalyst in these experiments was adjusted so that samples contain equivalent amounts of V_2O_5 in all the experiments.

2.3.9. X-ray Photoelectron Spectroscopy (XPS)

XPS is one of the most frequently used techniques in catalysis. It yields information on the elemental composition, the oxidation state of the elements and in favorable cases on the dispersion of one phase over another.

XPS [37-39] is based on the photoelectric effect. In this technique, sample surface is irradiated with X rays and the emitted photoelectrons are measured. When an atom absorbs a photon of energy hν, a core or valence electron with binding energy E_b is ejected with kinetic energy E_k:

$$E_k = h\nu - E_b - \varphi \qquad (2.8)$$

where h is Planck's constant, ν is the frequency of the exciting radiation, E_b is the binding energy of the photoelectron relative to the Fermi level of the sample and φ is the work function of the spectrometer.

XPS (also referred by the acronym ESCA, electron spectroscopy for chemical analysis) entails emission from both core and valence electrons of the solid, the stimulating X-ray sources being usually Al Kα (1486.6 eV) or Mg Kα (1253.6 eV). The XPS spectrum is usually a plot of the intensity of photoelectrons versus binding energy.

Since the electrons whose energies are analyzed in XPS arise from a depth of no greater than about 5 nm, the technique is highly surface specific. A set of binding energies is characteristic for an element and hence XPS can be used to analyze the composition of samples, considering the area of the peak and cross section for photoemission. Binding energies are not only element specific but contain chemical information like oxidation state, because the energy levels of core electrons depend slightly on the chemical state of the atom. Chemical shifts are typically in the range of 0-3 eV [1].

An experimental problem in XPS is that electrically insulating samples may charge during measurement, as photoelectrons leave the sample. Due to the positive charge on the sample, all XPS peaks in the spectrum shift by the same amount to higher binding energies. Calibration for this effect can be done by using C 1s binding energy of 284.9 eV from carbon contamination, which is present on most of the catalysts.

Though XPS can provide information about the oxidation state and the chemical environment of a given atom due to shifts in the binding energies [40-47], the structural

information is, however, limited in case of supported vanadium oxides since XPS cannot discriminate between different VO_x structures possessing the same oxidation state, i.e. between VO_6, VO_5 and VO_4. Another disadvantage is the use of ultrahigh vacuum conditions, which may result in the reduction of surface vanadium species in the measurement chamber. The technique only provides information about the catalyst surface. This is advantageous also since the vanadium oxide to support oxide ratio provides information on the dispersion of the vanadium oxide phase and the dimension of the vanadium oxide crystals at the catalyst surface. In addition, the technique allows verifying impurities (e.g. K, Na and Cl) potentially present in the catalyst material.

In the present study, X-ray Photoelectron spectra were acquired on a VG Microtech Multilab ESCA 3000 spectrometer using a non-monochromatized Mg Kα X-ray source (hν = 1253.6 eV) on '*in situ*' scraped fresh catalyst pellets at room temperature. Selected spectra were recorded with Al Kα X-ray (hν = 1486.6 eV) also to eliminate the overlap between different Auger and core levels. Base pressure in the analysis chamber was maintained at 3-6 x 10^{-10} Torr range. The energy resolution of the spectrometer was determined from the full width at half maximum of metallic gold and the value obtained is better than 0.8 eV for Mg K_α radiation and 1.1 eV for Al K_α radiation respectively, at a pass energy of 20 eV.

2.3.10. ^{51}V Solid-state Nuclear Magnetic Resonance Spectroscopy

Nuclear Magnetic Resonance (NMR) spectroscopy gives information on the interaction of a nucleus having a nuclear spin quantum number, I, greater than zero with an external magnetic field. The interaction of nuclear spins with the externally applied magnetic field, B_0, and their environment can be described by the spin Hamiltonian H:

$$H = H_Z + H_{CS} + H_Q + H_D + H_J \qquad (2.9)$$

H_Z is a Hamiltonian, which describes the interaction of the nuclear spin with the external field B_0 (Zeeman interaction). The chemical shift Hamiltonian H_{CS} gives the information on the local environment of a nucleus. The chemical shift is measured relative to that of a reference compound ($VOCl_3$ in case of ^{51}V NMR) and is expressed in Hertz or in ppm with respect to the resonance frequency of the reference compound.

H_Q describes the quadrupolar interaction of the nucleus with the surrounding electric field gradient. For ^{51}V nuclei, it is rather small. H_D describes the dipolar interaction with other nuclei, while H_J describes the interaction with other nuclei through J-coupling.

In solid-state NMR, the line shape is determined by dipolar and quadrupolar interactions. The lines are usually broader because the rigid structure of the solid phase prevents the averaging of the dipolar interaction (H_D) by motions. Since the first order quadrupolar and dipolar interactions are proportional to $(3\cos^2\theta - 1)$, where θ is the angle between an internuclear vector and the magnetic field, these interactions can be removed, to a first order approximation, by spinning the sample around the so-called magic angle β with respect to the external magnetic field, for which $3\cos^2\beta - 1 = 0$, i.e. $\beta = 54.74^0$. This technique is known as Magic Angle Spinning (MAS) [48,49].

Solid-state ^{51}V nuclear magnetic resonance (NMR) is a suitable technique to investigate supported V^{5+} oxides since the nuclear spin of vanadium is 7/2, its natural abundance is almost 100% and the capability of the technique to discriminate between different coordination environments of vanadium oxides [50-59]. The presence of paramagnetic species, such as V^{4+}, may broaden the NMR signal, and consequently, the signal due to V^{5+} can be lost. ^{51}V NMR has been used to characterize supported vanadium oxides on, e.g. silica, alumina, titania and zirconia. The limitation of the technique is the somewhat lower sensitivity, especially when compared with ESR techniques.

^{51}V MAS NMR experiments were performed at 131.54 MHz on a Bruker DRX-500 NMR spectrometer with a Bruker ^1H-BB CP-MAS probe head in the present study. The samples were spun using 4 mm diameter zirconia rotors at 8, 10 or 12 kHz. Spectra were obtained with a pulse length of 3 μs & recycle delay of 500 ms.

2.3.11. Electron Paramagnetic Resonance (EPR)

EPR has been applied to surface chemistry and catalysis for more than thirty years to investigate the nature of the catalytic site and its environment (symmetry, number and nature of the ligands, etc). The high sensitivity of the technique permits the study of low

concentrations of active sites. The technique has the limitation that diamagnetic species cannot be observed and hence only limited type of species can be studied. The same time, it is an advantage also since many highly reactive paramagnetic intermediates can be studied without any spectroscopic interference.

EPR technique is based on the interaction between electron magnetic moment and an external applied magnetic field designated as Zeeman interaction. When a system containing unpaired electrons (spin $\neq 0$) is placed in an external magnetic field H, the energy of the system is given by the equation $E = \pm (1/2)\, g_e \beta H$. When this system is irradiated by suitable electromagnetic radiation perpendicular to the magnetic field with a frequency ν, the transition between the two Zeeman levels occurs provided the photon energy $h\nu$ is such that the condition $\Delta E = g_e \beta H = h\nu$ is fulfilled. This is the resonance condition and results in an energy absorption. The actual EPR experiment consists of sweeping the magnetic field at constant microwave frequency until the resonance condition ($h\nu = g_e \beta H$) is obtained, resulting in an energy absorption by the sample. A solid sample may be analyzed as a single crystal or as a powder. Powders are generally placed in silica tubes, typically 5 or 6 mm in outer diameter. Recording may be performed in a wide range of temperatures, typically 77 to 600 K. The spectrometer usually works with a 9000 MHz klystron (λ = 3 cm, X band). However, for some experiments, other frequencies, such as 23, 000 MHz (K band) or 35,000 MHz (Q band) are used. The energy involved in spin-flip transitions is very small ($\cong 10^{-4}$ eV) which means EPR is not a destructive technique and therefore does not modify the catalysts during the analysis. The main information that may be gained from EPR experiments arises from the main parameters, g-factor, hyperfine interactions and superhyperfine interactions [60,61].

EPR is a powerful and quantitative technique to study especially the presence and coordination geometry of the paramagnetic V^{4+} (d^1) species even under *in situ* conditions [62-67]. The interaction of the unpaired electron with the vanadium nucleus, which has a nuclear spin of 7/2, result in a complex spectrum with a high number of hyperfine lines. This hyperfine splitting is sensitive to the chemical environment around the paramagnetic V^{4+} ion. Therefore, EPR is very well suited to characterize the molecular structure of surface V^{4+} species, whereas V^{3+} (d^2) ions can only be studied at specific conditions. The

fact that V^{4+} species can be observed in an easy way can be regarded both as an advantage and a disadvantage. Spin-spin coupling at high vanadium oxide loading may lead to inaccurate quantitative determinations of V^{4+} species.

2.4. CATALYST CHARACTERIZATION-RESULTS AND DISCUSSION

Table 2.1 shows the vanadium content, BET surface area and VO_x surface density of calcined VO_x/Al_2O_3 catalysts. Vanadium contents of the catalysts were determined by ICP analysis and VO_x surface density of each catalyst was calculated from its vanadium content and BET surface area (VO_x surface density is defined as the number of VO_x units present in unit specific surface area of the catalyst and expressed in VO_x nm^{-2}). The catalysts were calcined at 823 K for 4h. It is observed that specific surface area decreased with increasing vanadium content. The surface area normalized per amount of support (γ-Al_2O_3) is nearly constant (Table 2.1); hence this decrease corresponds to the low surface area of the added vanadia. However, for 20 VO_x/Al_2O_3, normalized surface area is comparatively lower that indicates blocking of some of the pores of support (γ-Al_2O_3) by vanadia crystallites in this case [68].

Table 2.1: Characteristics of alumina support and supported vanadia catalysts[#]

Sample	Vanadia content (wt%)	V content[*] (ICP, wt%)	Surface area (m^2/g)	VO_x surface density (VO_x/nm^2)	Surface area normalized by amount of support (m^2/g)	Crystallite size[**] (nm)
Al_2O_3	0	0	113	0	113	12.33
2 VO_x/Al_2O_3	2	1.06	105	1.26	107	12.39
5 VO_x/Al_2O_3	5	2.58	102	3.25	107	12.37
10 VO_x/Al_2O_3	10	4.74	95	6.97	106	11.99
20 VO_x/Al_2O_3	20	9.16	81	16.35	101	12.64

[#]*Catalysts calcined at 823 K for 4h. The characterization results discussed below are for catalysts calcined at 823 K for 4h unless otherwise specified*
[*]*Determined by ICP-AES*
[**]*Calculated using Debye-Scherrer equation*

2.4.1. X-Ray Diffractometry

Figure 2.1 shows the XRD patterns of VO_x/Al_2O_3 catalysts calcined at 823 K as a function of vanadia loading. For vanadia loadings up to 10 wt%, only the peaks characteristic of γ-Al_2O_3 (JCPDS 10-425) were observed. For the catalyst containing 20 wt% V_2O_5 (20 VO_x/Al_2O_3), well-defined peaks corresponding to crystalline V_2O_5 (JCPDS 9-387) have appeared in the XRD pattern. The diffractogram also shows the presence of aluminum orthovanadate, $AlVO_4$ (JCPDS 39-276) for 20 VO_x/Al_2O_3, which is the only stable ternary compound in the binary Al_2O_3-V_2O_5 system. The major peaks for both phases are indicated in Fig. 2.1. The peaks at 2θ = 25.6, 27.9 and 28.7 correspond to 012, 20 $\bar{1}$ and 02 $\bar{2}$ planes of $AlVO_4$ respectively. $AlVO_4$ phase forms from a solid-state reaction between V_2O_5 and Al_2O_3 of the following type, $V_2O_5 + Al_2O_3 \rightarrow 2\ AlVO_4$. $AlVO_4$ phase could be identified at temperatures as low as 823 K, which is much lower than that

required for the formation of bulk $AlVO_4$. One possible explanation is that at this temperature, the reaction is occurring mainly at the surface where diffusion rates are at least an order of magnitude faster than in the bulk [69]. The absence of any vanadia peaks for catalysts with 2-10 wt% vanadia loadings may be due to the high dispersion of vanadia on Al_2O_3 surface at these loadings with particle sizes less than 40 Å, which are not detectable by XRD. The Tamman temperature of V_2O_5 is approximately 449 K (melting point of bulk V_2O_5 is 963 K), so that surface spreading of V_2O_5 is likely to occur even at low temperatures of calcination.

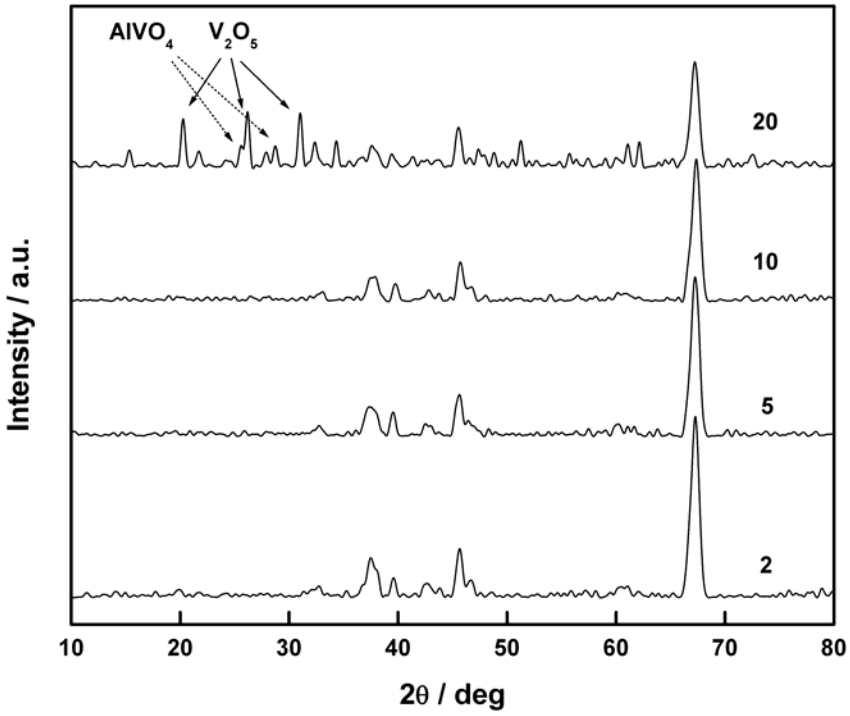

Fig. 2.1: *Powder X-ray diffraction patterns of calcined VO_x/Al_2O_3 catalysts as a function of vanadia loading in wt%.*

Figure 2.2 shows the X-ray diffractograms of 10 VO_x/Al_2O_3 at various stages of thermal treatment. Only the peaks characteristic of γ-Al_2O_3 are observed for the samples

dried at 383 K (Fig. 2.2) and calcined for 4 hours at temperatures up to 823 K. When the duration of calcination is increased to 8h at 823 K, the diffraction pattern shows the formation of $AlVO_4$. The catalyst calcined at 923 K for 4 h show very low intense peaks of $AlVO_4$ while major peaks corresponding to V_2O_5 are observed when the calcination temperature is raised to 1023 K. The absence of $AlVO_4$ peaks at 1023 K is in agreement with the fact that the compound melts incongruently above 973 K [70]. The peaks characteristic of γ-Al_2O_3 increase in intensity at 1023 K indicating an increase in crystallinity of the same.

The volume averaged particle sizes corresponding to different catalysts were calculated using Debye-Scherrer equation (equation 2.2) considering the most intense peak of γ-Al_2O_3 (d=1.40). This peak was fitted with Gaussian function for each catalyst from which the values of full width at half maximum (FWHM) were determined. The particle sizes are around 12 nm for VO_x/Al_2O_3 catalysts calcined at 823 K and don't vary significantly with vanadia loading (Table 2.1). When 10 VO_x/Al_2O_3 is subjected to calcination at different temperatures, particle size increased marginally till 923 K, however increased considerably at 1023 K (Table 2.2). This, together with the increase in intensity of peaks characteristic of γ-Al_2O_3, indicate the formation of more crystallites from amorphous material or the agglomeration of smaller crystallites to larger particles above 923 K.

Table 2.2: Particle size of 10 VO_x/Al_2O_3 as a function of thermal treatment

Calcination temperature (K)	Calcination time (h)	Particle size (nm)
Dried at 383 K	8	11.56
723	4	11.92
823	8	12.31
923	4	12.58
1023	4	17.37

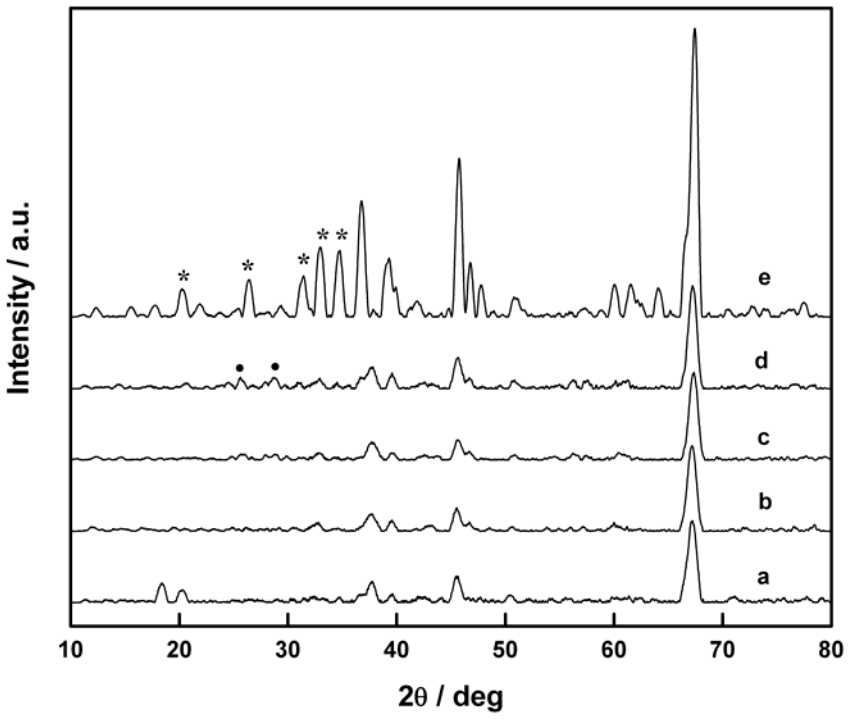

Fig. 2.2: *Powder X- ray diffraction patterns of 10 VO_x/Al_2O_3 catalysts (a) dried at 383 K and calcined at (b) 723, 4h (c) 823, 8h (d) 923, 4h (e) 1023, 4h. Major peaks of V_2O_5 and $AlVO_4$ are denoted by (∗) and (•) respectively.*

The powder X-ray diffraction patterns of bulk vanadium pentoxide and its mechanical mixtures with alumina, calcined at 1023 K, are given in Fig. 2.3 for comparison. Typical powder diffraction pattern of orthorhombic vanadium pentoxide is seen in Fig. 2.3 a. After thermal treatment at 1023 K for 4h, vanadium pentoxide exhibits intense peaks at 2θ values of 20.2 and 41.2 while all other peaks greatly reduced in intensity. The mechanical mixture containing 20 wt% vanadium pentoxide and 80% alumina gives diffraction pattern containing peaks of both phases on calcination at 1023 K. In contrast, the major peaks are due to vanadia for an equimolar mixture of vanadium pentoxide and alumina, calcined at the same temperature. The results show that the

structural integrity of vanadium pentoxide is retained to a large extent at calcination temperatures greater than its melting point when it contains alumina as a second phase, compared to unsupported vanadia. It can be also noted that the relative intensities of the peaks characteristic of vanadia phase differ according to the composition of the mixture, indicating different orientations of crystallites. The calcined equimolar mixture exhibits an intense (001) peak indicating preferential orientation in the <001> direction. Vanadia is present in an orthorhombic symmetry on calcined 20 VO_x/Al_2O_3 catalyst, the most intense peaks being (001), (110) and (400) peaks. These peaks, that correspond to 2θ values of 20.4, 26.2 and 31.2 respectively, are almost equally intense.

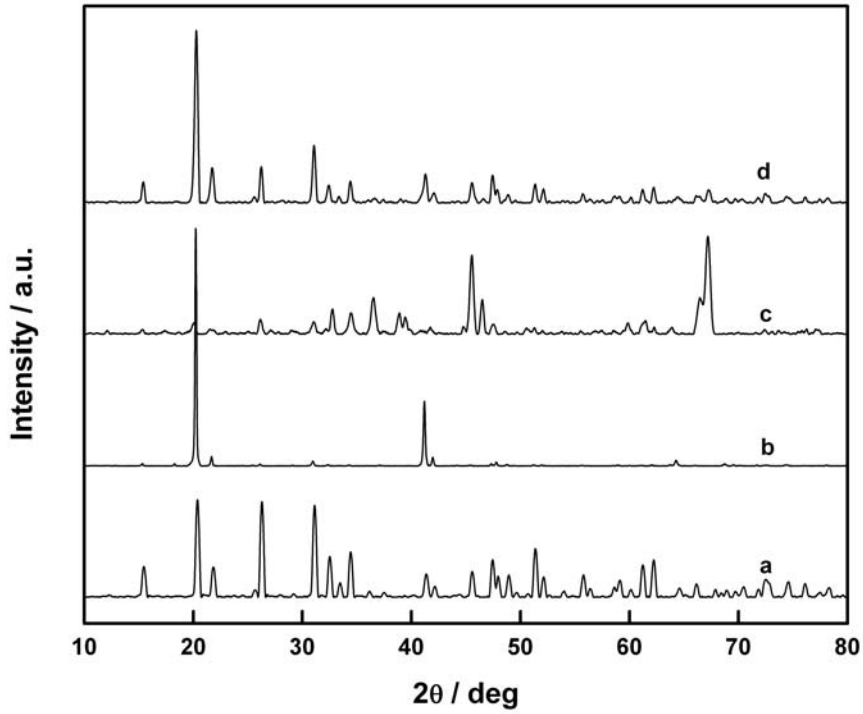

Fig. 2.3: *Powder X-ray diffraction patterns of (a) bulk V_2O_5 (b) V_2O_5 calcined at 1023 K for 4h (c) 20% V_2O_5+80% Al_2O_3 calcined at 1023 K for 4h (d) 1 mole V_2O_5 + 1 mole Al_2O_3 calcined at 1023 K for 4h.*

In conclusion, the X-ray diffraction results indicate that at low vanadia loading, highly dispersed amorphous vanadia phase is present while at higher loadings crystalline V_2O_5 co-exist with amorphous phase. Also, the structure of vanadia species is not only a function of vanadia loading but also depends on calcination temperature.

2.4.2. Scanning Electron Microscopy

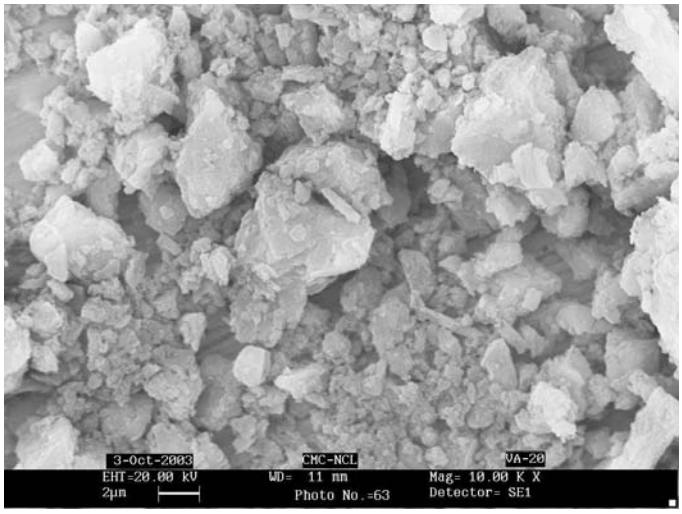

(a)

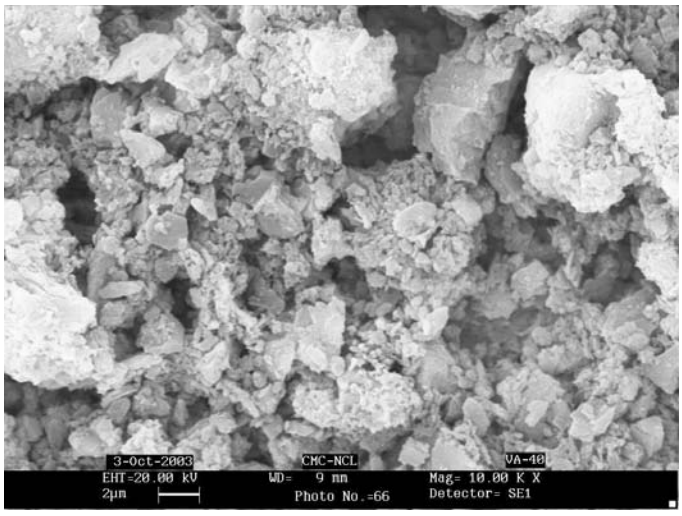

(b)

Fig. 2.4: *Scanning Electron Micrographs of calcined (a) 2 VO_x/Al_2O_3 and (b) 20 VO_x/Al_2O_3 catalysts. Magnification: 10 K.*

The scanning electron micrographs of VO_x/Al_2O_3 catalysts, calcined at 823 K for 4h, with vanadia loadings of 2 and 20 wt% are shown in Fig. 2.4. These images show that the morphology of the particles depends on the vanadium content. The particles of 2 VO_x/Al_2O_3 differ from that of 20 VO_x/Al_2O_3 in morphology. The samples of both catalysts contain particles with non-uniform size and shape.

2.4.3. Thermal Analysis

To investigate the changes occurring in the catalysts with thermal treatment, the dried (in air at 383 K for 12h) samples were subjected to thermal analysis. The TG, DTG and DTA profiles of 2, 5 and 20 VO_x/Al_2O_3 catalysts are shown in Fig. 2.5 a-c. The main weight loss is observed in two steps between 180-360 ^{0}C for all the samples. The first stage, i.e. the weight loss recorded up to 260 ^{0}C, may be ascribed to the removal of water. Endothermic peaks are observed in DTA in this temperature range, which arises due to the energy absorption required for water elimination.

The weight loss recorded in the region 260-360 ^{0}C increases with increase in vanadia loading and is much higher for 20 VO_x/Al_2O_3, approximately 11%, compared to 1.9 and 2.9% for 2 and 5 VO_x/Al_2O_3 respectively. This weight loss can be assigned as due to the decomposition of vanadyl oxalate. As mentioned in preparation procedure of the catalyst (section 2.2), the catalysts were impregnated with a solution of NH_4VO_3 in oxalic acid solution. The dissolution of NH_4VO_3 in aqueous solution of oxalic acid leads to the formation of light blue ammonium vanadyl oxalate which is get deposited on the support during impregnation. The total decomposition of this precursor during thermal treatment in air to yield supported vanadia can be written as:

$$(NH_4)_2[VO(C_2O_4)_2] + 4\,O_2 \rightarrow N_2 + 4\,CO_2 + 4\,H_2O + VO_x \qquad (2.10)$$

The weight loss in the range 260-360 ^{0}C should be due to the evolution of gaseous products like CO_2. An exothermic peak is observed in DTA of 20 VO_x/Al_2O_3 in this temperature range. The appearance of exothermic peak, though the decomposition of vanadyl oxalate is an endothermic process, can be explained as following:

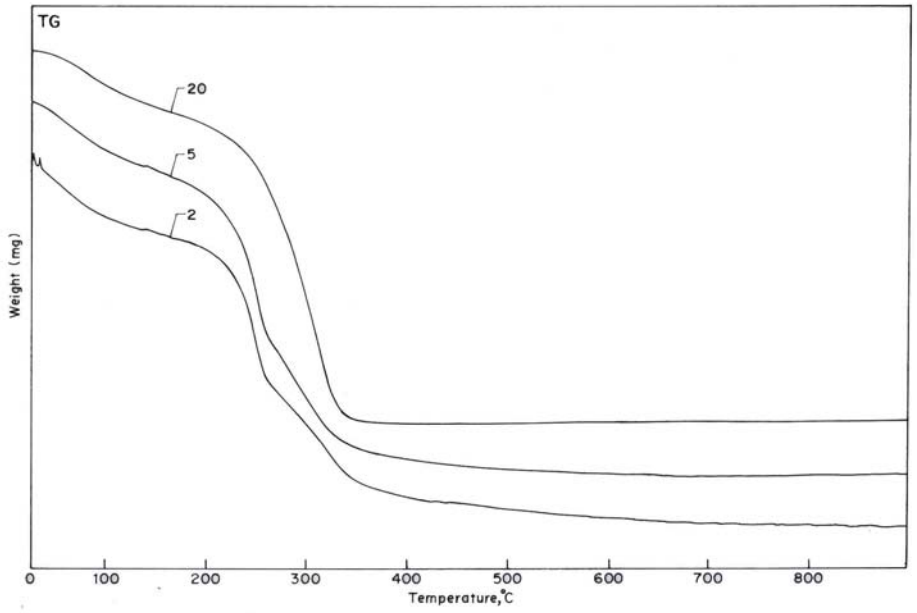

Figure 2.5a: *Thermogravimetric curves of as synthesized (dried) VO_x/Al_2O_3 catalysts. The numbers in figure indicate vanadia loadings as wt%.*

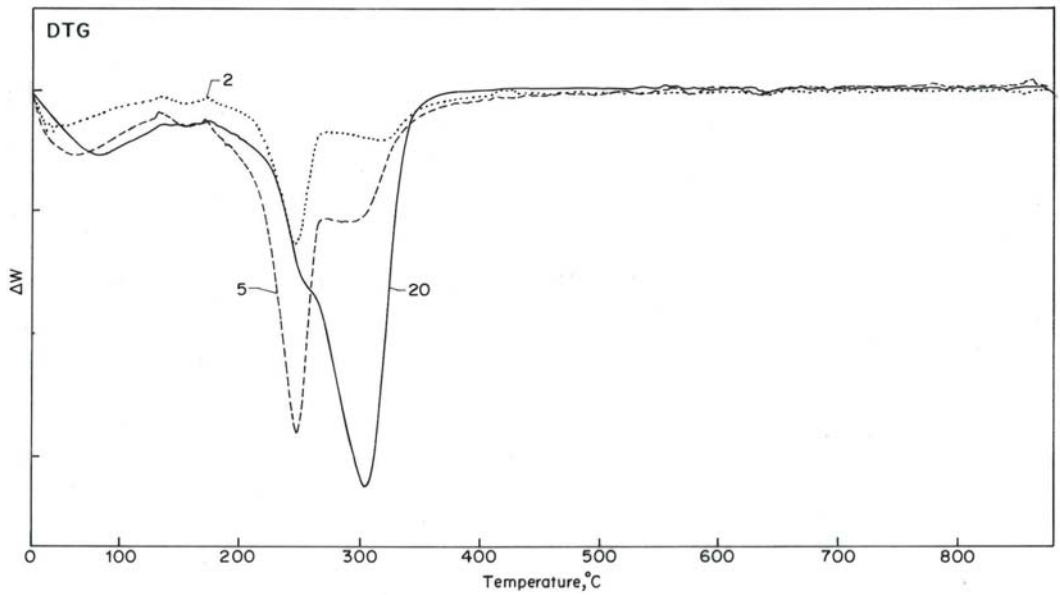

Figure 2.5b: *Differential thermogravimetric curves of as synthesized (dried) VO_x/Al_2O_3 catalysts. The numbers in figure indicate vanadia loadings as wt%.*

Ammonia can be formed and adsorbed on the acidic sites of γ-Al_2O_3 during impregnation and thermal treatments [71,72]. The desorption of NH_3 will occur at high temperatures because of higher desorption energy of NH_3 or NH_4^+ which is adsorbed on the acidic sites. Since the desorption is delayed, adsorbed NH_3 react with oxygen to form more water and the resulting exothermic effect compensates the endothermic effect of the decomposition of vanadyl oxalate [73].

The absence of well-defined peaks in the DTA profiles of catalysts with vanadia loadings lower than 20 wt% in the temperature range of 260-360 ^{0}C indicates that the heat release associated with the evolution of CO_2 from these samples are very small because of low loadings and were not detected by the technique.

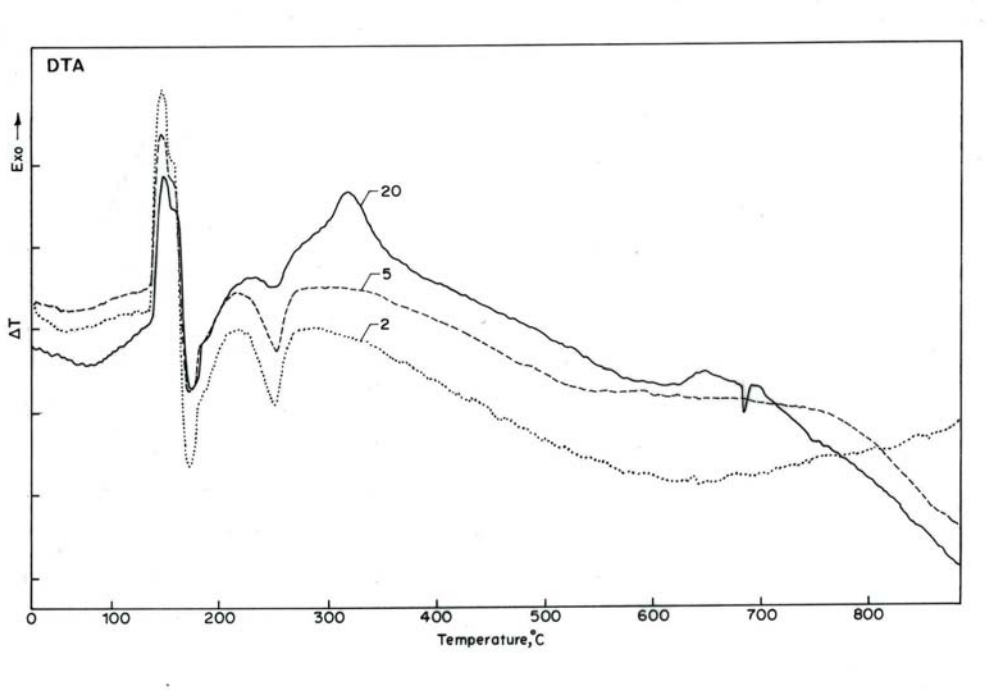

Figure 2.5c: *Differential thermoanalytical curves of as synthesized (dried) VO_x/Al_2O_3 catalysts. The numbers in figure indicate vanadia loadings as wt%.*

The endothermic peak observed in DTA of 20 VO_x/Al_2O_3 around 690 ^{0}C can be assigned to the melting of V_2O_5 since this temperature corresponds to the melting point of bulk vanadia. The TG of 20 VO_x/Al_2O_3 didn't record any weight loss in this temperature range, as expected.

2.4.4. Infra Red Spectroscopy

The FTIR spectra of calcined VO_x/Al_2O_3 catalysts and bulk V_2O_5 are shown in Fig. 2.6. The spectrum of bulk vanadia is characterized by the presence of bands centred at 1020 and 830 cm^{-1}. The spectrum of 20 VO_x/Al_2O_3 showed two bands centered at 1017 and 831 cm^{-1}. The first band corresponds to V=O stretching vibration in VO_5 trigonal bipyramids while the latter corresponds to V-O-V bending vibration [74]. The occurrence of these two bands which are characteristic of V_2O_5 species confirm the presence of well defined V_2O_5 crystallites on the surface of 20 VO_x/Al_2O_3 which is also observed by XRD. These bands are not observed for catalysts with lower loadings, indicating that vanadia exist as a different species which are not detectable as bulk V_2O_5. The assignment of bands in the region 500-800 cm^{-1} are difficult since Al-O groups also give vibrations in this region.

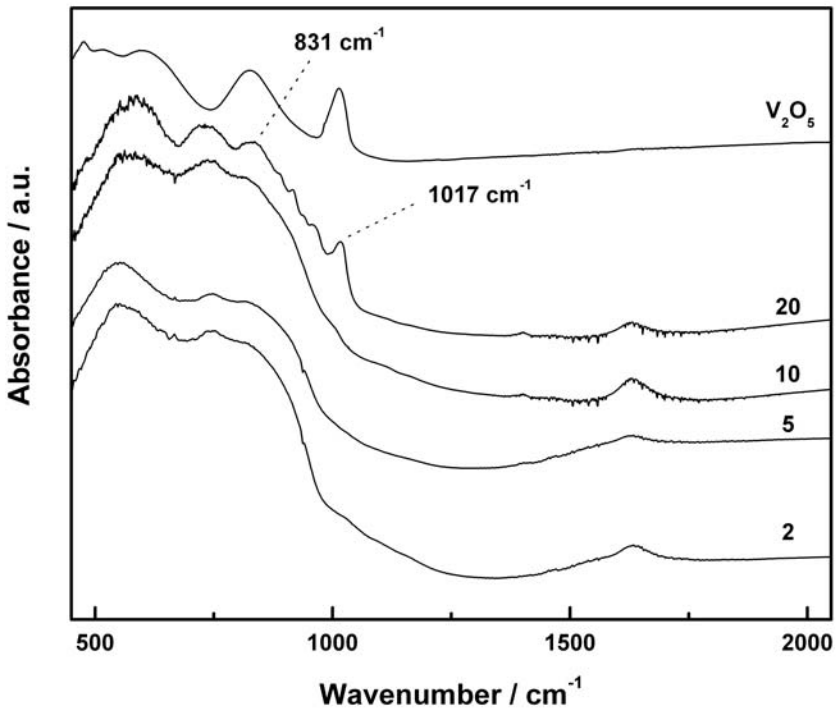

Figure 2.6: *FTIR spectra of calcined VO_x/Al_2O_3 catalysts (Legend: Vanadia loading in wt%) and bulk vanadium pentoxide.*

The FTIR spectra of 10 VO_x/Al_2O_3 as a function of calcination temperature are given in Fig. 2.7. The peak at 1020 cm^{-1} characteristic of bulk vanadia are not observed for catalysts calcined at 723, 823 and 923 K for 4h. The catalyst calcined at 823 K for a duration of 8h also doesn't show this peak. However, a peak at 1020 cm^{-1} is easily distinguishable for the catalyst calcined at 1023 K for 4h. The spectrum also shows well defined band between 770 and 870 cm^{-1} as observed for bulk vanadia indicating the presence of vanadium pentoxide for this catalyst.

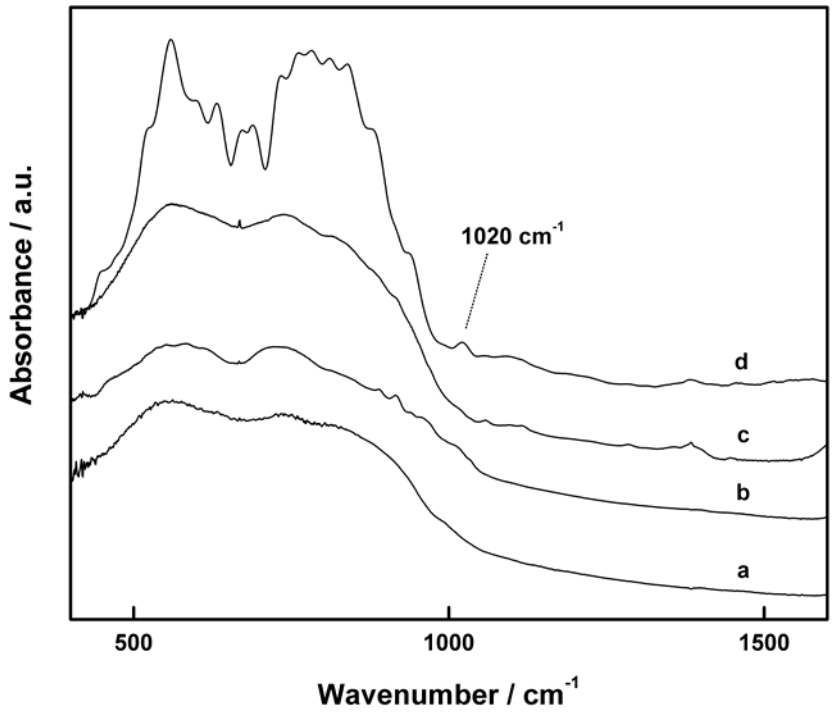

Fig. 2.7: *FTIR spectra of 10 VO_x/Al_2O_3 catalysts calcined at (a) 723 K, 4h (b) 823 K, 8h (c) 923 K, 4h (d) 1023 K, 4h.*

2.4.5. Laser Raman Spectroscopy

Figure 2.8 shows the laser Raman spectra of calcined VO_x/Al_2O_3 catalysts with different vanadia loadings and bulk V_2O_5. The spectra were recorded at ambient conditions after treating the sample at 473 K for 4 h in air. For the catalyst 20 VO_x/Al_2O_3 (Fig. 2.8b),

bands at 282, 303, 403, 484, 525, 701 and 992 cm^{-1} were observed. The fact that these bands are characteristic of bulk V_2O_5 (Fig. 2.8c) leads to the conclusion that bulk-like V_2O_5 crystals were formed when the vanadia loading is 20 wt%. The spectra of catalysts with vanadia loading 10 wt% and less didn't have any of these bands. However, this doesn't rule out completely the presence of V_2O_5 species in these samples since the bands may not appear if this species at low concentration is highly dispersed on the surface of the support. The catalyst 10 VO_x/Al_2O_3 (Fig. 2.8a) showed a broad feature between 700 and 1000 cm^{-1} that can be assigned to V-O-V stretches in two dimensional polyvanadates [21,24,68,75,76].

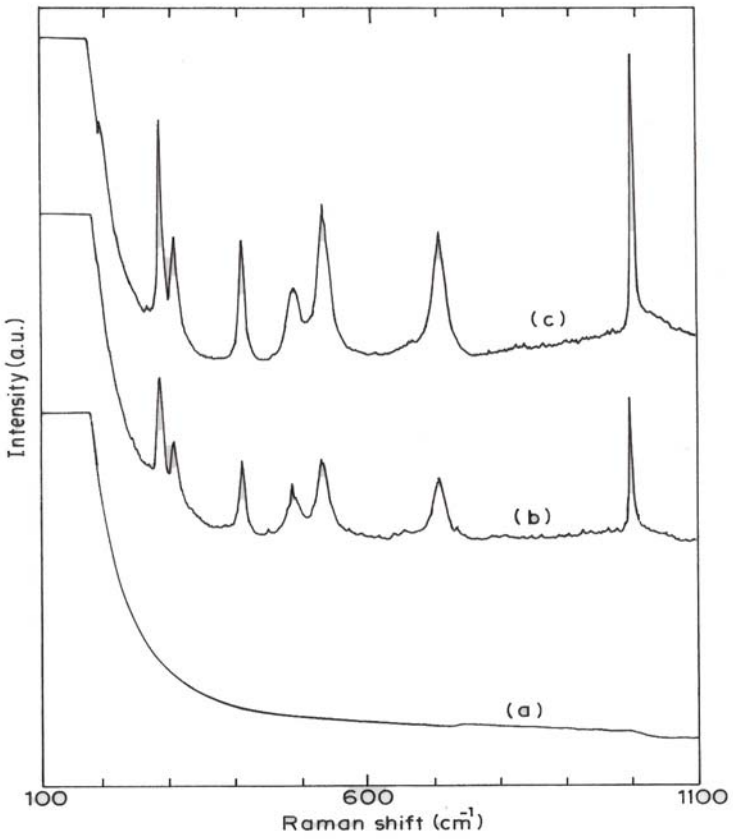

Fig. 2.8: *Laser Raman spectra of calcined (a) 10 VO_x/Al_2O_3 (b) 20 VO_x/Al_2O_3 and (c) bulk V_2O_5.*

2.4.6. Temperature Programmed Reduction

The TPR profiles of bulk V_2O_5 and calcined VO_x/Al_2O_3 catalysts are presented in Fig. 2.9. The reduction profile for bulk V_2O_5 exhibited four major peaks at 905, 945, 998 and 1103 K (Fig. 2.9). Bosch *et al* [77] and Koranne *et al* [78] have reported similar multiple major reduction peaks when bulk V_2O_5 is treated in 5% H_2 in Ar up to 1273 K. The presence of multiple peaks is attributed to the reduction of V_2O_5 to V_2O_3 through the intermediate formation of compounds with different oxidation states. A broad, minor reduction peak is also observed between 580 and 750 K. The reduction profiles for bulk vanadia reported in literature vary widely, probably because of the differences in factors such as method of preparation, level of impurities, partial pressure of H_2 used, rate of heating, reduction conditions *etc* [78].

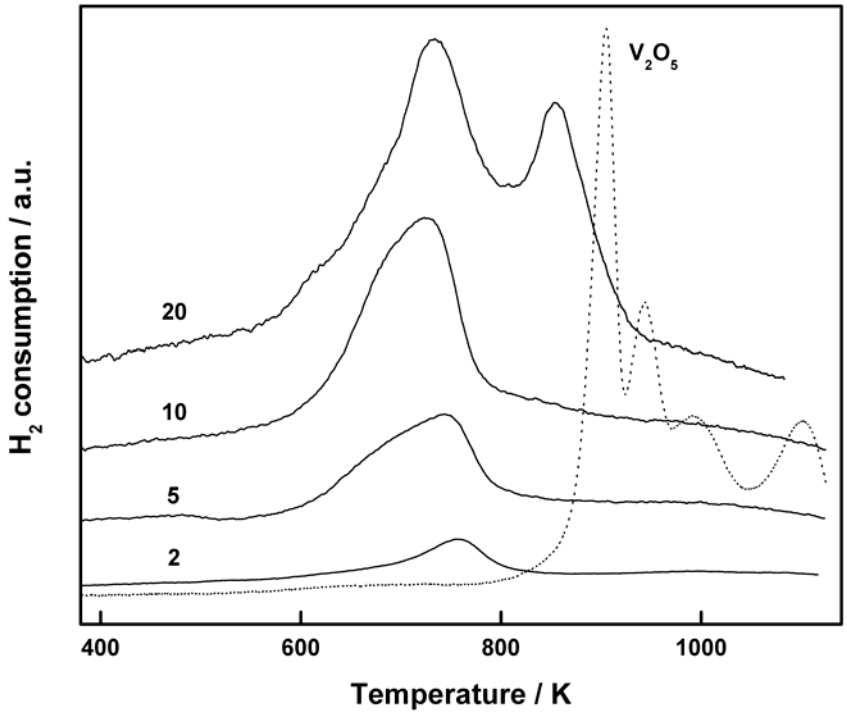

Figure 2.9: *Temperature programmed reduction profiles of bulk V_2O_5 and calcined VO_x/Al_2O_3 catalysts. The numbers in figure indicate vanadia loadings as wt%. The experimental conditions are: 5% H_2-Ar; heating rate, 5 K min^{-1}; flow rate, 40 ml min^{-1}.*

The TPR profiles of catalysts with vanadia loadings 2-10 wt% showed broad reduction peak, below 773 K (Fig. 2.9). The maximum temperature of the reduction peak (T_{max}) was 757 K for the catalyst 2 VO_x/Al_2O_3 and with the increase in vanadia content up to 10 wt %, T_{max} values shifted to lower temperature (Table 2.3). This shift results from the relative growth of a peak in the low temperature side with increasing vanadium content. This is illustrated by deconvolution of the experimental profile by two Gaussian curves for 10 VO_x/Al_2O_3 (Fig. 2.10). The values of Chi^2 and R^2 (parameters that determine the accuracy of fitting) indicate this procedure is reasonably good, however it is more appropriate to consider in a qualitative manner and interpretation based on areas of deconvoluted peaks are not attempted. The catalyst 20 VO_x/Al_2O_3 displayed two major reduction peaks. The T_{max} of first peak (734 K) is in the range of values of that are observed for lower vanadia loadings while the T_{max} of second peak corresponds to a higher reduction temperature (855 K). The latter peak can be attributed to the reduction of bulk-like V_2O_5 crystallites. This is in line with XRD, IR and Raman results that show the presence of bulk-like V_2O_5 crystallites of size greater than 4 nm for the 20 VO_x/Al_2O_3 catalyst. The T_{max} of this second peak is lower than the temperature of lowest reduction peak observed for pure bulk V_2O_5 because bulk vanadia is more difficult to reduce due to increased diffusional limitations [78].

The peak observed below 773 K for all the catalysts may be attributed to the reduction of monomeric, dimeric or low oligomeric surface vanadia species [50,78,79]. The shift in T_{max} to lower temperature, or more correctly the growing of a second peak in the low temperature side, with increasing vanadium content from 2 to 10 wt% may be as a result of the formation of polymeric vanadium species, at high vanadium loads, which are more easily reducible than monomeric ones, probably as a result of the weakening of the vanadium-oxygen bonds. Similar behavior has been described earlier for V_2O_5/Al_2O_3 catalysts [80,81]. The values of H_2 consumption and the corresponding degrees of reduction (Table 2.3) show increase with increase in vanadia loading from 2 to 10 wt%. The values of reduction degree are in agreement with the trend of enhanced reducibility as revealed by the observed decrease in the values of T_{max}.

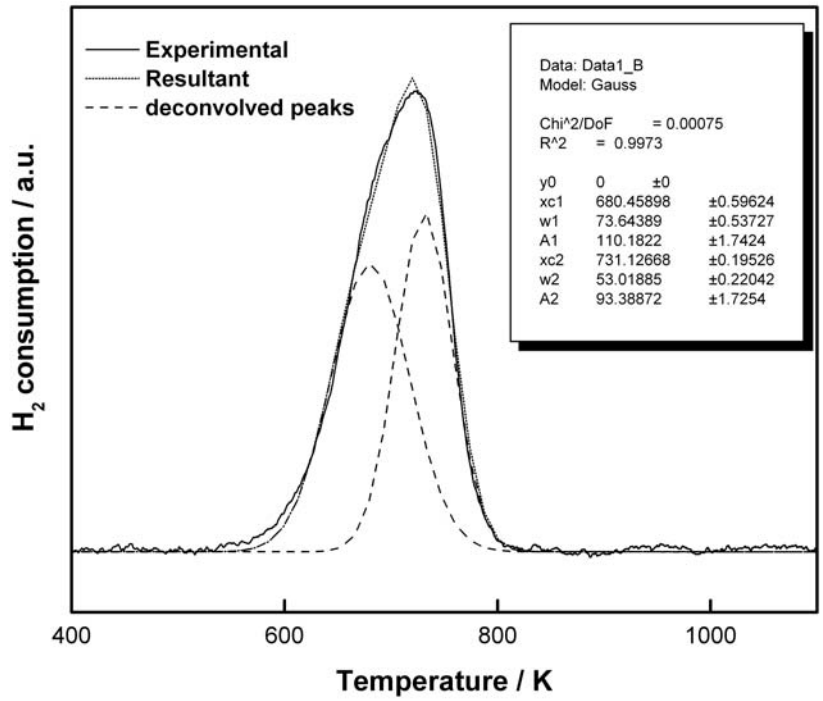

Fig. 2.10: *Deconvolution of TPR profile of 10 VO_x/Al_2O_3 using Gaussian model. The solid line represent experimental profile, dashed lines individual peak fits and dotted line the resultant of peak fits. Note that Chi^2 is low and $R^2 \sim 1$, implying the fit generated by the model is quite reasonable.*

Table 2.3: H_2 TPR results of VO_x/Al_2O_3 catalysts studied

Sample	T_{max1} (K)	T_{max2} (K)	H_2 consumption (μmol H_2/g cat.)	Reduction degree (%)*	Reduction degree (%)**
2 VO_x/Al_2O_3	757.2	-	137.5	132.7	66.4
5 VO_x/Al_2O_3	743.5	-	467.1	184.2	92.1
10 VO_x/Al_2O_3	724.2	-	1494.0	321.1	160.6
20 VO_x/Al_2O_3	733.6	854.6	2412.0	268.4	134.2

**Based on $V_2O_5 + H_2 \rightarrow V_2O_4 + H_2O$ ** Based on $V_2O_5 + 2\ H_2 \rightarrow V_2O_3 + 2\ H_2O$*

2.4.7. UV-visible spectroscopy

It is known that the coordination and/or the oxidation state of the vanadium ions strongly influence the lower-energy charge-transfer (LCT) bands in UV-visible spectrum, originating from the charge transfer between vanadium and oxygen [32,81-87]. In general, higher the coordination, higher is the wavelength at which absorption takes place. Thus, while the absorption band for vanadium (V^{5+}) ions with octahedral coordination is observed in the 350-500 nm region, the band in the 250-350 nm region is characteristic of vanadium (V^{5+}) ions with tetrahedral coordination. The d-d transition of V^{4+} (d^1) in a distorted octahedral symmetry gives broad band in the 550-850 nm region.

The diffuse reflectance UV-visible spectra of pure compounds ammonium metavanadate, sodium metavanadate, vanadium pentoxide and support γ-Al_2O_3 are given in Fig. 2.11. Three main absorption bands are observed for V_2O_5 at ~ 232, 336, and 473 nm. The first two bands are due to charge transfer transitions from terminal or bridging oxygen. The third band has been assigned tentatively to charge transfer to a delocalized acceptor site such as conjugated sites like those in octahedral VO_6 chains [85]. The lowest charge transfer (LCT) band is observed at 330 and 362 nm for $NaVO_3$ and NH_4VO_3 respectively while the second CT band appear at 282 and 286 nm. The LCT and second CT bands of these tetrahedral V^V compounds can be attributed to $(\pi)t_1 \rightarrow d(e)$ and $(\pi)t_2 \rightarrow d(e)$ oxygen to vanadium transitions respectively. The alumina support was almost totally transparent in the spectral region studied (wavelength, λ = 200-800 nm), although very weak absorptions, possibly associated to impurity ions, can be found in the range 200–350 nm (Fig. 2.11). The observation is well in line with the strongly insulating character of alumina, that is reported to have an E_g value as high as 7.2 eV [86].

The diffuse reflectance UV-visible spectra of calcined VO_x/Al_2O_3 catalysts are presented in Fig. 2.12. The spectrum of 2 VO_x/Al_2O_3 showed a wide band around 255 nm, characteristic of charge-transfer transition between vanadium (V) and oxygen. With increasing vanadium content, a red-shift of this band is observed. The spectrum observed for 5 VO_x/Al_2O_3 exhibited a shoulder around 350 nm. A relative growth of this band is observed with increasing vanadium content. The absorption band around 255 nm is

assigned to monomeric, tetrahedrally coordinated vanadium (V) species and that around 350 nm is associated to distorted (interacting with other vanadium ions) VO_4^{3-} tetrahedral [81,84]. The observed red-shift and the relative increment of the band at 350 nm indicates an increase in the degree of polymerization between isolated tetrahedral species as the vanadia loading is increased.

It is proposed that absorption band edge energies, which can be determined using Tauc's law [88], provide a more convenient description of the electronic properties of the solids. The theory and analysis of absorption edge energy is outlined in the following sections.

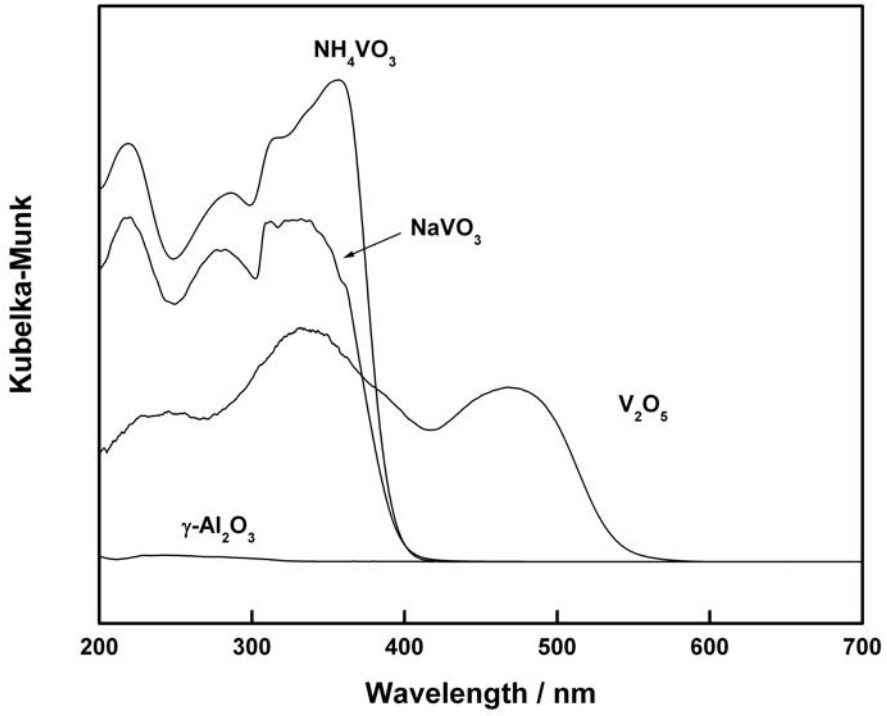

Fig. 2.11: *The diffuse reflectance UV-visible spectra of model compounds ammonium metavanadate, sodium metavanadate, vanadium pentoxide and support γ-Al_2O_3.*

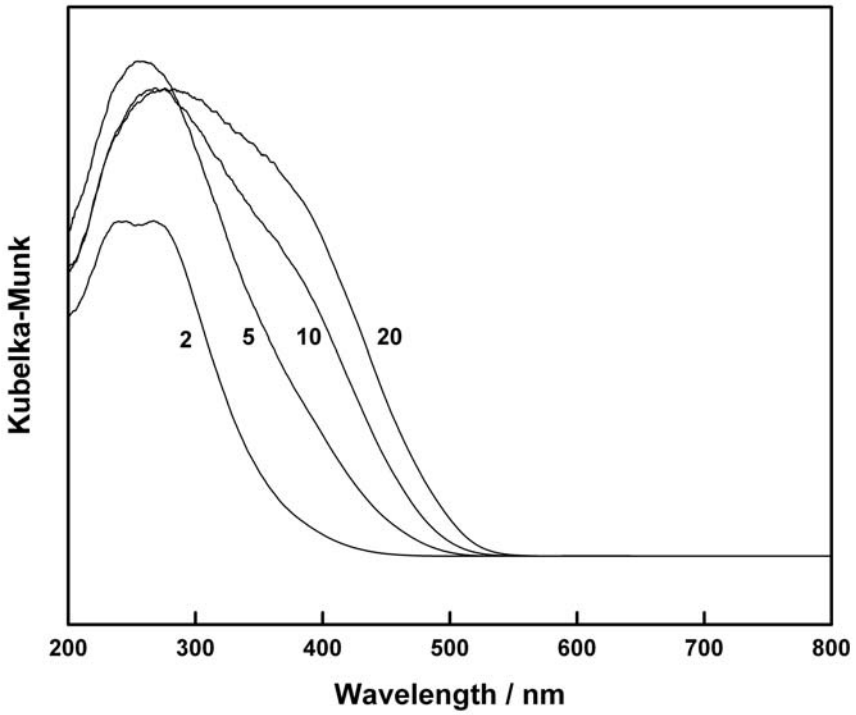

Fig. 2.12: *Diffuse reflectance UV–visible spectra of the calcined VO_x/Al_2O_3 catalysts (Legend: the loadings of vanadia in wt%).*

2.4.7.1. Analysis of UV-Visible Absorption edge energy

The UV spectrum of vanadium consists of the lower energy charge-transfer (LCT) band associated with an O to V electron transfer, while the optical band gap energy is represented by the energy edge. The optical absorption edge energy is defined as the minimum photon energy required to excite an electron from the highest occupied molecular orbital (HOMO, at the top of the valence band in semiconductor domains) to the lowest unoccupied molecular orbital (LUMO, at the bottom of the conduction band). There are two basic types of electronic transitions, direct and indirect [89]. In direct transitions, only photons excite electrons, while indirect transitions also require concerted vibrationsand energy from the crystal lattice (phonons). The energy dependence of the

absorption coefficient (α) for semiconductors in the region near the absorption edge is given by

$$\alpha \propto (h\nu - E_o)^{\eta} \ / h\nu \qquad (2.11)$$

where $h\nu$ is the energy of the incident photon and E_o is the optical absorption edge energy; the exponent η depends on the type of optical transition caused by photon absorption [89]. In crystalline semiconductors, where crystal momentum is conserved and electron transitions obey well-defined selection rules, η is 1/2, 3/2, 2 and 3 when the transitions are direct-allowed, direct forbidden, indirect-allowed and indirect-forbidden, respectively. In amorphous, homogeneous semiconductors, the value of η is 2 irrespective of the type of transition found in crystalline materials of the same composition [88]. With an appropriate choice of η, a plot of $(\alpha h\nu)^{1/\eta}$ vs $h\nu$ is linear near the edge and the intercept of the line on the abscissa (at $(\alpha h\nu)^{1/\eta} = 0$) gives the optical absorption edge energy E_o.

In the diffuse reflectance experiments, UV-vis reflectance data cannot be used directly to measure absorption coefficients (α) because of scattering contributions to the reflectance spectra. Scattering coefficients, however, depend weakly on energy and $F(R_\infty)$, where $F(R_\infty)$ is the Kubelka Munk function for an infinitely thick sample, can be assumed to be proportional to the absorption coefficient within the narrow range of energy containing the absorption edge features. Then, a plot of $(F(R_\infty)\ h\nu)^{1/\eta}$ vs $h\nu$ can be used to determine the absorption edge energy.

2.4.7.2. Absorption edge energy and molecular structure

The edge energy values have been recently used widely to characterize the domain sizes of VO_x, WO_x and MoO_x in catalytic solids and to correlate the catalytic activities with electronic properties of various solids [68,90,94-97]. The domain size (or molecular cage size) could be defined by the nearest-neighbor ligands (oxygen in this case) coordinating the vanadium center. It can also be described as an average bond distance, as proposed by Wong *et al* [93], $R = (1/n)_i \sum^n R_i$, where n is nearest-neighbor bonds. The domain size is closely related to the local symmetry of metal species (vanadium in the present case) and changes with variation in symmetry.

To understand the relation between absorption edge energy and molecular structure, a brief summary of some relevant findings in literature is reported here. A classic study is by Weber [90] who has determined edge energy for a series of molybdenum compounds in the classical fashion using the formalism for direct-allowed electronic transitions (η=1/2) and reported an apparent linear correlation between the number of nearest MoO_x neighbors in crystalline MoO_x standards and the absorption edge energy.

TABLE 2.4: Relationship between Domain Size (Local Symmetry) and UV Absorption Edge on Vanadium Model Compounds [92]

Vanadium model compounds	Local symmetry	Domain size (Å)	UV edge energy (eV)
Na_3VO_4	tetrahedral	1.729	3.21
$Mg_3(VO_4)_2$	tetrahedral	1.729	3.21
NH_4VO_3	distorted tetrahedral	1.735	3.20
V_2O_5	square pyramidal	1.978	2.41
PbV_2O_6	distorted octahedral	2.075	2.05

Di Wei *et al* [92] studied a series of vanadium model compounds with different, but well defined, local symmetry of vanadium, again using the classical formalism (η=1/2). Among these model compounds V_2O_5 has nearly square-pyramidal geometry around vanadium [85], consisting of four V-O bonds of similar length and a very short V=O bond. Metavanadates such as PbV_2O_6 or ZnV_2O_6 have a structure of strongly distorted octahedral pairs sharing corner oxygen atoms. In these compounds, there is one very long, two shorter, and three long V-O bonds. Monomeric orthovanadates such as Na_3VO_4 and $Mg_3(VO_4)_2$ have a structure formed by isolated, tetrahedrally coordinated V ions in a nearly symmetrical environment (three medium-short V-O bonds and one slightly longer V-O bond). Another type of metavanadate, such as NH_4VO_3, KVO_3, and $NaVO_3$, also has a tetrahedral environment, but it is strongly distorted and shares two bridging oxygen with

other polyhedra. The symmetry and domain size of model compounds and values of edge energies are summarized in Table 2.4, which shows that the edge energy decreases monotonically with the increasing domain size. This is quite useful in determining the local structure of vanadium, since domain size sensitively varied with the symmetry.

Table 2.5: Band maxima and Edge energies of vanadium reference compounds [98]

Compounds	Band maximum (nm)	Edge energy (eV)	Molecular structure
V_2O_5	236, 334, 481	2.3	polymerized VO_5/VO_6
MgV_2O_6 (meta-vanadate)	250, 370	2.8	polymerized VO_6
$NaVO_3$ (meta-vanadate)	281, 353	3.2	polymerized VO_4
NH_4VO_3 (meta-vanadate)	288, 363	3.2	polymerized VO_4
$Mg_2V_2O_7$ (pyro-vanadate)	280	3.5	dimeric VO_4
$Mg_3(VO_4)_2$ (ortho-vanadate)	260, 303	3.5	isolated VO_4
Na_3VO_4 (ortho-vanadate)	253, 294	3.9	isolated VO_4

Table 2.5 gives a similar study of model compounds by Gao *et al* [98] based on allowed transitions (η=1/2). The results show that the polymerization of VO_6 or VO_4 units tends to lower the edge energy, and the polymerized VO_6 structures exhibit the lowest edge energy. The lowest edge energy of 2.3 eV is observed for V_2O_5 crystallites that consist of polymerized, highly distorted VO_6 units, and compounds composed of isolated VO_4 units exhibit the highest edge energy. In general, these studies show that absorption edge energy

decreases with increasing domain size, degree of polymerization and coordination. These studies are based on the classical formalism (η=1/2), in-fact majority of studies reported in the literature are so, the relationships arrived are equally applicable for the method using η=2.

The fundamental absorption edge of V_2O_5 crystallites is caused by indirect electron transitions, although analysis based on direct transitions leads to similar qualitative trends with domain size. Methods based on direct transitions (η=1/2) emphasize the region of high optical absorption near the edge, where the Kubelka-Munk function becomes nonlinear in absorber concentration and underlying assumptions become inaccurate. This means that determination of edge energies using η=2 is more accurate. However, as mentioned previously, most of the earlier studies use η=1⁄2. Absorption edge energies of present series of VO_x/Al_2O_3 catalysts are determined by both methods. The values determined based on the method of η=1⁄2 are considered for discussion because the correlations with molecular structures are readily available for this method.

The edge energies, determined from the intercept of a straight line fitted through the rise of the function $[F(R_\infty)\ h\nu]^{1/2}$ or $[F(R_\infty)\ h\nu]^2$ plotted versus $h\nu$ [90], are presented in Table 2.6. An example for the determination of absorption edge energy from UV-visible spectral data is shown in Fig. 2.13 for 20 VO_x/Al_2O_3. The edge energy is 3.7 eV (based on η=1⁄2) for the catalyst 2 VO_x/Al_2O_3 and decreases to 2.6 eV with the increase in loading of vanadia to 20 wt%. For comparison, the edge energies of model compounds, ammonium metavanadate, sodium metavanadate and bulk vanadium pentoxide are also calculated in this work. The former two compounds, with distorted tetrahedral vanadium coordination, exhibit an edge energy value of 3.3 eV while the latter, with V^{5+} in distorted tetragonal pyramidal coordination, shows 2.33 eV. It is clear from the edge energy values, in comparison to values of model compounds and those reported in previous studies (Tables 2.4 and 2.5), that vanadium is, most probably, in a monomeric tetrahedral coordination in 2 VO_x/Al_2O_3. The decrease in edge energy with increasing vanadia loading suggests that the nature of vanadia species changes to oligomeric at higher vanadia loadings. This implies an increase in the degree of polymerization of vanadium (V) species, with increasing surface density of vanadia, ultimately leading to the appearance of octahedral polymeric species

similar to that exist in bulk V_2O_5 for the catalyst 20 VO_x/Al_2O_3. The fact that the edge energy for 20 VO_x/Al_2O_3 (2.6 eV) is slightly higher than that for bulk V_2O_5 shows the presence of some amount of tetrahedral vanadium species, co-existing with octahedral polymeric species, even at the highest loading studied.

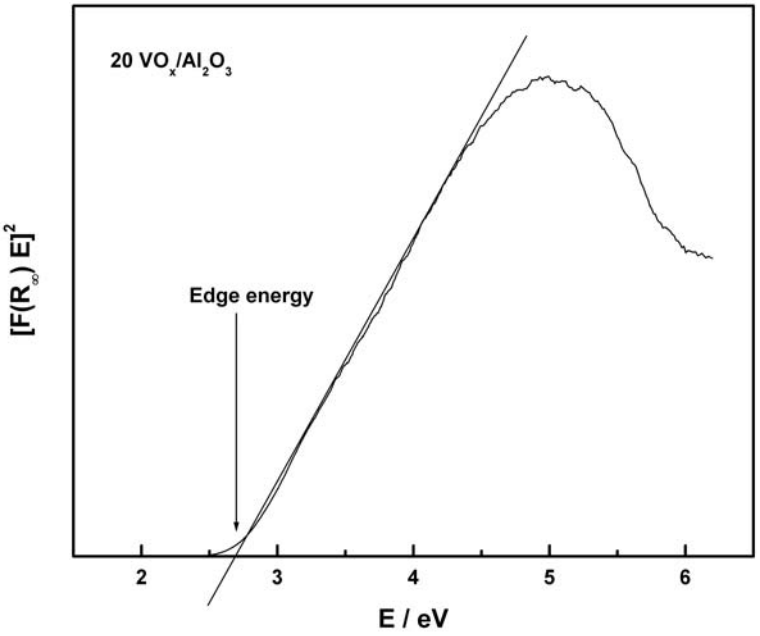

Fig. 2.13: *Exemplification of determination of absorption edge energy with reference to the UV-visible spectral data of 20 VO_x/Al_2O_3.*

The correlation between absorption edge energy and number of nearest vanadium neighbors for different model compounds, proposed by Cruz and Eon [99], was used to determine the condensation degree of samples in the present work (Table 2.6). The edge energy values for model compounds were taken from Gao *et al* [98] to draw standard correlation line. The absorption edge energies obtained based on direct transitions (η=1/2) were used in determining the condensation degrees since the same method is used in the above mentioned reports [98,99]. The catalyst 2 VO_x/Al_2O_3 has a very low condensation degree suggesting that isolated vanadium (V) species are the predominant species on the surface of this catalyst. With increasing vanadium loading, the condensation degree

increased suggesting an increase in the degree of polymerization of vanadium (V) species, as also obvious from the shift in the position of the bands towards higher wavelengths, ultimately leading to the appearance of octahedral polymeric species similar to that exist in bulk V_2O_5 for the catalyst 20 VO_x/Al_2O_3. The absorption edge energy values obtained can also be related with domain size of vanadia in line with the previous studies. Hence the decrease in edge energy with increasing surface density of vanadia also suggests an increase in domain size of vanadia. Infact, we can expect that the domain size and degree of polymerization of vanadia species are interrelated, since an increase in latter should naturally lead to an increase in former also. However, it should also be noted that the inverse relationship between absorption edge energy and domain size hold good mainly when the surface density does not exceed that required for monolayer coverage.

Table 2.6: The values of UV-visible Absorption edge energy and Condensation degree for calcined VO_x/Al_2O_3 catalysts

Sample	VO_x surface density (VO_x/nm^2)	Absorption edge energy (eV) (*η=2)*	Absorption edge energy (eV) (*η=1/2)*	Condensation degree∗
Al_2O_3	0	-	-	-
2 VO_x/Al_2O_3	1.19	2.61, 2.84	3.7	0.42
5 VO_x/Al_2O_3	2.99	2.38	3.4	1.77
10 VO_x/Al_2O_3	5.90	2.31	2.8	4.6
20 VO_x/Al_2O_3	13.36	2.22	2.6	5.5
NH_4VO_3	-	3.04	3.28	-
$NaVO_3$	-	3.02	3.26	-
V_2O_5	-	2.17	2.33	-

∗Based on correlation by Cruz and Eon [99] and data of model compounds from Gao et al [98] that uses direct transitions (η=1/2).

Table 2.7: Absorption edge energy values of 10 VO_x/Al_2O_3 as a function of thermal treatment

Calcination temperature (K)	Calcination time (h)	Absorption edge energy (eV) (η=2)	Condensation degree
723	4	2.33	6.04
823	8	2.35	5.92
923	4	2.37	5.80
1023	4	2.29	6.27

2.4.8. X-ray Photoelectron Spectroscopy

2.4.8.1. V 2p core level

The V $2p_{3/2}$ is the most intense peak of vanadium in its XPS spectrum. Figure 2.14 shows the V $2p_{3/2}$ photoelectron spectra of calcined VO_x/Al_2O_3 catalysts as a function of vanadia loading. Secondary radiations of Al Kα leads to satellite peaks of O 1s that overlaps with the V 2p core level peaks in the 515-525 eV range (Fig. 2.14a). This satellite peak of O 1s is subtracted from the original spectra to obtain the V 2p contribution alone. The V $2p_{3/2}$ peaks appear around 517 eV and the other component of the spin-orbit doublet, $2p_{1/2}$, appears at around 524.5 eV. The binding energy value of V $2p_{3/2}$ core level of bulk V_2O_5 ($3d^0$) is reported to be around 517 eV [100,101] and this value decrease, as expected from the increase in number of 3d electrons, for lower oxidation state vanadium compounds. The binding energy values of present series of catalysts indicate that the vanadia surface species are fully oxidized (V^{5+}).

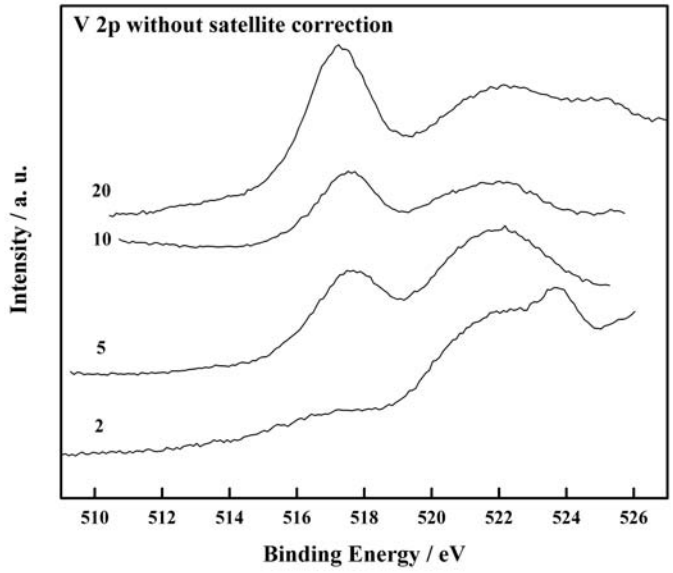

(a)

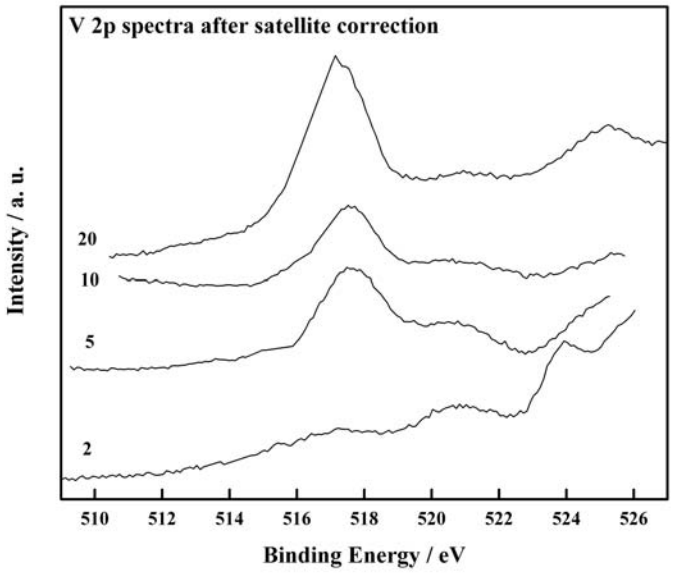

(b)

Fig. 2.14: *V 2p core-level spectra of calcined VO_x/Al_2O_3 catalysts* ***(a)*** *before satellite subtraction and* ***(b)*** *after satellite subtraction as a function of vanadia loading. Integers in figure indicate vanadia loading in wt%.*

The figure shows that the binding energy of V $2p_{3/2}$ peak shifts slightly with increasing vanadia loading. V $2p_{3/2}$ peak appear at 517.3 eV for 2 VO_x/Al_2O_3 and shifts to higher values with increase in vanadia loading up to 10 wt%. However, further increase in vanadia loading to 20 wt% decreases the binding energy to 517.2 eV. This can also be expressed using the splitting between the O 1s and V $2p_{3/2}$ binding energies (ΔE). The values of energy difference (ΔE) between the O 1s and V $2p_{3/2}$ transition centroids, determined after satellite removal, are given in Table 2.8. The samples 2 and 20 VO_x/Al_2O_3 exhibit similar ΔE, while the intermediate loadings show lower values. The positive shift in binding energy with increasing vanadia loading to 10 wt% may be explained as due to the increase in degree of polymerization of vanadium species, which causes weakening of the vanadium-oxygen bonds. Vanadium in a polymeric species experience considerably less charge density from the neighboring oxygen atoms than that in a monomeric species, which results in corresponding shift in binding energy. The previous XPS studies on V/SiO_2 catalysts report that the binding energy of V $2p_{3/2}$ level shift to higher values with vanadia loading [102,103]. When the loading of vanadia is 20 wt%, phases like disordered or paracrystalline V_2O_5 and $AlVO_4$ appear on the catalyst which may be the reason for observed negative shift in binding energy for this catalyst.

Surface atomic ratios of V and Al were calculated from the XPS peak intensities of V $2p_{3/2}$ and Al 2p and photoionization cross-section values (equation 2.12) for all vanadia loadings and are given in Table 2.8.

$$(V/Al)_{Surface} = \frac{I_v}{I_{Al}} \times \frac{\sigma_{Al}}{\sigma_V} \times \frac{(KE_V)^{1/2}}{(KE_{Al})^{1/2}} \qquad (2.12)$$

where σ is photoionization cross-section and KE = hν-BE, KE and BE being kinetic and binding energies of photoelectron, respectively.

Table 2.8: XPS data of calcined VO_x/Al_2O_3 catalysts

Sample	Binding energy, E (eV)		ΔE (eV)	FWHM (eV)		(V/Al) Surface
	V $2p_{3/2}$	O 1s		V $2p_{3/2}$	O 1s	
2 VO_x/Al_2O_3	517.3	531.1	13.8	n.d.	2.9	0.004
5 VO_x/Al_2O_3	517.7	531.1	13.4	2.78	2.7	0.015
10 VO_x/Al_2O_3	517.5	530.9	13.4	2.11	2.5	0.063
20 VO_x/Al_2O_3	517.2	531.0	13.8	2.6	2.9	0.075

Figure 2.15 shows the V/Al surface atomic ratio obtained by XPS as a function of total bulk V/Al atomic ratio of the catalysts determined by ICP. The surface atomic ratio increases sharply till bulk atomic ratio of 0.05 (10 wt% vanadia loading) and thereafter increases only marginally. This indicates that multilayerd vanadia structures appear beyond a vanadia loading of 10 wt%.

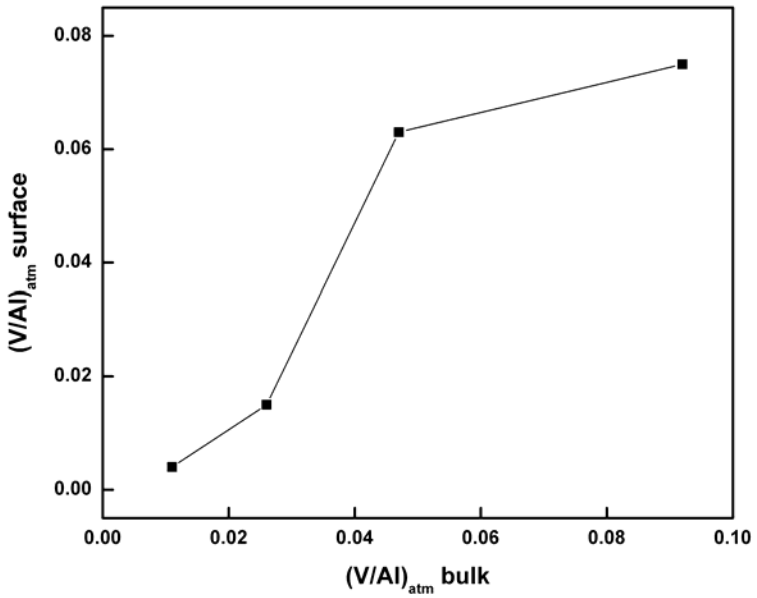

Fig. 2.15: *Surface V/Al obtained by XPS as a function of bulk atomic ratio. V $2p_{3/2}$ and Al 2p were used to determine surface atomic ratio by XPS.*

2.4.8.2. O 1s and Al 2p core level

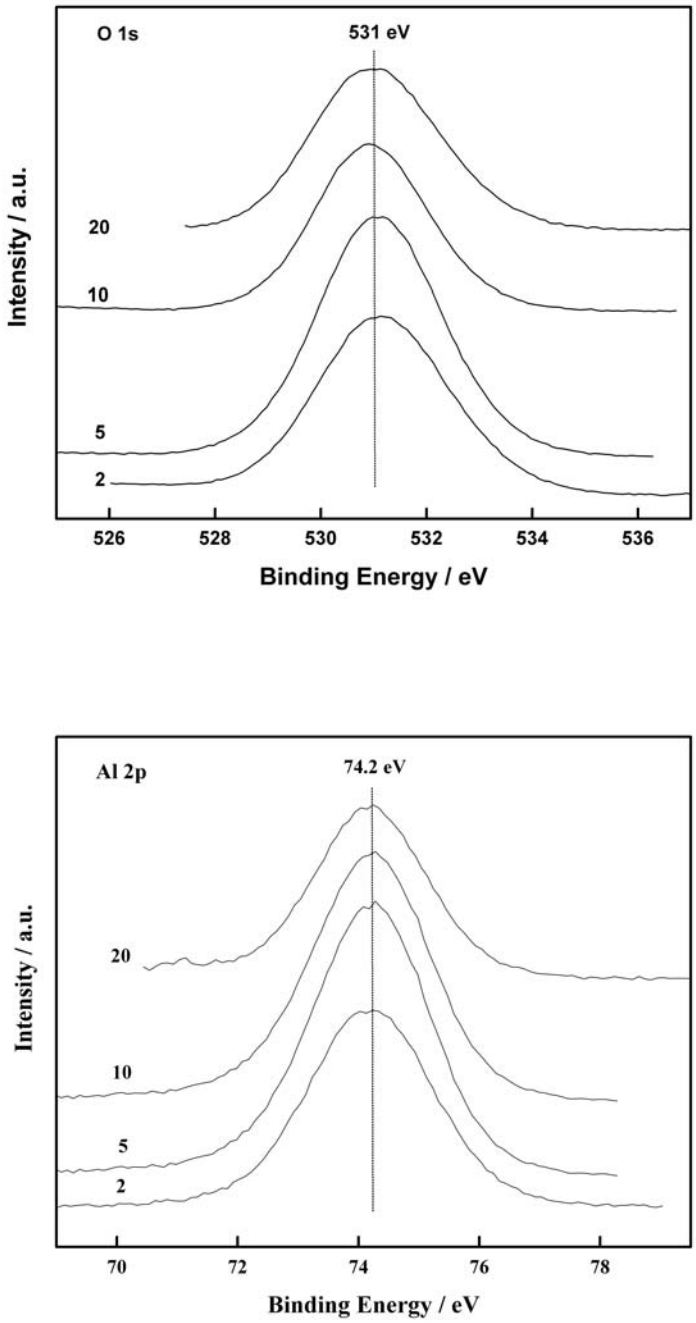

Fig. 2.16: *O 1s and Al 2p core-level spectra of calcined VO_x/Al_2O_3 catalysts as a function of vanadia loading in wt%.*

The O 1s spectra of the catalysts were rather independent of the vanadia loading. They are broad bands, almost symmetric in nature and centered at 530 ± 0.1 eV. Likely, there is a large overlap between the oxygen atoms associated with vanadium and aluminium and hence it was difficult to resolve the bands into individual contributions (Fig. 2.16 top).

The Al 2p peak of all the samples consists of a single component at a binding energy of 74.2 eV, which can be assigned to Al^{3+} species in Al_2O_3. With increasing vanadia loading, FWHM decreases (Fig. 2.16 bottom).

2.4.9. EPR Spectroscopy

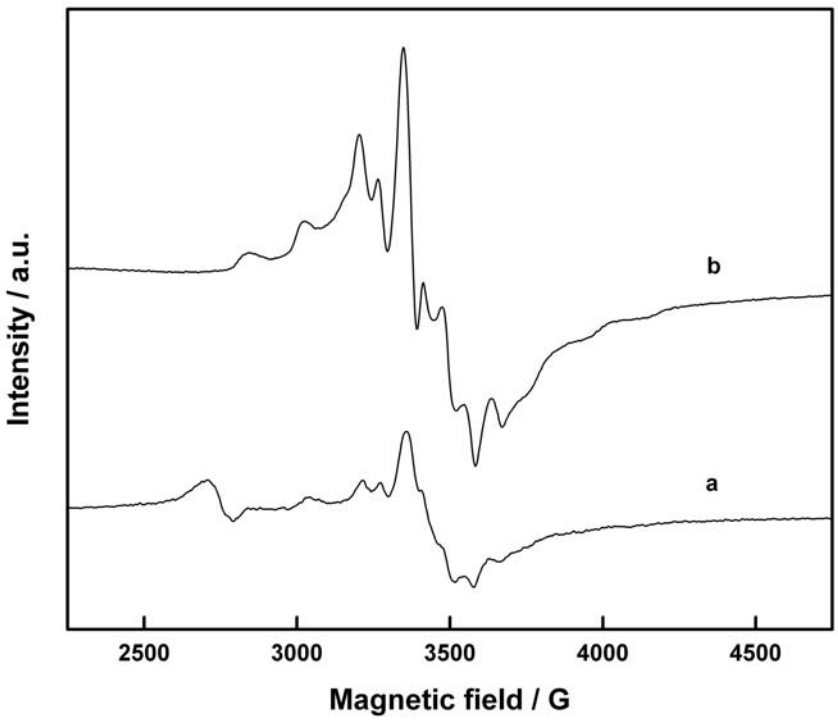

Fig. 2.17: *The EPR spectra of 20 VO_x/Al_2O_3, measured at 298 K, after* ***(a)*** *calcination at 823 K for 4h and* ***(b)*** *reduction in H_2 at 673 K for 4h.*

The EPR spectrum of the calcined 20 VO_x/Al_2O_3 catalyst, recorded at room temperature, is given in Fig. 2.17. It is clear from the UV-Visible spectroscopy that the

calcined sample contains mainly V^{5+} and only negligible V^{4+}, however EPR can detect these species because of its high sensitivity. The spectrum consists of well-resolved lines that can be assigned to V^{4+} ($3d^1$) species. The hyperfine structure is better resolved after the catalyst, 20 VO_x/Al_2O_3, is subjected to reduction in hydrogen flow at 673 K for 4h. The hyperfine structure is due to the interaction of the unpaired electron with the nuclear magnetic moment of vanadium with I = 7/2 (natural abundance 99.76%), giving rise to eight parallel and perpendicular components respectively [104]. The resolution of the hyperfine structure in the spectra indicates V^{4+} ions are highly dispersed.

The EPR spectra obtained in the present work are similar to those previously reported for Al_2O_3-supported vanadium oxide catalysts. The EPR signals and parameters obtained in different studies differ slightly which in some cases have been reported to depend on the vanadium content, preparation procedure and reduction pretreatment [76,105-107]. In general, the V^{4+} is considered to be present in an axially symmetric environment (VO^{2+} in C_{4v} environment). It can be expected that a relatively wide distribution of coordination geometries occur for vanadyl species immobilized on a support surface [107]. Though the g and A tensors become nonaxially symmetric due to the deviations from C_{4v} symmetry for individual ions, the average over geometries existing on the surface corresponds to C_{4v} symmetry [Fig. 2.18]. This is confirmed by the analysis of Sharma *et al* [107] who found that the observed spectra are well reproduced by an axially symmetric spin Hamiltonian. The environment of $(V=O)^{2+}$ on a support surface is described as tetragonally distorted octahedral with C_{4v} symmetry in most of the publications [76,105-107]. The assignment of the EPR signals to octahedral V^{4+} is usually supported on the detection of the signal at room temperature, since, in general, it is admitted that tetrahedral V^{4+} is observable only at low temperature due to relaxation effects. Thus, the EPR spectra shown in Fig. 2.17 can be tentatively attributed to V^{4+} in an octahedral coordination. Similar spectra with different intensities were obtained for all the catalysts studied here. It should be also mentioned here that there is at least one publication available in which [105] a signal detectable at 293 K and characterized by $g_\perp$ = 1.979-1.985, $g_\parallel$ = 1.931–1.934 (depending on the sample), $A_\perp$ = 74 G, $A_\parallel$ = 200 G has been assigned to V^{4+} in a distorted tetrahedral environment.

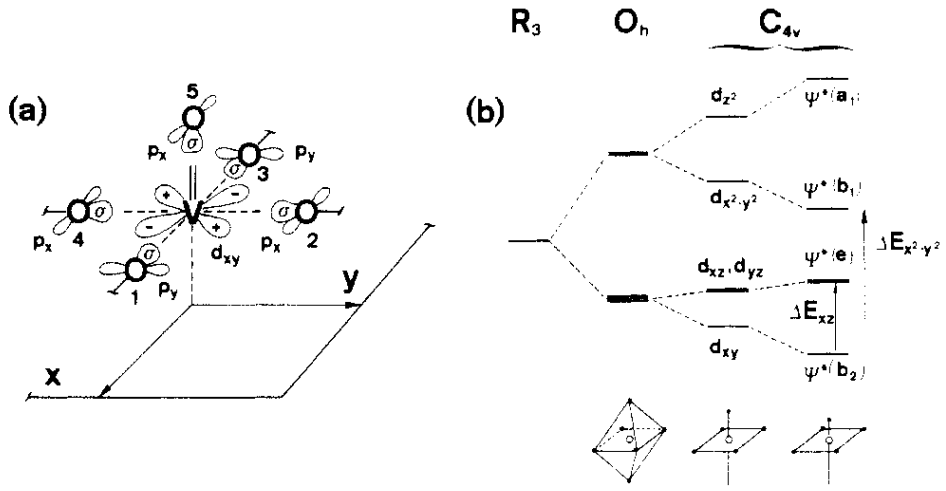

Fig. 2.18: *Geometry and energy level scheme of the surface vanadyl species.* ***(a)*** *The average symmetry corresponds to C_{4V} where the oxygen ligands 1-4 form a square parallel to the surface.* ***(b)*** *The variation in energy levels of O_h symmetry with tetragonal distortion (adapted from [107]).*

2.4.10. ^{51}V MAS NMR spectroscopy

The MAS spectra of the calcined VO_x/Al_2O_3 catalysts are shown in Fig. 2.19. The isotropic chemical shift values for each catalyst were determined by spinning the sample at different rates. The isotropic peaks does not change their position while side bands appear at different chemical shift values with variation in spinning speeds. For 2 VO_x/Al_2O_3, the isotropic peak appears at –582 ppm. This chemical shift value suggests the attribution of vanadia species to tetrahedral V^{5+}. The 4-coordinated vanadates can be classified into various groups of $Q^{(n)}$ species, according to the number of bridging oxygen atoms n that connect two different vanadium coordination polyhedra [50]. Based on this, vanadates can be distinguished into $Q^{(0)}$ species, i.e., monomeric VO_4^{3-} groups (orthovanadates); $Q^{(1)}$ species, i.e., dimeric $[O_3V\text{-}O\text{-}VO_3]^{4-}$ (pyrovanadates) and $Q^{(2)}$ species, i.e., polymeric $[O\text{-}V(O)_2\text{-}]^{2-}$ (alkali metavanadates). If we consider the chemical shift value alone, probably we can attribute the vanadia species to $Q^{(2)}$ type as in metavanadates NH_4VO_3 or $NaVO_3$, in agreement with the assignment made by Eckert and Wachs [50]. However, the broad

nature of the peaks and the fact that spinning at different rates couldn't narrow the peaks, indicate a broad range of vanadium (V) oxide environments, possibly including also different numbers of non-bridging oxygen atoms. It should be mentioned that isotropic chemical shifts alone do not provide accurate guidance for the exact identification of local symmetry among these and for this purpose, the determination of chemical shift anisotropy values and the knowledge of static NMR line-shapes are also needed which are not attempted in this work.

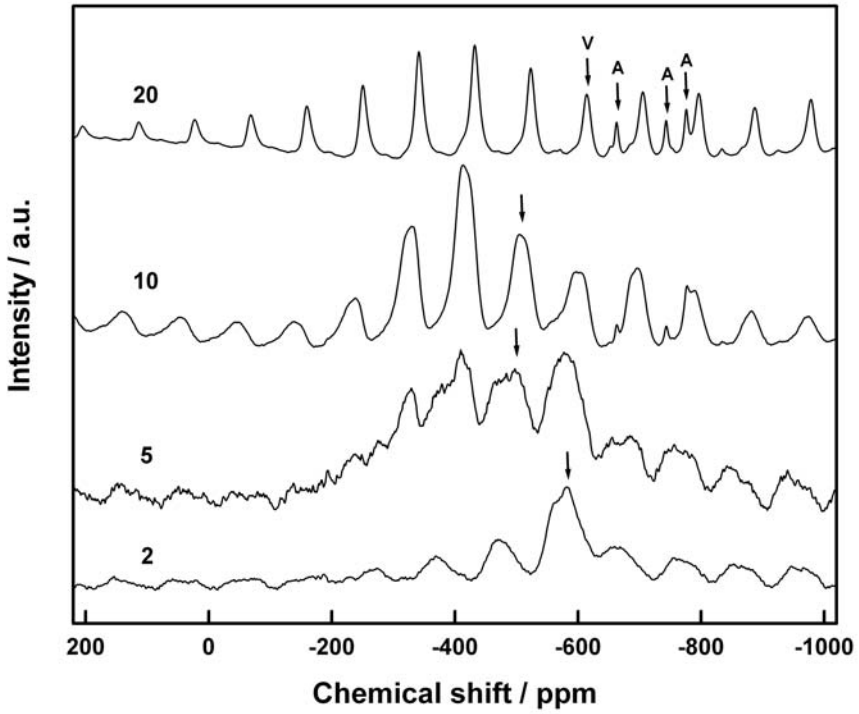

Fig. 2.19: *^{51}V MAS NMR spectra of the calcined VO_x/Al_2O_3 catalysts as a function of vanadia loading (in wt%). The spectra were obtained at a spinning rate of 12 kHz. The arrows indicate isotropic peaks. The alphabets 'A' and 'V' denote isotropic peaks of $AlVO_4$ and V_2O_5 respectively.*

For 5 VO_x/Al_2O_3, isotropic peak is observed to appear at –503 ppm. The position as well as the side band pattern of this species is similar to those of the "type a" signal

reported by Eckert and Wachs [50] on VO_x/TiO_2 and VO_x/Al_2O_3 catalysts. These species are attributed to V^{5+} in a distorted octahedral symmetry as in ZnV_2O_6 or PbV_2O_6. In each of these compounds, there are two shorter (1.6-1.7 Å), three moderately long (1.85-2.1 Å), and one extremely long (>2.5 Å) V-O bonds and hence described as distorted octahedral symmetry. This bonding geometry type gives rise to a characteristic line shape quite different from V_2O_5.

For 10 VO_x/Al_2O_3, the isotropic peak is observed at around -504 ppm indicating the presence of octahedral vanadia species for this catalyst also. Thus, we can conclude that at low surface concentration, the tetrahedral coordination of V^{5+} is favored, but upon increasing the vanadium concentration, octahedrally coordinated species are mainly observed by MAS NMR. Similar results have also been reported by other authors [50,76,78,105,108]. It should be noted here that the coordination of V^{5+} as revealed by MAS NMR cannot be described as pure isolated tetrahedral or octahedral, rather they are in distorted environments.

In the case of 20 VO_x/Al_2O_3, more than one isotropic peak was observed. The isotropic peak observed at –614 ppm can be attributed to bulk-like V_2O_5 since the position and side-band pattern of this peak are in good agreement with those reported for V_2O_5 in literature. Eckert and Wachs [50] reported δ_{iso} value of –609 ppm for V_2O_5. The bonding geometry in V_2O_5 is typically described as square-pyramidal, consisting of four equatorial V-O bonds of similar length and one very short axial V-O bond (1.58 Å). Alternatively, the environment could be described as 6-coordinate, if the very long (2.78 Å) second axial V-O distance is included. The XRD studies indicated that only one type of vanadium site (V1) and three different oxygen sites exist in crystalline V_2O_5, as shown in Fig. 2.20 [109]. The ^{51}V MAS spectrum of crystalline V_2O_5 experimentally measured using a rotation rate of 20 kHz and consistent with this structure is shown in Fig. 2.20 [109]. Note that the side band pattern observed around –614 ppm in MAS NMR spectrum of 20 VO_x/Al_2O_3 is similar to that measured for crystalline V_2O_5.

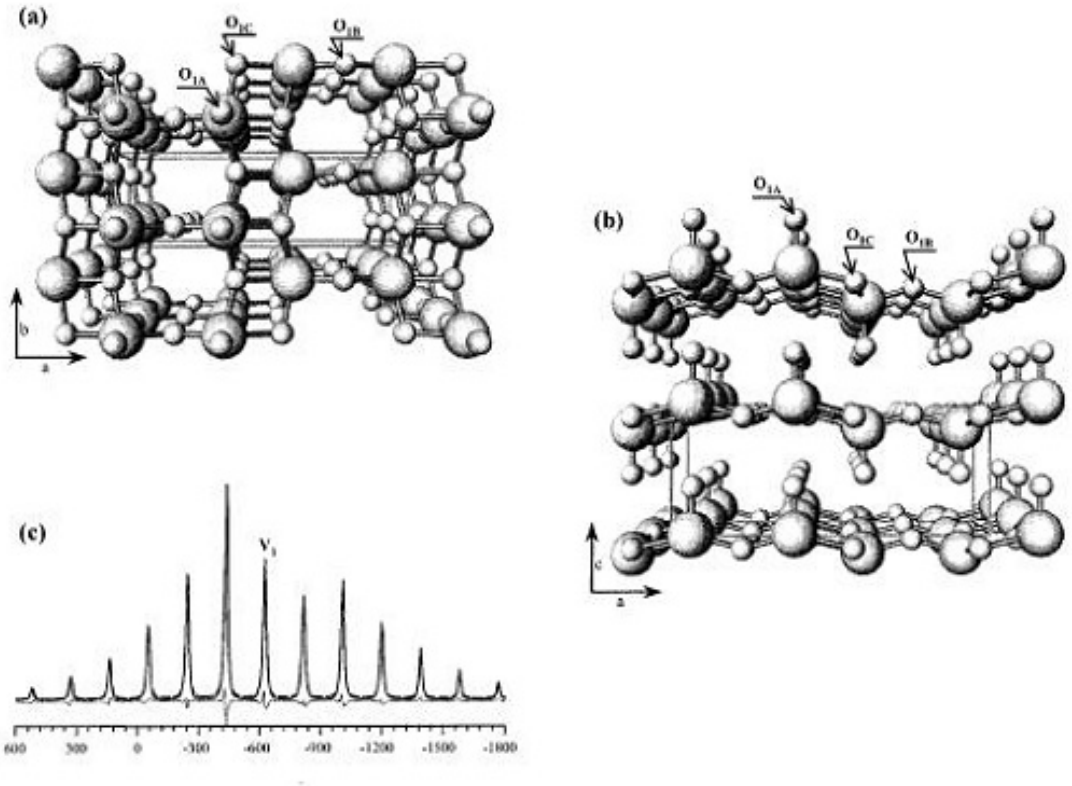

Fig. 2.20: *Crystalline V_2O_5:* ***(a)*** *001 plane and* ***(b)*** *010 plane obtained from the XRD studies. The markings in the diagram denote three different oxygen sites,* ***(c)*** *extended sideband pattern of ^{51}V MAS NMR spectra, measured using a rotation rate of 20 kHz (from [109]).*

The MAS NMR spectrum of 20 VO_x/Al_2O_3 also shows isotropic peaks at –663, -744, -774 ppm which can be attributed to the presence of $AlVO_4$. The V species in $AlVO_4$ is in a tetrahedral $Q^{(0)}$ coordination and the δ_{iso} values reported by Eckert and Wachs [50] are –661, -745 and –775 ppm. The values determined in our experiment are in good agreement with these values. The structure of $AlVO_4$ (Fig. 2.21), which was determined by a combination of simulated annealing and Rietveld refinement [110, 111], contains three distinct VO_4^{3-} tetrahedra, two AlO_6 octahedra and a pentacoordinated AlO_5 unit. The presence of three different vanadium (V) tetrahedra explains the origin of three isotropic peaks for vanadia species [110].

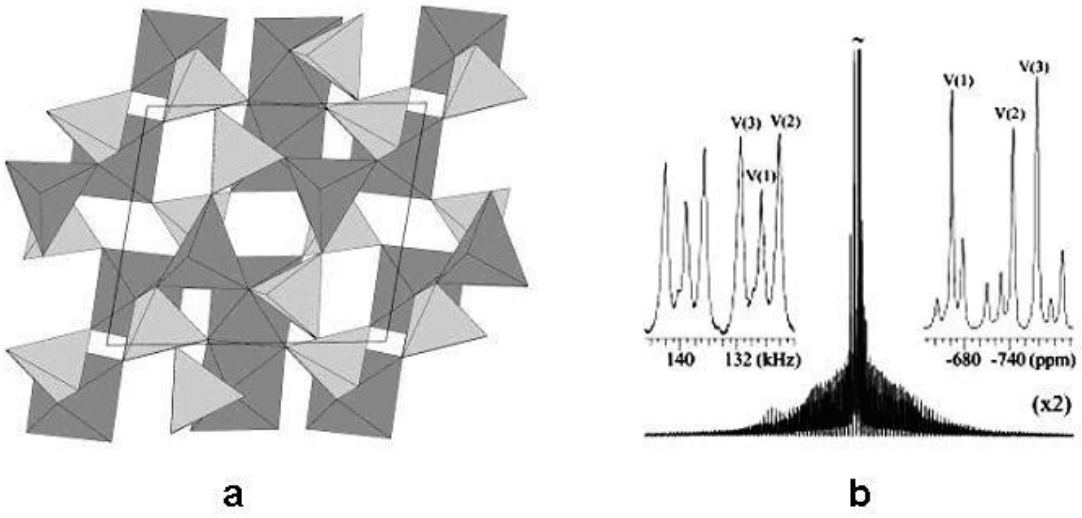

Figure 2.21: ***(a)*** *Polyhedral representation of the structure for $AlVO_4$ shown by a projection along the a axis. The light tetrahedra illustrate the isolated VO_4 units while the dark polyhedra show the coordination for aluminum.* ***(b)*** *^{51}V MAS NMR spectrum (14.1 T, ν_r=10.5 kHz) of the central and satellite transitions for $AlVO_4$ shown on a kilohertz scale relative to the isotropic peak for V(2). The right-hand insets show the spectral region for the isotropic peaks (on a ppm scale relative to $VOCl_3$) while the left-hand insets illustrate that the ssbs from the satellite transitions are almost completely separated for the three ^{51}V sites (from [110]).*

2.5. THE MOLECULAR STRUCTURE OF VANADIA SPECIES

As mentioned in Chapter 1, vanadia species can exist in different molecular structures when supported on metal oxide. Usually, when a catalytically active oxide is supported on the surface of an oxide support, the former remains in an X-ray diffraction amorphous state up to a loading equivalent to at least the theoretical monolayer coverage [112]. The surface free energy of bidimensional monolayer is higher than crystalline bulk vanadium oxide, however the interfacial cohesion between vanadium oxide and support oxide drives the spreading of the former over the surface of latter. Since the Tamman temperature of vanadium oxide is low (449 K), the rate of transformation is relatively fast during calcination. Assuming an ideal flat surface with a single type of surface geometry

and their close packing [112] (however the real situation may be different), the surface density that correspond to a theoretical polyvanadate monolayer can be calculated as ~ 7 VO_x nm^{-2} for the present series of catalysts (Fig. 2.22A). For a monovanadate monolayer, this value is ~ 2.3 VO_x nm^{-2}. Assuming a polyvanadate monolayer is more probable, we can expect that bulk phases of vanadia will appear only above a surface density of 7 VO_x nm^{-2} (~ 12 wt%).

The various characterization techniques show that the structure of dispersed VO_x species on Al_2O_3 support depends on the VO_x surface density. At low coverages (VO_x surface densities below 13 V nm^{-2}), XRD doesn't detect any vanadium phase while the catalyst with surface density 13.4 V nm^{-2} (20 VO_x/Al_2O_3) show peaks characteristic of bulk-like V_2O_5 and $AlVO_4$. UV-visible spectroscopy suggests that vanadia exist as V^{5+} species with distorted tetrahedral coordination at the lowest surface density studied (1.2 V nm^{-2} or 2 VO_x/Al_2O_3). The decrease in absorption edge energy with increasing surface density indicates the progressive condensation of vanadia species leading to polymeric V^{5+} species at higher loadings and finally to bulk-like vanadia crystallites at a surface density of 13.4 V nm^{-2}. The relevant point is that the absorption edge energy reflects electronic properties that matter for catalysis and the shift in the edge is a sign of oligomerization beyond monomeric structures. TPR spectra show a shift in T_{max} to lower temperatures as the surface density increases from 1.2 to 5.9 V $nm^{-2,\ which}$ can be attributed to the increased polymerization of vanadium species, which are more easily reducible than monomeric ones. The additional peak observed at 855 K at a surface density of 13.4 V nm^{-2} can be ascribed to the reduction of bulk-like V_2O_5 crystallites. Consistent with this interpretation, there is the presence of bands at 831 and 1017 cm^{-1} in the FTIR spectrum of this catalyst, which are characteristic of V-O-V bending vibration and V=O stretching vibration in bulk vanadia respectively. These bands are not observed for catalysts with lower vanadia loadings. Laser Raman spectrum of the 20 VO_x/Al_2O_3 catalyst shows the characteristic bands of bulk V_2O_5, which were not observed for lower vanadia loadings. The results of ^{51}V NMR experiments are also in agreement with the change in structure of vanadia species with surface density. Hence from the various characterization results, it can be concluded that tetrahedral V^{5+} species are present on the VO_x/Al_2O_3 catalyst at a surface

density of 1.2 V nm^{-2} (2 wt% vanadia loading), polymerization of V^{5+} species increases as the surface density increases (Fig. 2.22B) and formation of bulk-like V_2O_5 crystallites and aluminum orthovanadate takes place at a surface density of 13.4 V nm^{-2} (20 wt% vanadia loading).

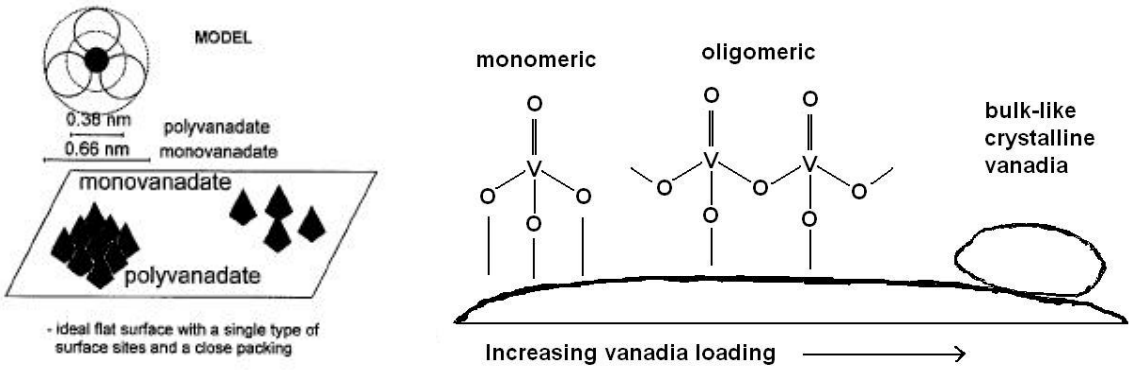

Fig. 2.22: (A) *The representation of theoretical situation for monolayer, assuming an ideal flat surface and* ***(B)*** *Schematic drawing of change in molecular structures of surface vanadia species with increasing vanadia loading.*

The situation we have arrived at is in agreement with the concept of monolayer. Below the surface density that corresponds to theoretical monolayer (7 VO_x nm^{-2}), only dispersed surface vanadia species were identified while above that, bulk phases like V_2O_5 and $AlVO_4$ were also detected. Now, if we look at the evolution in molecular structure of vanadia with increasing surface density, it can be observed that two types of changes are apparent, change in coordination and bridging. The expected coordination changes from tetrahedral (dispersed vanadia species at 1.2 V nm^{-2}) to trigonal bipyramidal or distorted octahedral (crystalline V_2O_5 at 13.4 V nm^{-2}). On the other side, there is the effect of bridging, which changes monomeric structures to polymeric structures. Can we separate

these two effects? As far as our study is concerned, it is not possible to separate conclusively the effects of coordination and bridging, since they occur together. As mentioned previously, the important thing is the oligomerization of vanadia species with increasing surface density. The next chapter describes how the catalytic activity changes with this structural evolution.

2.6. REFERENCES

[1] J. W. Niemantsverdriet, Spectroscopic methods in Heterogeneous catalysis, VCH, Weinheim, 1993.

[2] J. M. Thomas, W. J. Thomas, Principles and Practice of Heterogeneous catalysis, VCH, Weinheim, 1997.

[3] R. P. Eischens, W. A. Pliskin, Adv. Catal., 10 (1958) 1.

[4] P. Kubelka, F. Munk, Z. Tech. Phys., 12 (1931) 593.

[5] P. Kortum, W. Braun, C. Harzog, Angew. Chem. Int. Ed. Engl., 2 (1963) 333.

[6] P. Concepcion, B. M. Reddy, H. Knozinger, Phys. Chem. Chem. Phys., 1 (1999) 3031.

[7] L. J. Burcham, I. E. Wachs, Catal. Today, 49 (1999) 467.

[8] K. Hadjiivanov, P. Concepcion, H. Knozinger, Top. Catal., 11 (2000) 123.

[9] M. A. Centeno, I. Carrizosa, J. A. Odriozola, Appl. Catal. B: Environ., 29 (2001) 307.

[10] G. Martra, F. Arena, S. Collucia, F. Frusteri, A. Parmaliana, Catal. Today, 63 (2000) 197.

[11] N.-Y. Topsoe, Science, 265 (1994) 1217.

[12] N.-Y. Topsoe, J.A. Dumesic, H. Topsoe, J. Catal., 151 (1995) 241.

[13] N.-Y. Topsoe, H. Topsoe, J. A. Dumesic, J. Catal., 151 (1995) 226.

[14] L. J. Burcham, L. E. Briand, I. E. Wachs, Langmuir 17 (2001) 6164.

[15] P. L. Villa, F. Trifiro, I. Pasquon, React. Kinet. Catal. Lett., 1 (1974) 341.

[16] I. E. Wachs, J. M. Jehng, G. Deo, B. M. Weckhuysen, V. V. Guliants, J. B. Benziger, S. Sundaresan, J. Catal., 170 (1997) 75.

[17] U. Sharf, M. Schraml-Marth, A. Wokaun, A. Baiker, J. Chem. Soc., Faraday Trans. 87 (1991) 3299.

[18] T. J. Dines, C. H. Rochester, A. M. Ward, J. Chem. Soc., Faraday Trans. 87 (1991) 1617.

[19] F. Hatayama, T. Ohno, T. Maruoka, T. Ono, H. Miyata, J. Chem. Soc., Faraday Trans. 87 (1991) 2629.

[20] A. Burkart, W. Weisweiler, J. A. A. van den Tillaart, A. Schafer-Sindlinger, A. S. Lox, Top. Catal. 16 (2001) 369.

[21] B. Olthof, A. Khodakov, A. T. Bell, E. Iglesia, J. Phys. Chem. B 104 (2000) 1516.

[22] D. A. Bulushev, L. Kiwi-Minsker, A. Renken, Catal. Today, 57 (2000) 231.

[23] I. E. Wachs, G. Deo, M. A. Vuurman, H. Hu, D. S. Kim, J. M. Jehng, J. Mol. Catal., 82 (1993) 443.

[24] M. A. Vuurman, I. E. Wachs, J. Phys. Chem., 96 (1992) 5008.

[25] I. E. Wachs, Top. Catal., 8 (1999) 57.

[26] F. D. Hardcastle, I. E. Wachs, J. Phys. Chem., 95 (1991) 5031.

[27] B. M. Weckhuysen, R. A. Schoonheydt, Catal. Today, 49 (1999) 441.

[28] R. A. Schoonheydt, Diffuse Reflectance Spectroscopy, Chapter 4, in: Characterization of Heterogeneous Catalysts, F. Delannay (Ed.), Marcel Dekker, New York, 1984.

[29] X. T. Gao, I. E. Wachs, J. Phys. Chem. B 104 (2000) 1261.

[30] X. T. Gao, I. E. Wachs, J. Catal. 188 (1999) 325.

[31] B. M. Weckhuysen, I. P. Vannijvel, R. A. Schoonheydt, Zeolites 15 (1995) 482.

[32] E. V. Kondratenko, M. Baerns, Appl. Catal. A: Gen. 222 (2001) 133.

[33] K. Tran, M. A. Hanning-Lee, A. Biswas, A. E. Stiegman, G. W. Scott, J. Am. Chem. Soc., 117 (1995) 2618.

[34] B. C. Lippens and J. H. de Boer, J. Catal., 4 (1965) 319.

[35] E. P. Barret, L. G. Joyner and P. H. Halenda, J. Amer. Chem. Soc., 73 (1951) 373.

[36] J. I. Goldstein, H. Yakowitz (Eds.), Practical Scanning Electron Microscopy, Plenum Press, New York, 1975.

[37] T. A. Carlson, X-ray Photoelectron Spectroscopy, Dowden, Hutchinson & Ross: Stroudsburg, PA, 1978.

[38] D. Briggs, M. P. Seah (Eds.), Practical Surface Analysis, Vol. 1: Auger and X-ray Photoelectron Spectroscopy (2nd ed.) Wiley, New York, 1990.

[39] S. Hüfner, Photoelectron Spectroscopy, Springer-Verlag, Berlin, 1995.

[40] M. A. Eberhardt, A. Proctor, M. Houalla, D. M. Hercules, J. Catal. 160 (1996) 27.

[41] B. M. Reddy, B. Chowdhury, E. P. Reddy, A. Fernandez, Langmuir 17 (2001)

1132.

[42] F. Prinetto, G. Ghiotti, M. Occhiuzzi, V. Indovina, J. Phys. Chem. B 102 (1998) 10316.

[43] M. Wark, A. Bruckner, T. Liese, W. Grunert, J. Catal. 175 (1998) 48.

[44] M. A. Vuurman, I. E. Wachs, A. M. Hirt, J. Phys. Chem. 95 (1991) 9928.

[45] J. J. P. Biermann, F. J. J. G. Janssen, J. R. H. Ross, J. Phys. Chem. 94 (1990) 8598.

[46] M. Faraldos, J. A. Anderson, M. A. Banares, J. L. G. Fierro, S. W. Weller, J. Catal. 168 (1997) 110.

[47] G. C. Bond, J. Perez Zurita, S. Flamerz, Appl. Catal. 27 (1986) 353.

[48] R. A. Wind, in A. I. Popov, K. Hallenga (Eds.), Modern NMR Techniques and Their Application in Chemistry, p. 156, Marcel Dekker, Inc., New York, 1991.

[49] R. H. H. Smits, Ph. D. Thesis, Netherlands, 1994.

[50] H. Eckert, I. E. Wachs, J. Phys. Chem. 93 (1989) 6796.

[51] N. Das, H. Eckert, H. Hu, I. E. Wachs, J. F. Walzer, F. J. Feher, J. Phys. Chem. 97 (1993) 8240.

[52] J. H. Miller, L. J. Lakshmi, J. Mol. Catal. A: Chem. 144 (1999) 451.

[53] P. Kalinkin, O. Kovalenko, O. Lapina, D. Khabibulin, N. Kundo, J. Mol. Catal. A: Chem. 178 (2002) 173.

[54] O. B. Lapina, M. A. Matsko, T. B. Mikenas, V. A. Zkaharov, E. A. Paukshtis, D. F. Khabibulin, A. P. Sobolev, Kinet. Catal. 42 (2001) 609.

[55] V. V. Terskikh, O. B. Lapina, V. M. Bondareva, Phys. Chem. Chem. Phys. 2 (2000) 2441.

[56] A. A. Shubin, O. B. Lapina, V. M. Bondareva, Chem. Phys. Lett. 302 (1999) 341.

[57] A. A. Shubin, O. B. Lapina, D. Courcot, Catal. Today 56 (2000) 379.

[58] V. M. Bondareva, T. V. Andrushkevich, O. B. Lapina, Catal. Today 61 (2000) 173.

[59] O. B. Lapina, D. F. Khabibulin, A. A. Shubin, V. M. Bondareva, J. Mol. Catal. A: Chem. 162 (2000) 381.

[60] J. C. Vedrine, Electron Spin Resonance, Chapter 5 in: Characterization of

heterogeneous catalysts, F. Delannay (Ed.), Marcel Dekker, New York, 1984.

[61] M. Che, E. Giamello, Electron Paramagnetic Resonance, Chapter 5 in: Spectroscopic characterization of heterogeneous catalysts, J. L. G. Fierro (Ed.) Stud. Surf. Sci. Catal., Vol. 57 B, Elsevier, 1990.

[62] G. J. Wang, H. C. Ma, Y. Li, Z. Y. Liu, React. Kinet. Catal. Lett. 74 (2001) 103.

[63] V. Luca, D. J. Macklachlan, R. Bramley, Phys. Chem. Chem. Phys. 1 (1999) 2597.

[64] M. C. Paganini, L. Dall'Acqua, E. Giamello, L. Lietti, P. Forzatti, G. Busca, J. Catal. 166 (1997) 195.

[65] M. Che, B. Canosa, A. R. Gonzalez-Elipe, J. Phys. Chem. 90 (1986) 618.

[66] A. Davidson, M. Che, J. Phys. Chem. 96 (1992) 9909.

[67] K. V. R. Chary, B. M. Reddy, N. K. Nag, V. S. Subrahmanyam, C. S. Sunandana, J. Phys. Chem. 88 (1984) 2622.

[68] M. D. Argyle, K. Chen, A. T. Bell, E. Iglesia., J. Catal., 208 (2002) 139.

[69] O. Yamaguchi, T. Uegaki, Y. Miyata, K. Shimizu, J. Am. Ceram. Soc. 70 (8) (1987) 198.

[70] B. Leyer, H. Schmelz, H. Göbel, H. Meixner, T. Scherg, H. Knözinger, Thin Solid Films, 310 (1997) 228.

[71] R. A. Rajadhyaksha, H. Knözinger, Appl. Catal., 71 (1991) 1.

[72] Z. Sobalik, R. Kozloski, J. Haber, J. Catal., 127 (1991) 665.

[73] G. Dell Agli, S. M. Grippo, G. Mascolo, Thermochim. Acta, 227 (1993) 197.

[74] V. Dimitrov, Y. Dimitriev, A. Montenero, J. Non-Crystall. Sol., 180 (1994) 51.

[75] I. E. Wachs, Catal. Today, 27 (1996) 437.

[76] J. G. Eon, R. Olier, J. C. Volta, J. Catal., 145 (1994) 318.

[77] H. Bosch, B. J. Kip, J. G. Van Ommen, P. J. Gellings, J. Chem. Soc. Faraday Trans., 80 (1984) 2479.

[78] M. M. Koranne, J. G. Goodwin Jr., G. Marcelin, J. Catal., 148 (1994) 369.

[79] Z. Sobalik, O. B. Lapina, O. N. Novgorodova, V. M. Mastikin, Appl. Catal., 63 (1990) 191.

[80] A. W. Stobbe-Kreemers, G. C. van Leerdam, J.-P. Jacobs, H. H. Brongersma, J. J.

F. Scholten, J. Catal., 152 (1995) 130.

[81] M. A. Centeno, P. Malet, I. Carrizosa, J. A. Odriozola, J. Phys. Chem. B, 104 (2000) 3310.

[82] G. Lischke, W. Hanke, H-G. Jerchkewitz, G. Olmann, J. Catal., 91 (1985) 54.

[83] A. Corma, J. M. Lopez Nieto, N. Paredes, Appl. Catal. A, 104 (1993) 161.

[84] M. Schraml-Marth, A. Wokaun, M. Pohl and H. L. Krauss, J. Chem. Soc. Faraday Trans., 87 (1991) 2635.

[85] G. Centi, S. Perathoner, F. Trifiro, A. Aboukais, C. F. Aissi, M. Guelton, J. Phys. Chem., 96 (1992) 2617.

[86] M. A. Larrubia, G. Busca, Mater. Chem. Phys., 72 (2001) 337.

[87] A. Pantazidis, A. Burrows, C. J. Kiely, C. Mirodatos, J. Catal., 177 (1998) 325.

[88] J. Tauc, in: Amorphous and Liquid semiconductors, J. Tauc (Ed.) p.159, Plenum, London, 1974.

[89] R. A. Smith, Semiconductors (2nd ed.), Cambridge University Press, Cambridge, 1978.

[90] R. S. Weber, J. Catal. 151 (1995) 470.

[91] P. F. Carcia, E. M. McCarron, Thin Solid Films, 155 (1987) 53.

[92] Di Wei, H. Wang, X. Feng, Wei-Te Chueh, P. Ravikovitch, M. Lyubovsky, C. Li, T. Takeguchi, G. L. Haller, J. Phys. Chem. B, 103 (1999) 2113.

[93] J. Wong, F. W. Lytle, R. P. Messmer, D. H. Maylotte, Phys. Rev. B, 30 (1984) 5596.

[94] A. Khodakov, J. Yang, S. Su, E. Iglesia, A. T. Bell, J. Catal., 177 (1998) 343.

[95] D. Wei, G. L. Haller in: Proceedings of 2nd Memorial G. K. Boreskov international conference, p. 110, Novosibirsk, 1997.

[96] K. Chen, A. T. Bell, E. Iglesia, J. Catal., 209 (2002) 35.

[97] C. Pak, A. T. Bell, T. Don Tilley, J. Catal., 206 (2002) 49.

[98] X. Gao, S. R. Bare, B. M. Weckhuysen, I. E. Wachs, J. Phys. Chem. B, 102 (1998) 10842.

[99] A. M. A. Cruz, J. G. Eon, Appl. Catal. A, 167 (1998) 203.

[100] J. F. Moulder, W. F. Stickle, P. E. Sobol, K. D. Bomben, Handbook of XPS,

Perkin-Elmer, Eden Prairie, MN, 1992.

[101] J. F. Moulder, W. F. Stickle, P. E. Sobol, K. D. Bomben, in: Hand-book of X-ray Photoelectron Spectroscopy, J. Chastain, R. C. King Jr. (Eds.), p. 241, Physical Electronics Inc., Eden Prairie, 1995.

[102] J. L. G. Fierro, L. A. Gambaro, T. A. Cooper, G. Kremenic, Appl. Catal., 6 (1983) 363.

[103] F. J. Gil-Llambias, A. M. Escudey, J. L. G. Fierro and A. Lopez Agudo, J. Catal. 95, (1985) 527.

[104] T. Blasco, A. Galli, J. M. Lopez Nieto, F. Trifiro, J. Catal., 169 (1997) 203.

[105] K. V. R. Chary, G. Kishan, J. Phys. Chem. 99 (1995) 14424.

[106] M. Inomata, K. Mori, A. Miyamoto, Y. Murakami, J. Phys. Chem. 87 (1983) 761.

[107] V. K. Sharma, A. Wokaun, A. Baiker, J. Phys. Chem. 90 (1986) 2715.

[108] T. Blasco, J. M. Lopez Nieto, Colloids and Surfaces A: Physicochemical and Engineering Aspects, 115 (1996) 187.

[109] C. J. Fontenot, J. W. Wiench, G. L. Schrader, M. Pruski, J. Am. Chem. Soc., 124 (2002) 8435.

[110] U. G. Nielsen, A. Boisen, M. Brorson, C. J. H. Jacobsen, H. J. Jakobsen, J. Skibsted, Inorg. Chem., 41 (2002) 6432.

[111] A. A. Coelho, J. Appl. Crystallogr., 33 (2000) 899.

[112] G. Centi, Appl. Catal. A, 147 (1996) 267.

CHAPTER 3

Catalytic Activity Studies And Correlation With Structure Of VO_x/Al_2O_3 Catalysts

SECTION A-CATALYTIC ACTIVITY STUDIES

3.1. INTRODUCTION

Modern research in the field of catalysis is based on the establishment of empirical relations between behavior of the catalyst during the reaction at different reaction conditions and the catalyst composition, structure and texture, which can be studied *ex situ* or *in situ*. It is apparent that the study of the catalytic activity under determined reaction conditions with a combination of useful methods for catalyst characterization prior and subsequent to the reaction could maximize useful information about reaction pathways, active sites of reaction and the reaction mechanisms.

This section describes the results of studies of oxidative dehydrogenation of ethylbenzene to styrene in presence of N_2O using VO_x/Al_2O_3 catalysts, which can be represented as:

$$C_6H_5CH_2CH_3 + N_2O \rightarrow C_6H_5CH{=}CH_2 + N_2 + H_2O \qquad (3.1)$$

The general introduction about this reaction is given in Chapter 1. The activity and selectivity of the catalysts were correlated with the structural aspects of catalyst determined by comparative characterizations before and after ODH catalysis, which is described in section B.

3.2. CATALYTIC ACTIVITY MEASUREMENTS

3.2.1. Set-up for the catalytic evaluation

The catalytic tests are carried out in the set-up, which is shown schematically in Fig. 3.1. The set-up allows one to perform experiments with full control of all reaction parameters and to conduct the process in the presence of gases as reactant or carrier. The gaseous reactants (N_2O/N_2) are fed to the reactor at controlled flow rates using mass flow controllers (Hi-Tech, Bronkhorst, The Netherlands). Ethylbenzene was fed to the reactor with high accuracy using a high-pressure syringe pump (Isco 500 D).

The catalytic tests were performed in fixed bed down-flow glass reactors (40 cm length, 15 mm I.D.) placed inside an electrically heated split furnace (Geomechanique, France) that was controlled by a temperature controller. The catalyst particles, of size 10-

20 mesh, mixed with ceramic beads were held in the isothermal furnace zone between two quartz wool plugs. Ceramic beads are further used to minimize the dead volume of the reactor upstream the catalyst bed that also served as vaporizer cum pre-heater. The exact temperature of the catalyst bed was monitored by a thermocouple, placed at the center of the catalyst bed. The catalyst was activated before each run, by heating at 773 K in a flow of dry air for 8 hours and then cooled to the desired reaction temperature. The products of the reaction were passed through a condenser, circulated with chilled water, and collected in a receiver. The set-up also consists of provision for online gas chromatographic analysis of gaseous effluents.

3.2.2. Analytical method

A Hewlett-Packard 6890 plus gas chromatograph, equipped with a flame ionization detector, was used for the analysis of condensed reaction products (styrene, benzene, toluene, styrene oxide). The separation of various products was achieved using a capillary column (BPX5, 50 m × 0.32 mm i.d.). The actual amount of each component in the product mixture was determined by using the response factor of that compound. The initial confirmation/identification of reaction products was done by GC-MS and GC-IR. The gaseous products were analyzed online with a Chemito 1000 gas chromatograph equipped with TCD, using a spherocarb column (mesh size 80/100, 8', 1/8" dia).

The possible contribution of homogenous, gas-phase reactions was tested by comparing the EB conversions obtained with the empty reactor and the reactor filled with quartz wool plugs and ceramic beads. The EB conversions obtained in such catalytic tests were very low, maximum 2%, up to a temperature range of 773 K. The experiments were repeated to check the accuracy of results and were found to be reproducible within the normal experimental error.

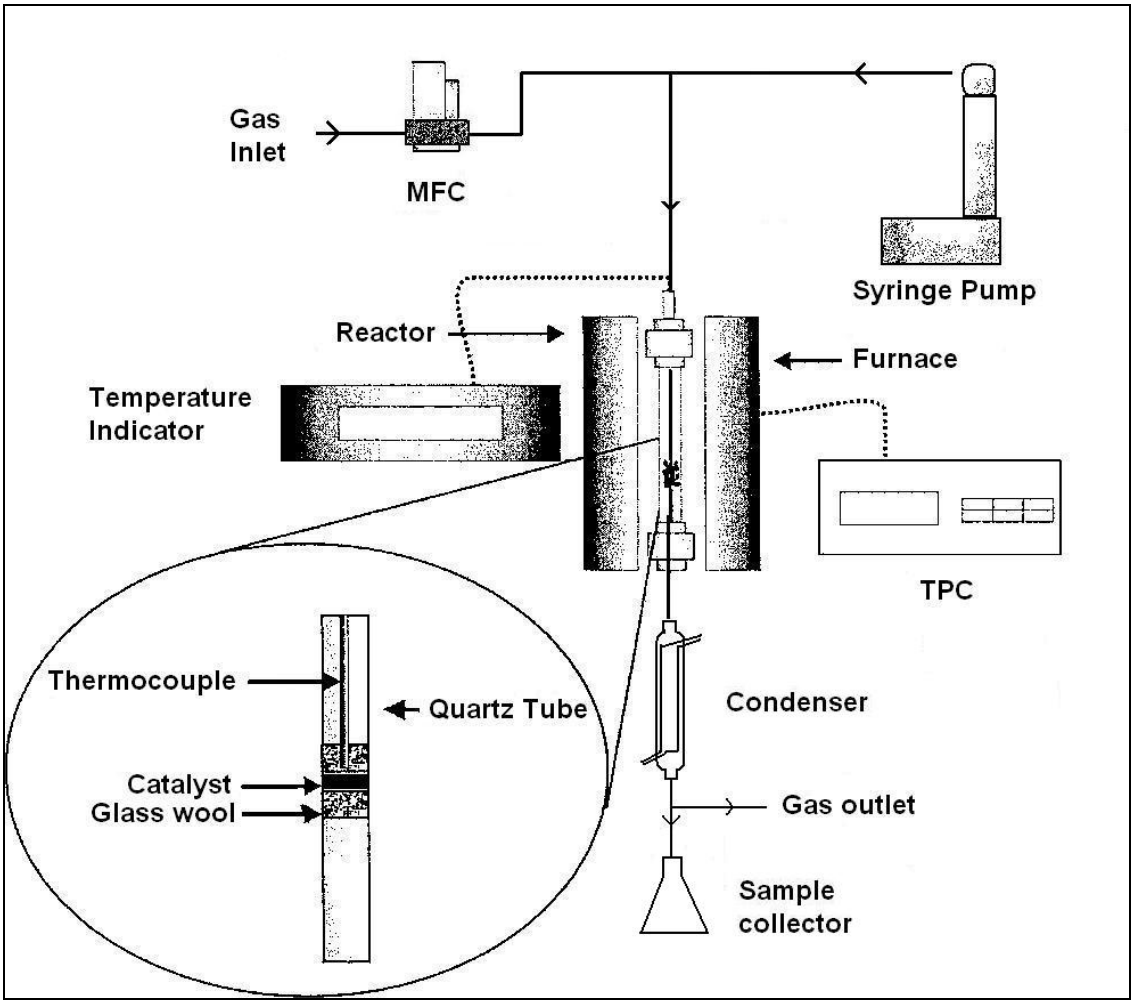

Figure 3.1: *Scheme of the reactor set-up used for the catalytic experiments. MFC: Mass Flow Controller, TPC: Temperature Programmer Controller.*

The parameters of the catalytic performance are defined by the following equations:

$$\text{EB conversion (\%)} = (C_{EBin} - C_{EBout} / C_{EBin}) \times 100 \quad (3.2)$$

$$\text{Selectivity to Styrene (\%)} = (C_{ST} / C_{EBin} - C_{EBout}) \times 100 \quad (3.3)$$

$$\text{Styrene yield (\%)} = (C_{ST} / C_{EBin}) \times 100 \quad (3.4)$$

where C denote the concentration and the subscripts, "in" and "out", the respective concentrations in the feed and outlet. The relative yields of by-products were calculated by the same way and the results are given in wt%.

The reaction rates of oxidative dehydrogenation of ethylbenzene to styrene based on vanadium concentration were calculated according to the following equation:

$$r = F\ X / n_V \quad (3.5)$$

with F being flow rate in mol/s, X being the conversion and n_V being the number of moles of vanadium per gram of catalyst.

The areal reaction rates (rate based on surface area of catalyst) of ODH of EB to ST were calculated according to the equation:

$$r_A = F\ X / S \quad (3.6)$$

where S is the BET surface area in $m^2\ g^{-1}$ of the catalyst.

The reaction kinetics may be determined by diffusion processes, if the rates of heat and mass transfer to the catalyst are less than the rate of the reaction on the catalyst surface. The limitation by diffusion processes can be checked by determining the conversion values at different linear flow rates but at the same contact time. A series of experiments was performed at 773 K at a constant contact time (Volume of catalyst/Flow rate). The linear flow rates of ethylbenzene were changed and the catalyst amounts were proportionally increased for maintaining contact time constant. The differences in the catalytic performances were minimal indicating that diffusion limitations can be neglected under the present reaction conditions. However, limitation by intra-particle diffusion cannot be excluded by this study.

3.3. RESULTS AND DISCUSSION

3.3.1. Nitrous oxide as oxidizing agent

The catalytic activity and selectivity of VO_x/Al_2O_3 catalysts were investigated using nitrous oxide as an oxidant. To compare the effectiveness of N_2O as an oxidant, the reaction was also conducted in the presence of nitrogen alone. Figure 3.2 shows the yield of styrene and selectivities of other products observed at 623 K in nitrous oxide and nitrogen atmospheres for 20 VO_x/Al_2O_3. The reactions were performed under identical conditions, keeping EB space velocity 1 h^{-1} and N_2/N_2O flow rate (GHSV) 1200 h^{-1}. It can be seen that the styrene yield in the presence of nitrous oxide is at least 2-3 times higher than that in nitrogen atmosphere at 623 K. The yield of styrene decreased with reaction

time for both N_2O and N_2 atmospheres, however the yield remained at a much higher level in N_2O atmosphere throughout the period studied. The selectivities of benzene and toluene, which are the dealkylation products of ethylbenzene, were lower under N_2O flow as compared to that under N_2 flow. However, a higher selectivity for styrene oxide was observed in N_2O atmosphere, probably because the availability of oxygen by the dissociation of N_2O increases the secondary reaction, the conversion of styrene to styrene oxide. The results were similar for other reaction temperatures also.

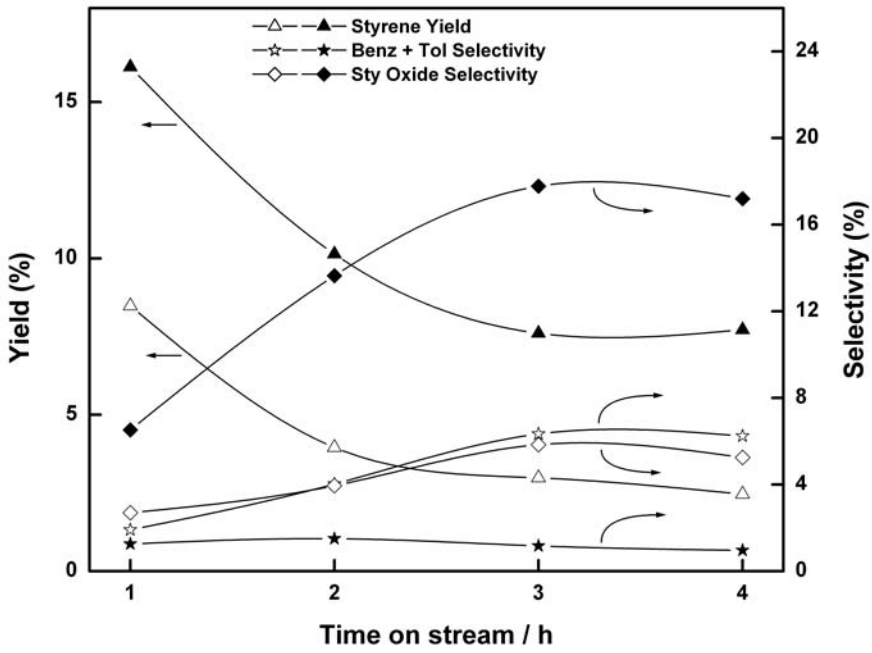

Figure 3.2*: The yield of styrene and selectivities of benzene, toluene, styrene oxide in nitrogen and nitrous oxide atmospheres as a function of time on stream. Solid symbols, under nitrous oxide flow; open symbols, under nitrogen flow;* (7) *styrene yield;* (ξ) *sum of benzene and toluene selectivities;* (∧) *styrene oxide selectivity.*
Reaction conditions: Temperature, 623 K; WHSV of EB, 1 h^{-1}; GHSV of N_2/N_2O, 1200 h^{-1}; catalyst, 20 VO_x/Al_2O_3.

The reaction was also conducted at different temperatures in nitrogen and nitrous oxide atmospheres. Fig. 3.3 shows the conversion of ethylbenzene and yield of styrene at different temperatures for 20 VO_x/Al_2O_3. The results show that enhancement of

dehydrogenation reaction in nitrous oxide atmosphere is observed at all temperatures. The figure also shows results observed with 5 VO_x/Al_2O_3 at 623 and 773 K. The conversion of ethylbenzene and selectivity of styrene observed in nitrous oxide atmosphere are well above that in nitrogen atmosphere, the difference being more pronounced at higher temperatures.

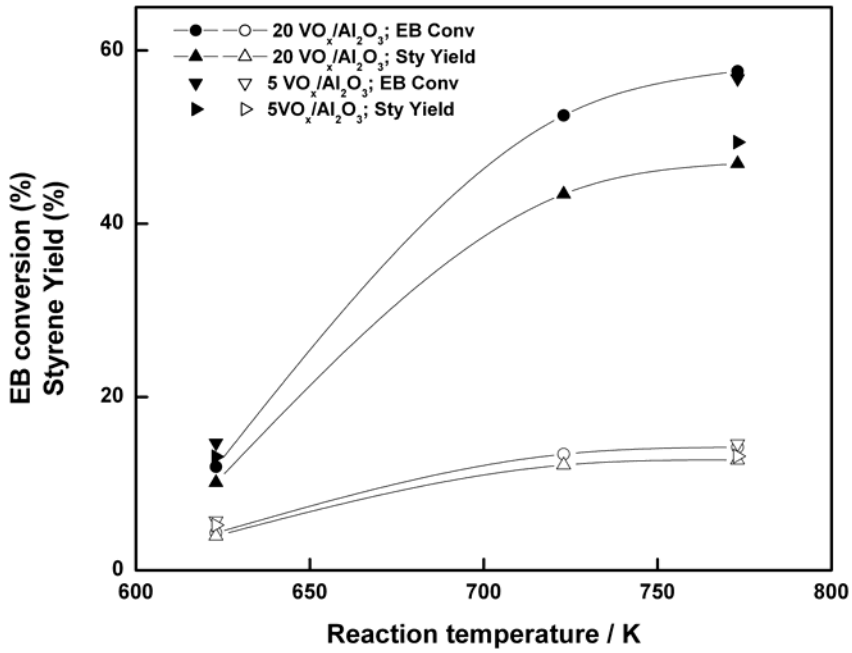

Figure 3.3*: The yield of styrene and conversion of ethylbenzene in nitrogen and nitrous oxide atmospheres as a function of reaction temperature for 5 and 20 VO_x/Al_2O_3. Solid symbols, under nitrous oxide flow; open symbols, under nitrogen flow; ethylbenzene conversion for 5 VO_x/Al_2O_3 (X B) and for 20 VO_x/Al_2O_3 (, –); styrene yield for 5 VO_x/Al_2O_3 (χ β) and for 20 VO_x/Al_2O_3 (7 8).*
Reaction conditions: WHSV of EB, 1 h^{-1}; GHSV of N_2 / N_2O, 1200 h^{-1}; TOS, 2h.

These results allow us to conclude that nitrous oxide enhance the rate of ODH reaction irrespective of reaction temperature and vanadia loading and this enhancement is stable with reaction time.

3.3.2. The effect of reaction temperature

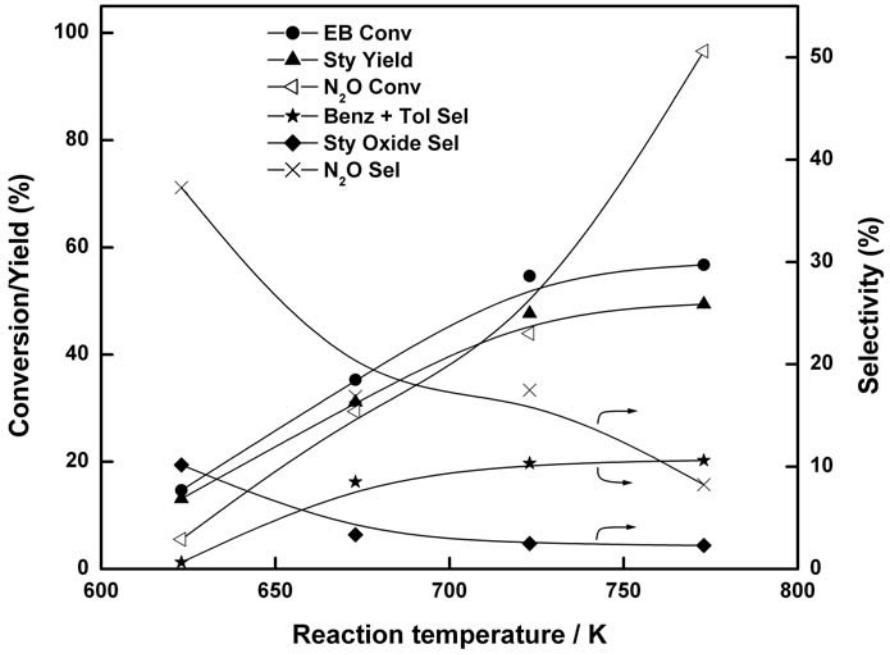

***Figure 3.4**: Effect of temperature on product yields.* (.) *ethylbenzene conversion;* (7) *styrene yield;* (Ξ) *N_2O conversion;* (ξ) *sum of benzene and toluene selectivities;* (∧) *styrene oxide selectivity;* (□) *N_2O utilized for ethylbenzene conversion.*
Reaction conditions: Catalyst, 5 VO_x/Al_2O_3; TOS, 2 h; GHSV of N_2O, 1200 h^{-1}; WHSV of EB, 1 h^{-1}.

Figure 3.4 presents the effect of reaction temperature on the styrene yield in N_2O atmosphere at time on stream (TOS) of 2 h. The EB conversion as well as styrene yield increased monotonically with increasing temperature in the interval studied (623-773 K). At 623 K, the conversion of ethylbenzene and yield of styrene were low, being 15% and 13% respectively, however when the temperature increased to 673 K, they were increased more than two times. The figure also shows the conversion of N_2O and selectivity of N_2O for ethylbenzene reaction as a function of temperature. The former increases with increasing temperature and reaches 96% at 773 K while the amount of N_2O utilized for ethylbenzene conversion decreases, which indicate that though most of the N_2O decomposes, the amount reacting with ethylbenzene is lower at higher temperatures. With

increasing temperature, selectivity of styrene oxide decreased while that of dealkylation products, benzene and toluene, increased. Hence higher temperatures cause higher dealkylation of ethylbenzene and formation of lower amounts of styrene oxide despite the presence of nitrous oxide. These trends in activity and selectivity were similar for catalysts with other vanadia loadings also. The activity by bulk V_2O_5 was very low under these experimental conditions.

3.3.3. The effect of contact time

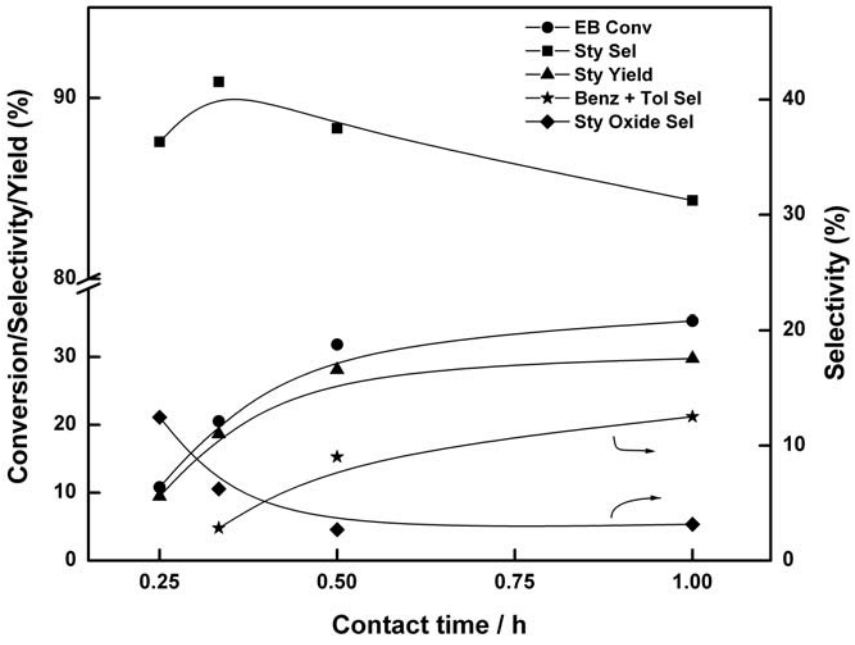

Figure 3.5: *Influence of contact time on the product yields.* (.) *ethylbenzene conversion;* (!) *styrene selectivity;* (7) *styrene yield;* (ξ) *sum of benzene and toluene selectivities;* (∧) *styrene oxide selectivity.*
Reaction conditions: Temperature, 673 K; TOS, 2 h; GHSV of N_2O, 1200 h^{-1}; catalyst, 5 VO_x/Al_2O_3.

The effect of contact time of ethylbenzene with catalyst (inverse of space velocity), on the dehydrogenation of EB is illustrated in Fig. 3.5. The results are obtained at a reaction time of 2h at 673 K with a nitrous oxide space velocity of for 5 VO_x/Al_2O_3. The amount of catalyst was kept constant during these experiments and the feed rate of EB was

changed to vary the contact time. With increasing contact time, conversion of ethylbenzene increased and selectivity for styrene decreased. The increase in styrene yield with increasing contact time, as observed from the figure, is due to the increase in conversion of ethylbenzene and does not reflect the decrease in selectivity. The loss in selectivity for styrene is the gain in selectivity for benzene and toluene, since these dealkylation products increase with increasing contact time. Hence higher contact time increase dealkylation more than it do for dehydrogenation of ethylbenzene. Styrene oxide was observed mainly at low contact time and decreased with increasing contact time. Considering the fact that selectivity of styrene decreases with increasing contact time, it can be assumed that styrene oxide is secondary product and results from styrene epoxidation by nitrous oxide. Hence the formation of styrene oxide is a consecutive reaction.

3.3.4. The effect of nitrous oxide space velocity

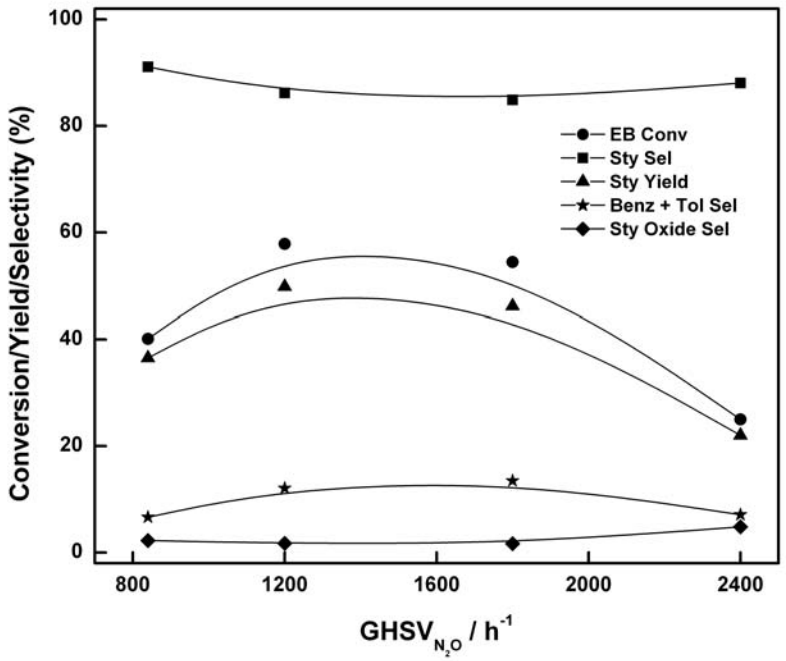

Figure 3.6: *Activity and selectivity as a function of nitrous oxide flow rate. (•) ethylbenzene conversion; (■) styrene selectivity; (▲) styrene yield; (★) sum of benzene and toluene selectivities; (◆) styrene oxide selectivity.*
Reaction conditions: Temperature, 773 K; TOS, 3 h; WHSV of EB, 1 h^{-1}; catalyst, 10 VO_x/Al_2O_3.

The influence of nitrous oxide space velocity on the activity and selectivity was investigated and the results are summarized in Fig. 3.6. The conversion of ethylbenzene and yield of styrene were higher at intermediate space velocities. Both lower and higher space velocities decreased the conversion and yield.

3.3.5. The time on stream behavior

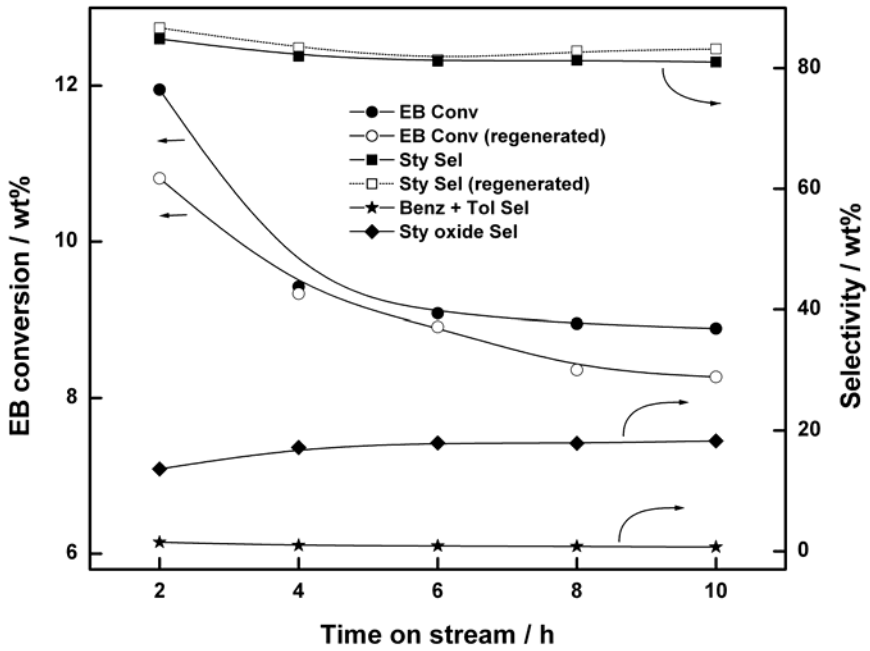

Figure 3.7: *The activity and selectivity behaviour in nitrous oxide atmosphere as a function of time on stream. Solid symbols, reaction with fresh catalyst; open symbols, reaction with regenerated catalyst.*
Reaction conditions: Temperature, 623 K; WHSV of EB, 1 h^{-1}; GHSV of N_2O, 1200 h^{-1}; catalyst, 20 VO_x/Al_2O_3.

The variation in activity and selectivity of the catalyst in nitrous oxide atmosphere with reaction time (TOS) is shown in Fig. 3.7. The reaction is conducted at 623 K with 20 VO_x/Al_2O_3 at an ethylbenzene space velocity of 1 h^{-1} for 10 hours. It can be seen that after an initial deactivation period, the catalyst shows a steady activity and selectivity. After a reaction time of 10 hours, the catalyst is regenerated in a flow of air at 773 K for 8h and

the reaction is conducted under similar conditions with regenerated catalyst. Ethylbenzene conversion levels were slightly lower compared to the initial run using fresh catalyst and selectivity for styrene remained similar to that of initial run. The overall behaviour of the catalyst after regeneration shows that the catalyst possesses an acceptable level of stability under the present experimental conditions.

3.3.6. The effect of vanadium surface density

The effect of vanadium surface density (equivalent to vanadia loading) on initial rate of ethylbenzene conversion per V atom (extrapolated to zero residence time) at 673 K is shown in Fig. 3.8. The apparent turnover rate increases as the surface density increases and reaches a maximum at vanadium surface density of 6 V/nm^2. The rate decreases thereafter when the surface density increased to 13.4 V/nm^2.

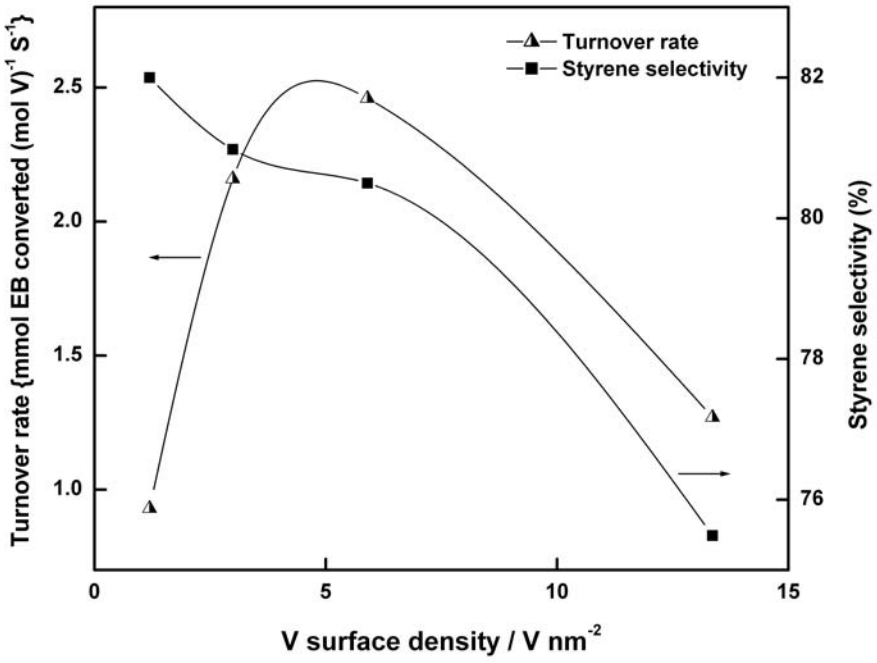

Figure 3.8: *Effect of VOx surface density on the initial rate of ethylbenzene conversion at 673 K normalized per V atom (?) and the selectivity of styrene extrapolated to zero conversion (!).*

The specific activity at 673 K, conversion of ethylbenzene per unit surface area of the catalysts, increased rapidly with increasing surface density up to about 6 V nm^{-2}, then only marginally increased with further increase in surface density (Fig. 3.9).

The variation in selectivities of various products with vanadium surface density at zero conversion of ethylbenzene is presented in Fig. 3.8. As the vanadium surface density increases, the selectivities of styrene and styrene oxide decrease. The selectivity of dealkylation products increases with increasing surface density (not shown in figure).

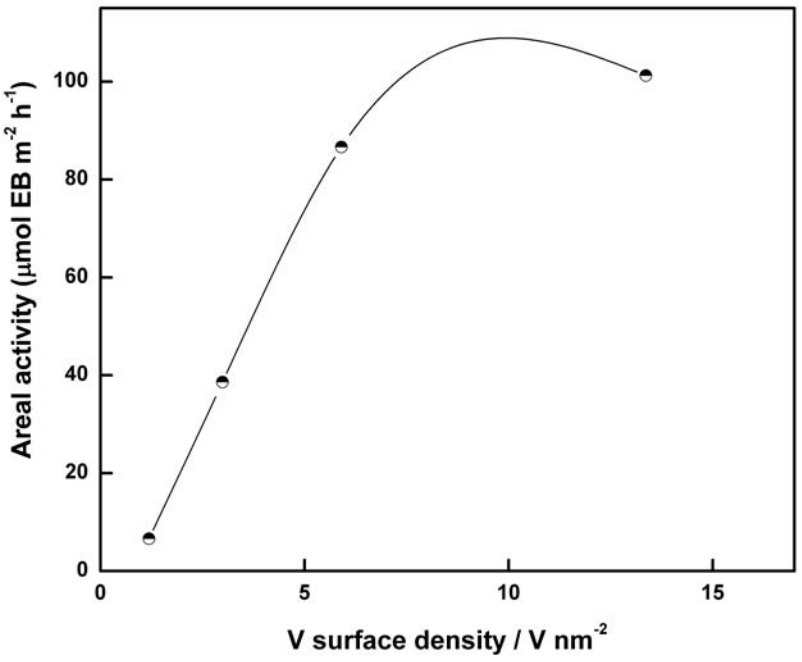

Figure 3.9: *Effect of VO_x surface density on the initial rate of ethylbenzene conversion at 673 K normalized per total surface area of the catalyst.*

3.3.7. The effect of calcination temperature of catalyst

The effect of calcination temperature on the activity and selectivity of the VO_x/Al_2O_3 catalyst is examined, considering 10 VO_x/Al_2O_3 calcined at different temperatures as an example. The reaction data is illustrated in Fig. 3.10. As the calcination

temperature increases, activity that is expressed in terms of styrene yield, decreases. This decrease is gradual for the catalysts calcined up to 923 K. However, the catalyst calcined at 1023 K shows a drastic decrease in activity. The selectivity behavior is not affected significantly with calcination temperature except at 1023 K, where slight increase in selectivity of dealkylation products observed. Figure 3.10 also shows that the styrene yield is lower when 10 VO_x/Al_2O_3 is calcined for a longer duration, i.e., 8 hours instead of 4 hours.

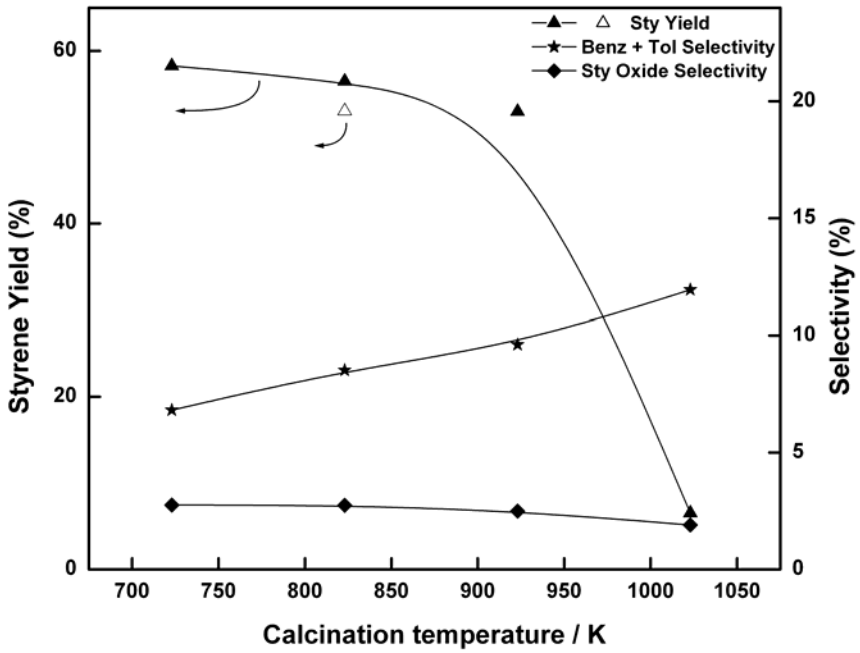

Fig. 3.10: *Effect of catalyst calcination temperature on the activity and selectivity of catalyst.*
Reaction conditions: Catalyst, 10 VO_x/Al_2O_3; Reaction temperature, 673 K; TOS, 3h; WHSV of EB, $1h^{-1}$; GHSV of N_2O, 1200 h^{-1}.

The activation energy of the reaction was determined from the plot of ln k versus reciprocal temperature in the range 623-698 K (Fig. 3.11) for 2 and 5 VO_x/Al_2O_3. The activation energy is found to be of the order of 50-52 kJ/mol under these conditions.

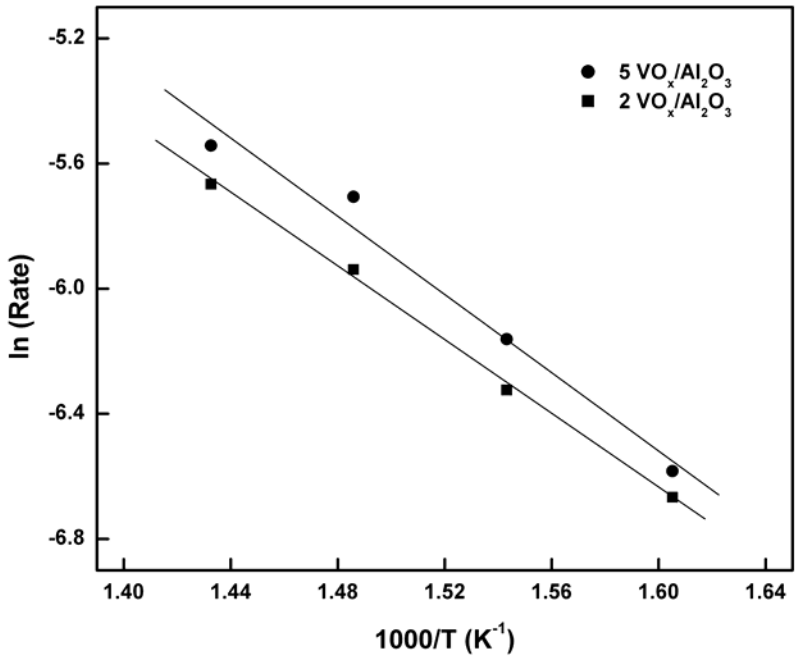

Fig. 3.11: *Plot of natural log of rate constant for the reaction at different temperatures versus the inverse of the absolute temperature for 2 and 5 VO_x/Al_2O_3 catalysts in the range 623-698 K.*

The catalytic activity studies show that the activity is higher at higher temperatures, higher contact time and intermediate flow rates of N_2O. The catalysts with vanadia loadings that correspond to near monolayer values are desirable and bulk vanadia phases are not desired. Higher calcination temperatures of catalyst lead to decrease in the activity. Hence the optimum conditions for maximum styrene yield can be summarized as: higher reaction temperature, higher contact time of ethylbenzene, GHSV of N_2O near 1200 h^{-1}, vanadia loadings corresponding to that of monolayer and catalyst calcination temperatures below 923 K.

SECTION B- CHARACTERIZATION OF SPENT CATALYSTS AND STRUCTURE-ACTIVITY CORRELATION

3.4. CHARACTERISATION OF SPENT CATALYSTS- OXIDATION ABILITY OF NITROUS OXIDE

The X-ray diffraction patterns of 20 VO_x/Al_2O_3 after dehydrogenation reaction at 673 K for 4 h in nitrogen and nitrous oxide atmospheres are shown in Fig. 3.12. After reaction in nitrous oxide atmosphere, catalyst still exhibits peaks characteristic of V_2O_5 and $AlVO_4$, though with reduced intensities, compared to that of fresh catalyst. However, the diffraction profile of the catalyst after reaction in nitrogen atmosphere was devoid of the peaks that correspond to these phases. This shows the catalyst structure is less affected when the reaction is carried out in nitrous oxide atmosphere.

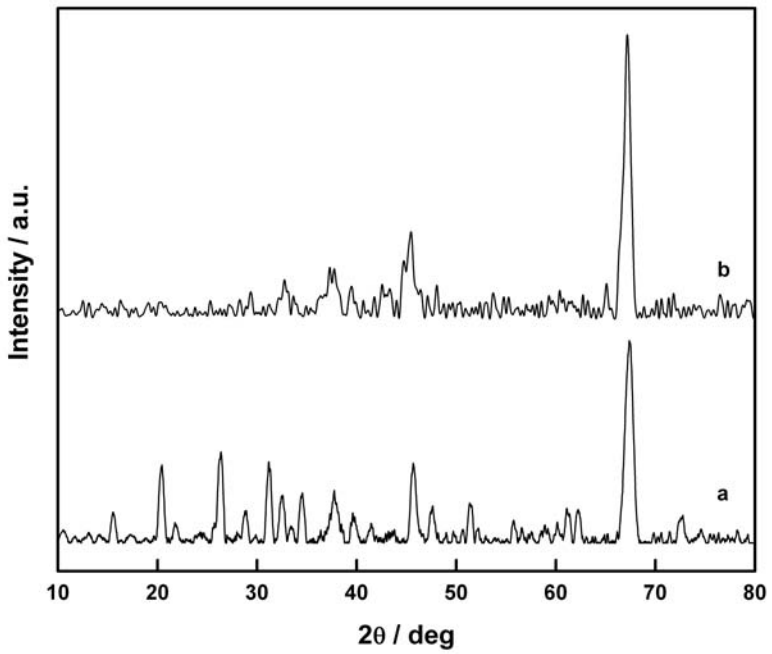

Fig. 3.12: *Powder X-ray diffraction patterns of 20 VO_x/Al_2O_3 after reaction at 673 K for 4 h* ***(a)*** *under N_2O flow* ***(b)*** *under N_2 flow.*

The FTIR spectra of 20 VO_x/Al_2O_3 recorded after dehydrogenation reaction in nitrogen and nitrous oxide atmospheres are shown in Fig. 3.13. The band at 1017 cm^{-1}, observed for the fresh catalyst, disappeared after the dehydrogenation reaction in N_2 atmosphere at 673 K. The band disappeared also when 20 VO_x/Al_2O_3 is treated in H_2 atmosphere at 673 K for 4 h. However, this band was still observed with reduced intensity for the 20 VO_x/Al_2O_3 catalyst used for the dehydrogenation reaction in N_2O atmosphere. This shows the presence of bulk-like vanadium pentoxide on the catalyst when the reaction is carried out in N_2O atmosphere as compared to N_2 atmosphere.

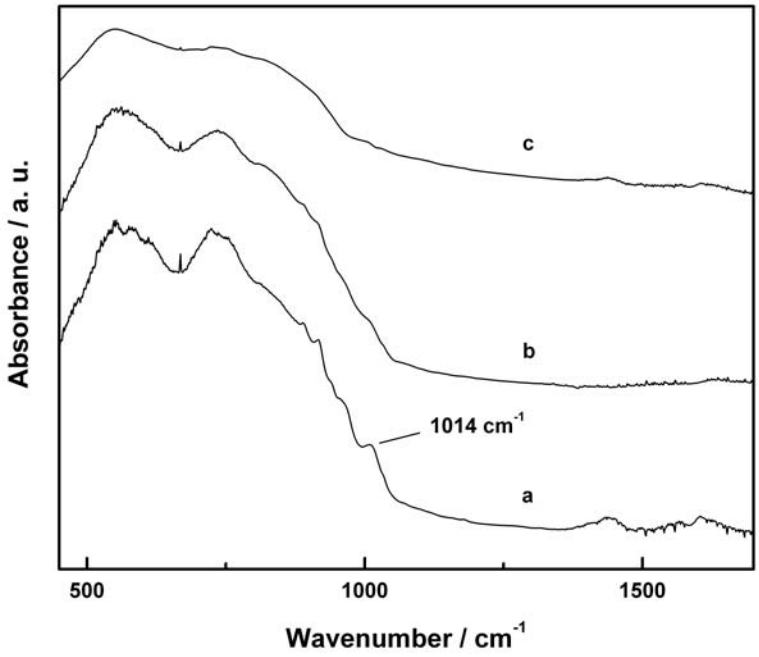

Figure 3.13: *FTIR spectra of 20 VO_x/Al_2O_3 after* ***(a)*** *dehydrogenation reaction under N_2O flow at 673 K for 4 h* ***(b)*** *dehydrogenation reaction under N_2 flow at 673 K for 4 h* ***(c)*** *after reduction with H_2 at 673 K for 4 h.*

Figure 3.14 shows the diffuse reflectance UV-visible spectra of catalyst 20 VO_x/Al_2O_3 after various treatments like reduction by H_2, dehydrogenation reactions in presence of N_2O and N_2. After reaction in N_2 atmosphere at 673 K for 4 h, the catalyst

showed a weak, broad band in the region 500-800 nm. This band can be assigned to forbidden d-d transitions of V^{4+} and / or V^{3+} since it is clearly developed for 20 VO_x/Al_2O_3 that was subjected to reduction under H_2 at 673 K for 4 h. The band disappeared when the reduced sample is treated with N_2O at 673 K for 4 h and exhibited a spectrum similar to that of fresh, calcined catalyst. The band is much more intense for the 20 VO_x/Al_2O_3 catalyst after dehydrogenation in N_2 atmosphere, compared to that used in N_2O atmosphere which again shows the ability of N_2O to keep the active species at higher oxidation state during the reaction (Fig. 3.14).

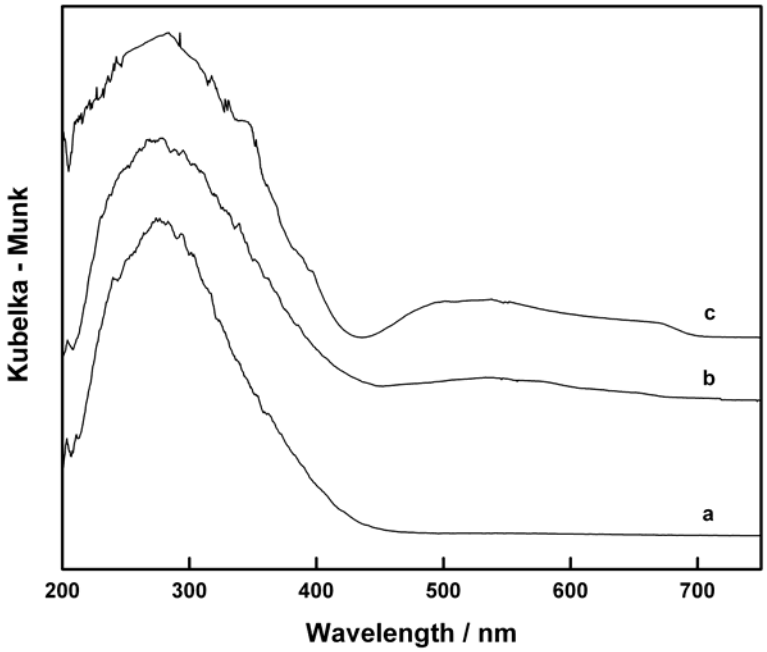

Figure 3.14: *Diffuse reflectance UV–visible spectra of 20 VO_x/Al_2O_3 after* ***(a)*** *dehydrogenation reaction under N_2O flow at 673 K for 4 h* ***(b)*** *dehydrogenation reaction under N_2 flow at 673 K for 4 h* ***(c)*** *after reduction with H_2 at 673 K for 4 h.*

The EPR spectra of 20 VO_x/Al_2O_3, recorded at room temperature, after oxidative dehydrogenation reaction in nitrous oxide and nitrogen atmospheres at 673 K for 4h, are given in Fig. 3.15, which is similar to that of fresh, calcined 20 VO_x/Al_2O_3 but with higher intensity indicating reduction of the catalyst during the reaction. The spectrum consists of, as described for the fresh catalyst, well-resolved lines which can be assigned to V^{4+} ($3d^1$) in an axially symmetric environment (VO^{2+} in C_{4v} environment). The g values and the hyperfine coupling constants of the V^{4+} signal from 20 VO_x/Al_2O_3 after reaction are g_{iso} = 1.968, $A_\perp$ = 50 G and $A_\parallel$ = 176 G. Similar spectra, without any additional signal, were also recorded at 77 K. The reduction is more for the catalyst used for the reaction in nitrogen flow, as can be observed from a comparison of the intensities of the spectra. The hyperfine structure is superimposed on a broad isotropic singlet produced by the dipolar interactions of weakly interacting (or associated) VO^{2+} species [1,2], which is also observed to be more intense with the catalyst used for reaction in nitrogen atmosphere.

The EPR spectra obtained in the present work are similar to those previously reported for Al_2O_3-supported vanadium oxide catalysts. The g values and the hyperfine coupling constants of the V^{4+} signal obtained by Blasco *et al* [1] for VO_x/Al_2O_3 catalysts after the catalytic test in the ODH of ethane are $g_\perp$ = 1.965 (±0.005), $g_\parallel$ = 1.947 (±0.005), $A_\perp$ = 78 G (±3 G) and $A_\parallel$ = 190 (±3 G). Eon *et al* [3] recorded the ESR spectra of VO_x/Al_2O_3 catalysts after the ODH of propane and obtained a signal with spectral parameters ($g_\perp$ = 1.982, $g_\parallel$ = 1.919, $A_\perp$ = 70 G, and $A_\parallel$ = 190 G), which was attributed to an amorphous surface vanadium oxide phase.

It is also clear from the EPR spectra that a strong signal is superimposed on the spectrum of V^{4+} which is not observed for the fresh, calcined catalyst. This may be originated from the paramagnetic centers of the carbon deposited on the catalyst during the reaction. Since this signal is very intense for the catalyst used for the dehydrogenation reaction in nitrogen, it can be inferred that the deposition of coke is more for this catalyst compared to that used for the reaction in nitrous oxide.

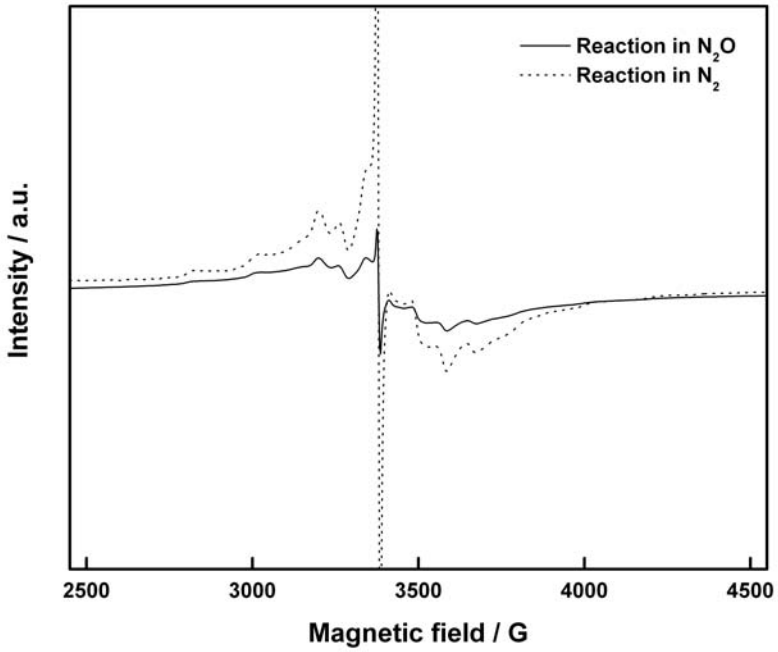

Fig. 3.15: *EPR spectra of 20 VO_x/Al_2O_3, measured at 298 K, after dehydrogenation reaction in presence of nitrous oxide (solid line) and nitrogen (dotted line). The reactions were performed at 673 K for 4h.*

3.5. ACTIVITY AND STRUCTURE OF THE CATALYSTS- DISCUSSION

As described in the Chapter 2, the structure of dispersed VO_x species on Al_2O_3 support depends on the VO_x surface density. At the lowest surface density, 1.2 V nm^{-2} (2 VO_x/Al_2O_3), vanadia exists as monomeric V^{5+} species with tetrahedral coordination and with increasing surface density, the fraction of polymeric V^{5+} species increases. Bulk-like crystallites of vanadia and aluminum orthovanadate appear at a surface density of 13.4 V nm^{-2}.

The relationship observed between the turn-over rate and vanadium surface density (Fig. 3.8) can be explained based on the degree of polymerization of vanadium species. Activity for the catalyst with the surface density of 1.2 V nm^{-2} is the lowest since the monomeric vanadia species, predominant on this catalyst, are less active than the

polymeric V^{5+} species since the course of the reaction involves the oxidation-reduction cycles of V^{5+} species and V-O-Al species appear to be more difficult to reduce than V-O-V or V=O sites in polymeric species. This conclusion is also supported by the fact that reducibility of the samples increases with increase in vanadia loading from 2 to 10 wt% as evidenced by the shift in T_{max} to lower temperatures in TPR experiments (Fig. 2.9). The activity decreases again when multilayers of polymerized V^{5+} species are formed on the surface, at higher surface densities (13.4 V nm^{-2}), which prevents the accessibility of the reactants to all the vanadium atoms. Hence the maximum turnover rate is observed at intermediate surface densities corresponding to the formation of a vanadia monolayer on the surface of the support. The observation that areal rate increases rapidly till 6 V nm^{-2} and thereafter only marginally (Fig. 3.9), confirms the occurrence of multilayers or crystallites of vanadia above this surface density in which most of the vanadium atoms are inaccessible by the reactant molecules. The decrease in activity with increasing calcination temperature of the catalyst and the very low activity by 10 VO_x/Al_2O_3, calcined at 1023 K (Fig. 3.10), confirm that bulk phases are less active than dispersed vanadia phases.

The observation of a maximum in activity at intermediate surface density was reported previously for the ODH of ethane and propane over vanadia catalysts supported on MgO [4-6], Al_2O_3 and ZrO_2 [7-9] and is attributed to the structure of the VO_x overlayer [8,9]. The observed dependence of selectivities of the products on the surface density (Fig. 10) reveals that monomeric V^{5+} species are better suited for the dehydrogenation of ethylbenzene since the maximum selectivity for styrene is observed at the lowest surface density studied (1.2 V nm^{-2}). The bulk-like vanadia crystallites present at a surface density of 13.4 V nm^{-2} cause dealkylation of ethylbenzene resulting in an increase in the formation of benzene and toluene. This seems the case for the catalysts calcined at higher temperatures, which give more dealkylation products. A priori, it seems that bulk phases cause higher cracking than dispersed phase.

The effect of N_2O in the dehydrogenation reaction is significant as is evident from the higher styrene yield observed in N_2O compared to that in N_2 atmosphere. The vanadium species is continuously reduced during the reaction in N_2 while it is kept at a higher oxidation state when the reaction is carried out under N_2O atmosphere as evidenced

from the results of characterization of spent catalysts by X-ray diffraction, infra-red, UV-visible and EPR spectroscopies (Fig. 3.12-3.15) in comparison with fresh catalysts as discussed previously. The enhancement in the specific activity in presence of N_2O is similar to the effect of CO_2 on dehydrogenation reaction of EB reported by Sakurai *et al* [10]. This was termed as the promoting effect of CO_2 by these authors and is ascribed to the ability of CO_2 to oxidize the reduced species during reaction that helps to keep it in a higher oxidation state. They observed an increase in styrene yield with an increase in the loading level of vanadium from 0 to 1.0 mmol/g of MgO but further increases in the loading level did not increase the styrene yield. According to Sakurai *et al* [10], at low loadings only isolated VO_4 species were dispersed over MgO support, whereas at a loading of 3 mmol/g of MgO, polymeric V^{5+} species with bridging V-O-V oxide ions forming MgV_2O_6 and $Mg_2V_2O_7$ structures was proposed to co-exist, hence the degree of polymerization of vanadate species increases with loading level, leading to the increase in styrene yield concurrently.

The vanadium surface density required for a theoretical polyvanadate monolayer can be calculated as approximately 7 V nm^{-2} for the present system of catalysts. Below this surface density (vanadia loading 2-10 wt%), it is observed that turn-over rates increase with increasing surface density (Fig. 3.8) while UV-visible absorption edge energies decrease (Table 2.6), that is, there is an inverse relationship between the turn-over rates and edge energies. This correlation observed between the turnover rates and UV-visible absorption edge energies, within monolayer coverage is similar to that reported previously for small alkanes over two dimensional transition metal oxides like VO_x, MoO_x and WO_x dispersed over Al_2O_3, ZrO_2 and MgO [11]. For ODH of propane, the turnover rates were found to increase in parallel with a decrease in the UV-visible absorption edge energies and is explained based on the activation energy for the dissociation of first methylene C-H bond which is the rate determining step. The similarity in the relationship between turn-over rate and absorption edge energy suggests that C-H bond dissociation of ethylbenzene proceeds via transition states requiring electron transfer from oxygen atoms to vanadium centers and the energy needed for this decides both the energy for C-H bond activation of ethylbenzene, which determines the turnover rate, and the energy at which absorption

occurs in the UV-visible spectrum. The increase in the turnover rates with increasing surface density is accounted by the fact that these electronic transitions require lower energies because of increase in oxide domain size as the surface density increases. The accommodation of transition state and the products in the rate-determining step requires two vanadium atoms which explains, along with the low reducibility of V-O-Al species mentioned earlier, the low turnover rates observed for catalysts with low vanadia loadings having monomeric vanadium (V) as the predominant species (Fig. 3.8).

3.6. SUMMARY

The catalytic properties of VO_x/Al_2O_3 catalysts with different vanadia loadings were evaluated for the oxidative dehydrogenation of EB in the presence of N_2O. Structural characterization of these catalysts shows that isolated monovanadate species is predominant at vanadia loadings below 5 wt%. With increasing vanadia loading, formation of polyvanadate species occurs and at vanadia loading of 20 wt%, V_2O_5 domains are observed. The rate of ethylbenzene conversion per V atom found to increase with vanadia loading, reaches a maximum at 10 wt% and decreases when the loading is increased to 20 wt%. Results of the structural characterization indicate that the most active form of the catalyst is one that in which the surface of Al_2O_3 support is covered by two dimensional polyvanadate species. The formation of bulk-like V_2O_5 on the surface at high loadings leads to the decrease in activity due to the inaccessibility of a large fraction of V atoms that lie below the catalyst surface. The styrene yield was much higher in the presence of N_2O than in N_2 atmosphere, since the surface vanadium species are kept in a high oxidation state during the dehydrogenation reaction by N_2O. Within the monolayer coverage of VO_x, the turnover rates for ethylbenzene increase in parallel with a decrease in the UV-Visible absorption edge energies. This suggests that the stability of the activated complexes in C-H bond dissociation steps depends sensitively on the ability of the active oxide domains to transfer electrons from lattice oxygen atoms to metal centers as proposed in the case of ODH of propane.

SECTION C- PREFERENTIAL OXIDATION OF CO IN THE PRESENCE OF H_2 AND CO_2

3.7. INTRODUCTION

This section describes the results of studies of preferential oxidation of CO in presence of excess hydrogen (PROX) using VO_x/Al_2O_3 catalysts. The general introduction about this reaction is given in Chapter 1. The activity of the catalysts is correlated with their structure, which is determined by various characterization techniques as described in Chapter 2.

3.8. EXPERIMENTAL

The reaction of selective oxidation of CO in excess hydrogen was carried out in a fixed-bed continuous flow quartz reactor (8 mm I.D.) at temperatures of 373-548 K under atmospheric pressure. Catalyst (0.5 c.c.), pelletized, crushed and sieved in the 10-20 mesh range was used for each experiment. Figure 3.16 is a diagram of the reactor setup. The catalyst bed was held in place with quartz-wool plugs. The reaction temperature was measured with a thermocouple located at the end of the catalyst bed in the reactor. Another thermocouple, which was placed inside the furnace, was used to control the reaction temperature.

A standard gas mixture with the composition 0.49% CO, 23.26% CO_2, 74.17% H_2 and 2.08% CH_4 was used as the feed and its flow rate was set and controlled by a mass flow controller (Hi-Tech, Bronkhorst, The Netherlands). Required O_2, in the form of air, controlled through mass flow controller (Matheson, USA) was pre-mixed with the feed gas in a pre-heater zone. The inlet and outlet gas mixtures were analyzed on-line by a gas chromatograph (Chemito 1000) using Spherocarb column (mesh size 80/100, 8', 1/8" dia), TCD detector and a methanizer. An online CO analyzer (Fuji Electric, Japan) that can measure CO down to 0.1 ppm was also used for measuring CO concentration at the outlet of PROX reactor. The activity was evaluated on the basis of CO and O_2 conversions, which can be determined from CO and O_2 concentrations after the catalyst bed, respectively. The

selectivity of CO oxidation is defined as the ratio of O_2 consumed for the CO oxidation to the total O_2 consumed, as the oxygen is consumed for H_2 oxidation also.

The conversions of CO (X_{CO}) and O_2 (X_{O2}) and the selectivity of CO oxidation (S_{CO}) were calculated using the following formulas:

$$X_{CO}\,(\%) = ([CO]_{in}\text{-}[CO]_{out}/[CO]_{in})\times 100 \quad (3.7)$$

$$X_{H2}\,(\%) = ([H_2]_{in}\text{-}[H_2]_{out}/[H_2]_{in})\times 100 \quad (3.8)$$

$$X_{O2}\,(\%) = ([O_2]_{in}\text{-}[O_2]_{out}/[O_2]_{in})\times 100 \quad (3.9)$$

$$S_{CO}\,(\%) = \{0.5([CO]_{in}\text{-}[CO]_{out})/([O_2]_{in}\text{-}[O_2]_{out})\}\times 100 \quad (3.10)$$

where $[CO]_{in}$, $[H_2]_{in}$ and $[O_2]_{in}$ are the inlet concentrations, $[CO]_{out}$, $[H_2]_{out}$ and $[O_2]_{out}$ are the outlet concentrations.

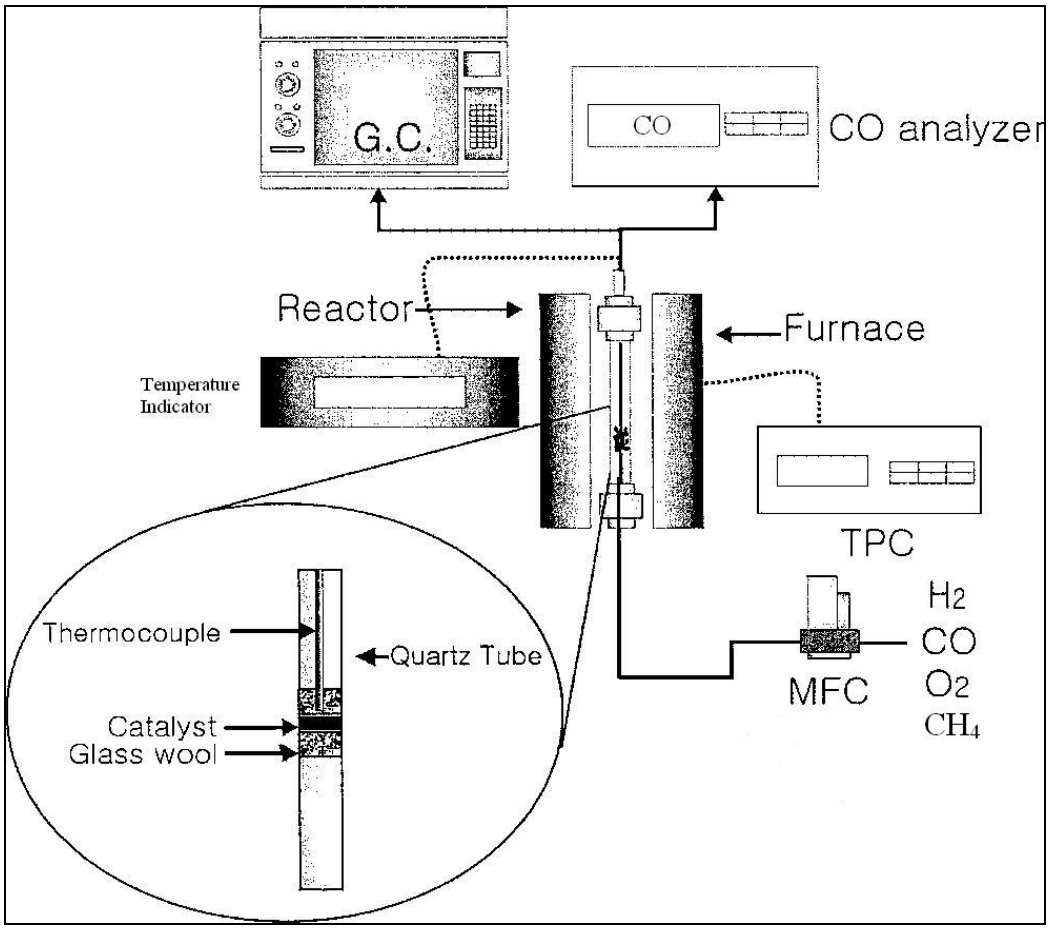

Fig. 3.16: *Experimental setup for the preferential oxidation of CO in presence of H_2. G.C.: Gas Chromatograph, TPC: Temperature Programmer Controller, MFC: Mass Flow Controller.*

3.9. CATALYTIC ACTIVITY STUDIES

3.9.1. Catalyst activity and selectivity as functions of reaction temperature and vanadia loading

The effect of V content on the PROX was examined as a function of temperature at a GHSV of 5000 with the gas stream of composition 0.49% CO, 0.49% O_2, 23.26% CO_2, 74.17% H_2 and 2.08% CH_4. Figure 3.17 shows the conversion of CO as well as the selectivity for CO oxidation reaction as a function of temperature over the VO_x/Al_2O_3 catalyst with different vanadia loadings. All catalysts exhibit a maximum in CO conversion and CO oxidation selectivity. The variation in CO oxidation selectivities with vanadia loading is better pronounced at low temperatures, at higher temperatures, catalysts exhibit similar levels of selectivity. No scattering was seen in the performance of catalysts, independent of operating conditions, indicating that catalysts were very stable in the temperature range and the duration examined.

The rate of the reaction is calculated by using the equation [12]:

$$\text{Rate} = FX/\nu W \tag{3.11}$$

where F is the inlet molar flow rate of the particular gas, X is the fractional conversion of the gas at a particular temperature, ν is the stoichiometric coefficient of the gas and W is the weight of the catalyst. The rates of oxidation of H_2 and rate of consumption of oxygen as functions of vanadia loading and reaction temperature are given in Fig. 3.18.

It can be seen that the rate of O_2 consumption increased continuously with increasing temperature. The oxidation of H_2 showed a steady rate at lower temperatures but increased sharply after around 498 K. CO conversion also increases with increasing reaction temperature, but reaches a maximum at 498 K. For temperatures above 498 K, all catalysts show a reduction in CO conversion and selectivity, although O_2 conversion remained high. This indicates that either a larger fraction of O_2 is being consumed for H_2 oxidation at higher temperatures or CO is re-generated through reverse water gas shift reaction ($CO_2 + H_2 \Leftrightarrow CO + H_2O$). However, the former is more probable. Hence, the decrease of CO conversion above 498 K is a consequence of the loss of selectivity since the amount of O_2 available for CO oxidation is determined by the amount of O_2 consumed

for the simultaneously occurring H_2 oxidation reaction. The general trend of exhibiting a maximum in CO conversion and selectivity with increasing reaction temperature is also observed in previous studies of selective CO oxidation [13].

The observed loss of selectivity of CO oxidation at high temperatures can be explained based on the relative coverage by CO on the surface. When a mixture of CO and H_2 is subjected to oxidation, CO competes with H_2 for O_2 in the reaction. The continuous decrease in selectivity at higher temperature indicates higher activation energy for the H_2 oxidation than for the CO oxidation [14]. It can be assumed that at lower temperatures, CO covers the metal surface and inhibits the hydrogen oxidation. In an adsorption study of CO on a Pt catalyst using FT-IR [15], full coverage of CO was observed at temperatures below 200 ^{0}C for 0.01% CO mixture and 300 ^{0}C for 1% CO. With increasing temperature, CO was partially desorbed and the degree of CO coverage decreased. The partial coverage allows the hydrogen oxidation to proceed much faster than the CO oxidation, resulting in decreased selectivity with increasing temperature, as can be seen in Fig. 3.17 b. The variation of selectivity in the low temperature region, which shows a steady increase initially, followed by a maximum, is in agreement with the studies of Watanabe *et al* [16] and Kahlich *et al* [17]. This trend can be explained, as proposed by Kahlich *et al* [17], based on the assumption that H_2 and CO are co-adsorbed on the surface so that the selectivity for CO oxidation should be inversely proportional to θ_H/θ_{CO}. The lower adsorption energy of hydrogen compared to CO, leads to a reduction of the (small) hydrogen surface coverage with increasing temperature, while θ_{CO} remains close to saturation. This leads to a decrease in θ_H/θ_{CO}, which is equivalent with an increase of the selectivity of CO oxidation.

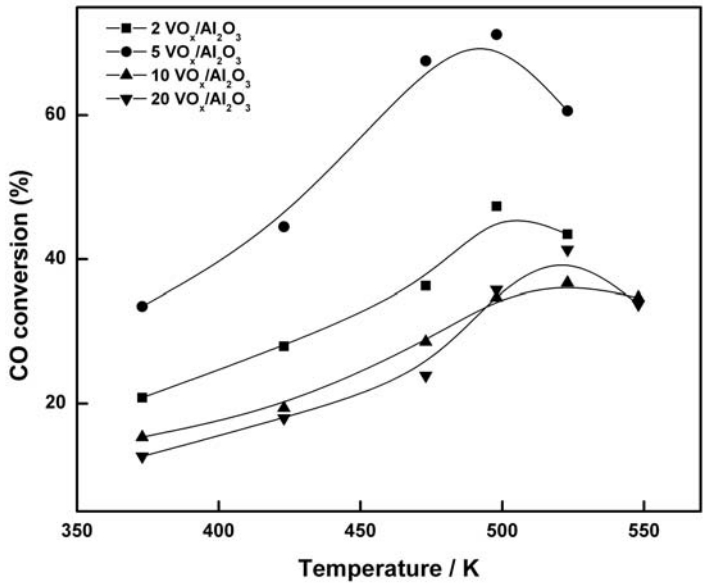

(a)

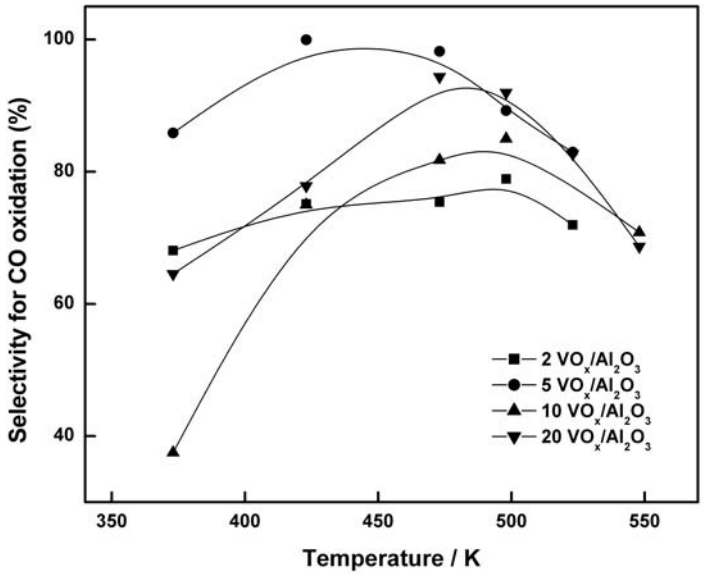

(b)

Fig. 3.17: *Dependence of CO conversion* ***(a)*** *and CO oxidation selectivity* ***(b)*** *on reaction temperature at different vanadia loadings.*
Reaction conditions: GHSV, 5000 h^{-1}; Feed composition, 0.49% CO, 0.49% O_2, 23.26% CO_2, 74.17% H_2 and 2.08% CH_4; O_2/CO, 1 (mol/mol).

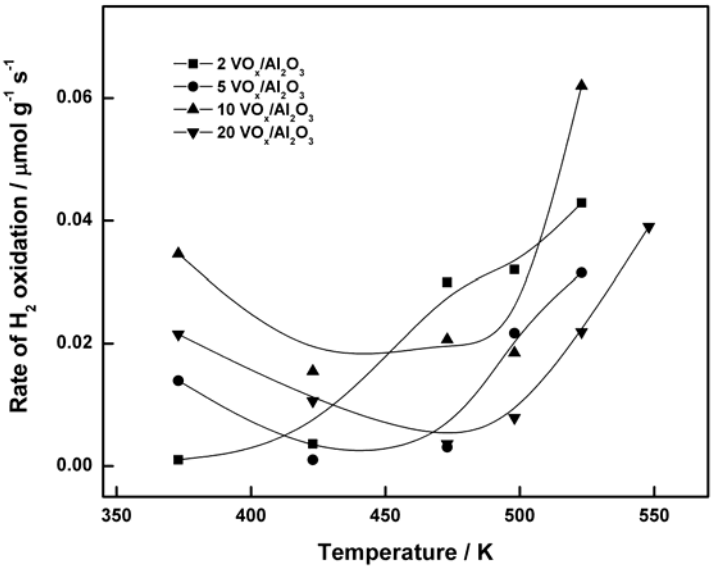

(a)

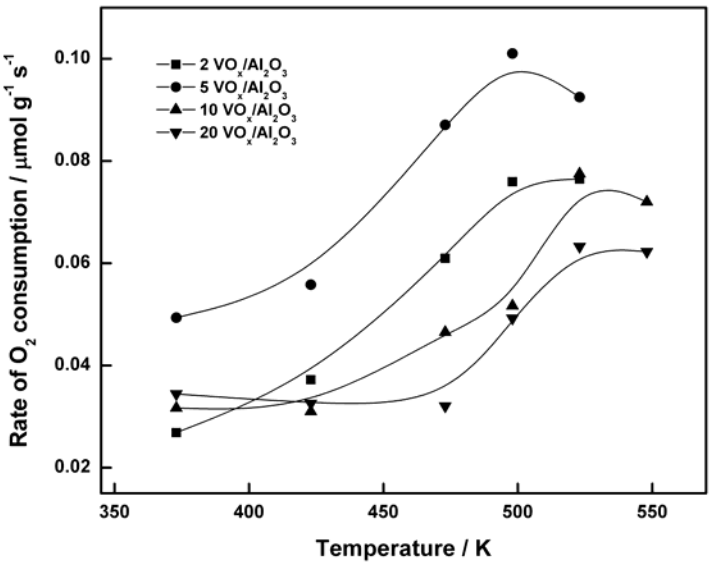

(b)

Fig. 3.18: *Rate of H_2 oxidation* ***(a)*** *and O_2 consumption* ***(b)*** *as a function of reaction temperature at different vanadia loadings.*
Reaction conditions: GHSV, 5000 h^{-1}; Feed composition, 0.49% CO, 0.49% O_2, 23.26% CO_2, 74.17% H_2 and 2.08% CH_4; O_2/CO, 1 (mol/mol).

3.9.2. CO oxidation with varying O_2 concentration

The results of the reaction between CO and O_2 with varying O_2 concentration in the feed are presented in Fig. 3.19. The reaction was conducted at 498 K at GHSV = 5000 h^{-1} over 5 VO_x/Al_2O_3 catalyst using a feed containing 74.17% H_2, 0.49% CO and 23.26% CO_2. Conversion of CO increased with increase in O_2/CO mole ratio from 0.5 to 1 and reached a plateau with further increase of mole ratio beyond 1. The selectivity for CO oxidation remains high at these reaction conditions and is not affected significantly with mole ratio.

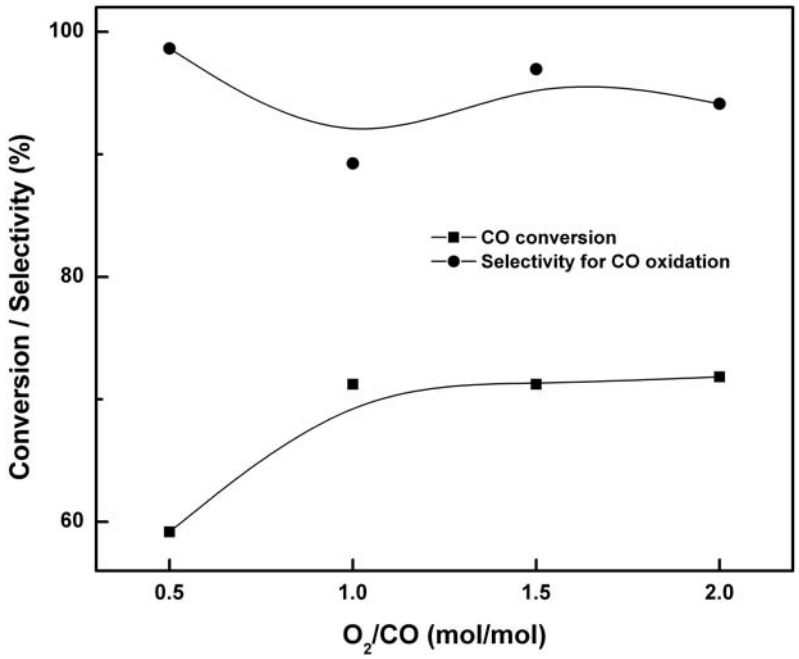

Fig. 3.19: *Conversion of CO and selectivity for CO oxidation as a function of molar ratio of O_2 and CO.*
Reaction conditions: Catalyst, 5 VO_x/Al_2O_3; Temperature, 498 K; GHSV, 5000 h^{-1}.

3.9.3. CO oxidation with varying space velocity

It is important for a PEFC fuel processor to exhibit high CO conversion and CO oxidation selectivity over a wide range of contact time (1/SV where SV is the space

velocity). Fig. 3.20 shows dependency of the performance of 5 VO_x/Al_2O_3 on the space velocity. The CO conversion decreases with increasing space velocity (shorter contact time), reflecting the low catalytic activity for the CO oxidation even at 498 K, although the CO oxidation selectivity was changed only slightly in the GHSV range 5000 to 20000 h^{-1}. The conversion of O_2 also decreases with increasing space velocity, indicating that the drop in activity is due to shorter contact times. Kim *et al* [13] observed that below 300 ^{0}C, the CO conversion decreased with the increasing total flow rate while the selectivity was more or less constant in the range 3000-12,000 ml/h over Pt/Al_2O_3 catalysts.

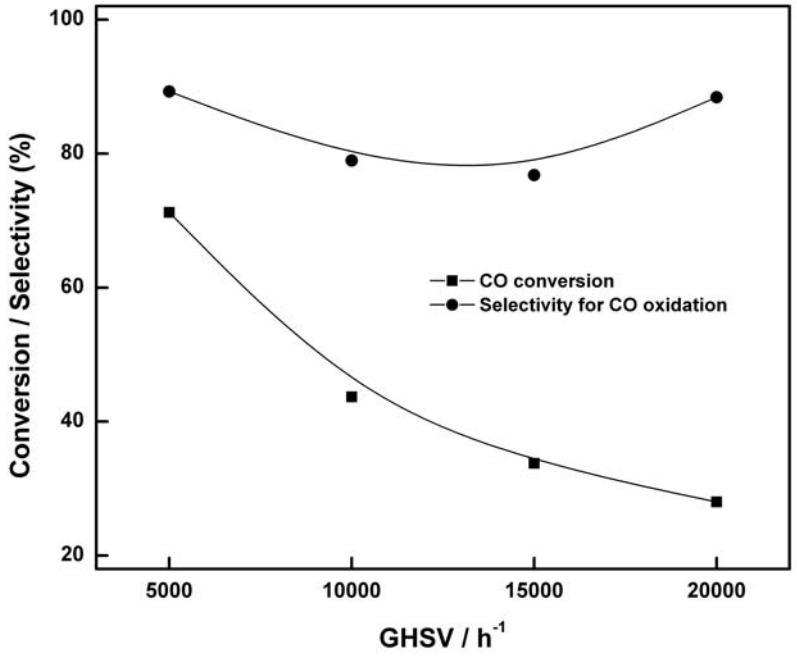

Fig. 3.20: *Conversion of CO and selectivity for CO oxidation as a function of space velocity.*
Reaction conditions: Catalyst, 5 VO_x/Al_2O_3; Temperature, 498 K; O_2/CO, 1 (mol/mol).

3.9.4. The catalyst structure and activity

The turnover frequencies (TOF) of CO oxidation, expressed in inverse seconds, at different temperatures have been calculated which are shown in Fig. 3.21 for different

vanadia loadings. TOF values are highest for 2 VO_x/Al_2O_3 catalyst in the entire temperature range studied and at any particular temperature, TOF is inversely proportional to the vanadia loading.

The structural characterization of VO_x/Al_2O_3 catalysts, as discussed in Chapter 2, indicate that monovanadates are predominant for 2 VO_x/Al_2O_3 and polymerization of vanadia species increases with increasing vanadia loading. At higher vanadia loadings, the fraction of polyvanadate species is higher at the expense of monovanadate species. After 7 V/nm^2, which corresponds to roughly 10 wt% vanadia loading, formation of multilayers of vanadia occurs. The decrease in activity per V atom with increasing surface density (or vanadia loading) indicates that isolated vanadium sites favor CO oxidation reaction. Polyvanadates and vanadia aggregates are intrinsically less active than isolated vanadium species.

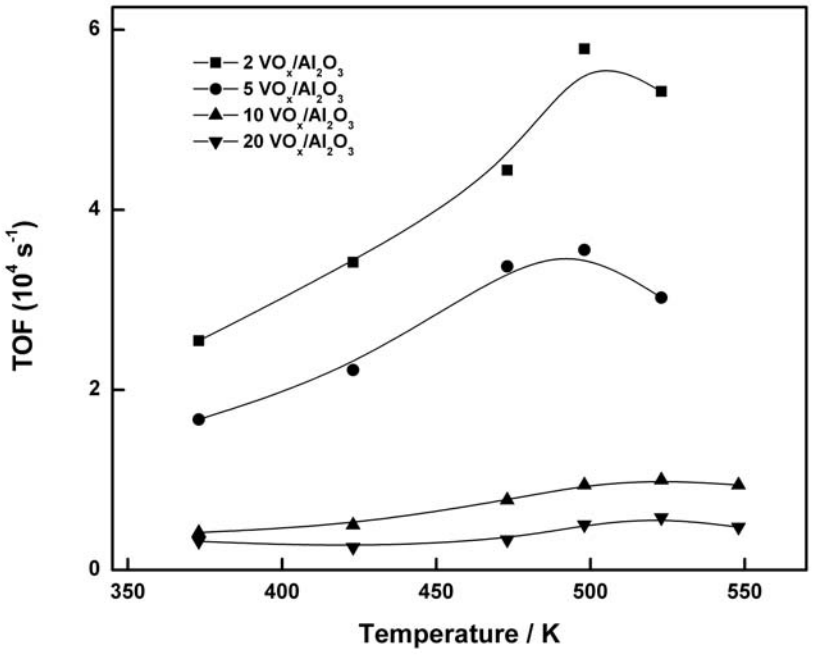

Fig. 3.21: *Turnover frequencies of CO oxidation as a function of reaction temperature at different vanadia loadings.*

The apparent activation energy (E_a) for CO oxidation reaction, calculated from Arrhenius plots of ln (rate) vs. 1/T, over these catalysts range from 28 to 36 kJ/mol. These were obtained from the best fit (r^2>0.95) values of linear regression of low temperature data. In the literature, values of E_a reported for this reaction are 31.2 kJ mol^{-1} over Pt/CeO_2 and 53.9 kJ mol^{-1} for Pt/Al_2O_3 [18]. An apparent activation energy of 31 kJ mol^{-1} is reported over Au/α-Fe_2O_3 [19] for oxidation of CO in simulated reformer gas (low partial pressures of CO and O_2, 75 kPa H_2, balance N_2).

3.9.5. Summary of section C

The preferential oxidation reaction of CO in presence of excess of H_2 is studied using VO_x/Al_2O_3 catalysts. The activity and selectivity for CO oxidation increases with temperature and exhibit a maximum around 498 K. Activity increases with increasing O_2/CO ratio till 1 and thereafter remains more or less similar. An increase in space velocity decreases activity. Turnover frequencies for CO oxidation decrease with increasing vanadia loading. This indicates that higher amounts of polymeric species do not favor the activity of catalyst. Polymerization of vanadia species is higher at higher loadings, as revealed by structural characterization discussed in Chapter 2. The results show that VO_x/Al_2O_3 catalysts are promising for PROX reaction, being active and selective for CO oxidation.

3.10. REFERENCES

[1] T. Blasco, A. Galli, J. M. Lopez Nieto, F. Trifiro, J. Catal., 169 (1997) 203.

[2] E. V. Kondratenko, M. Baerns, Appl. Catal. A, 222 (2001) 133.

[3] J. G. Eon, R. Olier, J. C. Volta, J. Catal. 145 (1994) 318.

[4] C. Pak, A. T. Bell, T. Don Tilley, J. Catal., 206 (2002) 49.

[5] D. Siew Hew Sam, V. Soenen , J. C. Volta, J. Catal., 123 (1990) 417.

[6] P. M. Michalakos, M. C. Kung, H. H. Kung, J. Catal., 140 (1993) 226.

[7] M. D. Argyle, K. Chen, A. T. Bell, E. Iglesia., J. Catal., 208 (2002) 139.

[8] A. Khodakov, J. Yang, S. Su, E. Iglesia, A. T. Bell, J. Catal., 177 (1998) 343.

[9] A. Khodakov, B. Olthof, A. T. Bell, E. Iglesia, J. Catal., 181 (1999) 205.

[10] Y. Sakurai, T. Suzaki, K. Nakagawa, N. Ikenaga, H. Aota, T. Suzuki, J. Catal., 209 (2002) 16.

[11] K. Chen, A. T. Bell, E. Iglesia, J. Catal., 209 (2002) 35.

[12] J. C. Summers, S. A. Ausen, J. Catal. 58 (1979) 131.

[13] D. H. Kim, M. S. Lim, Appl. Catal. A: General, 224 (2002) 27.

[14] A. Luengnaruemitchai, S. Osuwan, E. Gulari, Int. J. Hydrogen Energy, 29 (2004) 429.

[15] O. Dulaurent, D. Bianchi, Appl. Catal. A 196 (2000) 271.

[16] M. Watanabe, H. Uchida, K. Ohkubo, H. Igarashi, Appl. Catal. B: Environmental 46 (2003) 595.

[17] M. J. Kahlich, H. A. Steiger, R. J. Behm, J. Catal. 171 (1997) 93.

[18] P. Bera, K. C. Patil, V. Jayaram, G. N. Subbanna, M. S. Hegde, J. Catal. 196 (2000) 293.

[19] M. J. Kahlich, H. A. Gasteiger, R. J. Behm, J. Catal. 182 (1999) 430.

CHAPTER 4
Preparation And Characterization Of V-Mg-O Catalysts

4.1. INTRODUCTION

In this chapter, the preparation and characterization of V-Mg-O catalysts are described. The catalysts were prepared by aqueous impregnation method and characterized by various physico-chemical techniques such as X-ray diffractometry, ICP-AES, infrared spectroscopy, surface area by nitrogen physisorption, SEM, TG-DTA, TPR, EPR, NMR etc.

4.2. CATALYST PREPARATION

MgO support was prepared by thermal decomposition of magnesium oxalate, according to a reported procedure [1]. MgC_2O_4 was precipitated from a magnesium nitrate (Merck, India, GR grade) solution with oxalic acid (s. d. fine-chem ltd., LR grade) of the same concentration (2 M) and heated at 343 K. the pH of the solution was kept at 7.0 by the addition of required amount of NH_4OH. The precipitate was filtered off and washed several times with distilled water. The precipitate was dried at 383 K and calcined in air at 773 K for 8h to decompose MgC_2O_4 to MgO. Vanadia catalysts supported on MgO were prepared by impregnating MgO with NH_4VO_3 (s. d. fine-chem ltd., AR grade) dissolved in an aqueous solution of oxalic acid in 1:2 weight ratio at a pH of ~ 1.9. After impregnation, the samples were dried in air at 383 K for 12 h and calcined in air at 823 K for 4 h. The catalysts are represented by n V-Mg-O throughout the thesis where 'n' represents vanadia loading in weight percent.

4.3. CATALYST CHARACTERIZATION

The vanadium content, determined by ICP-AES, BET surface area and VO_x surface density of the V-Mg-O catalysts, calcined at 823 K, are presented in Table 4.1. The BET surface area of the prepared MgO support was 109 m^2/g and the surface area decreased with increasing vanadia loading. The apparent surface density of VO_x, assuming all of the vanadium is exposed on the surface, increases from 1.02 to 29.25 VO_x/nm^2 (Table 4.1).

4.3.1. X-ray Diffractometry

The XRD patterns of the V-Mg-O catalysts after calcination at 823 K are shown in Fig. 4.1 as a function of vanadia loading. The patterns show intense peaks centered at 43 and 62^0 which correspond to the (200) and (220) diffraction lines of MgO (JCPDS 4-829). No vanadium containing phases were detectable for catalysts with vanadia loading from 2 to 20 wt%, thus indicating a high dispersion of vanadium or a very small crystallite size at these loadings. When the loading was increased to 30 wt%, peaks at about $2\theta = 35^0$ characteristic of magnesium orthovanadate, $Mg_3(VO_4)_2$ (JCPDS 37-351), were clearly developed in the XRD pattern. The major peaks of this phase correspond to d values, 2.55, 3.03, 2.49, 3.29, 2.08 and 2.86 Å in the order of decreasing intensity. The intensity of the most intense peak of $Mg_3(VO_4)_2$ is approximately equal to that of (200) peak of MgO indicating the formation of well-crystallized orthovanadate phase. The peaks attributable to V_2O_5 were not detected at any of the vanadia loadings.

Table 4.1: Characteristics of magnesia support and supported vanadia catalysts

Sample	V content (ICP, wt%)	Surface area ($m^2 g^{-1}$)*	VO_x surface density ($V nm^{-2}$)*	Particle size (nm)	
				823 (K)**	923 (K)**
MgO	0	109	0	-	-
2 V-Mg-O	1.39	161	1.02	10.87	n.d.
5 V-Mg-O	2.69	147	2.16	10.88	14.51
10 V-Mg-O	6.07	117	6.13	11.46	12.93
20 V-Mg-O	8.21	94	10.33	11.35	11.90
30 V-Mg-O	15.09	61	29.25	10.33	13.17

**Calcination temperature is 823 K*
***Calcination temperature of V-Mg-O catalysts*

Figure 4.2 shows X-ray diffraction patterns of V-Mg-O catalysts calcined at 923 K. Peaks characteristic of orthovanadate phase were observable with 20 V-Mg-O itself at this calcination temperature, indicating the formation of the same depends on the calcination temperature also. The calcination of 30 V-Mg-O at 923 K enhances the formation of orthovanadate phase, as revealed by the intensities of diffraction peaks.

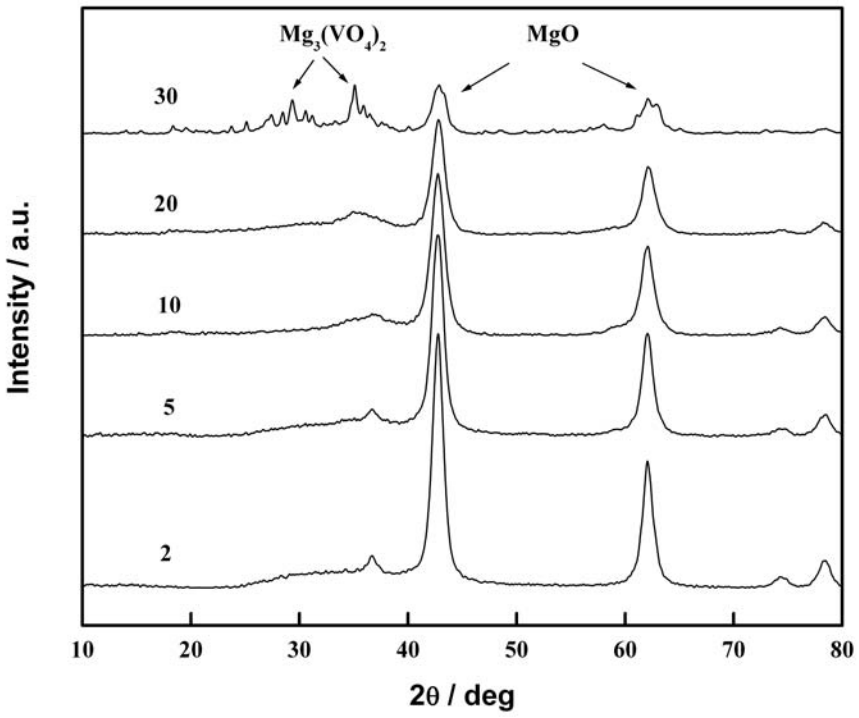

Fig. 4.1: *Powder X-ray diffraction patterns of V-Mg-O catalysts, calcined at 823 K, as a function of vanadia loading in wt%. Only the major peaks are marked in the figure.*

The volume averaged particle sizes corresponding to different catalysts were calculated using Debye-Scherrer equation considering the most intense peak of MgO (*d*=2.11). This peak was fitted with Gaussian function for each catalyst from which the values of full width at half maximum (FWHM) were determined. The particle sizes are around 10-15 nm for V-Mg-O catalysts calcined at 823 and 923 K and don't vary significantly with vanadia loading (Table 4.1). However calcination at higher temperatures causes definite increase in particle size.

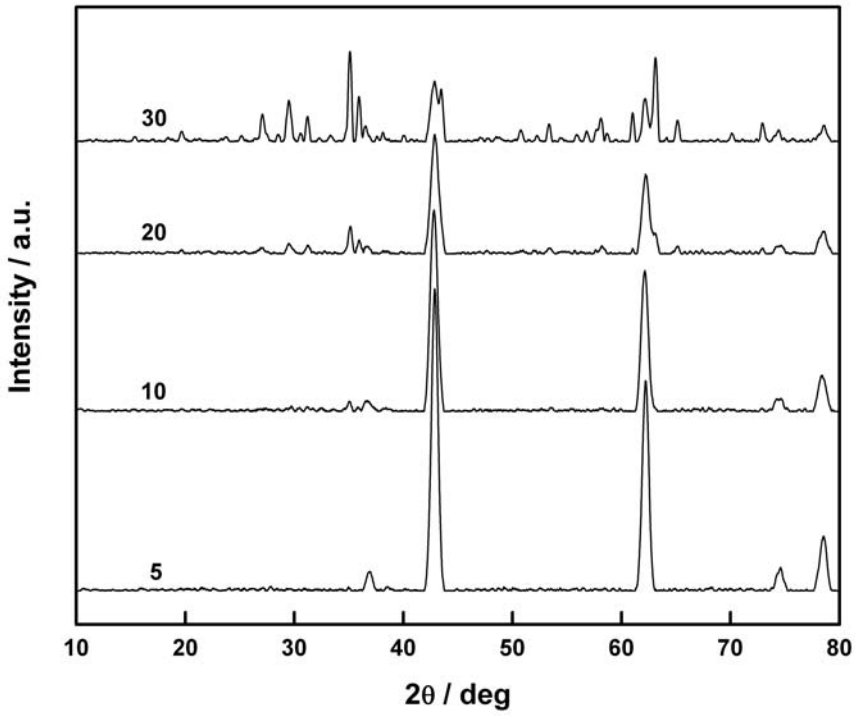

Fig. 4.2: *Powder X-ray diffraction patterns of V-Mg-O catalysts calcined at 923 K as a function of vanadia loading in wt%.*

4.3.2. Scanning Electron Microscopy

The scanning electron micrographs of V-Mg-O catalysts, calcined at 823 K, with vanadia loadings of 2, 20 and 30 wt% are shown in Fig. 4.3. These images show that the morphology of the particles depends on the vanadium content. The samples contain particles with non-uniform size and shape. Particles of 2 V-Mg-O appeared to be the aggregates of porous, fluffy and irregularly shaped particles. 20 V-Mg-O also is composed of non-uniform aggregates of highly spongy and porous particles. 30 V-Mg-O consists of almost well crystallized particles with mostly non-porous character and non-uniform size.

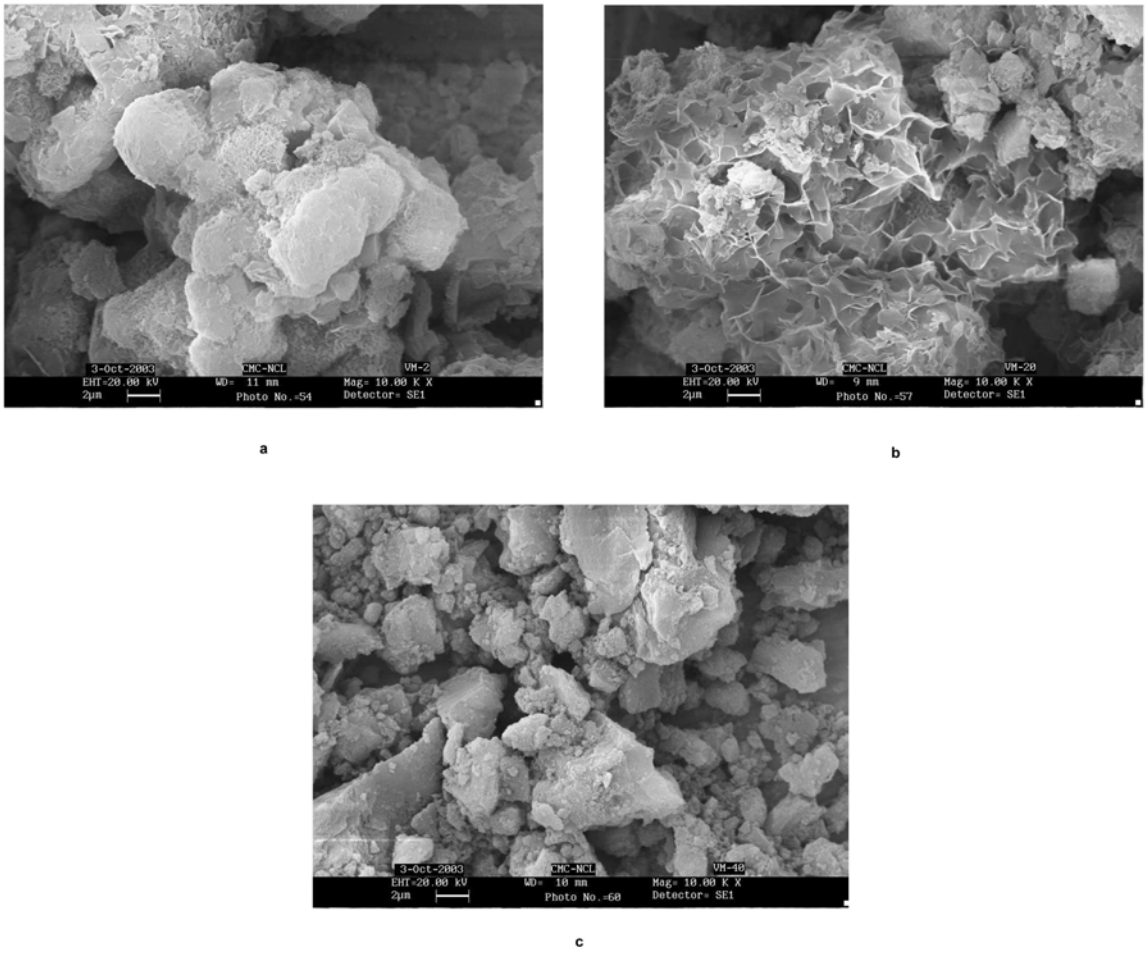

Fig. 4.3: *Scanning electron micrographs of calcined V-Mg-O catalysts with vanadia loading* ***(a)*** *2* ***(b)*** *20 and* ***(c)*** *30 wt%. Magnification = 10.00 K. The label 'VM-40' in figure c is erroneous and should be read as VM-30.*

4.3.3. Thermal analysis

The TG, DTG and DTA curves for as-synthesized samples 2, 5 and 20 V-Mg-O are shown in Fig. 4.4 a-c. In low temperature region, the weight loss occurs between 150-200 ^{0}C for all the three catalysts and additional weight loss occurs between 200 and 250 ^{0}C for 20 V-Mg-O. Endothermic peaks are observed in DTA in these temperature regions. The next weight loss appears between 300 and 460 ^{0}C, the peak maximum in DTG shifts to

higher temperatures with increasing vanadia loading within this temperature range. At temperatures that correspond to these DTG peaks, DTA shows endothermic peaks. All the samples show weight loss again in the temperature range 460-550 ^{0}C. An endothermic peak is observed in DTA in this temperature range for 20 V-Mg-O only. Another weight loss is observed between 550 and 680 ^{0}C for 20 V-Mg-O whose DTA shows an exothermic peak in this region.

The weight loss below 250 ^{0}C can be attributed to the elimination of weakly bonded water molecules. The weight loss in the temperature range 300-460 ^{0}C may be due to either the loss of strongly bonded water or the decomposition of $Mg(OH)_2$ to MgO. The decomposition of pure $Mg(OH)_2$ is usually observed in this temperature range with an endothermic peak in DTA. The shift in temperature, at which weight loss occurs, to higher values with increasing vanadia loading may be due to the retardation of decomposition of $Mg(OH)_2$ by the added vanadia. The weight loss observed between 460 and 550 ^{0}C can be attributed to the decomposition of ammonium vanadyl oxalate [2], as represented below:

$$(NH_4)_2[VO(C_2O_4)_2] + 2.5\ O_2 \rightarrow 2\ NH_3 + 4\ CO_2 + H_2O + VO_x \qquad (4.1)$$

Since MgO is a basic oxide support, the NH_4^+ ions and/or NH_3 desorb easily and rarely take part in the reaction with oxygen. This leads to endothermic peak in DTA unlike in the case of VO_x/Al_2O_3 system, where exothermic peak is observed in the DTA due to the reaction of strongly adsorbed NH_4^+ and/or NH_3 with oxygen. The weight loss in this temperature region increases with vanadia loading, as expected, since the amount of ammonium vanadyl oxalate is proportional to the vanadia loading. Vanadium is in 4+ oxidation state in ammonium vanadyl oxalate, however, oxidation to 5+ state is expected to occur during the thermal process.

Confusion exists in the literature about the temperature at which the formation of vanadate phases occurs. The thermal studies in this area are limited and publications differ in the reported values of temperature range. The temperature at which the formation of bulk vanadate phase occurs cannot serve as a guideline accurately since the formation temperature of supported phase may significantly differ. Said *et al* [3] studied the solid-solid interactions in V_2O_5-MgO system by TG-DTA and reported that the formation of

$Mg_3V_2O_8$ phase occurs at around 550 ^{0}C and MgV_2O_6 at 650-700 ^{0}C, as represented below:

$$3\ MgO + V_2O_5 \xrightarrow{823\ K} Mg_3V_2O_8 \quad (4.2)$$

$$MgO + V_2O_5 \xrightarrow{973\ K} MgV_2O_6 \quad (4.3)$$

The precursors were $Mg(OH)_2$ and ammonium metavanadate and the thermal analysis was performed in flowing air (40 ml min^{-1}) at a heating rate of 10 ^{0}C min^{-1}. The formation of orthovanadate, $Mg_3V_2O_8$, is proposed to occur at 540-600 ^{0}C and pyrovanadate, $Mg_2V_2O_7$, at as low as 408 ^{0}C by Sam *et al* [4] in DTA study of impregnated $NH_4VO_3/Mg(OH)_2$ system. Again the analysis was performed at a heating rate of 10 ^{0}C min^{-1} under a flow of air. Corma *et al* [5] reported low formation temperatures for orthovanadate (~ 420 ^{0}C) and pyrovanadate (~ 410 ^{0}C) based on thermogravimetric analysis of vanadyl oxalate/MgO system. The measurements have been carried out at a heating rate of 10 ^{0}C min^{-1}, under a flow of air (100 ml min^{-1}).

It is clear that even the temperature of formation of supported phase differ from catalyst to catalyst, depending on the preparation conditions, precursors used and thermal analysis conditions. For the present series of catalysts, the temperature of formation of orthovanadate phase may tentatively be assigned to 550-680 ^{0}C. The XRD data shows that calcination temperature greater than 550 ^{0}C is needed for the formation of orthovanadate phase in 20 V-Mg-O since the phase appears only when it is calcined at 650 ^{0}C.

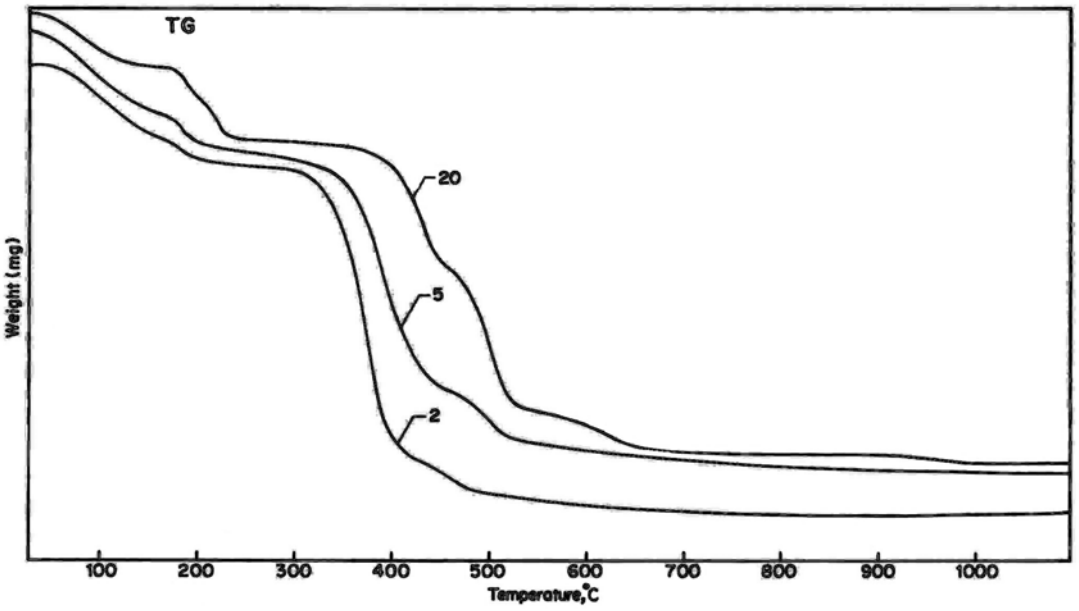

Fig. 4.4a: *Thermogravimetric curves of as synthesized V-Mg-O catalysts. The integers in figure indicate vanadia loading as wt%.*

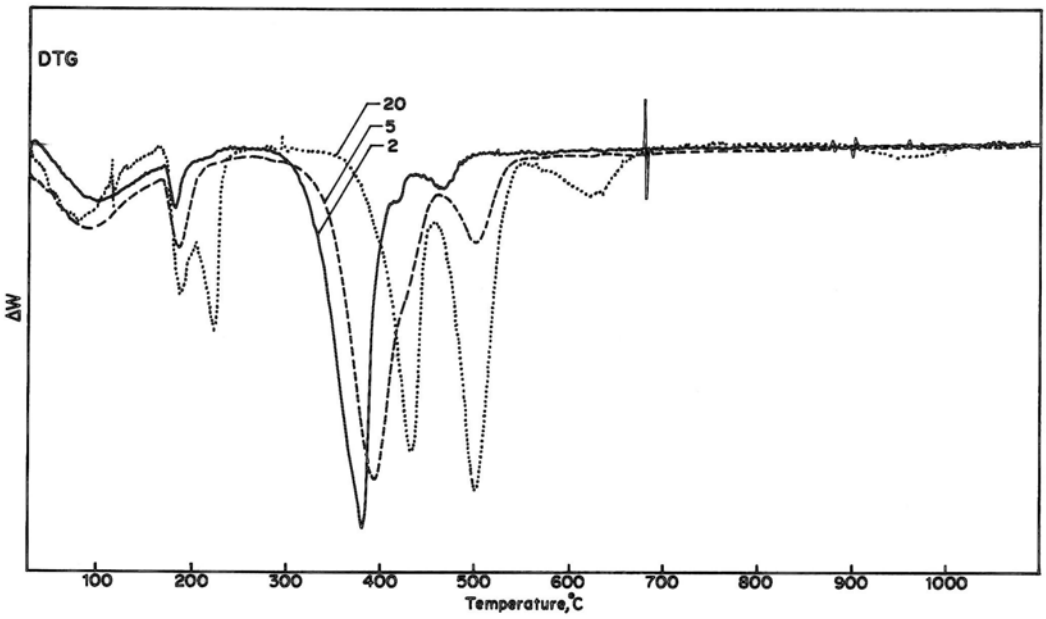

Fig. 4.4b: *Differential thermogravimetric curves of as synthesized V-Mg-O catalysts. The integers in figure indicate vanadia loading as wt%.*

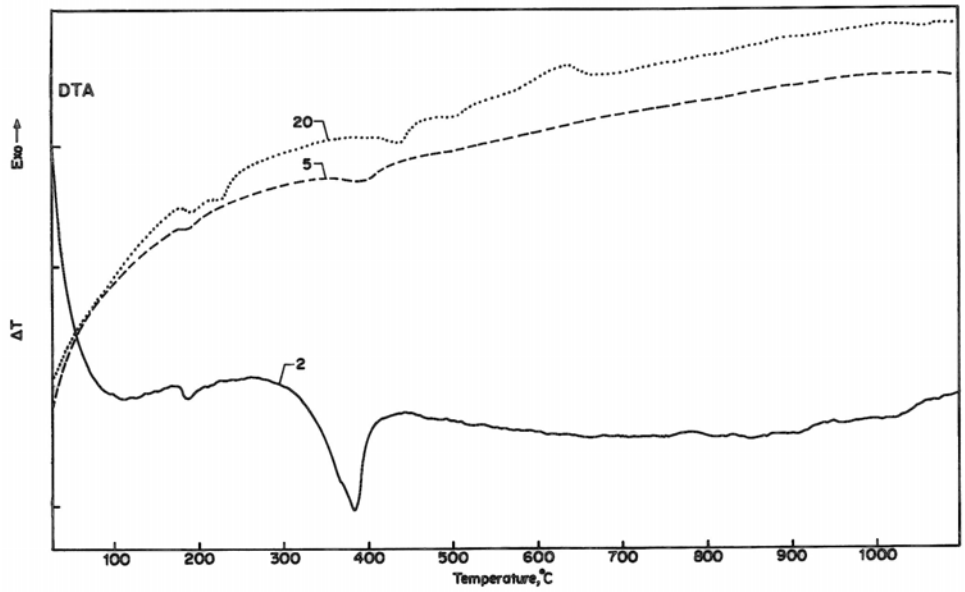

Fig. 4.4c: *Differential thermoanalytical curves of as synthesized V-Mg-O catalysts. The integers in figure indicate vanadia loading as wt%.*

4.3.4. Infrared Spectroscopy

FTIR spectra of the V-Mg-O catalysts, calcined at 823 K, are shown in Fig. 4.5. The spectra were recorded at ambient conditions. All catalysts exhibited a band around 860 cm^{-1} in their spectra and this band is very prominent and broad for 30 V-Mg-O. A band centered at 680 cm^{-1} is also observed for 30 V-Mg-O. From the investigation of IR spectra of magnesium vanadate reference phases, the band at 860 cm^{-1} can be assigned to ν_3 antisymmetric stretch of $(VO_4)^{3-}$ anions and the band at 680 cm^{-1} to ν_{as} (VOV) [4,6-9]. These bands are reported as characteristic of magnesium orthovanadate, $Mg_3(VO_4)_2$. Hence the presence of (VO_4) species on the present series of catalysts can be confirmed by IR spectra. These species may exist as isolated species or as amorphous $Mg_3(VO_4)_2$ domains at lower loadings. The presence of strong bands at 860 and 680 cm^{-1} for 30 V-Mg-O indicate the presence of bulk-like orthovanadate for this catalyst. The spectra for magnesium pyrovanadate and metavanadate, $Mg_2V_2O_7$ and MgV_2O_6, are reported to have absorption bands in the region 500-600 cm^{-1} that are absent in the orthovanadate spectrum

[6]. The present catalysts didn't show any absorption bands in this region, thus excluding the presence of meta and pyrovanadates. The spectra did not show any evidence for the formation of V_2O_5 since the band at 1020 cm^{-1} that is usually assigned to the stretching vibration of V^{5+}=O species was not observed for any of the catalysts.

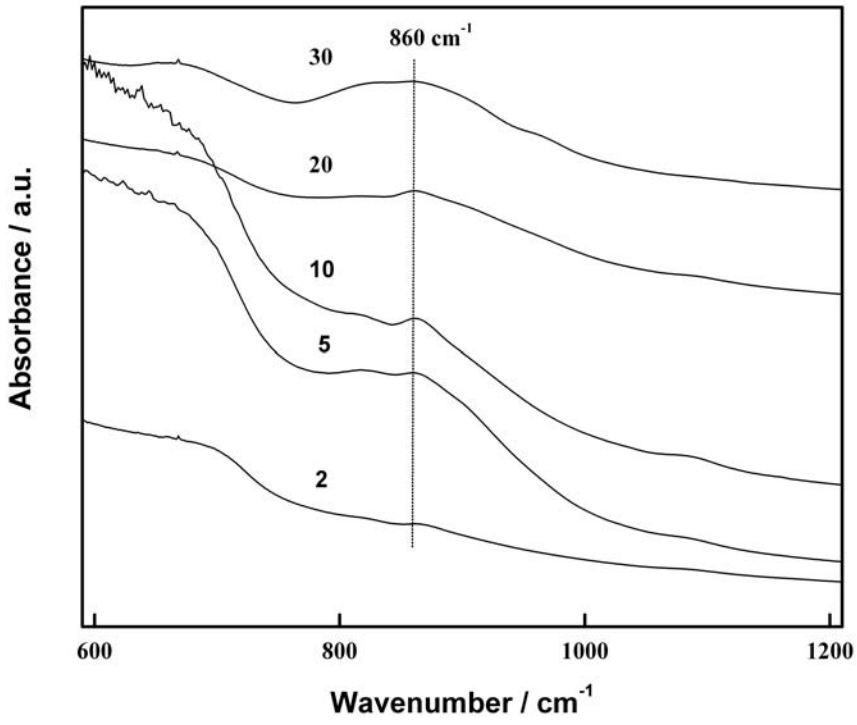

Fig. 4.5: *FTIR spectra of V-Mg-O catalysts, calcined at 823 K, as a function of vanadia loading in wt%.*

4.3.5. Diffuse reflectance UV-visible spectroscopy

The lower-energy absorption bands for the vanadium ions in the diffuse reflectance UV-visible spectra, which are associated with oxygen to vanadium charge transfer, are strongly influenced by the coordination, polymerization degree and/or the oxidation state of vanadium ions in the sense that the lower the coordination and polymerization of vanadium, the lower is the wavelength [9-11]. The absorption band at 400-500 nm is usually considered as characteristic of V^{5+} in octahedral environment, while the band at 250-350 nm is due to V^{5+} in a tetrahedral environment. The d-d transitions of V^{4+} (d^1) in a

distorted octahedral symmetry give a broad band in 550-850 nm region. As described in Chapter 2, the UV-visible spectra of NH_4VO_3 and $NaVO_3$, characterized by the presence of polymeric tetrahedral VO_4, possess absorption band centered at 291 nm while V_2O_5, having distorted tetragonal pyramidal V^{5+} species show bands at 336 and 472 nm. The band at 472 nm has been tentatively assigned to charge transfer to a delocalized acceptor site such as conjugated sites like those in octahedral VO_6 chains and the bands at lower wavelengths to charge-transfer transitions.

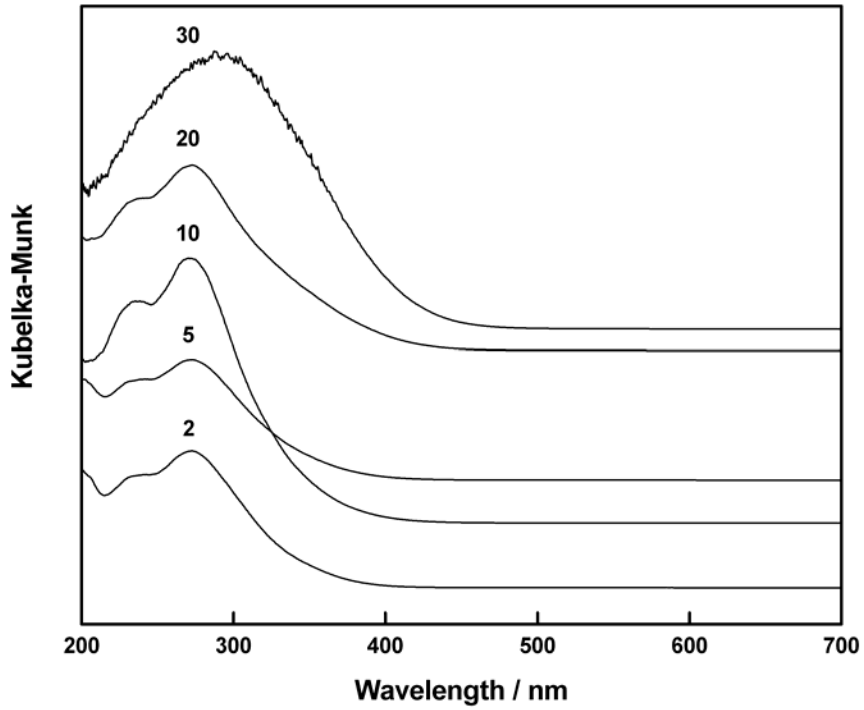

Fig. 4.6: *Diffuse reflectance UV-visible spectra of V-Mg-O catalysts, calcined at 823 K, as a function of vanadia loading in wt%.*

Table 4.2: Assignment of bands characteristic of vanadium-oxy species*

V_2O_5	V_2O_3	$Mg_3(VO_4)_2$	$Mg_2V_2O_7$	MgV_2O_6	Assignment
					CT transitions of tetrahedral vanadium (V) framework:
		265	245		$(\pi)t_2 \rightarrow (d)e$
			292		$(\pi)t_1 \rightarrow (d)t_2$
		334	333		$(\pi)t_1 \rightarrow (d)e$
					CT transitions of octahedral vanadium (V) oxy-ions:
250				245	$e(\pi_0) \rightarrow b_2(xy)$
303				292	$a_2, b_1(\pi) \rightarrow e_\pi^x$
385				392	$a_2, b_1(\pi) \rightarrow b_2(xy)$ LCT
	244				CT transitions of vanadium (III)
	323				oxy-ions
					d-d transitions of vanadyl species:
465				513	$b_2(xy) \rightarrow a_1^x(z^2)$
				730	$b_2(xy) \rightarrow e_\pi^x(xz, yz)$
					d-d transitions of the $V^{III}O_6$ chromophore:
	395				$^3T_{1g}(F) \rightarrow {}^3T_{1g}(P)$
	571				$^3T_{1g}(F) \rightarrow {}^3T_{2g}$

**The values represent wavelengths in nm at which maximum absorption occurs.*

The diffuse reflectance UV-visible spectra of V-Mg-O catalysts, calcined at 823 K, are presented in Fig. 4.6. The spectra show broad absorptions around 270 nm and the maximum of this absorption shifts slightly to higher wavelengths with increasing vanadia loading. The absorptions are broader in nature, especially for 20 and 30 V-Mg-O catalysts. The band around 270 nm is characteristic of isolated VO_4 tetrahedra associated with the

presence of $Mg_3(VO_4)_2$. The various bands observed for vanadium oxy-species and their assignment to electronic transitions are given in Table 4.2 based on the data available in literature [6]. Hanuza *et al* [6] constructed an energy diagram for VOO_5' centrum in V_2O_5/MgO catalysts which explain all these electronic transitions. According to this, the band at 270 nm can be assigned to the transition from t_2 level of oxygen to e level of vanadium (V). Though the main band is observed at 270 nm and can be assigned to orthovanadate phase, the broad nature of the bands, especially for 30 V-Mg-O, makes it impossible to say that they originate only from this phase. The presence of other vanadate phases cannot be excluded conclusively.

Table 4.3: Absorption edge energy and TPR data for V-Mg-O catalysts*

Sample	Absorption edge energy (eV)	H_2-TPR T_{max} (K)	Total H_2 consumption (μmol H_2/g cat.)
2 V-Mg-O	3.63	791	121
5 V-Mg-O	3.62	821	604
10 V-Mg-O	3.60	867	1008
20 V-Mg-O	3.22	893	1940
30 V-Mg-O	3.16	925	3422

**Calcined at 823 K*

Absorption band edge energies, which can be determined using Tauc's law [12,13] provide more quantitative structural information, as described for VO_x/Al_2O_3 catalysts in Chapter 2. The edge energies for the present series of catalysts are given in Table 4.3. The values were determined, based on the allowed transitions, by finding the intercept of the straight line in the low-energy rise of a plot of $[F(R_\infty)\ h\nu]^2$ against $h\nu$, where $F(R_\infty)$ is Kubelka-Munk function and $h\nu$ is the incident photon energy [13-15]. The edge energy values reported in the literature for the reference compounds $Mg_3(VO_4)_2$, $Mg_2V_2O_7$, MgV_2O_6, with isolated, dimerised and two-dimensionally polymerized vanadium (V)

species, are 3.4, 3.2 and 2.4 eV respectively. The edge energy of bulk V_2O_5 having distorted tetragonal pyramidal coordination of vanadium sharing edges and corners, which can be regarded as polymerized VO_5 units, is reported as 2.2-2.4 eV [15]. The edge energy values for the V-Mg-O catalysts in the present study (Table 4.3) fall in the narrow range 3.2-3.6, suggesting that the molecular structure of the surface vanadium oxide is similar, though the vanadium loading varies. The closeness of edge energy values to that of magnesium orthovanadate suggests that the structure of surface vanadium species in the present series of catalysts are essentially similar to that of orthovanadate, composed of isolated tetrahedrally coordinated vanadium (V) species [14,16]. The presence of MgV_2O_6 in the present series of catalysts can be ruled out definitely, however the presence or absence of $Mg_2V_2O_7$ is still in ambiguity, since the edge energy values for ortho and pyrovanadate phases are not so different.

4.3.6. Temperature Programmed Reduction

Figure 4.7 shows the TPR patterns of V-Mg-O catalysts, calcined at 823 K, as a function of vanadia loading. The reduction peak is observed at 791 K for 2 V-Mg-O catalyst and the maximum of the peak shifts to higher temperatures with increasing vanadia loading (Table 4.3). This peak can be attributed to the reduction of V^{5+} in $Mg_3(VO_4)_2$. The shift in T_{max} to higher temperatures with increasing vanadia loading may be due to the increased difficulty in reduction as the size of the $Mg_3(VO_4)_2$ domains increases. The TPR profiles and the range of reduction temperatures are in agreement with previous studies on V-Mg-O catalysts [16-18]. Similar shift in T_{max} is reported previously and has been ascribed to the increase in bulk-like character of $Mg_3(VO_4)_2$ domains with increasing vanadia loading, since the bulk orthovanadate is more difficult to reduce [16]. Table 4.3 also report the values of total hydrogen consumption during the TPR experiment, which shows an increase with increasing vanadia loading, as expected.

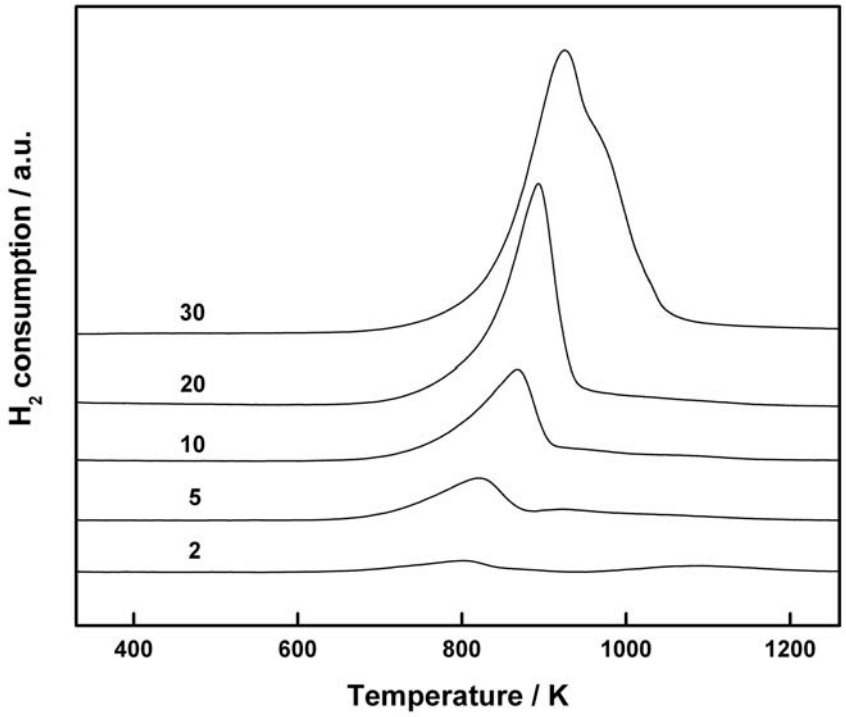

Fig. 4.7: *TPR profiles of V-Mg-O catalysts calcined at 823 K. The integers in figure indicate vanadia loading in wt%.*

4.3.7. Laser Raman Spectroscopy

Figure 4.8 shows the laser Raman spectra of V-Mg-O catalysts, calcined at 823 K, as a function of vanadia loading. No characteristic peaks were observed for 2 V-Mg-O while the catalysts with 5-30 wt% vanadia loading showed well-defined bands. For 5 V-Mg-O catalyst, the band was observed at around 834 cm^{-1} that can be assigned to V-O-V or V-O-Mg vibrations of tetrahedrally coordinated VO_4 species [16,19]. The maximum of the band shifted to around 856 cm^{-1} for the catalysts with higher vanadia loadings. The intensity of this band increased with increasing vanadia loading. The position of the band agrees well with that reported for magnesium orthovanadate, $Mg_3(VO_4)_2$ [5,6,9,16,20-26]. The band is relatively narrow for 30 V-Mg-O compared to that of catalysts with lower vanadia loadings. The broadening of the band at lower loadings could be probably due to the distortion of the crystalline network or due to high dispersion of vanadate phase

[26,27]. The peaks characteristic of isolated vanadyl species (~1000 cm^{-1}), $Mg_2V_2O_7$ (902 cm^{-1}) or V_2O_5 were not observed at any vanadia loading.

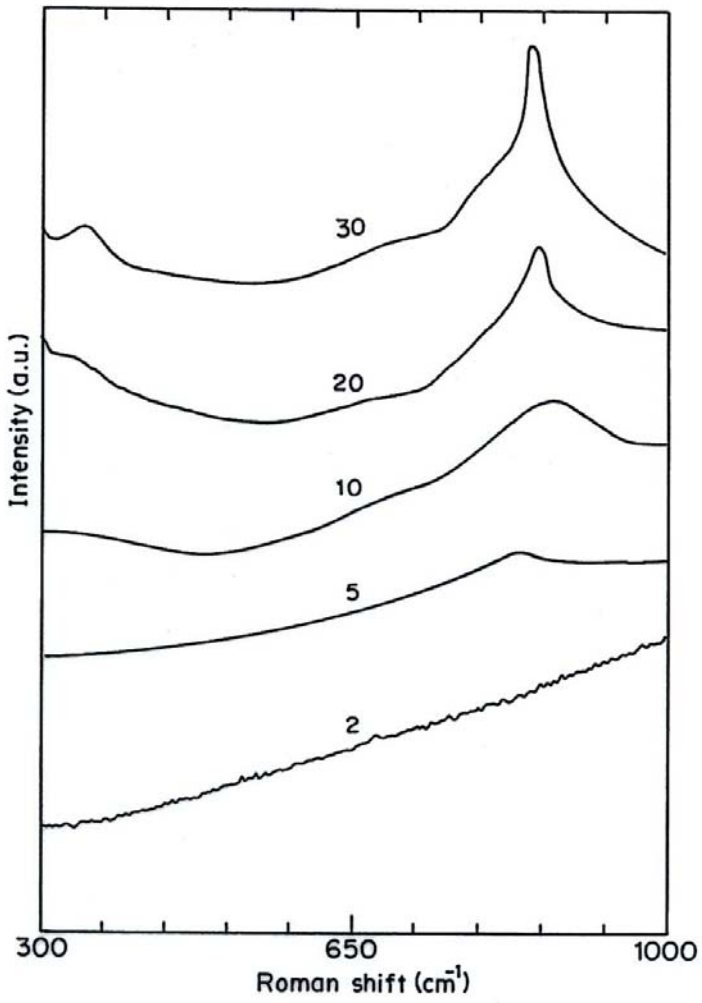

Fig. 4. 8: *Laser Raman spectra of V-Mg-O catalysts, calcined at 823K, as a function of vanadia loading. Numbers in the figure indicate vanadia loading in wt%.*

4.3.8. ^{51}V MAS NMR spectroscopy

The ^{51}V NMR spectra of the magnesium vanadates were reported to be of different nature depending on the local environment of vanadium atoms in individual vanadates

[27,28]. Magnesium orthovanadate, which is composed of isolated nearly tetrahedral VO_4 species, gives an isotropic NMR spectrum (Fig. 4.9). In pyrovanadates, the nonequivalent vanadium atoms in $V_2O_7^{2-}$ fragments lead to spectra consisting of two different lines. In the case of metavanadate, the vanadium atom is in a strongly distorted octahedral environment with respect to oxygen and the spectrum of this compound has three-dimensional anisotropy of the chemical shift tensor. The ^{51}V MAS NMR spectra and parameters of the chemical shift tensor of bulk magnesium vanadates reported by Lapina *et al* [28] are given in Fig. 4.9 and Table 4.4 respectively. The isotropic peak appears at –557 ppm for $Mg_3(VO_4)_2$. Two isotropic peaks are observed for pyrovanadates, viz, at –555 and –617 ppm for α-phase and at –560 and –650 ppm for β-phase. The metavanadate shows isotropic peak at –576 ppm. Figure 4.10 a and b shows the ^{51}V MAS NMR spectra of the present series of catalysts obtained at two different spinning rates, viz, 8 and 10 kHz respectively. The spectra of all the samples show a single narrow intense peak, the chemical shift values of the same are around -556 ppm. This peak can be assigned to the presence of $Mg_3(VO_4)_2$ phase since the isotropic nature and chemical shift of the peak resemble that of pure $Mg_3(VO_4)_2$ reference compound [4,16,27,28]. The comparison of spectra obtained in the present work with that of bulk magnesium vanadates (Fig. 4.9) and the chemical shift values with that reported in Table 4.4 confirms the presence of $Mg_3(VO_4)_2$ phase.

Table 4.4: Parameters of the ^{51}V NMR chemical shift tensor of magnesium vanadates*

Compound	$-\delta_1$	$-\delta_2$	$-\delta_3$	δ_{iso}	$\Delta\delta$
$Mg_3(VO_4)_2$	557	557	557	557	0
α-$Mg_2V_2O_7$ V_1	510	570	585	555	75
V_2	570	580	700	617	130
β-$Mg_2V_2O_7$ V_1	460	560	680	560	220
V_2	590	660	700	650	110
α-$Mg(VO_3)_2$	310	470	950	576	640

**from [28]*

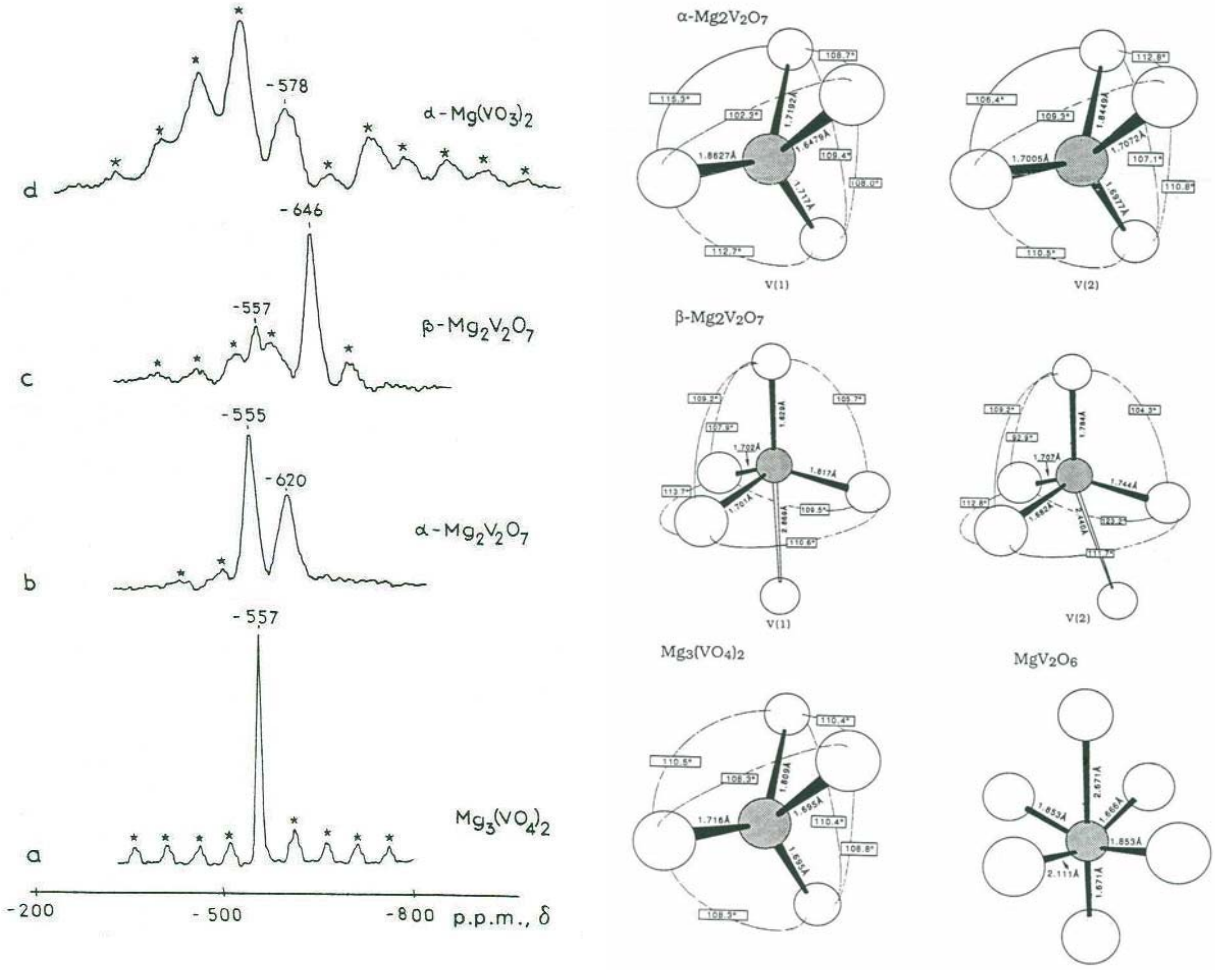

Fig. 4.9: *^{51}V MAS NMR spectra of bulk magnesium vanadates, measured at 298 K, frequency 78.86 MHz, pulse duration 1 s and relaxation decay 0.1 s [28]. The asterisks denote MAS side bands. The chemical shift values are given relative to $VOCl_3$. The structures of different magnesium vanadates are also displayed.*

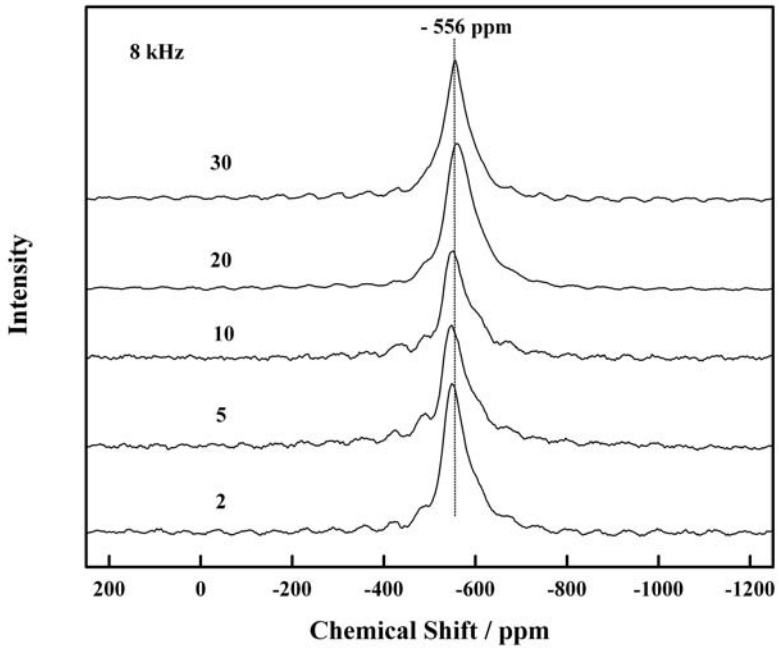

(a)

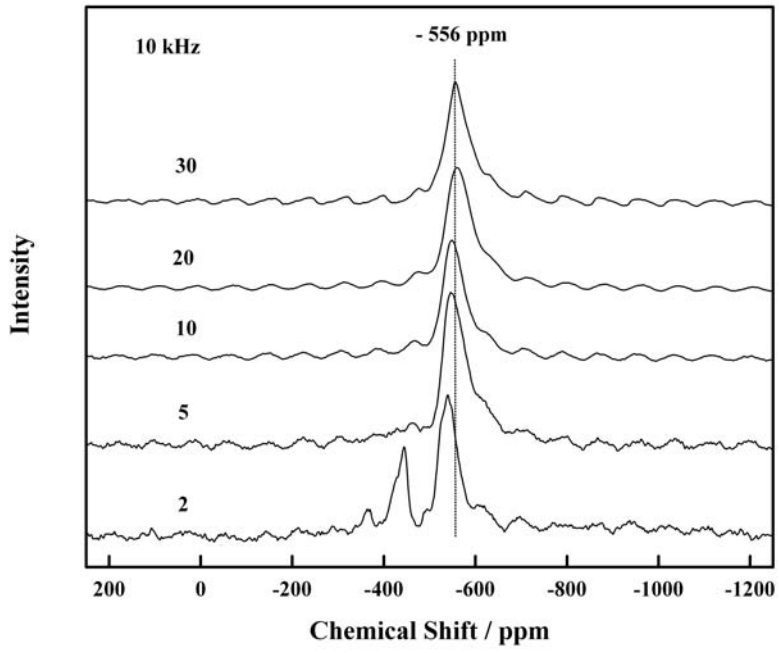

(b)

Fig. 4.10: *^{51}V MAS NMR spectra of V-Mg-O catalysts as a function of vanadia loading at spinning rates of **(a)** 8 kHz and **(b)** 10 kHz. The catalysts were calcined at 823 K.*

4.3.9. Electron Paramagnetic Resonance Spectroscopy

Fig. 4.11 shows the EPR spectra of V-Mg-O catalysts, calcined at 823 K, as a function of vanadia loading. The spectra are similar, except, slight variations in intensity of the lines. The well-resolved hyperfine structure with eight parallel and perpendicular components, observed in the spectra, can be assigned to the V^{4+} ion [7] and is originated from the interaction between the unpaired electron and the ^{51}V nucleus. The spin Hamiltonian constants obtained from the spectra are $g_{\|} = 1.937$, $g_{\perp} = 1.952$, $A_{\|} = 173$ G and $A_{\perp} = 50$ G. These parameters are in the same range of those reported for other VO complexes with oxygen donor ligands (Table 4.5) and are in agreement with those reported for V_2O_5/MgO catalysts by Hanuza *et al* [6]. The parameters obtained in their study are $g_{\|} = 1.949$, $g_{\perp} = 1.959$, $A_{\|} = 161$ G and $A_{\perp} = 48$ G. The g values obtained for solid V_2O_5 are $g_{\|} = 1.88$ and $g_{\perp} = 1.99$ which give a mean value of $1/3(g_{\|}+2g_{\perp})$ equal to 1.96. The coordination system around the vanadium atom is a strongly distorted square pyramid and is closer to a trigonal pyramid in shape. The EPR parameters suggest such a structure for the VO^{2+} ion containing active sites whose symmetry is close to C_s.

Table 4.5: Spin-Hamiltonian constants for VO^{2+} in different lattices [6]

Sample	$g_{\|}$	$g_{\perp}$	$A_{\|}$ (G)	$A_{\perp}$ (G)
VO^{2+} in GeO_2	1.929	1.976	175	68
VO^{2+} in SnO_2	1.943	1.921	140	31
VO^{2+} $VOCl_5^{3-}$	1.945	1.985	173	64
VO^{2+} in $VO[(CH_3CO)_2CH]_2$	1.944	1.996	173.5	63.5
VO^{2+} in $VO(L_4)$ complexes	1.934-1.956	1.979-1.992	150-178	40-66
VO^{2+} in tetraphenyl porphyrin	1.964	1.989	159	54
VO^{2+} in V_2O_5/MgO catalysts	1.949	1.959	161	48

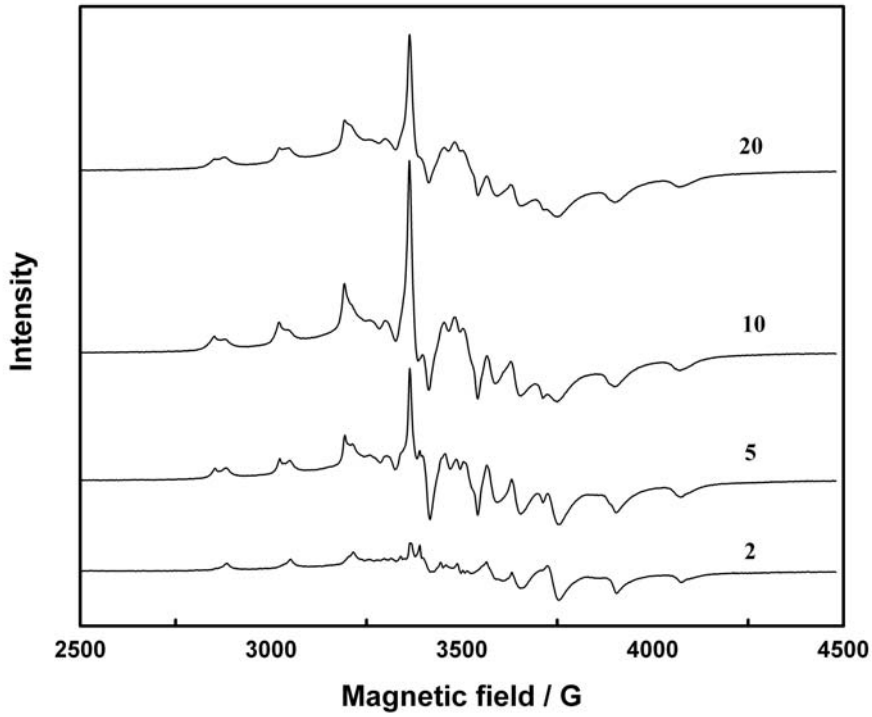

Fig. 4.11: *Electron paramagnetic resonance spectra of V-Mg-O catalysts, calcined at 823 K. The vanadia loading indicated in figure are in wt%.*

The hyperfine splitting multiplet in the EPR signal, given by V-Mg-O catalysts, is overlapped on a broad and distinct spectrum. Hanuza *et al* [6] assigned these spectra to two types of vanadium centers in the catalysts, the first being vanadyl in the surface layer which gives the spectrum with hyperfine structure and the second being in the bulk of catalyst. This amorphous vanadyl species gives the spectrum without hyperfine features.

Figure 4.12 shows the spectra of 5 V-Mg-O, which is calcined at 823 K, and those obtained after reduction of 5 V-Mg-O catalyst in H_2 flow at various temperatures, as indicated in figure. As the temperature increases, degree of reduction increases. The amount of V^{4+} increased when the calcined catalyst is heated at 473 K in H_2 flow, as can be observed from the intensity of spectral lines. The broad spectrum without hyperfine structure, on which the hyperfine spectrum is overlapped, is strong indicating that some

amounts of V^{5+} in the bulk also undergo reduction to V^{4+} at this temperature. At 673 K, new eight lines appeared with a smaller hyperfine coupling constant, which is superimposed on the V^{4+} signals. This eight line spectrum is assigned to the V^{2+} ion in octahedral symmetry by Sharma *et al* [7] and shows that, apart from the V^{4+} ions, the catalyst contains V^{2+} ions. There may be V^{3+} ions also on the catalyst, however they are not EPR visible. At 723 K, the eight line spectrum of V^{2+} is very prominent revealing the greater extent of reduction to V^{2+} ion.

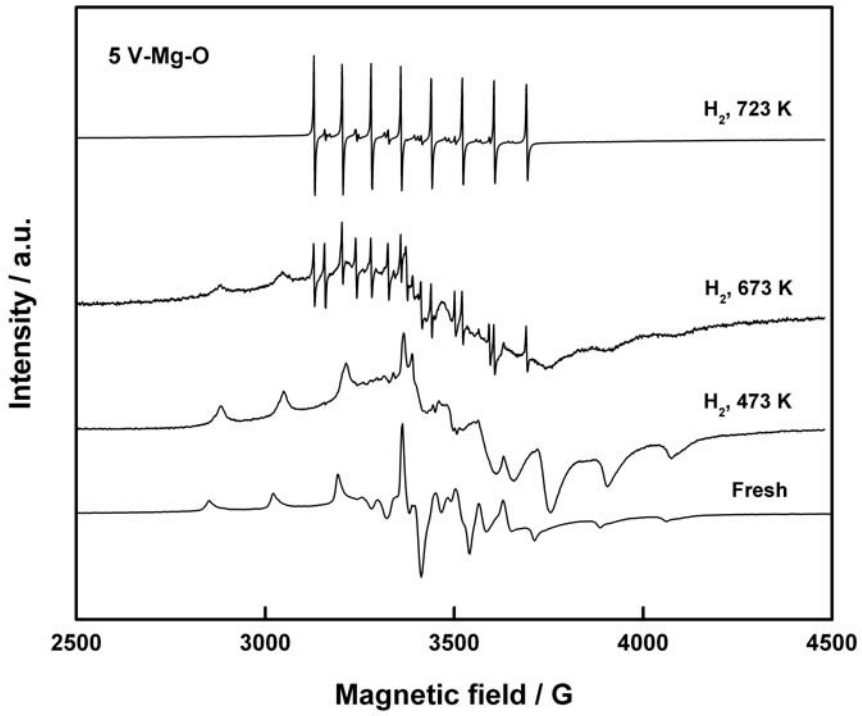

Fig. 4.12: *Electron paramagnetic resonance spectra, measured at 298 K, of fresh and reduced 5 V-Mg-O catalyst. The reduction temperatures are indicated in figure.*

The amount of V^{4+} is very small in the fresh, calcined V-Mg-O catalysts since other characterization studies indicate that most of the vanadium species were tetrahedral V^{5+} and $Mg_3V_2O_8$ (diamagnetic), which are not EPR visible. Sakurai *et al* [29] proposed that a slight anion vacancy existed in the $Mg_3V_2O_8$ structure and V^{4+} ions are highly dispersed in

the V^{5+} ions, which explain the presence of some amount of V^{4+} on all the calcined catalysts.

4.4. STRUCTURE OF V-Mg-O CATALYSTS- THE FINAL WORD

In the case of V_2O_5-MgO system, four magnesium vanadates (orthovanadate, metavanadate and pyrovanadates) are stable at room temperature. Each characterization technique provides valuable information regarding the nature of vanadate phase for the present series of catalysts. A single technique alone cannot give conclusive evidence, whereas, data from different characterization techniques, taken together, will provide the information about the structure of catalyst conclusively. XRD indicate that bulk-like magnesium orthovanadate phase is formed on 30 V-Mg-O and doesn't detect any vanadia phase below the vanadia loading, 30 wt%. This shows the amorphous nature (more accurately, X-ray amorphous) of vanadia phase below this loading. The presence of (VO_4) species at all vanadia loadings is indicated by FTIR. Since this type of monomeric, tetrahedral V^{5+} species is characteristic of magnesium orthovanadate, it can be assumed that orthovanadate phase is more probable on the surface, rather than pyro or metavanadates. In pyrovanadates, vanadium exists as (V_2O_7) fragments and in metavanadate, it is in a distorted octahedral environment. Similar to FTIR, DR UV-visible spectroscopy suggests the presence of monomeric tetrahedral vanadium (V) species at all vanadia loadings. This strongly supports the presence of orthovanadate phase, but again, due to the broad nature of the peaks, the bands cannot be resolved sufficiently to exclude the presence of pyrovanadates. However, UV-visible spectroscopy rules out the presence of metavanadate based on a comparison between experimental and reference absorption edge energy values. TPR shows peaks that can be attributed, most probably, to the reduction of V^{5+} in orthovanadate domains and the shift in T_{max} to higher temperatures indicate an increase in crystallinity of the domain with increase in vanadia loading. Laser Raman spectra show bands in the range 825 and 860 cm^{-1}, again due to the orthovanadate phase but here also the broad nature of bands prevents the investigation of presence or absence of pyrovanadate phase, which is supposed to give a band around 902 cm^{-1}. The most conclusive evidence for the nearly dominant presence of orthovanadate phase

originates from ^{51}V MAS NMR spectroscopy. The isotropic nature, side band pattern and chemical shift values observed for the catalysts with different vanadia loadings strongly suggest the presence of magnesium orthovanadate phase on the surface. The other phases may be either absent or present in only in negligible amounts. Hence it can be concluded that among different vanadates, mainly orthovanadate is formed on the surface of present catalysts and the size of these domains increases with increasing vanadia loading, finally leading to the appearance of bulk-like $Mg_3(VO_4)_2$ on 30 V-Mg-O. There is no evidence for V_2O_5 domains in the present series of catalysts by any of the characterization techniques.

Though much of the thermodynamic data published on V_2O_5-MgO system are contradictory, Köbel *et al* [30] have prepared a tentative phase diagram, mainly based on the data of Clark and Morley [31] and of Kerby and Wilson [32]. This diagram (Fig. 4.13) includes the compounds, $Mg_3V_2O_8$, $Mg_2V_2O_7$ and MgV_2O_6 and left out all other phases that were not verified in their work. According to the diagram, below approximately 25 mol% V_2O_5 and between 400 and 1200 ^0C, $Mg_3V_2O_8$ is the vanadium containing phase observed, which is in agreement with our observation. It should be noted that, this phase diagram is based on limited number of studies and not an absolute one.

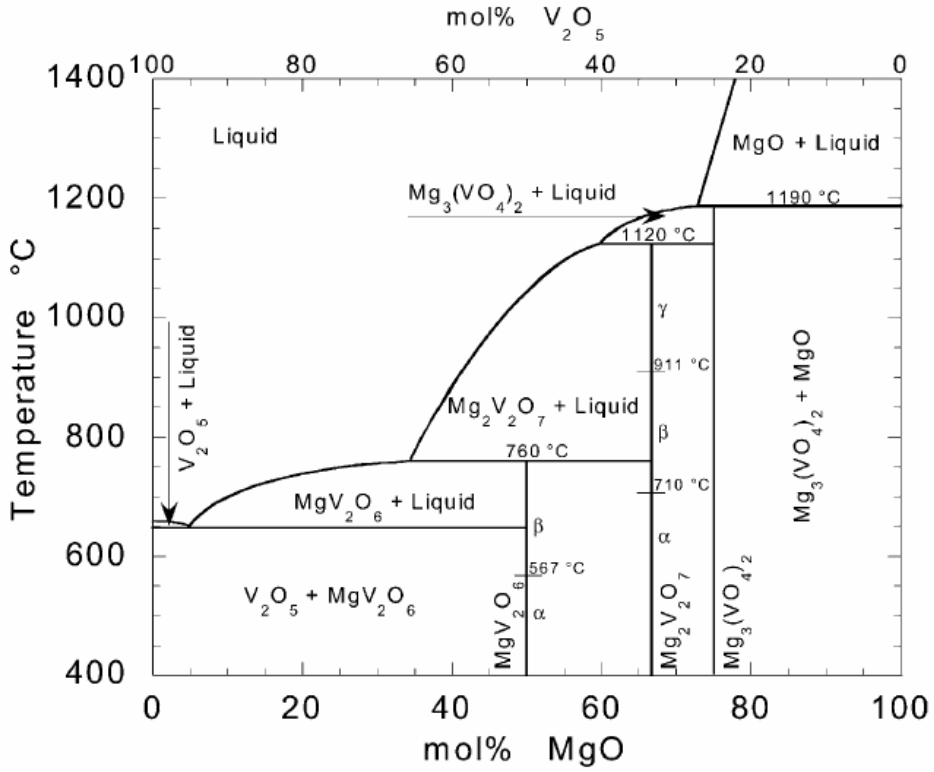

Fig. 4.13: *Tentative phase-diagram of V_2O_5–MgO, drawn by Köbel et al [30] based on the data of Clark and Morley [31] and of Kerby and Wilson [32]. Markers indicate polymorphic transitions.*

4.5. REFERENCES

[1] W. Oganowski, J. Hanuza, L. Kepiński, Appl. Catal. A, 171 (1998) 145.

[2] X. S. Li, L. Y. Chen, C. Y. Xie, Y. F. Miao, D. M. Li, Q. Xin, Thermochimica Acta, 260 (1995) 115.

[3] A. A. Said, M. M. M. Abd El-Wahab, Thermochimica Acta 249 (1995) 313.

[4] D. Siew Hew Sam, V. Soenen, J. C. Volta, J. Catal., 123 (1990) 417.

[5] A. Corma, J. M. López Nieto, N. Paredes, J. Catal., 144 (1993) 425.

[6] J. Hanuza, B. Jezowska-Trzebiatowska, W. Oganowski, J. Mol. Catal., 29 (1985) 109.

[7] V. Sharma, A. Wokaun, A. Baiker, J. Phys. Chem., 90 (1986) 2715.

[8] A. A. Rar, A. V. Simakov, S. A. Veniaminovv, React. Kinet. Catal. Lett., 39 (1989) 299.

[9] A. Corma, J. M. Lopez Nieto, N. Paredes, Appl. Catal. A, 104 (1993) 161.

[10] G. Centi, S. Perathoner, F. Trifiro, A. Aboukais, C. F. Aissi, M. Guelton, J. Phys. Chem., 96 (1992) 2617.

[11] G. Lischke, W. Hanke, H-G. Jerchkewitz, G. Olmann, J. Catal., 91 (1985) 54.

[12] J. Tauc, in: Amorphous and Liquid semiconductors, J. Tauc (Ed.), Plenum, London, 1974.

[13] R. S. Weber, J. Catal., 151 (1995) 470.

[14] X. Gao, S. R. Bare, B. M. Weckhuysen, I. E. Wachs, J. Phys. Chem. B, 102 (1998) 10842.

[15] A. M. A. Cruz, J. G. Eon, Appl. Catal. A, 167 (1998) 203.

[16] C. Pak, A. T. Bell, T. Don Tilley, J. Catal., 206 (2002) 49.

[17] F. Arena, F. Frusteri, A. Parmaliana, Catal. Lett., 60 (1999) 59.

[18] F. Arena, F. Frusteri, A. Parmaliana, Appl. Catal. A, 176 (1999) 189.

[19] G. Deo, I. E. Wachs, J. Phys. Chem., 95 (1991) 5889.

[20] A. Corma, J. M. López Nieto, N. Paredes, M. Perez, Appl. Catal. A, 97 (1993) 159.

[21] M. L. Occelli, J. M. Stencel, ACS Symp. Ser., 375 (1988) 195.

[22] P. Concepción, J. M. López Nieto, J. Perez-Pariente, J. Mol. Catal. A**,** 97 (1995) 173.

[23] G. Busca, G. Ricchiardi, D. S. H. Sam, S. C. Volta, J. Chem. Soc. Faraday Trans., 90 (1994) 1161.

[24] X. Gao, P. Ruiz, Q. Xin, X. Guo, B. Delmon, J. Catal., 148 (1994) 56.

[25] X. Gao, P. Ruiz, Q. Xin, X. Guo, B. Delmon, Catal. Lett., 23 (1994) 321.

[26] R. X. Valenzuela, V. Cortés Corberán, Top. Catal., 11/12 (2000) 153.

[27] M. L. Occelli, R. S. Maxwell, H. Eckert, J. Catal., 137 (1992) 36.

[28] O. B. Lapina, A. V. Simakov, V. M. Mastikhin, S. A. Veniaminov, A. A. Shubin, J. Mol. Catal., 50 (1989) 55.

[29] Y. Sakurai, T. Suzaki, K. Nakagawa, N. Ikenaga, H. Aota, T. Suzuki, Chem. Lett., (2000) 526.

[30] S. Köbel, D. Schneider, C.Chr. Schüler, L.J. Gauckler, J. Eur. Ceram. Soc., 24 (2004) 2267.

[31] G. M. Clark, R. J. Morley, Solid State Chem., 16 (1976) 429.

[32] R. C. Kerby, J. R. Wilson, Can. J. Ceram, 51(7), (1973) 1032.

CHAPTER 5

Catalytic Activity Studies And Correlation With Structure of V-Mg-O Catalysts

SECTION A-CATALYTIC ACTIVITY STUDIES

5.1. INTRODUCTION

The first part of this Chapter discusses the results of oxidative dehydrogenation of ethylbenzene to styrene using N_2O over V-Mg-O catalysts. The catalysts were characterized after the reaction and the results are included in Section B. The relation ship of activity and selectivity of the catalysts with their structure, determined by characterization of fresh and spent catalysts, is also discussed. The experimental setup and analytical procedure are same as those described in Chapter 3.

5.2. RESULTS AND DISCUSSION

5.2.1. Effect of nitrous oxide

Table 5.1 shows the styrene yields observed at 773 K in nitrous oxide and nitrogen atmospheres. The reaction was conducted using 30 V-Mg-O at an ethylbenzene WHSV of 1 h^{-1} and at a nitrous oxide flow rate of 1200 h^{-1}.

Table 5.1: Dehydrogenation of ethylbenzene under nitrous oxide and nitrogen flows over V-Mg-O catalyst

	N_2O atmosphere					N_2 atmosphere				
TOS (h)	EB Conv (%)	Sty Sel (%)	Sty Yield (%)	(Benz + Tol) Sel (%)	Sty oxide Sel. (%)	EB Conv (%)	Sty Sel (%)	Sty Yield (%)	(Benz + Tol) Sel (%)	Sty oxide Sel. (%)
2	65.34	97.23	63.53	2.08	0.69	11.42	78.63	8.98	21.19	0.61
3	64.48	97.69	62.99	2.11	0.20	10.53	78.35	8.25	21.46	0.76
4	58.36	97.38	56.83	2.04	0.57	9.78	82.31	8.05	17.69	0.51

Reaction conditions: *Catalyst, 30 V-Mg-O; Reaction temperature, 773 K; WHSV of EB, 1 h^{-1}; GHSV of N_2O, 1200 h^{-1}.*

The styrene yield in the presence of nitrous oxide is at least 5 times higher than that in nitrogen atmosphere at 773 K. The yield of styrene decreased with time on stream for both N_2O and N_2 atmospheres, however it was considerably higher in N_2O atmosphere throughout the period studied. The combined selectivity for benzene and toluene was lower in nitrous oxide atmosphere, indicating a lower rate of dealkylation of ethylbenzene, as observed for VO_x/Al_2O_3 catalysts.

5.2.2. Effect of reaction temperature

The effect of reaction temperature on the dehydrogenation of ethylbenzene for 30 V-Mg-O catalyst at a reaction time of 3 h is shown in Fig. 5.1. The conversion of ethylbenzene is low at 623 K, being 9.6% and increased to 58.4% at 773 K. The styrene yield also increased with increasing reaction temperature. At low temperatures, conversion of N_2O was low and increase in temperature enhanced the conversion. The amount of N_2O that react with ethylbenzene showed a decrease with increasing temperature. Hence most of the N_2O converted at higher temperatures undergo decomposition, rather than reaction with ethylbenzene. The selectivity of styrene oxide, which is around 20% at 623 K, decreased with increasing temperature. Hence the conversion of styrene to styrene oxide is more probable at lower temperatures. The dealkylation of ethylbenzene leading to the formation of benzene and toluene increased slightly with increasing temperature. The total yield of benzene, toluene and styrene oxide was very low, being less than 5% at all temperatures.

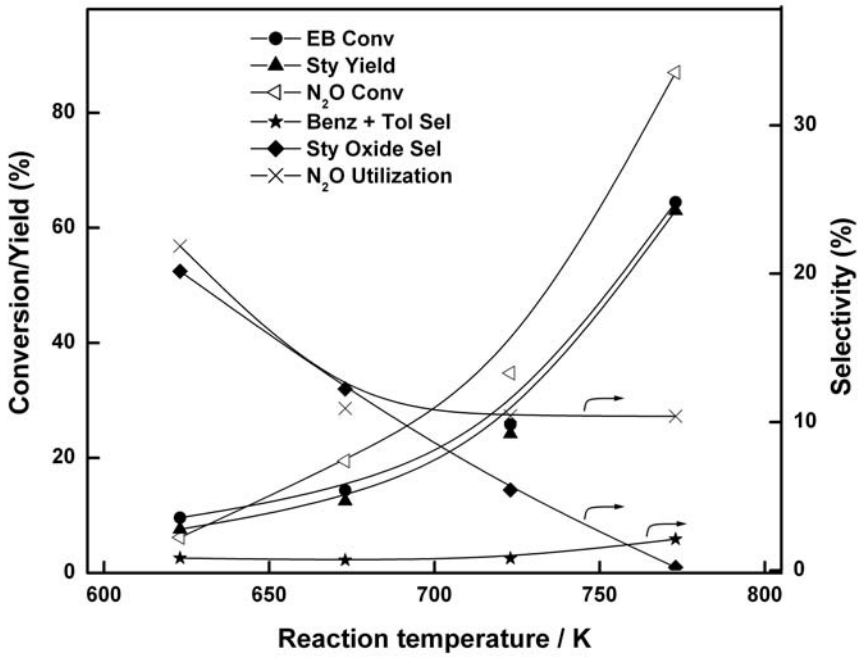

Figure 5.1: *Effect of reaction temperature on conversions of ethylbenzene and N_2O, styrene yield and selectivities of products. (,) ethylbenzene conversion; (7) styrene yield; (Ξ) N_2O conversion (ξ) sum of benzene and toluene selectivities; (Λ) styrene oxide selectivity; (□) N_2O utilized for ethylbenzene conversion.*
Reaction conditions: Catalyst, 30 V-Mg-O; TOS, 3 h; GHSV of N_2O, 1200 h^{-1}; WHSV of EB, 1 h^{-1}.

5.2.3. Turnover rate, Areal rate and Styrene selectivity

Figure 5.2 shows the initial rates of ODH of ethylbenzene per vanadium atom at 623 K plotted as a function of vanadia loading. The turnover rate increased with increasing vanadia loading up to 10 wt% (surface density from 1 to 6 V nm^{-2}) and then decreased with further increase in vanadia loading. Since the catalysts contain magnesium orthovanadate as the vanadium-containing phase, the difference in activity may be attributed to the size of the orthovanadate domains, which varies as a function of vanadia loading. The characterization of catalysts, discussed in Chapter 4, reveals that the surface possesses monomeric, tetrahedral vanadium (V) species, similar to that exist in magnesium

orthovanadate. As the vanadia loading increases, the size of domains containing these vanadium species increases. The trend exhibited by turnover rate with vanadia loading shows that vanadia domains should be of appropriate size for maximum activity. The activity of very large domains (bulk-like phases) and very small domains are lower than that of domains of intermediate size. Similar trend of activity with surface density was observed for the ODH of propane on V-Mg-O, VO_x/ZrO_2 and VO_x/Al_2O_3 catalysts [1,2]. It is proposed for these catalysts that the decrease in specific activity after reaching the maximum is due to the formation of multilayers of the active form of vanadia which prevents the accessibility of V atoms lying below the surface which is the most probable explanation in the present case also. The specific activity, conversion of ethylbenzene per unit surface area of the catalysts, increased rapidly with increasing vanadia loading up to 10 wt% (surface density up to about 6 V nm^{-2}), then decreased and remained constant with further increase in vanadia loading (Fig. 5.2). This confirms the proposition that formation of larger crystallites of $Mg_3(VO_4)_2$ occur when the surface density exceeds 6 V nm^{-2} due to which all the vanadium atoms are not accessible for the reactants. This is similar to the trend observed by Pak *et al* [3] for ODH of propane using V-Mg-O catalysts. Hence it can be concluded that activity of these catalysts is due to the presence of small, two-dimensional domains of $Mg_3(VO_4)_2$ on the surface of MgO rather than crystallites of bulk $Mg_3(VO_4)_2$.

Figure 5.2 also shows the styrene selectivity at an ethylbenzene conversion level of 10% as a function of the vanadia loading at 623 K. The selectivity to styrene increased with vanadia loading up to 10 wt% (6 V nm^{-2}), after which it decreased. The trend is similar to that observed for activity and size of the domains containing vanadium species seems to be the determining factor here also. The dehydrogenation of ethylbenzene to styrene is most favorable when the domains are of intermediate size and the rate of side reactions like dealkylation seems to be higher with bulk-like phases. Hence styrene selectivity decreases with formation of multilayers of vanadia species. The observed trend in selectivity with the apparent surface density of VO_x is very similar to that reported previously for vanadia dispersed on MgO, ZrO_2 and Al_2O_3.

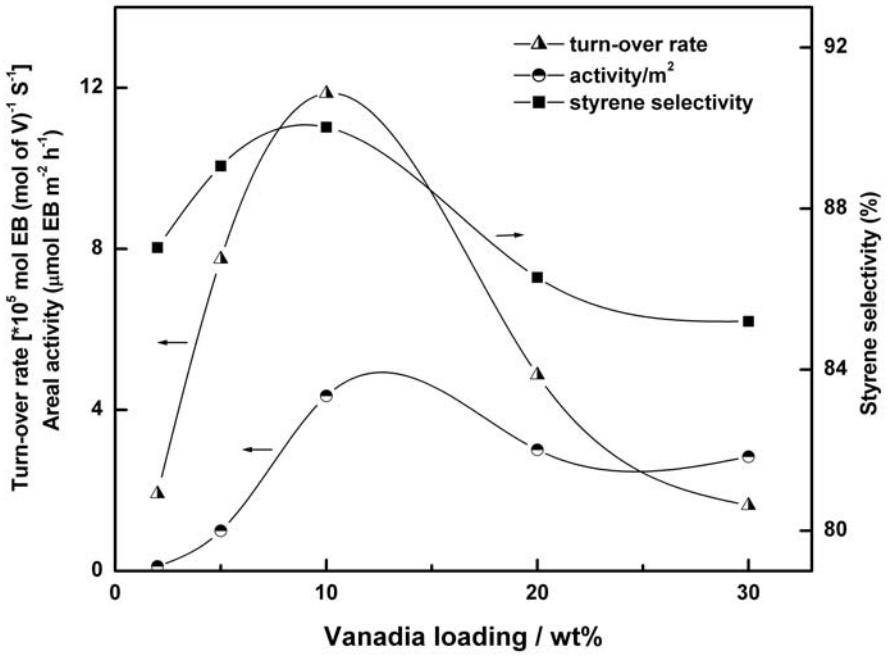

Figure 5.2: *Effect of vanadia loading on the initial rate of ethylbenzene conversion normalized per V atom (▲), per unit surface area of the catalyst (●) and the selectivity of styrene at 10% conversion level (■). Reaction temperature, 623 K.*

5.2.4. Effect of space velocity

Figure 5.3 shows the effect of variation of space velocity of ethylbenzene on the dehydrogenation of ethylbenzene. The feed rate of ethylbenzene was changed in these experiments, keeping the amount of catalyst constant, to vary the space velocity. With increasing space velocity, ethylbenzene conversion and styrene yield decreased while the amount of styrene oxide increased. Hence the dehydrogenation of ethylbenzene to styrene is higher at higher contact time. The total selectivity of dealkylation products, benzene and toluene, decreased marginally with increasing space velocity, indicating the rate of dealkylation is proportional to contact time.

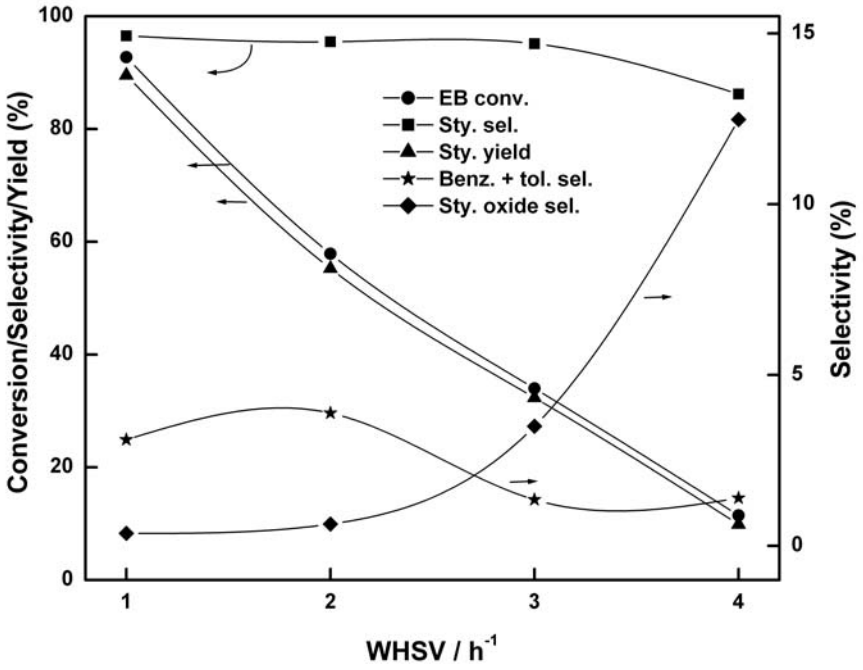

Figure 5.3: *Effect of variation of space velocity of ethylbenzene on ethylbenzene conversion, styrene yield and product selectivities. (.) ethylbenzene conversion; (!) styrene selectivity (7) styrene yield; (ξ) sum of benzene and toluene selectivities; (Λ) styrene oxide selectivity.*
Reaction conditions: Catalyst, 10 V-Mg-O; Reaction temperature, 723 K; TOS, 3 h; GHSV of N_2O, 1200 h^{-1}.

5.2.5. Effect nitrous oxide flow rate

Figure 5.4 shows the variation in yields of styrene and by-products as a function of nitrous oxide flow rate. The yield of styrene decreased when GHSV of N_2O is lower than 1200 h^{-1} while at space velocities higher than this, the yield was more or less similar. This means that very high flow rates of N_2O are not much helpful in increasing styrene yield since the maximum possible yield of styrene at the reaction temperature is already achieved. The selectivities of benzene and toluene increased only marginally with increasing flow rate.

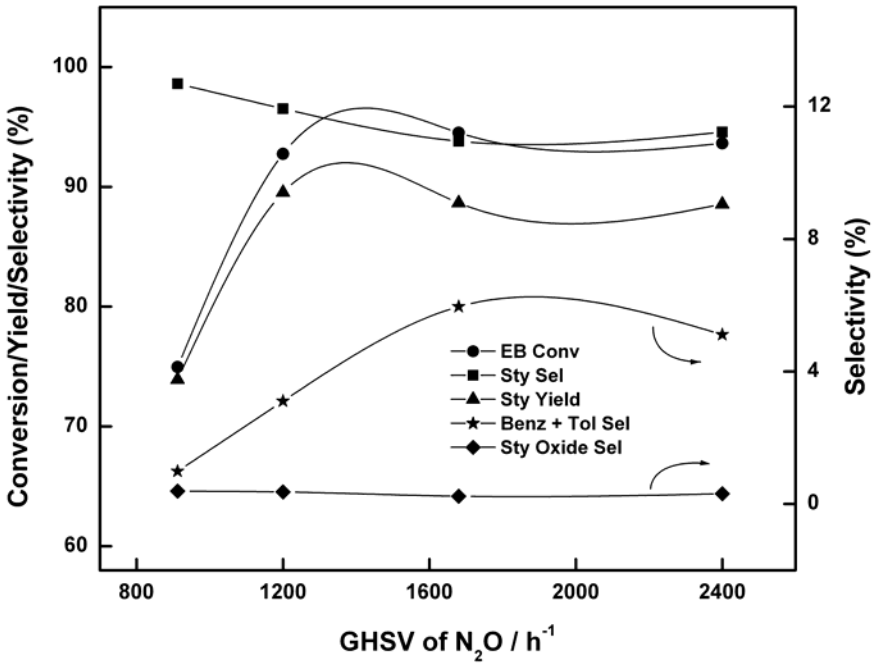

Figure 5.4: *Conversion of ethylbenzene, yield and selectivities of styrene and by-products as a function of nitrous oxide flow rate. (.) ethylbenzene conversion; (!) styrene selectivity (7) styrene yield; (ξ) sum of benzene and toluene selectivities; (ʌ) styrene oxide selectivity. Reaction conditions: Catalyst, 10 V-Mg-O; Reaction temperature, 723 K; reaction time, 3 h; WHSV of EB, 1h^{-1}.*

5.2.6. The time on stream behavior

The activity and selectivity of the V-Mg-O catalyst were studied as a function of time on stream. The results of the reaction conducted at 723 K using 5 V-Mg-O with EB WHSV of 1 h^{-1} and at a nitrous oxide flow rate of 1200 h^{-1} are given in Fig. 5.5. A slow and steady decrease in conversion of ethylbenzene was observed with time on stream, the decrease being around 7.5% after 10 hours of reaction. The selectivity of styrene slightly increased with time on stream showing that, under the present experimental conditions, the selectivity is better for catalyst with marginal deactivation. The catalyst was regenerated in flowing dry air at 773 K for 8h and the experiment was repeated under similar reaction conditions, the results of which are also shown in same figure. The trends observed in

activity and selectivity are more or less similar, indicating the stability and regenerability of the catalyst.

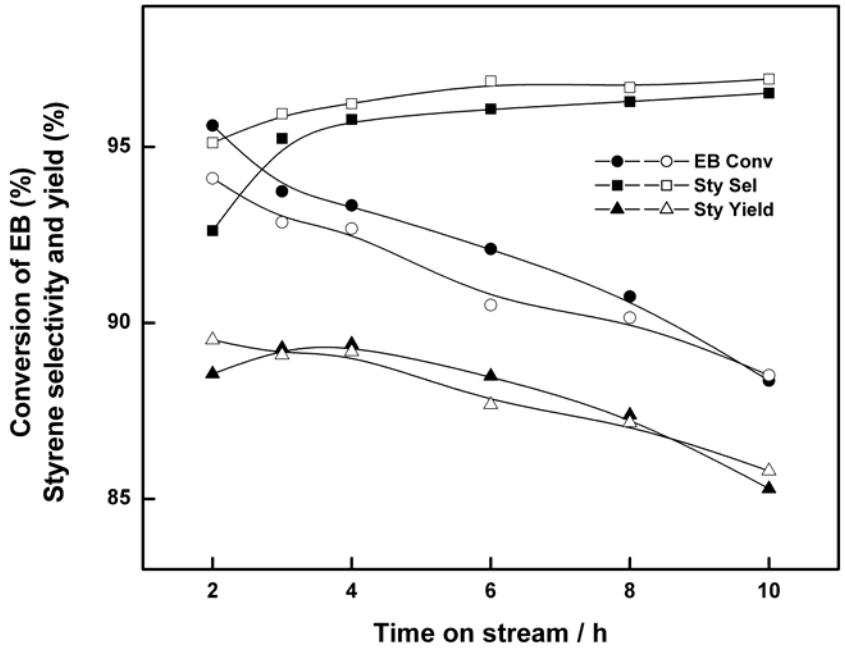

Figure 5.5: *The activity and selectivity of fresh and regenerated catalysts as a function of time on stream. (,) ethylbenzene conversion; (!) styrene selectivity; (7) styrene yield. Solid symbols, reaction with fresh catalyst; open symbols, reaction with regenerated catalyst. Reaction conditions: Catalyst, 5 V-Mg-O; Reaction temperature, 723 K; WHSV of EB, 1h^{-1}; GHSV of N_2O, 1200 h^{-1}.*

It can be summarized that higher temperatures, higher contact time of ethylbenzene with catalyst and intermediate flow rates of N_2O favor higher styrene yield in oxidative dehydrogenation of ethylbenzene with N_2O over V-Mg-O catalysts. This is similar to the observation made for ODH of EB using VO_x/Al_2O_3 catalysts, as described in Chapter 3. The structure of vanadia species on V-Mg-O catalysts is very important in determining the catalytic performance. The catalysts with intermediate vanadia loadings (near monolayer catalysts) are more active than those having bulk vanadia phases.

SECTION B- CHARACTERIZATION OF SPENT CATALYSTS AND STRUCTURE-ACTIVITY CORRELATION

5.3. CHARACTERIZATION OF SPENT CATALYSTS

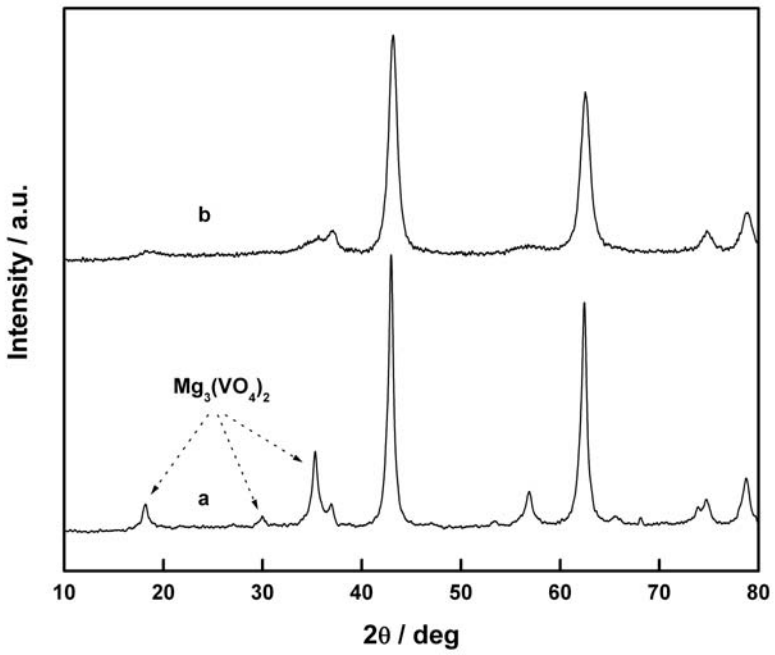

Figure 5.6: *Powder X- ray diffraction patterns of 30 V-Mg-O after* ***(a)*** *dehydrogenation reaction under N_2O flow at 673 K for 4 h* ***(b)*** *dehydrogenation reaction under N_2 flow at 673 K for 4 h.*

The XRD patterns of the catalyst, 30 V-Mg-O after dehydrogenation reaction at 773 K for 4 h in N_2O and N_2 atmospheres are shown in Fig. 5.6. The pattern of the sample after dehydrogenation reaction in N_2O atmosphere shows peaks characteristic of magnesium orthovanadate, though the intensity of these peaks reduced considerably compared to that of fresh catalyst. However, these peaks were completely disappeared after the dehydrogenation reaction in N_2 atmosphere.

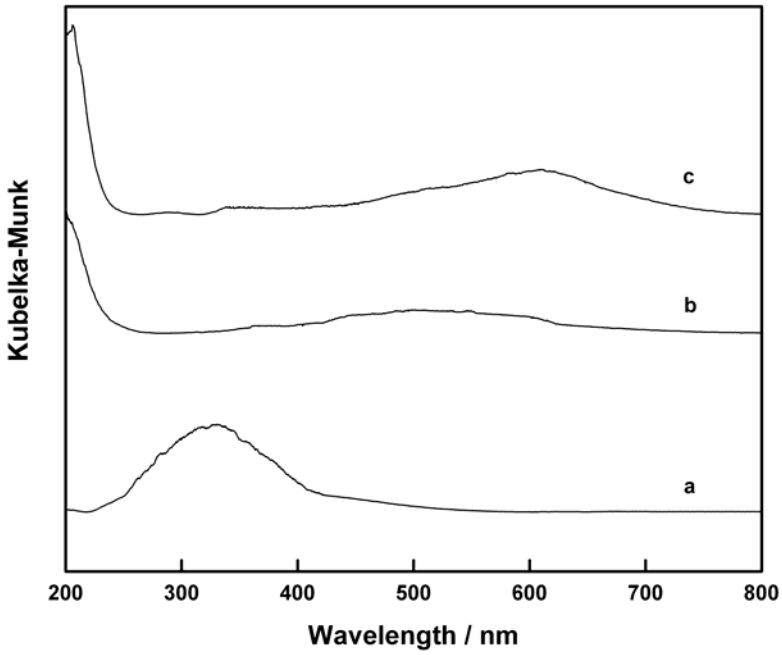

Figure 5.7: *Diffuse reflectance UV–visible spectra of 30 V-Mg-O after* ***(a)*** *dehydrogenation reaction under N_2O flow at 673 K for 4 h* ***(b)*** *dehydrogenation reaction under N_2 flow at 673 K for 4 h* ***(c)*** *after reduction with H_2 at 673 K for 4 h.*

The diffuse reflectance UV-visible spectra of 30 V-Mg-O catalysts after various treatments are shown in Fig. 5.7. After the dehydrogenation of ethylbenzene in presence of N_2, the catalyst showed a new broad and weak band with an absorption maximum between 500 and 700 nm that is characteristic of the V^{4+} d-d transitions (Fig. 5.7b). This band can be observed prominently after the reduction of fresh 30 V-Mg-O catalyst with H_2 at 773 K (Fig. 5.7c). This band was not observed for the catalyst used for dehydrogenation in N_2O atmosphere (Fig. 5.7a). Hence a higher extent of reduction of vanadium species occurs during the reaction in N_2 atmosphere. The reduction of vanadium species during the reaction is reversible since the band at 270 nm reappeared and the band due to V^{4+} disappeared when the reduced catalyst is treated in N_2O atmosphere at 773 K for 4 h (not shown).

Figure 5.8 shows the FTIR spectra of 30 V-Mg-O catalyst after different treatments. The intensity of the band at 860 cm^{-1}, characteristic of $Mg_3(VO_4)_2$, was reduced after the dehydrogenation reaction in N_2O atmosphere (Fig. 5.8a) while the band disappeared after the reaction in N_2 atmosphere (Fig. 5.8b). This again shows a greater extent of reduction for the catalyst when the reaction is carried out in N_2 atmosphere. The spectra of 30 V-Mg-O reduced in H_2 and reoxidised in N_2O are also given in Fig. 5.8 for comparison. The band at 860 cm^{-1}disappeared after treating fresh 30 V-Mg-O in H_2 at 773 K and reappeared when the reduced catalyst was treated in N_2O atmosphere at 773 K for 4 h.

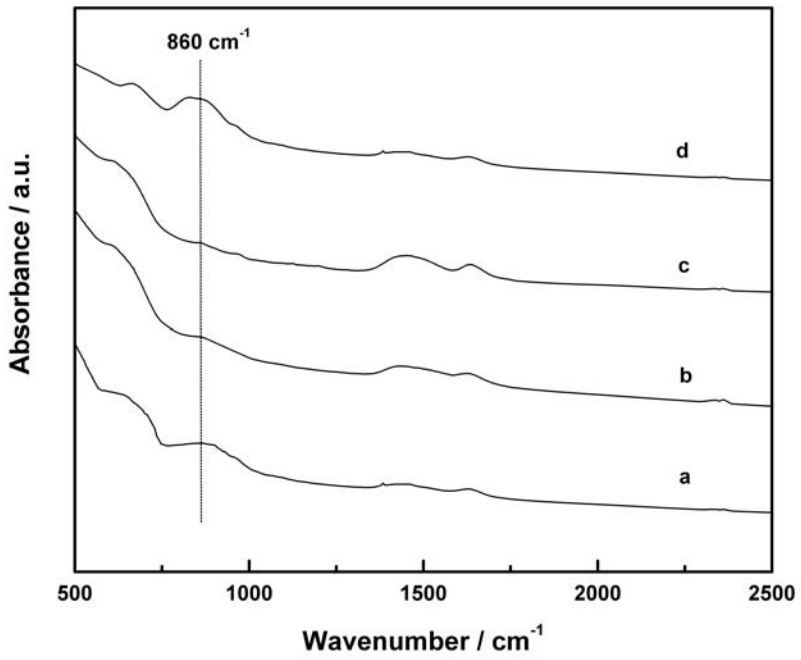

Figure 5.8: *FTIR spectra of 30 V-Mg-O after* ***(a)*** *dehydrogenation reaction under N_2O flow at 673 K for 4 h* ***(b)*** *dehydrogenation reaction under N_2 flow at 673 K for 4 h* ***(c)*** *after reduction with H_2 at 673 K for 4 h* ***(d)*** *after treating the reduced catalyst under N_2O flow at 673 K for 4h.*

The EPR spectra of 5 V-Mg-O, measured at 298 K, after dehydrogenation reaction in presence of nitrous oxide and nitrogen, at 673 K for 4h, are given in Fig. 5.9 together with the spectrum of freshly calcined sample. The EPR spectra of the catalysts after the

dehydrogenation reaction contain a strong signal superimposed on the spectrum of V^{4+} that may be originated from the paramagnetic centers of the carbon deposited on the catalyst during the reaction. As observed for VO_x/Al_2O_3 catalyst, this signal is more intense for the catalyst used for dehydrogenation reaction in nitrogen, indicating higher carbon deposition, compared to that in nitrous oxide. It should also be mentioned that the intensity of the signal corresponding to deposited carbon is lower for spent V-Mg-O catalysts as compared to that of spent VO_x/Al_2O_3 catalysts. The lesser coke deposition for V-Mg-O catalysts may be ascribed to the basicity of the support, MgO while in VO_x/Al_2O_3 catalysts, the support is acidic.

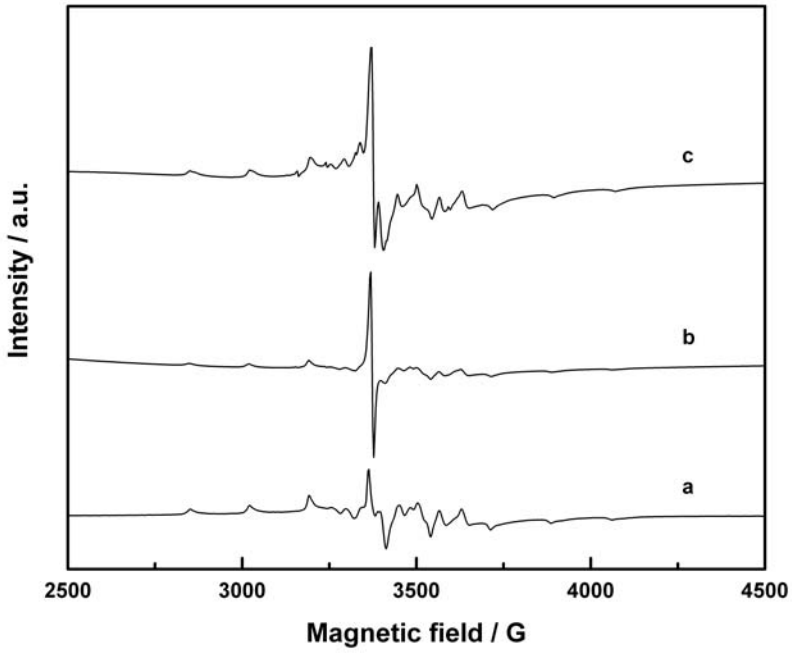

Fig. 5.9: *The electron paramagnetic resonance spectra of 5 V-Mg-O catalyst, measured at 298 K,* ***(a)*** *calcined at 823 K for 4h* ***(b)*** *after oxidative dehydrogenation reaction in nitrous oxide atmosphere at 673 K for 4h and* ***(c)*** *after oxidative dehydrogenation reaction in nitrogen atmosphere at 673 K for 4h.*

It is also clear from the spectra that when the dehydrogenation is carried out in nitrogen atmosphere, the catalyst undergoes deeper reduction than that occurs during the

dehydrogenation reaction in nitrous oxide atmosphere. As mentioned in the previous chapter, the vanadium (V) species in the surface layer, on reduction in H_2 environment, gives EPR signal with hyperfine pattern, while those in the bulk give signal without hyperfine features. The broad signal overlapping the hyperfine splitting pattern, observed for the catalyst used for dehydrogenation reaction in nitrogen atmosphere, shows the presence of reduced bulk vanadium species in this case.

The characterization of catalysts after reaction reveals that the vanadium species is continuously reduced when the dehydrogenation is carried out in N_2 atmosphere. Though the reduction of vanadium species does takes place during the reaction in N_2O atmosphere, the reoxidation of the vanadium species must be occurring in this case, owing to the mild oxidizing property of N_2O. The higher styrene yield in the presence of N_2O than that in N_2 atmosphere can be ascribed to the ability of N_2O to reoxidise vanadium that got reduced during the reaction, though the complete reoxidation was not observed. This is similar to the effect reported by Sakurai *et al* [4] for the dehydrogenation of ethylbenzene with CO_2 in which the vanadium species was kept at a higher oxidation state during the reaction due to the oxidation capability of CO_2.

5.4. CATALYTIC ACTIVITY AND STRUCTURE OF V-Mg-O CATALYST

As mentioned in the previous chapter, structural characterization of V-Mg-O catalysts shows that at lower loadings, isolated VO_4 species similar to that exist in magnesium orthovanadate and at higher loadings, magnesium orthovanadate domains are present on catalysts. With increasing vanadia loading, the size of orthovanadate domains increase, finally leading to the appearance of bulk-like $Mg_3(VO_4)_2$ on 30 V-Mg-O. The rate of ethylbenzene conversion per V atom increases with increasing vanadia loading, reaches a maximum at 10 wt% and decreases when the loading is increased further (Fig. 5.2). Consideration of the structural characterization data together with catalytic activity indicates that the surfaces of most active catalysts possess small domains of $Mg_3(VO_4)_2$. The formation of bulk-like orthovanadate on the surface at high loadings leads to decrease in activity and selectivity, since the fraction of V atoms that lie below the first layer are not accessible to the reactants. Previous reports suggest that $Mg_3(VO_4)_2$ phase is mainly

responsible for the activity and selectivity for the dehydrogenation of ethylbenzene, in the presence of CO_2 [4] and oxygen [5]. Moreover, the most active species for propane ODH is also suggested as VO_4^{3-} species existing in a surface structure that is essentially identical to that present in $Mg_3(VO_4)_2$, for V-Mg-O catalysts prepared by conventional and thermolytic methods [3,6-10].

In the case of VO_x/Al_2O_3 catalysts, the structure of dispersed VO_x species depends on the VO_x surface density, transforming from monomeric to polymeric V^{5+} species and bulk-like vanadia phases with increasing surface density. Here the maximum activity, in terms of turnover rate, is observed for catalyst with monolayer vanadia loading. For V-Mg-O catalysts also, the maximum activity is observed for intermediate vanadia loadings, however, a direct comparison with VO_x/Al_2O_3 catalysts is not possible since the molecular structure of vanadia species is different. For V-Mg-O catalysts, the concepts of vanadia monolayer and surface density are not very appropriate, though these terms are mentioned in this Chapter in some places, since MgO support doesn't disperse vanadia species like alumina support. A gradual transformation from monomeric to polymeric vanadia species and the formation of a monolayer, as described for VO_x/Al_2O_3 catalysts, cannot be anticipated for V-Mg-O catalysts. Instead, it forms mixed phase with vanadia at low loadings itself due to its basic nature. Hence, it is more appropriate to explain the variation in activity and selectivity with vanadia loading based on the domain size of the mixed phase, magnesium orthovanadate, for V-Mg-O catalysts.

As observed for VO_x/Al_2O_3 catalysts, V-Mg-O catalysts show enhancement in styrene yield in presence of N_2O. N_2O is able to keep vanadium at a higher average oxidation state, as evidenced by characterization of spent catalysts, due to which styrene yield is higher compared to that in N_2 atmosphere. Since this enhancement in specific activity is observed for both series of catalysts, it seems that the effect is independent of support and vanadia molecular structure.

Hanuza *et al* [11] suggested that catalytic properties of V_2O_5/MgO catalysts are related to the structure of their active sites consisting of V(V) and V(IV) ions. The oxygen bridge linking these ions allows electron exchange between them and acts as an electron transmitter. It is suggested that both V(V) and V(IV) cooperate closely in the oxidative

dehydrogenation process and hence the activity in oxidative dehydrogenation process depends critically on the equilibrium between these two oxidation states. It can be inferred that N_2O helps to maintain this equilibrium and hence leads to higher activity.

Two mechanisms have been suggested for the oxidative dehydrogenation of ethylbenzene in presence of molecular oxygen. The first one involves the formation of a π-complex involving ethylbenzene and surface V=O group. The second mechanism proceeds through the formation of the σ-complex [11]. Chen *et al* [12-14] proposed a mechanism for ODH of propane over VO_x-based catalysts. All of these mechanisms of ODH reactions are based on a highly dynamic model of the working catalyst. Figure 5.10 shows a plausible mechanism for the current reaction investigated, ODH of ethylbenzene with N_2O, based on the above-proposed mechanisms. It can be assumed that the methylene C-H bond in ethylbenzene molecule first interacts with lattice oxygen leading to weak adsorption of the molecule on the oxide surface (II in Fig. 5.10). The adsorbed ethylbenzene molecule reacts with a vicinal lattice oxygen atom to form an alkoxide species and an OH group (III). This involves a transition state in which two electrons are transferred from lattice oxygens to metal centers. The transition state contains incipiently cleaved C-H and V-O bonds and partially formed O-C and O-H bonds. It is found for ODH of propane that that the turnover rate is controlled by the dissociation of the first methylene C-H bond in propane. The same may be true for ODH of ethylbenzene also. The C-H activation step ultimately involve two lattice oxygen atoms and each one provides one electron to either a single vanadium center, leading to a two-electron reduction (V^{5+} to V^{3+}), or to two vanadium centers, each of which undergoes a one-electron reduction (V^{5+} to V^{4+}). The second path is more probable because of lower activation energy [15]. The activation of second C-H bond forms styrene and a surface hydroxyl group (IV). In the next step, elimination of water molecule occurs via the condensation of surface hydroxyl groups (V). Finally, N_2O reoxidise the reduced vanadium centers.

This mechanism is applicable for both V-Mg-O and VO_x/Al_2O_3 catalysts and explains why turnover rates are higher at intermediate vanadia loadings. At least two adjacent vanadium atoms are required to accommodate the transition state and the products in the rate-determining step, which demands vanadium oxide domains of suitable

dimensions. Very small oxide domains should undergo less favorable two-electron reduction of individual vanadium atoms during each ODH catalytic turnover and hence exhibit low turnover rates. It explains also why N_2O enhances the activity. The role of N_2O as oxidizing agent is crucial in the final step wherein the active oxygen species generated from nitrous oxide reoxidize the reduced vanadium centers and the catalytic cycle is continued. It should be made clear that the mechanism proposed is a hypothetical one and has to be supported by experimental evidences or by molecular simulation studies. Nevertheless, it is the most probable mechanism, consistent with the current experimental observations, as explained in the preceding sentences.

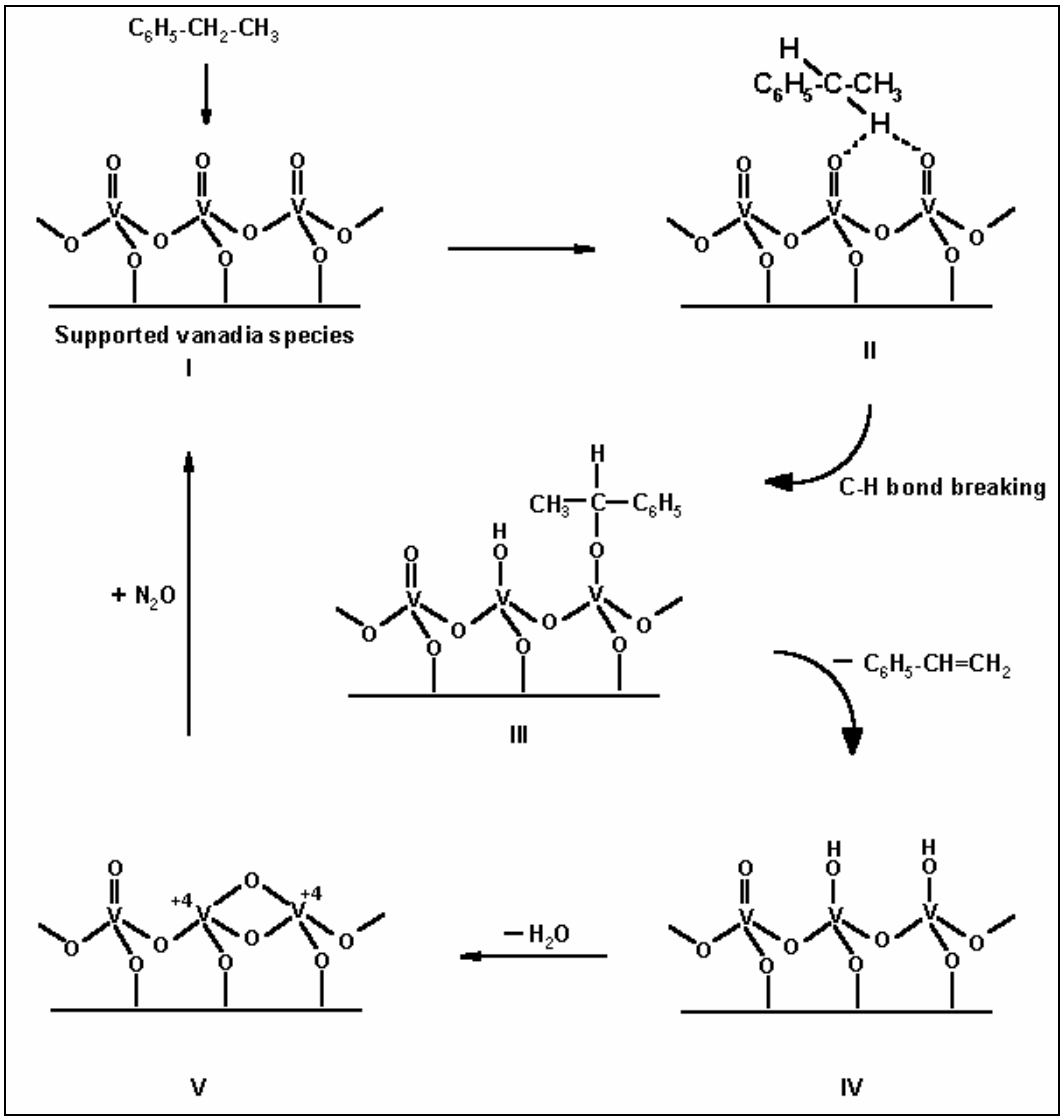

Fig. 5.10: Tentative mechanism of oxidative dehydrogenation of ethylbenzene to styrene in presence of N_2O as oxidizing agent on supported vanadia catalysts.

5.5. REFERENCES

[1] A. Khodakov, J. Yang, S. Su, E. Iglesia, A. T. Bell, J. Catal., 177 (1998) 343.

[2] A. Khodakov, B. Olthof, A. T. Bell, E. Iglesia, J. Catal., 181 (1999) 205.

[3] C. Pak, A. T. Bell, T. Don Tilley, J. Catal., 206 (2002) 49.

[4] Y. Sakurai, T. Suzaki, N. Ikenaga, T. Suzuki, Appl. Catal. A., 192 (2000) 281.

[5] W. S. Chang, Y. Z. Chen, B. L. Yang, Appl. Catal. A, 124 (1995) 221.

[6] J. M. Lopez Nieto, A. Dejoz, M. I. Vazquez, W. O'Leary, J. Cunningham, Catal. Today, 40 (1998) 215.

[7] M. A. Chaar, D. Patel, M. C. Kung, H. H. Kung, J. Catal., 105 (1987) 483.

[8] D. Patel, M. C. Kung, H. H. Kung, in: Proc. 9th Int. Congr. Catal., Calgary, Vol. 4, p.1554, M. J. Phillips, M. Ternan (Eds.), The Chemical Institute of Canada, Ottawa (2nd. ed.), 1988.

[9] A. Corma, J. M. López Nieto, N. Paredes, A. Dejoz, I. Vasquez., in "New Developments in Selective Oxidation II", C. Cortés Corberán, S. Vic Bellón (Eds.), Stud. Surf. Sci. Catal., Vol. 82, p. 113, Elsevier, Amsterdam, 1994.

[10] M. C. Kung, H. H. Kung. J. Catal., 134 (1992) 668.

[11] J. Hanuza, B. Jezowska-Trzebiatowska, W. Oganowski, J. Mol. Catal., 29 (1985) 109.

[12] K. Chen, A. T. Bell, E. Iglesia, J. Catal., 209 (2002) 35.

[13] K. Chen, A. Khodakov, J. Yang, A. T. Bell, E. Iglesia, J. Catal., 186 (1999) 325.

[14] K. Chen, E. Iglesia, A. T. Bell, J. Phys. Chem. B, 105 (2001) 646.

[15] F. Gilardoni, A. T. Bell, A. Chakraborty, P. Boulet, J. Phys. Chem. B, 104 (2000) 12250.

CHAPTER 6

General Conclusions And Recommendations For Further Research

6.1. Summary

This thesis describes the preparation, characterization and catalytic evaluation of alumina and magnesia supported vanadia catalysts (VO_x/Al_2O_3 and V-Mg-O). The reactions studied were oxidative dehydrogenation of ethylbenzene to styrene and preferential oxidation of CO in presence of excess hydrogen (PROX). VO_x/Al_2O_3 catalysts were found to be active for both reactions while V-Mg-O catalysts didn't show considerable activity for PROX reaction. This chapter present a brief summary of the work described in previous chapters, general conclusions arrived from the work and suggestions for further research.

Chapter 1 gives an introduction about supported vanadia catalysts, ethylbenzene dehydrogenation to styrene and preferential oxidation of CO. It is mainly a review of the literature on these topics. The current-knowledge about the structure of supported vanadia catalysts is briefly discussed. The chemistry, thermodynamics and current commercial processes for the dehydrogenation of ethylbenzene to styrene are also described in this chapter. It gives the limitations of current processes, which necessitates the development of alternate processes. A brief description about the current research for alternate processes is also given. The chapter also gives a brief introduction about preferential oxidation of CO. Finally, the aim of the thesis is given: to check the viability of oxidative dehydrogenation of ethylbenzene using nitrous oxide as an alternate process and to understand the relation between structure of supported vanadia catalysts and their catalytic activity for the above said reaction and PROX reaction.

Chapter 2 describes the preparation and characterization of VO_x/Al_2O_3 catalysts. The catalysts with different vanadia loadings were prepared by impregnation and characterized by ICP-AES, XRD, SEM, surface area (by BET method), TG-DTA, IR, Laser Raman, UV-visible, XPS, EPR and solid-state NMR. Theory and experimental procedure for each technique are also described briefly in this chapter.

The characterization of catalysts revealed that the molecular structure of vanadia species depends on the coverage of vanadia on alumina support. Monomeric vanadia species are predominant at low vanadia loadings while polymeric vanadia species increase

with increasing vanadia loading. When vanadia loading exceeds that required for a monolayer, bulk-like phases of $AlVO_4$ and V_2O_5 are formed on the catalyst.

Chapter 3 describes the investigation of oxidative dehydrogenation of ethylbenzene in presence of N_2O over VO_x/Al_2O_3 catalysts. The catalyst showed good activity and selectivity for the dehydrogenation of ethylbenzene to styrene which is much better than those observed when the reaction is carried out in N_2 atmosphere. In general, the activity increases with reaction temperature, contact time and shows a maximum at intermediate nitrous oxide flow rate. The activity critically depends on the molecular structure of vanadia species. The turnover rate increases with increasing vanadia loading till the formation of a monolayer which means that polymeric vanadia species is more active than monomeric species for this reaction. Activity decreases again when the vanadia loading exceeds that required for a monolayer which shows the inherent low activity of bulk vanadia phases. Hence, a monolayer containing polymeric vanadia species is most suitable for this reaction.

This chapter also describes the characterization of spent catalysts. Investigation of the spent catalysts with XRD, FTIR, UV-visible and EPR showed that on an average, vanadium is in a higher oxidation state after the reaction in nitrous oxide atmosphere compared to that in nitrogen atmosphere. The higher activity in nitrous oxide atmosphere can be attributed to higher average oxidation state of vanadium due to the mild oxidation capability of N_2O.

The results of preferential oxidation of CO in excess of H_2 are also given in Chapter 3. The activity and selectivity for CO oxidation exhibit maximum values at intermediate temperature in the range studied. The activity is higher at higher contact time and O_2/CO ratios. The decrease in activity with increasing vanadia loading shows that the presence of monomeric vanadia species is more favourable for this reaction.

Chapter 4 describes the preparation and characterization of V-Mg-O catalysts. The catalysts were prepared by impregnation and characterized by ICP-AES, XRD, SEM, surface area (by BET method), TG-DTA, IR, Laser Raman, UV-visible, EPR and solid-state NMR. The amount of vanadia deposited on the catalysts varied from 2 to 30 wt%.

As observed for VO_x/Al_2O_3 catalysts, the molecular structure of vanadia species on V-Mg-O catalysts depends on the coverage of vanadia on magnesia support. At lower vanadia loadings, vanadia exist in an X-ray amorphous state. However, these are mainly isolated tetrahedral vanadium (V) species, similar to that exist in magnesium orthovanadate, $Mg_3(VO_4)_2$, as revealed by techniques like UV-visible, ^{51}V solid state NMR and laser Raman spectroscopies. Bulk-like orthovanadate phase, detectable by XRD, appear at a vanadia loading of 30 wt%.

Chapter 5 describes the investigation of oxidative dehydrogenation of ethylbenzene in presence of N_2O over V-Mg-O catalysts. As observed for VO_x/Al_2O_3 catalysts, V-Mg-O catalysts also showed good activity and selectivity for the dehydrogenation of ethylbenzene to styrene which is much better than those observed when the reaction is carried out in N_2 atmosphere. In general, the activity increases with reaction temperature, contact time and shows a maximum at intermediate nitrous oxide flow rate. The turn-over rate is maximum at intermediate vanadia loading. This shows that vanadia species in two dimensional domains of appropriate size is most active while bulk vanadia phases are less active.

Characterization of spent catalysts with FTIR, UV-visible, EPR spectroscopies and XRD showed that vanadium exist in a higher oxidation state after the reaction in nitrous oxide atmosphere compared to that in nitrogen atmosphere. The higher average oxidation state of vanadium in nitrous oxide atmosphere explain the higher activity compared to that in nitrogen atmosphere. This is similar to the observation made for VO_x/Al_2O_3 catalysts.

Finally, Chapter 6 summarises the conclusions reached in this thesis and gives suggestions for further research.

6.2. General conclusions

It has been observed from this work that oxidative dehydrogenation of ethylbenzene using nitrous oxide as an oxidant is a promising alternate route for the production of styrene. The reaction can be operated at lower temperatures compared to the conventional catalytic dehydrogenation process. There is no need of huge amounts of steam which makes conventional process highly energy intensive. N_2O is a mild oxidizing agent unlike strongly

reactive molecular oxygen and gives only nitrogen as the by-product, which makes it a suitable oxidant for this reaction. The conversion of nitrous oxide is very high; hence the abatement of this green house gas can be achieved which reduce the problem of its emission to environment.

The catalytic performance is sensitive to structure of vanadia species. As revealed by this study, bulk vanadia phases are intrinsically less active than dispersed phases whether it is VO_x/Al_2O_3 or V-Mg-O catalysts. For both series, catalysts with apparent monolayer of vanadia species are most active. The nature of vanadia species depends on the support. When support is alumina, there is a gradual variation in molecular structure, from monomeric to polymeric and then finally to bulk-like vanadia species with increasing surface density (loading). Such a distinction is not clear when the support is MgO. Here, the interaction of added vanadia with the support is higher even at low loadings and results in amorphous magnesium orthovanadate phases at lower loadings and crystalline orthovanadate at higher loadings. This may be due to the higher basicity of MgO that cause greater interaction with slightly acidic vanadia leading to the formation of mixed phase even at low loadings. Alumina being acidic, the interaction of vanadia with alumina support is lower which is the reason for the formation of mainly vanadia phases in this case instead of mixed phases.

It is also an interesting observation that the activity, in terms of turnover rate, exhibits a different trend in PROX reaction for VO_x/Al_2O_3 catalysts. Here, the activity is inversely proportional to the vanadium surface density (loading), leading to the conclusion that monomeric vanadia species are most active. The monolayer loading doesn't seem to have much importance, unlike ODH of ethylbenzene. This may be explained probably considering the difference in nature of reactants. In PROX, the main reactants are CO and O_2 and monomeric vanadia species are sufficient for their adsorption before reaction. At low loadings, the dispersion of vanadia species is higher, hence the activity is higher. However, for geometrical reasons, adsorption of ethylbenzene will be more feasible when more than one vanadia species occur together on the surface which explains the higher activity with higher fraction of polymeric vanadia species for ODH of ethylbenzene. The bulk phases are very less active for both cases because of the lesser number of vanadia species available for reaction since the vanadium atoms that lie below the surface are not accessible for reactant molecules. The fact that VO_x/Al_2O_3 catalysts are active for PROX reaction while V-Mg-O catalysts are

not significantly active indicates the structure sensitivity of this reaction and the importance of nature of vanadia species and support interaction. The reaction may require dispersed vanadia species rather than mixed vanadia phases. The exact reasons have to be investigated in detail.

6.3. Suggestions for further research

This work shows that ODH of ethylbenzene using N_2O as the oxidant is promising as an alternate method for the conventional process. However, this is just a preliminary investigation in laboratory scale and a lot more work has to be carried out for developing a process. Only alumina and magnesia supports were examined in the current study while many other oxides like TiO_2, ZrO_2, CeO_2, SiO_2 and mixed metal oxides like Al_2O_3-SiO_2, CeO_2-ZrO_2, CeO_2-TiO_2 can be used as supports. The activity and selectivity of supported vanadium oxide catalysts are significantly affected by the properties of the support oxide material, which is generally known as the metal oxide-support effect [1]. The support has a strong influence on the overall reactivity. For example, the turnover frequency for the oxidation of methanol to formaldehyde varies by several orders of magnitude for the following supports: Al_2O_3, Nb_2O_5, TiO_2, ZrO_2, CeO_2 [2]. Hence the effect of different supports on the catalytic performance should be further investigated.

In the present study, catalysts were prepared by impregnation method. However, the effect of other preparation methods has to be studied. A method of preparation, which may increase the amount of vanadium that can be added to the catalyst without the formation of mixed oxides, will help to increase the activity. The catalysts can also be prepared with the controlled doping of a metal oxide additive like the oxides of K, Mo, W etc. The addition of these may improve the catalytic performance, which has to be investigated in detail. The selectivity of the catalyst has to be still improved, minimizing the amount of by-products to the maximum possible extent. Typical interacting additives like P and alkali/alkaline earth oxides (K, Na, Ca, etc.) modify the local structure of the surface vanadia species [3]. Typical non-interacting additives like surface oxides of W, Nb, S, Si, Mo, Ni, Co and Fe indirectly affect the molecular structure of the surface vanadia species via lateral interactions. Such lateral interactions have been found to influence the

ratio of polymerized to isolated surface vanadia species. However, the role of dopants on the structure and properties of supported vanadia is not yet fully understood.

The nature of active site may be investigated further, preferably *in situ* since the actual active species in the real reaction conditions can be revealed by these studies only. The techniques used in the present work are all *ex situ*, which reveal only the structure at ambient conditions that may or may not be similar to that in actual reaction conditions.

One significant problem observed with the present series of catalysts is deactivation. The industrial operation requires stable catalytic activity for a significantly longer period. Further research has to be carried out to optimize the catalyst, probably with the help of a promoter element, to achieve slow rate of deactivation.

It is also shown in the present work that alumina supported vanadia catalysts are reasonably active in preferential oxidation of CO in excess of hydrogen (PROX). Here also the reaction is very sensitive to catalyst structure. Polymeric and bulk vanadia phases on alumina are less active than monomeric species while vanadia supported on MgO is not significantly active which shows the structure sensitivity of the reaction. The activity shown by alumina supported vanadia assumes significance since the current operating PROX catalysts are prepared from costly alumina-supported Pt, Pd, Ru and Rh. Here also extensive further studies are required. The catalyst structure has to be optimized by varying different parameters like preparation methods, promoters etc. The rate of deactivation has to be minimized in this case also through suitable modification of the catalyst.

6.4. References

[1] B. M. Weckhuysen, D. E. Keller, Catal. Today, 78 (2003) 25.

[2] I. E. Wachs, G. Deo, M. V. Juskelis, B. M. Weckhuysen, in: Dynamics of Surfaces and Reaction Kinetics in Heterogeneous Catalysis, G. F. Froment, K. C. Waugh (Eds.), p. 305, Elsevier, Amsterdam, 1997.

[3] I. E. Wachs, B. M. Weckhuysen, Appl. Catal. A, 157 (1997) 67.